May 2019

Application of X-ray Grating Interferometry to Polymer/Flame Retardant Blends in Additive Manufacturing

Omoefe Joy Kio
Louisiana State University and Agricultural and Mechanical College

APPLICATION OF X-RAY GRATING INTERFEROMETRY TO POLYMER/FLAME RETARDANT BLENDS IN ADDITIVE MANUFACTURING

A Dissertation

Submitted to the Graduate Faculty of the
Louisiana State University and
Agricultural and Mechanical College
in partial fulfillment of the
requirements for the degree of
Doctor of Philosophy

in

The Department of Chemistry

by
Omoefe Joy Kio
B.S., University of Lagos, 2007
August 2019

To the creator of all, the God of the universe.

ACKNOWLEDGEMENTS

My sincere gratitude goes to Dr. Leslie Butler, my research advisor. By accepting me into his research group this project was set in motion. His guidance and instruction helped make this milestone a reality. He was approachable and patient as we tackled this project.

I would also like to thank Dr. Kyungmin Ham of LSU CAMD, her expertise came into play over and over again. She was easy to work with and had a great sense of humor. I would like to appreciate Dr. Miriam Sibenbeurger who has been a great help in the SAXS aspect of this work.

Former members of the Butler group; Adam Brooks, Mutairo Olatinwo and Jumao; Gerry Knapp and Bridget Cadigan are here acknowledged. Together we learnt and shared knowledge as we trod a somewhat unique path in the Chemistry department.

My warm thanks go to Dr. Andrew Maverick, Dr. Revati Kumar and Dr. Richard Kurtz for choosing to be part of my exam committee. Other faculty and staff of the chemistry department including Dr Thomas Weldgeghoris –of the NMR facilty and Ms. Kim Mollere are also appreciated.

Now to my family. I really appreciate the love and support I have enjoyed from my Husband, Dr. Abiola Olabode who was a wonderful example of a Ph.D. student to me. My love and appreciation go to our son Mark who always got me to make time for play. I appreciate my parents for the good upbringing I was given, and my siblings. My family has been a lovely one to be a part of and strong members of my support team.

To everyone mentioned here and those not mentioned that contributed one way or the other to this milestone, I cannot repay you. God bless you.

TABLE OF CONTENTS

ILLUSTRATIONS

Table

Figures

ABSTRACT

X-ray grating interferometry is a nondestructive tool for visualizing the internal structures of samples. Image contrast can be generated from the absorption of X-rays, the change in phase of the beam and small-angle X-ray scattering (dark-field). The attenuation and differential phase data obtained complement each other to give the internal composition of a material and large-scale structural information. The dark-field signal reveals sub-pixel structural detail usually invisible to the attenuation and phase probe, with the potential to highlight size distribution detail in a fashion faster than conventional small-angle scattering techniques. This work applies X-ray grating interferometry to the study of additively manufactured polymeric objects.

Additively manufactured bunnies made from single material—acrylonitrile butadiene styrene (ABS) and polylactic acid (PLA)—were studied by grating-based X-ray interferometric two-dimensional imaging and tomography. The dark-field images detected poor adhesion in the plane perpendicular to the build plate. Curvature analysis of the sample perimeter revealed a slightly higher propensity to errors in regions of higher curvature.

Incorporation of flame-retardant molecules to near-surface regions of otherwise flammable objects through the fused deposition modeling additive manufacturing technique was also explored. The anticipated advantage was efficient use of the flame retardants while keeping them away from the surface for safety.

To determine heat propagation effects, two-dimensional grating-based interferometry imaging at LSU CAMD was used to study heated samples. The focus was on the dark-field signals to highlight voids and gaps arising from layer delamination or gasification of chemical components. The resulting differential phase and dark-field

images were tainted by fringes attributed to inaccuracies in the grating-step position. Attempts to correct this will be presented. Interferometric tomography was also carried out on the heated samples using the W. M. Keck interferometric system at LSU. Grating-based interferometry was also used to probe scattering structure sizes of heated samples. Comparison of the data with the conventional small-angle x-ray scattering technique, SAXS, is being pursued.

The results obtained so far from the above-mentioned experimental works are presented in this document.

CHAPTER 1
INTRODUCTION

Since their discovery by Roentgen, X-rays have revolutionized the study of the composition of materials. X-ray imaging has become an indispensable tool in medical and materials imaging, amongst other applications. The wide applications of X-ray imaging drove research into improved devices for X-ray generation and detection.[1-4] Basic X-ray imaging yields a two-dimensional projection image based on the attenuation of the radiation through sample components of differing density or elemental composition. Repeated projection images of a sample from different angles can be collected digitally and superimposed by mathematical algorithms to obtain a three-dimensional representation of the sample. This technique called computed tomography (CT), enables visualization of components contributing to the two-dimensional projection. To obtain other contrast information, additional optical and electronic devices are incorporated into the imaging system. A recently developed evaluation technique, X-ray grating-based interferometry, that simultaneously yields three sets of signals—absorption, dark-field (small angle scattering) and phase contrast signals—has attracted some attention. The details of this technique will be presented later in this dissertation. Studies have been carried out to explore areas where this technique can be applied. In the pursuit of medical applications, X-ray grating-based interferometry has been used to study biological samples. Dark-field imaging of a healthy rat detected the collapsed lungs with improved contrast compared to phase imaging while undetectable with absorption imaging.[1] X-ray grating-based interferometry has also been used to visualize morphological changes in the lungs associated with pulmonary fibrosis in mice, with dark-field imaging detecting these changes well before they were observed in the absorption images.[5]

In the area of materials science, X-ray grating-based interferometry has been applied to cement, concrete and wood.[6-9] Following the comparison of different pearl products, it was reported that X-ray grating-based interferometry required shorter exposure time than that used in conventional radiography.[10] Application of X-ray grating-based interferometry to additively manufactured polymeric and metal parts has been pioneered by our group and some of the results will be presented in this dissertation.[11-14] The effect of incorporating flame retardants into otherwise flammable polymeric parts by additive manufacturing is also being explored.

1.1 Additive Manufacturing

Initially referred to as rapid prototyping and utilized for making prototypes and models, additive manufacturing (AM) has metamorphosed into a technology used for a variety of commercial manufacturing applications ranging from prototyping to end-use materials. The additive manufacturing process involves loading the CAD drawing of a desired object into a printer slicing software. The printer deposits material or energy based on the design slice-by-slice till the bulk material is complete or formed. The advantages of this technique over the conventional welding, molding or milling manufacturing technique are the reduction of waste and the ease of making complex geometries.[15,16] The wide application of additive manufacturing is however limited by the availability of raw materials in a suitable form and long production time thus, it is mostly applied in custom, low-volume production usually where there is some economic advantage.[16,17] There are different additive manufacturing processes including: stereolithography, 3D printing (3DP), fused deposition modeling (FDM), electron beam melting (EBM) and selective laser melting (SLM); Figure 1.1.[18,19] Depending on the

process, the feedstock can be in powder, filament, sheet or liquid form. Materials used include polymers, ceramics and metals.[15,20] There are a limited number of metal alloys available for AM, with Ti-6Al-4V being the most investigated.[13,20] Others are Al-Si-Mg, Inconel 625, stainless steel 316 and 420 etc.[20]

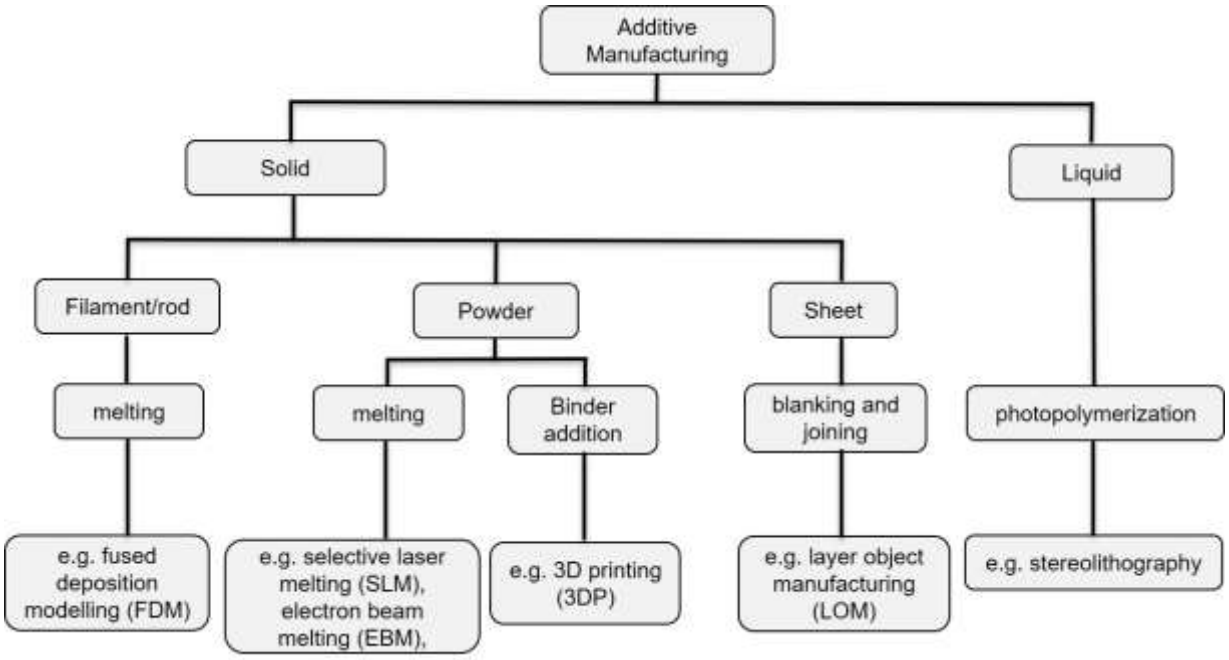

Figure 1.1. Classification of additive manufacturing techniques based on the physical state of feedstock. Adapted from reference 19.[19]

Additive manufacturing has found application in orthodontics; in orthopedics, research is still ongoing into its potential application as scaffolding for bone regeneration.[21-23] Patient-tailored medication via FDM has also been investigated.[24] The introduction of conductive inks into additive manufacturing increased the potential for printing of electronic components or devices.[25-27] General Electric's additively manufactured LEAP engine fuel nozzle currently powers planes around the world.[28,29] SpaceX's first manned spacecraft, Dragon V2, featured additively manufactured

combustion chambers.[30] Marchelli *et al.* investigated the use of virgin and recycled glass as a raw material for the 3D printing AM technique.[31]

It is important that the performance of additively manufactured parts is comparable to that of parts manufactured by conventional techniques. The slicing step typically introduces a staircase effect most evident on curved or inclined surfaces.[32] Temperature variation across print layers can lead to microstructural differences within a part, delamination of print layers, cracking and warpage in parts.[20,33] There is a general mechanical weakness in printed parts in the plane normal to the print bed.[20,34] These, in addition to the use of support structures usually necessitate one or more post-processing steps and may prevent the use of an additively manufactured part in some applications. Various research projects have been done on improving the mechanical strength of AM parts. Fiber reinforcement during printing for 3DP parts has been reported.[35] Shaffer *et al*. reported improving the thermomechanical properties of FDM objects by exposing the objects, post printing, to gamma radiation.[36] The polymers used were blended with special radiation sensitizers.

The fused deposition modeling AM technique involves extruding semi-molten thermoplastic polymers based on the slice model (Figure 1.2). The bulk part is the result of the cooling of fused slices. The common thermoplastics used are acrylonitrile butadiene styrene copolymers (ABS), polylactic acid (PLA), polycarbonate (PC), and polyamides (PA).[37,38] The potential of polypropylene as a material for FDM has also been studied.[39] Research into replacing polypropylene with poly-hydroxyalkanoates like poly(3-hydroxybutyrate) which is naturally occurring and exhibits similar properties as

polypropylene, is ongoing.[40,41] Poly(3-hydroxybutyrate) is also promising for tissue engineering via additive manufacturing.[42,43]

Studies on improving the mechanical properties of FDM parts have included reinforcements with other materials and print parameter optimization.[38,44-46] It was noted that ABS has been the material most studied.[46] Hwang *et al*. reported a decrease in the tensile strength of ABS-copper and ABS-iron composite parts.[45] Mohamed *et al*. presented an extensive review on research works into the effect of print parameters on surface roughness, dimensional accuracy and mechanical properties.[46] An integrated process-materials-design methodology for optimizing the mechanical performance of

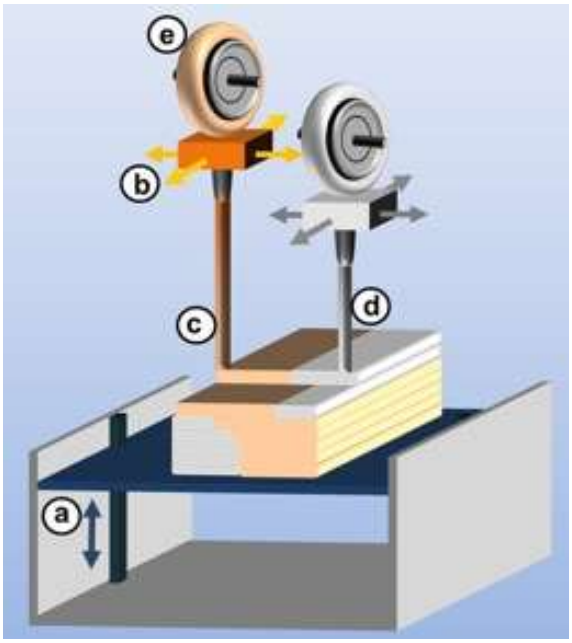

Figure 1.2. Schematic of a fused deposition modeling printer.[37] The components are (a) the build platform, (b) the print head where feedstock is heated and extruded from a nozzle, (c) one type of feedstock, (d) another type of feedstock and (e) the spool of a feedstock filament. Reprinted from Chemical Reviews, 117, Ligon S. C., Liska R., Stampfl J. R., Gurr M., and Mülhaupt R., Polymers for 3D printing and customized additive manufacturing, 10212 - 10290, Copyright (2017) with permission from ACS. https://pubs.acs.org/doi/abs/10.1021/acs.chemrev.7b00074. Permission requests should be directed to ACS.

ABS-based FDM parts was reported by Rodriguez et al.[47] Infrared thermography have been used to study temperature profiles of an FDM printed part during printing.[34]

The susceptibility of additively manufactured parts to faults and associated failures requires greater attention to quality evaluation. Internal evaluation of additively manufactured parts has majorly involved X-ray computed tomography.[48-51] Tetrahertz tomography imaging has been reported for the study of polymer-based parts and suggested as a cheaper alternative to X-ray CT.[52] SEM imaging can be applied to study failure regions of fractured parts.[53] Our research group pioneered the application of X-ray and neutron grating-based interferometry to study additively manufactured parts. Some of our works have been recently reported in peer reviewed journals.[11-14] Grating-based interferometry provides two additional sources of contrast mechanisms than X-ray radiography. Thus, there is a potential to extract more information about the printed part. A chapter is dedicated to addressing X-ray grating based interferometry (Chapter 3). Neutron interferometry studies of selective laser melted stainless steel tensile bars predicted the failure region before failure occurrence.[11,12]

The control in material placement afforded by additive manufacturing can be applied in material reaction or functionality, specifically in the way in which flame retardants are incorporated into otherwise flammable objects. It is important to see how the bulk material, with specific flame-retardant regions, “holds up” when exposed to heat.

1.2 Flame Retardants in Polymeric Materials

For the year 2017, the National Fire Protection Association reports that 3400 civilians died in fires and it is estimated that property damage was about $23 billion.[54] Due to the human and financial losses associated with fires, the flammability of polymeric

materials is of huge concern. The chemical reactions involved take place in three interdependent regions namely: within the condensed phase of the polymer itself, at the interface between the condensed phase and the gas phase, and in the gas phase (Fig. 1.3).[55,56] Volatile decomposition products may serve as fuel to sustain the burning process and/or pose a risk of asphyxiation or toxicity on inhalation. The combustion of the volatiles in the presence of oxygen involve a free radical chain mechanism.[57,58]

The following chemical reactions are possible steps in the combustion of methane and show how the very reactive species H•, OH• and O• may be formed.[58]

$$CH_4 + O_2 \rightarrow CH_3\bullet + H\bullet + O_2$$

$$H\bullet + O_2 \leftrightarrow OH\bullet + O\bullet$$

$$CH_4 + OH\bullet \rightarrow CH_3\bullet + H_2O$$

$$CH_3\bullet + O\bullet \rightarrow CH_2O + H\bullet$$

$$CH_2O + OH\bullet \rightarrow CHO\bullet + H_2O$$

$$CHO\bullet + O_2 \rightarrow H\bullet + CO + O_2$$

$$CO + OH\bullet \rightarrow CO_2 + H\bullet$$

In order for the process to be self-sustaining, it is necessary for the burning gases to feed back sufficient heat to the material to continue the production of gaseous fuel vapors or volatiles.[59] The main exothermic reaction that provides most of the heat to sustain burning is the reaction forming CO_2.[60]

In practice, the mechanism of polymer decomposition, and hence the nature of the products formed, depends strongly on polymer structure and, in particular, on the nature of the substituent groups attached to the main chain.[56] With thermoplastics, such as polyolefins and polystyrene, the primary polymer chain breakdowns and in extreme cases

simply ‘unzips’ to reform the original monomer leading to complete gasification and loss of physical integrity of the polymer.[56] Thus, relatively large amounts of combustible volatiles are formed.

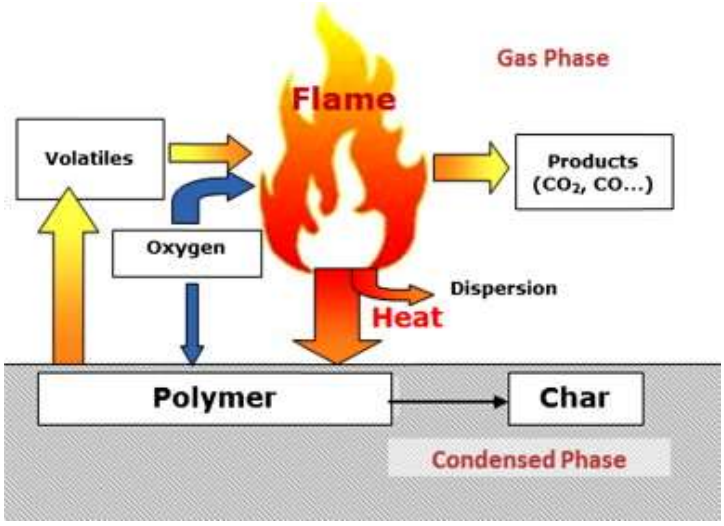

Figure 1.3. The polymer combustion cycle.[55] Oxygen in the air and flammable volatiles produced as the polymer thermally decomposes, burn and supply heat to sustain the combustion of the polymer. Reprinted from Materials Science and Engineering R, 84, Malucelli G., Carosio F., Alongi J., Fina A., Frache A., and Camino G., Materials engineering for surface-confined flame retardancy, 1 - 20, Copyright (2014), with permission from Elsevier.

With other polymers, the breakdown process consists merely of the detachment of the side chains; some volatile products are thus formed but the main chain remains virtually intact and provides some solid residue.[56] Alternatively, the polymer may suffer a molecular rearrangement, with hardly any weight loss or formation of volatile products, to give a polymer with a different structure.[56] This is the case with thermosetting plastics (e.g. phenolic resins and polyethers), where combustion is mainly that of the smoldering combustion of a solid residue or char.[56] Charring may slowdown the combustion process by inhibiting heat and mass transfer (volatiles) across the material’s surface thus, preventing complete breakdown of the material.[61]

In addition to the chemical changes occurring due to heating, thermoplastics may undergo a deformation into a fluid state where the material can flow or drip.[59] The effect of dripping or flowing material may be positive, where non-flaming material flows away from the heat source; or negative, where flaming material causes the fire to spread.[59,62] Crystallinity, aromatic content and crosslinking can raise the glass transition temperature of a polymer.[59]

Today, synthetic polymeric materials find applications as effective substitutes for steel, metal, wood etc.[63] It is important then that the flammability of the most widely used polymers in applications where fire safety is a concern, is addressed.[64] These areas include building and construction, electrical and electronics, and furniture and furnishings.[64] Examples of these polymers are acrylonitrile butadiene styrene (ABS), low density polyethylene (LDPE), polycarbonate, polystyrene, polyvinyl chloride, polyurethanes etc.[64] In a number of applications these material can be used only if they have been provided with a satisfactory fire retardant behavior.[55]

Though a flammable material cannot be made completely non-combustible, flame retardants can make ignition more difficult and/or decrease the rate of flame propagation when the material is exposed to a source of heat.[57] With a decreased rate of flame propagation there is an increase in time available for escape and rescue from a fire.[64] Flame retardants can act physically and/or chemically in one or more of the combustion regions to limit a material's flammability.[58,61] Physical action involves char formation, dilution of combustible volatiles by the formation of inert gases and heat sink effects where endothermic reactions occur leading to lower temperatures.[57,61,65] Chemical action

primarily involves intercepting the scavenging free radicals responsible for the branching of radical chain reactions in the flame.[62]

Different ways have been suggested to improve the fire behavior of polymers, such as the incorporation of FRs into polymers via melt blending (physical methods), the incorporation of FRs into the chemical structure of polymers (chemical methods, e.g. via copolymerization or grafting) and the coating of a FR layer on the surface of the material.[66,67] Depending on how they are incorporated into the substrate, flame retardants can be classified as reactive (chemically modifying the polymer or monomer) or additive (physically incorporated). In principle, incorporation of FRs into the chemical structure of polymers is the simplest way to achieve flame retardancy however, the resulting materials are generally very expensive to produce and do not possess many of the other physical properties such as processability, needed for wide acceptance.[56,61] Among these strategies, the incorporation of FRs into polymers via melt blending provides an acceptable compromise between cost and properties.[61,67]

Flame retardant additives are available as metal hydroxides, borates, halogenated compounds, phosphorus-based compounds, nanoclays and nanotubes etc.[65] For halogenated flame retardants, the choice halogens are bromine and chlorine as they can be readily released within the range of polymer combustion temperatures.[65] Halogenated flame retardants represent the most diversified class of flame retardants of which, brominated flame retardants maintain a good balance of physical properties, such as good impact and tensile strength and a high heat distortion temperature.[62]

On pyrolysis halogenated flame retardants yield HX, X_2 and RX products, where X is a halogen atom.[63] Halogenated flame retardants mostly function in the vapor phase by

intercepting the combustion free radical reactions, where halogen radicals replace the more reactive H•, OH• and O• in the vapor phase.[57,58,62,63,65] In the presence of a halogenated flame retardant the following reactions are possible.[65]

$$RX \rightarrow R\bullet + X\bullet$$

$$CH_4 + X\bullet \rightarrow HX + CH_3\bullet$$

$$HX + H\bullet \rightarrow H_2 + X\bullet$$

$$HX + OH\bullet \rightarrow H_2O + X\bullet$$

The hydrogen halide HX is readily regenerated from the from halide species and the combustible volatile (methane in this example). Antimony(III) oxide Sb_2O_3 has been found to be synergistic with halogenated flame retardants, catalyzing the dehalogenation of the flame retardant and prolonging the residence of the halogens in the flame zone.[62]

Previously common additive flame retardants—polybrominated biphenyls (PBBs), hexabromocyclododecane (HBCD) and polybrominated diphenyl ether (PBDE) compounds like penta- and octa-BDE have been phased out.[68] Examples of Brominated flame retardants currently used are shown in Fig. 1.4. 1,2,5,6-tetrabromocyclooctane (TBCO; used in expanded polystyrene), 1,2-dibromo-4-(1,2-dibromoethyl) cyclohexane (TBECH; used in polystyrene and polyurethane), and decabromodiphenylethane (DBDPE; used in styrene) are used as additive brominated flame retardants.[68] Reactive brominated flame retardants include tetrabromobisphenol A (TBBPA; used in epoxies and ABS), tetrabromophthalic anhydride (TBPA; used in unsaturated polyesters, styrene-butadiene copolymers etc.), 2,4,6-tribromophenol (TBP; used in phenolics, epoxies).[68] TBBPA is used as an additive flame retardant in a few applications.

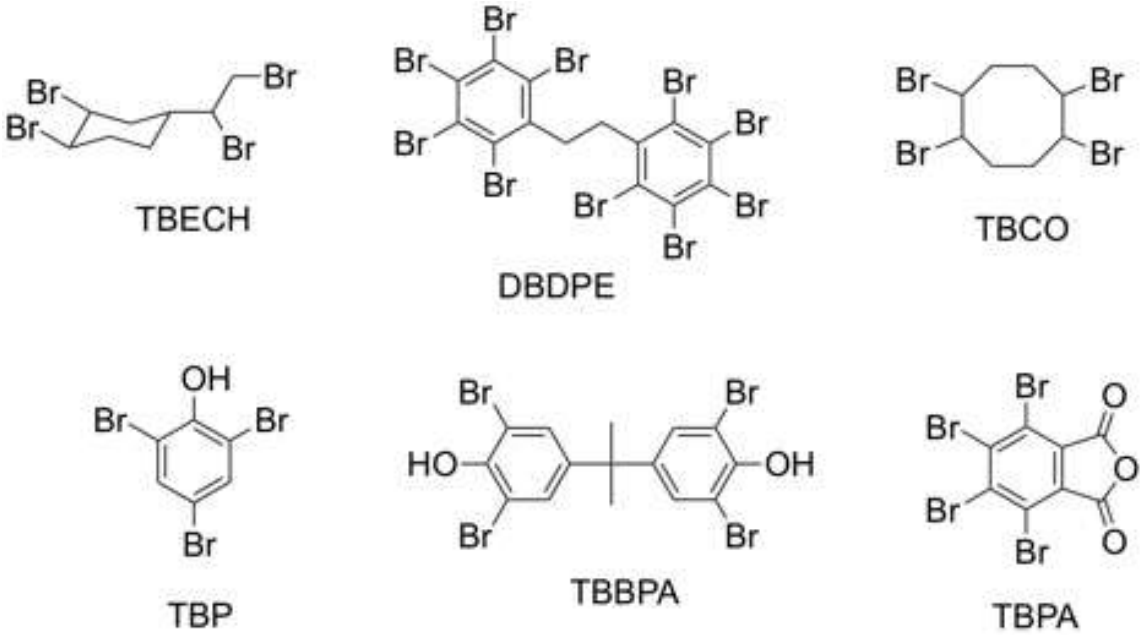

Figure 1.4. Examples of common brominated flame retardants.

Phosphorus-based flame retardants are the second most widely used class of flame retardants but are more specific in their action on certain polymers than the halogen-based products i.e. the mechanism of action depends on both the type of phosphorus compound and the specific polymer.[62] Phosphorus compounds are effective flame retardants for oxygen- or nitrogen-containing polymers and show little efficacy in polyolefins and styrenics.[58,62] Phosphorus-containing flame retardants include phosphate esters, phosphonates, phosphine oxides, chlorophosphates, chlorophosphonates, red phosphorus, and inorganic phosphates.[58] They appear to function in the condensed phase where they can promote char or coat the char surface with viscous phosphoric acids, in the vapor phase where they can function by the free radical trap process, or physically by promoting dripping of the burning polymer.[58]

Red phosphorus acts in the vapor phase through its breakdown in fire to produce P_2 molecules.[69] It is used in polycarbonates, polyamides, polyethylene terephthalate etc.[70] Though red phosphorus can react with moisture to form the toxic phosphine gas,

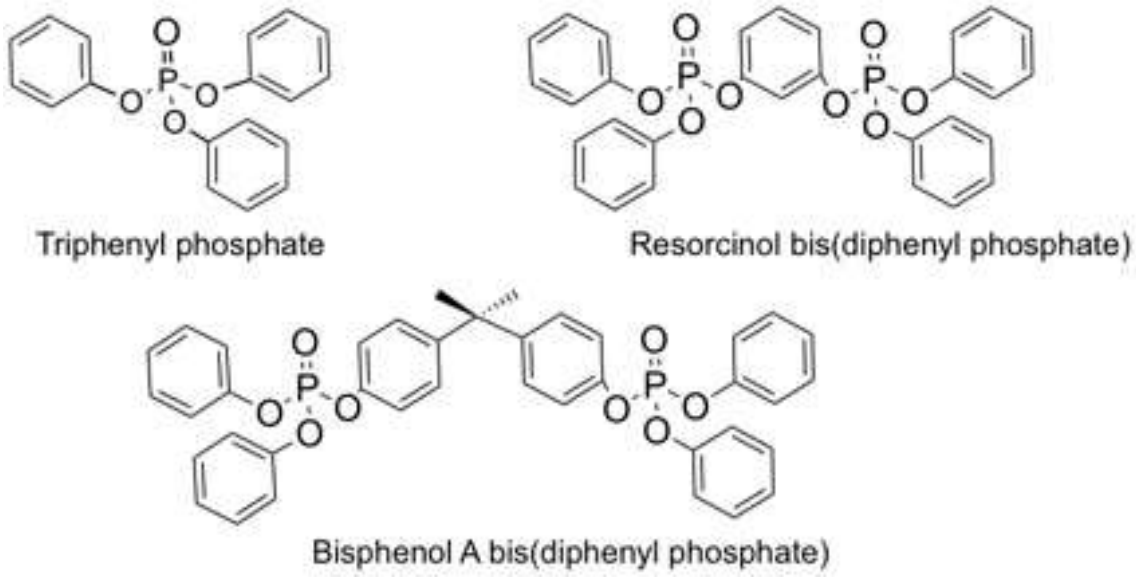

Figure 1.5. Examples of Phosphorus-based flame retardants.

phosphorus-based flame retardants are generally not harmful.[69] Thermal oxidation of phosphorus compounds mostly yield P_2O_5 which then hydrolyses to polyphosphoric acid and contributes to char.[69] Ammonium phosphate is a polymeric compound used in intumescent coatings and paints.[70] Phosphorus-based flame retardants have found application in polycarbonates e.g. bisphenol A bis(diphenyl phosphate), in textiles e.g. diethylphosphinate salts, in epoxies e.g derivatives of 9,10-dihydro-9-oxa-10-phosphaphenanthrene-10-oxide (DOPO) etc.[71,72] Triphenyl phosphate and resorcinol bis(diphenyl phosphate) are used to retard flammability in polycarbonates and polycarbonate blends such as polycarbonate/ABS.[58] Structures of some common phosphorus-based flame retardants are shown in Fig. 1.5. There are some phosphorus-

based flame retardants that also contain halogens.[70] They may be used in combination with a bromine flame retardant. The mode of action is presumably in the vapor phase as these materials are volatile.[58] Starch in addition to phosphorus-based flame retardant improved the drippling behavior of PLA sheets and foams.[73]

Inorganic metal compounds e.g. aluminum hydroxide, magnesium hydroxide, and magnesium carbonate decompose endothermically lowering temperature and releasing water to dilute volatile products.[58,69] They are cheap and easy to obtain but require high loadings to be effective which can unfavorably modify the substrates' properties.[69] Major applications include unsaturated polyester and polyethylene.[58] Compounds of boron interfere with the decomposition process to favor carbon formation over CO or CO_2.[74] They have a synergistic effect particularly with halogen systems.[74] Aromatic boric acids are used for ABS and polycarbonate systems.[74] Sang *et al.* published an extensive review on the studies of graphene and graphene oxide as stand-alone flame retardants and in combination with known flame retardants.[67] Inorganic nanomaterials-graphene composites were deemed most promising. The flammability of paper was suppressed by coating pulp fibers with nanometer thin films of cationic chitosan and anionic poly(vinylphosponic acid).[75] Starch in addition to phosphorus-based flame retardant improved the dripping behavior of PLA sheets and foams.[73]

Restrictions on halogen-based fire retardants have led to an increased interest in building fire protections onto the polymer surface to prevent heat transfer and diffusion of volatiles across the material surface.[55] A review by Malucelli *et al.* covers how new nanotechnologies, like layer by layer nano-deposition, developed for polymer surface engineering, can be exploited for flame retardancy.[55]

Acrylonitrile-butadiene-styrene (ABS) is widely used due to an excellent combination of mechanical, thermal and electrical properties, and chemical resistance.[76] Fire retardance is generally imparted to ABS by means of additives, among which brominated organic compounds are widely used.[76] In a study of the fire retarding effect of the brominated additives nonabromobiphenyl (NBBP), octabromodiphenyl oxide (OBDPO) and bis(tribromophenoxy) ethane (BTBPE) on ABS, it was reported that their fire retarding abilities depended on chemical structure.[76] It was also concluded that the antimony-bromine synergism in these systems, was mostly independent of the chemical structure of the brominated additive.[76]

Flame retardancy can be characterized using various tests such as cone calorimetry, limiting oxygen index (LOI), UL-94, single burning item (SBI) and glow wire.[65,66,77-79] Flame retardancy has also been studied using X-ray K-edge tomography and X-ray interferometry.[80,81] A method to estimate the relationship between a molecule's structure and its flammability by calculating an interaction index has been purposed.[82]

1.3 Flammability Tests

1.3.1 Limiting Oxygen Index (LOI)

This is a simple and common test standardized as ASTM D2863 and ISO 4589. It determines the minimum oxygen concentration in an oxygen/nitrogen mixture that will just about support flaming combustion of a plastic substrate for a given amount of time or consume a certain amount of the substrate depending on the sample form.[65,83] It is carried out in a transparent glass tube chimney, which is purged with the oxygen/nitrogen gas mixture before the material is ignited (Figure 1.6). LOI is expressed in volume percent as:

$$LOI = 100\frac{[O_2]}{[O_2] + [N_2]},$$

where $[O_2]$ and $[N_2]$ refers to the volume concentrations of oxygen and nitrogen in the mixture used.

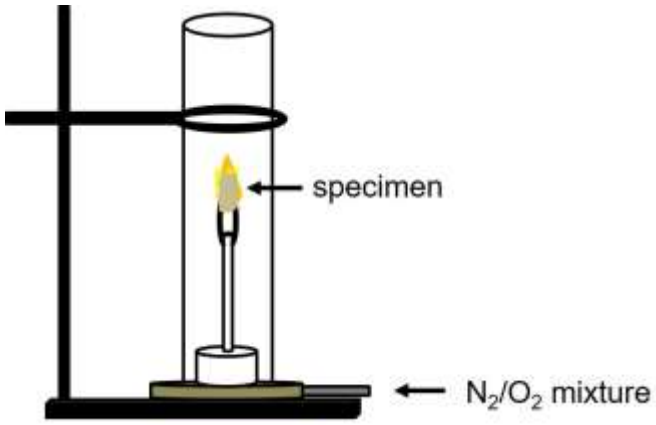

Figure 1.6. The limiting oxygen index flammability test.

1.3.2 UL-94 Test

This test is approved by the Underwriters Laboratories to test the flammability of plastics used in devices and appliances. It is standardized in the United States as ASTM D3801. Test specimens of a prescribed dimension are clamped with the longitudinal axis vertically oriented (Figure 1.7). A blue flame with a 20 mm high central cone and a power of 50 W is applied to the test specimen for 10 s.[65] The afterflame time t_1 (the time required for the flame to extinguish) is recorded. After extinction, the flame is applied for another 10 s and the afterflame time t_2 as well as the afterglow time t_3 (the time required for the fire glow to disappear) are recorded.[65,84] Occurrence of material dripping and ignition of a cotton ball placed beneath the tested specimen is noted. The test must be repeated for a total of five identical specimens. Depending on the afterflame and afterglow times and the ignition of the cotton ball by flaming drops or particles; the material may be classified as V-0, V-1 or V-2. V-2 is for a case where the cotton ball ignites.

A paper by Dupretz *et al.* introduced additional instrumentation to the UL-94 test to measure the weight of droplets, the weight loss of the sample as well as the temperature gradients during the fire test with the aim of better understanding the mechanisms occurring in the material during the test.[79]

1.3.3 Glow-wire Ignition Test

The glow-wire test was designed to assess the susceptibility of electrical insulating materials or parts in contact with wires to ignition due to a glowing wire.[85] Standardized in the United States as ASTM D6194, it involves exposing a vertically supported standardized test specimen to electrical heating from a glow-wire set at pre-determined temperatures.[86] The glow-wire apparatus is designed to apply a force of 1 ±0.2 N to the specimen. By increasing the applied temperature, the minimum temperature for glow-wire ignition is determined.

1.3.4 Cone Calorimeter Test

The cone calorimeter is a specialized piece of fire test equipment that is used to assess heat release data, as well as ignitability, mass loss and smoke released by burning materials.[87] A schematic representation of the equipment is shown in Figure 1.8. The cone calorimeter test is standardized in the United States as ASTM E1354 and internationally as ISO 5660. It is based on the measurement of the decreasing oxygen concentration in the combustion gases of a sample subjected to a given heat flux (in general from 10 to 100 kW/m^2).[65] The gas flow; oxygen, CO and CO_2 concentrations and smoke density are measured during the test.[65]

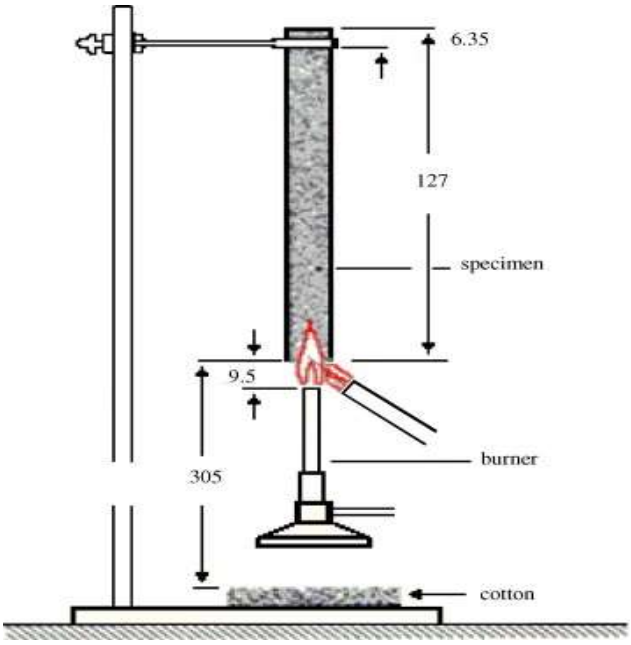

Figure 1.7. The UL-94 flammability test.[65] Reprinted from Materials Science and Engineering R, 63, Laoutid F., Bonnaud L., Alexandre M., Lopez-Cuesta J.-M., and Dubois Ph., New prospects in flame retardant polymer materials: From fundamentals to nanocomposites, 100 -125, Copyright (2008), with permission from Elsevier.

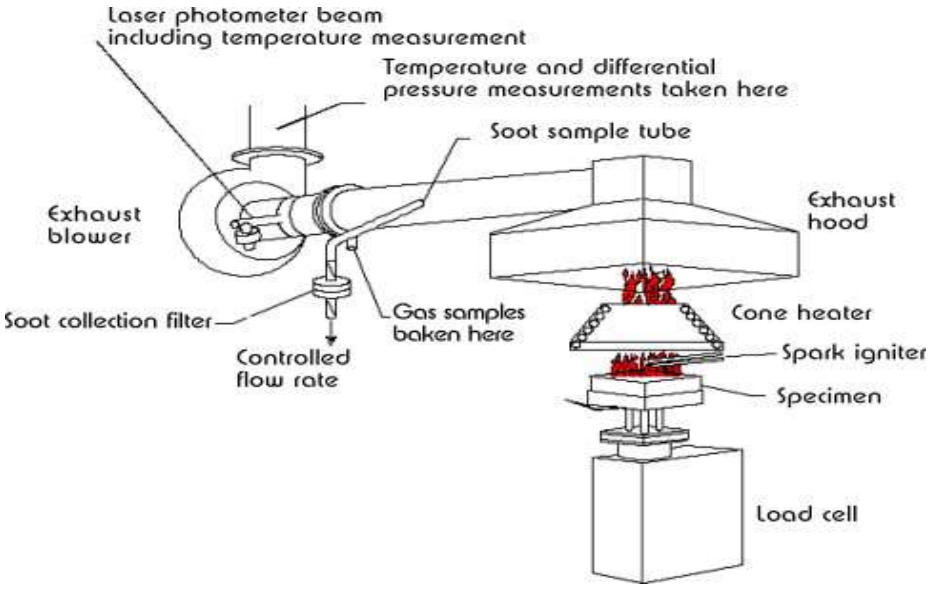

Figure 1.8. The cone calorimeter.[65] The volatile combustion products, smoke and soot are collected through the exhaust hood for analyses. Reprinted from Materials Science and Engineering R, 63, Laoutid F., Bonnaud L., Alexandre M., Lopez-Cuesta J.-M., and Dubois Ph., New prospects in flame retardant polymer materials: From fundamentals to nanocomposites, 100 -125, Copyright (2008), with permission from Elsevier.

In this dissertation, subsurface incorporation of flame retardants by additive manufacturing was explored. Heat effects was studied by X-ray grating interferometry imaging with a modified glow-wire incorporated into the X–ray grating interferometer.

1.4 References

1. Gkoumas, S.; Wang, Z.; Abis, M.; Arboleda, C.; Tudosie, G.; Donath, T.; Brönnimann, C.; Schulze-Briese, C.; Stampanoni, M., Grating-based interferometry and hybrid photon counting detectors: Towards a new era in X-ray medical imaging. *Nuclear Instruments and Methods in Physics Research Section A: Accelerators, Spectrometers, Detectors and Associated Equipment* **2016,** *809*, 23-30.

2. Panetta, D., Advances in X-ray detectors for clinical and preclinical Computed Tomography. *Nuclear Instruments and Methods in Physics Research Section A: Accelerators, Spectrometers, Detectors and Associated Equipment* **2016,** *809*, 2-12.

3. Donald, H. B.; Pascal, E.; Edgar, W., Review of third and next generation synchrotron light sources. *Journal of Physics B: Atomic, Molecular and Optical Physics* **2005,** *38* (9), S773-S797.

4. Nakajima, K., Towards a table-top free-electron laser. *Nature Physics* **2008,** *4*, 92-93.

5. Yaroshenko, A.; Hellbach, K.; Yildirim, A. Ö.; Conlon, T. M.; Fernandez, I. E.; Bech, M.; Velroyen, A.; Meinel, F. G.; Auweter, S.; Reiser, M.; Eickelberg, O.; Pfeiffer, F., Improved In vivo Assessment of Pulmonary Fibrosis in Mice using X-Ray Dark-Field Radiography. *Scientific Reports* **2015,** *5*, No. 17492.

6. Prade, F.; Chabior, M.; Malm, F.; Grosse, C. U.; Pfeiffer, F., Observing the setting and hardening of cementitious materials by X-ray dark-field radiography. *Cement and Concrete Research* **2015,** *74*, 19-25.

7. Sarapata, A.; Ruiz-Yaniz, M.; Zanette, I.; Rack, A.; Pfeiffer, F.; Herzen, J., Multi-contrast 3D X-ray imaging of porous and composite materials. *Applied Physics Letters* **2015,** *106* (15), 154102.

8. Trtik, P.; Dual, J.; Keunecke, D.; Mannes, D.; Niemz, P.; Stähli, P.; Kaestner, A.; Groso, A.; Stampanoni, M., 3D imaging of microstructure of spruce wood. *Journal of Structural Biology* **2007,** *159* (1), 46-55.

9. Malecki, A.; Eggl, E.; Schaff, F.; Potdevin, G.; Baum, T.; Garcia, E. G.; Bauer, J. S.; Pfeiffer, F., Correlation of X-Ray Dark-Field Radiography to Mechanical Sample Properties. *Microscopy and Microanalysis* **2014,** *20* (05), 1528-1533.

10. Revol, V.; Hanser, C.; Krzemnicki, M., Characterization of pearls by X-ray phase contrast imaging with a grating interferometer. *Case Studies in Nondestructive Testing and Evaluation* **2016,** *6, Part A*, 1-7.

11. Brooks, A. J.; Yao, H.; Yuan, J.; Kio, O.; Lowery, C. G.; Markötter, H.; Kardjilov, N.; Guo, S.; Butler, L. G., Early detection of fracture failure in SLM AM tension testing with Talbot-Lau neutron interferometry. *Additive Manufacturing* **2018,** *22*, 658-664.

12. Brooks, A. J.; Hussey, D. S.; Yao, H.; Haghshenas, A.; Yuan, J.; LaManna, J. M.; Jacobson, D. L.; Lowery, C. G.; Kardjilov, N.; Guo, S.; Khonsari, M. M.; Butler, L. G., Neutron interferometry detection of early crack formation caused by bending fatigue in additively manufactured SS316 dogbones. *Materials & Design* **2018,** *140*, 420-430.

13. Brooks, A. J.; Ge, J.; Kirka, M. M.; Dehoff, R. R.; Bilheux, H. Z.; Kardjilov, N.; Manke, I.; Butler, L. G., Porosity detection in electron beam-melted Ti-6Al-4V using high-resolution neutron imaging and grating-based interferometry. *Progress in Additive Manufacturing* **2017,** *2* (3), 125-132.

14. Kio, O. J.; Yuan, J.; Brooks, A. J.; Knapp, G. L.; Ham, K.; Ge, J.; Van Loo, D.; Butler, L. G., Non-destructive evaluation of additively manufactured polymer objects using X-ray interferometry. *Additive Manufacturing* **2018,** *24*, 364-372.

15. Ribeiro, F., 3d printing with metals. *Computing & Control Engineering Journal* **1998,** *9* (1), 31-38.

16. Campbell, T.; Williams, C.; Ivanova, O.; Garrett, B., Could 3D printing change the world? Technologies, Potential, and Implications of Additive Manufacturing. *Strategic Foresight Report, Atlantic Council, Washington, DC* **2011**.

17. Conner, B. P.; Manogharan, G. P.; Martof, A. N.; Rodomsky, L. M.; Rodomsky, C. M.; Jordan, D. C.; Limperos, J. W., Making sense of 3-D printing: Creating a map of additive manufacturing products and services. *Additive Manufacturing* **2014,** *1*, 64-76.

18. Wong, K. V.; Hernandez, A., A review of additive manufacturing. *ISRN Mechanical Engineering* **2012,** *2012*, No. 208760.

19. Wendel, B.; Rietzel, D.; Kühnlein, F.; Feulner, R.; Hülder, G.; Schmachtenberg, E., Additive processing of polymers. *Macromolecular materials and engineering* **2008,** *293* (10), 799-809.

20. Frazier, W. E., Metal Additive Manufacturing: A Review. *Journal of Materials Engineering and Performance* **2014,** *23* (6), 1917-1928.

21. Martorelli, M.; Gerbino, S.; Giudice, M.; Ausiello, P., A comparison between customized clear and removable orthodontic appliances manufactured using RP and CNC techniques. *Dental Materials* **2013,** *29* (2), e1-e10.

22. Inzana, J. A.; Olvera, D.; Fuller, S. M.; Kelly, J. P.; Graeve, O. A.; Schwarz, E. M.; Kates, S. L.; Awad, H. A., 3D printing of composite calcium phosphate and collagen scaffolds for bone regeneration. *Biomaterials* **2014,** *35* (13), 4026-4034.

23. Zhou, Z.; Buchanan, F.; Mitchell, C.; Dunne, N., Printability of calcium phosphate: Calcium sulfate powders for the application of tissue engineered bone scaffolds using the 3D printing technique. *Materials Science and Engineering: C* **2014,** *38*, 1-10.

24. Skowyra, J.; Pietrzak, K.; Alhnan, M. A., Fabrication of extended-release patient-tailored prednisolone tablets via fused deposition modelling (FDM) 3D printing. *European Journal of Pharmaceutical Sciences* **2015,** *68*, 11-17.

25. Walker, S. B.; Lewis, J. A., Reactive silver inks for patterning high-conductivity features at mild temperatures. *Journal of the American Chemical Society* **2012,** *134* (3), 1419-1421.

26. Wei, T.-S.; Ahn, B. Y.; Grotto, J.; Lewis, J. A., 3D Printing of Customized Li-Ion Batteries with Thick Electrodes. *Advanced Materials* **2018,** *30* (16), No. 1703027.

27. Hoerber, J.; Glasschroeder, J.; Pfeffer, M.; Schilp, J.; Zaeh, M.; Franke, J., Approaches for additive manufacturing of 3D electronic applications. *Procedia CIRP* **2014,** *17*, 806-811.

28. Yokozeki, S.; Suzuki, T., Shearing Interferometer Using the Grating as the Beam Splitter. *Appl. Opt.* **1971,** *10* (7), 1575-1580.

29. Seifi, M.; Salem, A.; Beuth, J.; Harrysson, O.; Lewandowski, J. J., Overview of Materials Qualification Needs for Metal Additive Manufacturing. *JOM* **2016,** *68* (3), 747-764.

30. Waller, J. M.; Parker, B. H.; Hodges, K. L.; Burke, E. R.; Walker, J. L. *Nondestructive evaluation of additive manufacturing state-of-the-discipline report*; Nov 2014.

31. Bourell, D.; Stucker, B.; Marchelli, G.; Prabhakar, R.; Storti, D.; Ganter, M., The guide to glass 3D printing: developments, methods, diagnostics and results. *Rapid Prototyping Journal* **2011,** *17* (3), 187-194.

32. Oropallo, W.; Piegl, L., Ten challenges in 3D printing. *Engineering with Computers* **2015**, 1-14.

33. Turner, B. N.; Gold, S. A., A review of melt extrusion additive manufacturing processes: II. Materials, dimensional accuracy, and surface roughness. *Rapid Prototyping Journal* **2015,** *21* (3), 250-261.

34. Seppala, J. E.; Migler, K. D., Infrared thermography of welding zones produced by polymer extrusion additive manufacturing. *Additive manufacturing* **2016,** *12*, 71-76.

35. Christ, S.; Schnabel, M.; Vorndran, E.; Groll, J.; Gbureck, U., Fiber reinforcement during 3D printing. *Materials Letters* **2015,** *139*, 165-168.

36. Shaffer, S.; Yang, K.; Vargas, J.; Di Prima, M. A.; Voit, W., On reducing anisotropy in 3D printed polymers via ionizing radiation. *Polymer* **2014,** *55* (23), 5969-5979.

37. Ligon, S. C.; Liska, R.; Stampfl, J. r.; Gurr, M.; Mülhaupt, R., Polymers for 3D printing and customized additive manufacturing. *Chemical reviews* **2017,** *117* (15), 10212-10290.

38. Domingo-Espin, M.; Puigoriol-Forcada, J. M.; Garcia-Granada, A.-A.; Lluma, J.; Borros, S.; Reyes, G., Mechanical property characterization and simulation of fused deposition modeling Polycarbonate parts. *Materials & Design* **2015,** *83*, 670-677.

39. Carneiro, O. S.; Silva, A. F.; Gomes, R., Fused deposition modeling with polypropylene. *Materials & Design* **2015,** *83*, 768-776.

40. Dunn, E. W.; Coates, G. W., Carbonylative Polymerization of Propylene Oxide: A Multicatalytic Approach to the Synthesis of Poly(3-Hydroxybutyrate). *Journal of the American Chemical Society* **2010,** *132* (33), 11412-11413.

41. Leja, K.; Lewandowicz, G., Polymer Biodegradation and Biodegradable Polymers-a Review. *Polish Journal of Environmental Studies* **2010,** *19* (2), 256-266.

42. Přemysl, M.; Radek, P.; Ivana, S.; Veronika, M.; Soňa, K.; Silvestr, F.; Pavol, A.; Ján, B., Effect of Selected Commercial Plasticizers on Mechanical, Thermal, and Morphological Properties of Poly(3-hydroxybutyrate)/Poly(lactic acid)/Plasticizer Biodegradable Blends for Three-Dimensional (3D) Print. *Materials, Vol 11, Iss 10, p 1893 (2018)* **2018,** (10), No. 1893.

43. Saska, S.; Pires, L. C.; Cominotte, M. A.; Mendes, L. S.; de Oliveira, M. F.; Maia, I. A.; da Silva, J. V. L.; Ribeiro, S. J. L.; Cirelli, J. A., Three-dimensional printing and in vitro evaluation of poly(3-hydroxybutyrate) scaffolds functionalized with osteogenic growth peptide for tissue engineering. *Materials Science & Engineering C* **2018,** *89*, 265-273.

44. Ning, F.; Cong, W.; Qiu, J.; Wei, J.; Wang, S., Additive manufacturing of carbon fiber reinforced thermoplastic composites using fused deposition modeling. *Composites Part B: Engineering* **2015,** *80*, 369-378.

45. Hwang, S.; Reyes, E. I.; Moon, K.-s.; Rumpf, R. C.; Kim, N. S., Thermo-mechanical Characterization of Metal/Polymer Composite Filaments and Printing Parameter Study for Fused Deposition Modeling in the 3D Printing Process. *Journal of Electronic Materials* **2015,** *44* (3), 771-777.

46. Mohamed, O. A.; Masood, S. H.; Bhowmik, J. L., Optimization of fused deposition modeling process parameters: a review of current research and future prospects. *Advances in Manufacturing* **2015,** *3* (1), 42-53.

47. Rodríguez, J. F.; Thomas, J. P.; Renaud, J. E., Design of Fused-Deposition ABS Components for Stiffness and Strength. *Journal of Mechanical Design* **2003,** *125* (3), 545-551.

48. Moini, M.; Olek, J.; Magee, B.; Zavattieri, P.; Youngblood, J. In *Additive Manufacturing and Characterization of Architectured Cement-Based Materials via X-ray Micro-computed Tomography*, Cham, Springer International Publishing: Cham, 2018; pp 176-189.

49. Carlton, H. D.; Haboub, A.; Gallegos, G. F.; Parkinson, D. Y.; MacDowell, A. A., Damage evolution and failure mechanisms in additively manufactured stainless steel. *Materials Science and Engineering: A* **2016,** *651*, 406-414.

50. Thompson, A.; Maskery, I.; Leach, R. K., X-ray computed tomography for additive manufacturing: a review. *Measurement Science and Technology* **2016,** *27* (7), No. 072001.

51. Shah, P.; Racasan, R.; Bills, P., Comparison of different additive manufacturing methods using computed tomography. *Case Studies in Nondestructive Testing and Evaluation* **2016,** *6*, 69-78.

52. Perraud, J. B.; Obaton, A. F.; Bou-Sleiman, J.; Recur, B.; Balacey, H.; Darracq, F.; Guillet, J. P.; Mounaix, P., Terahertz imaging and tomography as efficient instruments for testing polymer additive manufacturing objects. *Appl. Opt.* **2016,** *55* (13), 3462-3467.

53. Ziemian, C.; Sharma, M.; Ziemian, S., Anisotropic mechanical properties of ABS parts fabricated by fused deposition modelling. In *Mechanical engineering*, InTechOpen: 2012.

54. Evarts, B. *Fire Loss in the United States During 2017*; National Fire Protection Association, Quincy, MA: 2018.

55. Malucelli, G.; Carosio, F.; Alongi, J.; Fina, A.; Frache, A.; Camino, G., Materials engineering for surface-confined flame retardancy. *Materials Science and Engineering: R: Reports* **2014,** *84*, 1-20.

56. Cullis, C. F., Thermal stability and flammability of organic polymers. *British polymer journal* **1984,** *16* (4), 253-257.

57. Camino, G.; Costa, L., Performance and mechanisms of fire retardants in polymers—A review. *Polymer Degradation and Stability* **1988,** *20* (3), 271-294.

58. Green, J., Mechanisms for flame retardancy and smoke suppression-a review. *Journal of Fire & Flammability* **1996,** *14* (6), 426-442.

59. Beyler, C. L.; Hirschler, M. M., Thermal decomposition of polymers. *SFPE handbook of fire protection engineering* **2002,** *2*, 110-131.

60. Xu, T., Recent Developments in Different Techniques Used for the Flame Retardancy. In *Flame Retardants: Polymer Blends, Composites and Nanocomposites*, Visakh, P. M.; Arao, Y., Eds. Springer International Publishing: Cham, 2015; pp 45-77.

61. Bourbigot, S.; Fontaine, G., Flame retardancy of polylactide: an overview. *Polymer Chemistry* **2010,** *1* (9), 1413-1422.

62. Levchik, S. V., Introduction to flame retardancy and polymer flammability. *Flame retardant polymer nanocomposites* **2007**, 1-29.

63. Aseeva, R. M.; Zaikov, G. E., Flammability of polymeric materials. In *Key Polymers Properties and Performance*, Springer: 1985; pp 171-229.

64. Hirschler, M. M., Flame retardants and heat release: review of data on individual polymers. *Fire and Materials* **2015,** *39* (3), 232-258.

65. Laoutid, F.; Bonnaud, L.; Alexandre, M.; Lopez-Cuesta, J. M.; Dubois, P., New prospects in flame retardant polymer materials: From fundamentals to nanocomposites. *Materials Science and Engineering: R: Reports* **2009,** *63* (3), 100-125.

66. Vahabi, H.; Sonnier, R.; Ferry, L., Effects of ageing on the fire behaviour of flame-retarded polymers: a review. *Polymer International* **2015,** *64* (3), 313-328.

67. Sang, B.; Li, Z.-w.; Li, X.-h.; Yu, L.-g.; Zhang, Z.-j., Graphene-based flame retardants: a review. *Journal of materials science* **2016,** *51* (18), 8271-8295.

68. Guerra, P.; Alaee, M.; Eljarrat, E.; Barceló, D., Introduction to Brominated Flame Retardants: Commercially Products, Applications, and Physicochemical Properties. In *Brominated Flame Retardants*, Eljarrat, E.; Barceló, D., Eds. Springer Berlin Heidelberg: Berlin, Heidelberg, 2011; pp 1-17.

69. Rakotomalala, M.; Wagner, S.; Döring, M., Recent developments in halogen free flame retardants for epoxy resins for electrical and electronic applications. *Materials* **2010,** *3* (8), 4300-4327.

70. Mihajlović, I., Recent Development of Phosphorus Flame Retardants in Thermoplastic Blends and Nanocomposites. In *Flame Retardants: Polymer Blends, Composites and Nanocomposites*, Visakh, P. M.; Arao, Y., Eds. Springer International Publishing: Cham, 2015; pp 79-114.

71. Levchik, S. V.; Weil, E. D., A Review of Recent Progress in Phosphorus-based Flame Retardants. *Journal of Fire Sciences* **2006,** *24* (5), 345-364.

72. Pack, S. In *A review of non-halogen flame retardants in epoxy-based composites and nanocomposites: Flame retardancy and rheological properties*, Flame Retardants, Springer: 2015; pp 115-130.

73. Wang, J.; Ren, Q.; Zheng, W.; Zhai, W., Improved flame-retardant properties of poly (lactic acid) foams using starch as a natural charring agent. *Industrial & Engineering Chemistry Research* **2014,** *53* (4), 1422-1430.

74. Lu, S.-Y.; Hamerton, I., Recent developments in the chemistry of halogen-free flame retardant polymers. *Progress in Polymer Science* **2002,** *27* (8), 1661-1712.

75. Köklükaya, O.; Carosio, F.; Grunlan, J. C.; Wågberg, L., Flame-Retardant Paper from Wood Fibers Functionalized via Layer-by-Layer Assembly. *ACS Applied Materials & Interfaces* **2015,** *7* (42), 23750-23759.

76. di Cortemiglia, M. L.; Camino, G.; Costa, L.; Roma, P.; Rossi, A., Mechanism of action and pyrolysis of brominated fire retardants in acrylonitrile-butadiene-styrene polymers. *Journal of Analytical and Applied Pyrolysis* **1987,** *11*, 511-526.

77. Claus, V.; Anett, M.; Dieter, L.; Frank, T., Characterization of the Burning Behaviour of Plastics by a New Method. *Open Journal of Polymer Chemistry* **2012,** *2*, 86-90.

78. Acquasanta, F.; Berti, C.; Colonna, M.; Fiorini, M.; Karanam, S., Glow wire ignition temperature (GWIT) and comparative tracking index (CTI) of glass fibre filled engineering polymers, blends and flame retarded formulations. *Polymer Degradation and Stability* **2011,** *96* (12), 2098-2103.

79. Dupretz, R.; Fontaine, G.; Duquesne, S.; Bourbigot, S., Instrumentation of UL-94 test: understanding of mechanisms involved in fire retardancy of polymers. *Polymers for Advanced Technologies* **2015,** *26* (7), 865-873.

80. Olatinwo, M. B.; Ham, K.; McCarney, J.; Marathe, S.; Ge, J.; Knapp, G.; Butler, L. G., Analysis of flame retardancy in polymer blends by synchrotron X-ray K-edge tomography and interferometric phase contrast movies. *The Journal of Physical Chemistry B* **2016,** *120* (9), 2612-2624.

81. Olatinwo, M. B.; Ham, K.; McCarney, J.; Marathe, S.; Ge, J.; Knapp, G.; Butler, L. G., Recent applications of X-ray grating interferometry imaging to evaluate flame retardancy performance of brominated flame retardant. *Polymer Degradation and Stability* **2017,** *138*, 1-11.

82. Sonnier, R.; Negrell-Guirao, C.; Vahabi, H.; Otazaghine, B.; David, G.; Lopez-Cuesta, J. M., Relationships between the molecular structure and the flammability of polymers: Study of phosphonate functions using microscale combustion calorimeter. *Polymer* **2012,** *53* (6), 1258-1266.

83. ASTM, Standard Test Method for Measuring the Minimum Oxygen Concentration to Support Candle-Like Combustion of Plastics (Oxygen Index). ASTM International: West Conshohocken, PA 2017; Vol. D2863 − 17a.

84. ASTM, Standard Test Method for Measuring the Comparative Burning Characteristics of Solid Plastics in a Vertical Position. ASTM International: West Conshohocken, PA 2010; Vol. D3801 − 10.

85. Guillaume, E.; Yardin, C.; Aumaitre, S.; Rumbau, V., Uncertainty determination of glow-wire test for ignition of materials. *Journal of Fire Sciences* **2011,** *29* (6), 509-518.

86. ASTM, Standard Test Method for Glow-Wire Ignition of Materials. ASTM International: West Conshohocken, PA, 2014; Vol. D6194 − 14.

87. Hirschler, M. M., Flame retardants and heat release: review of traditional studies on products and on groups of polymers. *Fire and Materials* **2015,** *39* (3), 207-231.

CHAPTER 2
FROM X-RAYS TO IMAGES

Since its published existence by W. C. Röntgen in 1896, X-rays have become an indispensable tool in seeing the inside of materials that are opaque to visible light.[1,2] Soon after its discovery, X-ray imaging became the general technique for imaging bones. X-rays have found wide application in medicine and materials science.[3-5]

X-rays originate from the deceleration of fast-moving particles (*bremsstrahlung* radiation) or from the relaxation of outer-shell electrons to vacant inner-shell positions where the energy difference falls within the range for X-rays (fluorescent radiation). The common X-ray sources are X-ray tubes and synchrotrons.

This chapter focuses on the common sources of X-rays used in imaging as well as the detection and conversion of X-ray signal intensities to usable images.

2.1 X-ray Interaction with Matter

As observed with visible light, X-ray photons can be scattered or absorbed. Due to the higher energy of X-rays however, the level of interaction involved is different and the effects e.g. refraction, reflection and the photoelectric effect are not visible to the naked eye. X-rays are electromagnetic waves with energy in the range of about 0.12 keV to over 100 keV (wavelength of 103 Å to 0.124 Å, respectively).[6] These energies increase the probability of X-rays interacting more with tightly bound inner-shell electrons than with valence electrons. For instance, X-rays of energy 1.84 keV or more can remove a K-shell electron from a silicon atom. Based on the wave-particle duality concept, X-rays can be

treated as consisting of packets of energy or photons, the energy of which is calculated as,

$$\mathcal{E} = hv = h\frac{c}{\lambda}, \qquad [2.1]$$

where h = 6.626 x 10^{-34} J s is Planck's constant, ν is the frequency of the radiation/waves, c = 2.998 x 10^{8} m/s is the speed of light in a vacuum and λ is the wavelength in vacuum. Details on the forms of X-ray interaction with matter are presented below.

2.1.1 Scattering of X-rays

X-rays travelling through a material are primarily scattered by electrons. Classically, when an X-ray beam interacts with an electron, the oscillating electric field of the waves causes the electron to oscillate with the same frequency and direction.[7,8] As expected for a moving charged particle, this vibration is accompanied by the radiation of electromagnetic radiation. The emitted radiation has similar energy as the incident radiation thus, scattering is elastic and described as Thomson scattering.[7,8] The interaction is depicted in Figure 2.1, where k_i and k_f are the wavevectors of the incident and scattered waves, respectively. The vectorial difference between the incident and

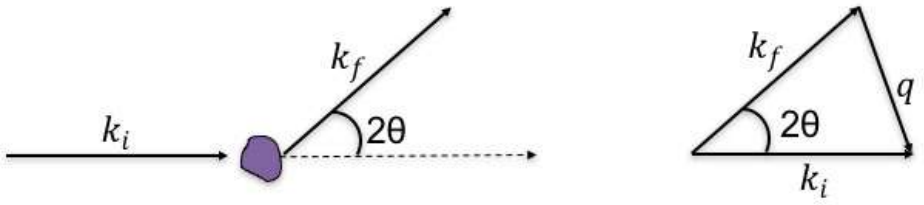

Figure 2.1. Elastic scattering of X-rays. (a) No change in energy i.e. $k_i = k_f$. (b) The vectorial difference, q, between the incident and scattered rays is easily determined geometrically.

scattered rays, $k_i - k_f = q$, is called the scattering vector and for elastic scattering at an angle 2θ it has a magnitude of $q = 4\pi/\lambda \sin\theta$.

The ability of an electron to scatter X-rays is expressed in terms of a scattering length. For the elastic scattering of an unbound electron it is referred to as the Thomson scattering length, r_0, calculated as:[8]

$$r_0 = \left(\frac{e^2}{4\pi\epsilon_0 mc^2}\right) = 2.82 \times 10^{-5}\text{Å}. \qquad [2.2]$$

Where e and m are the charge and mass of an electron, respectively. ϵ_0 is the permittivity of a vacuum valued at 8.85 x 10^{-12} F/m. Another name for r_0 is the classical electron radius.

A quantum description of electromagnetic radiation however acknowledges the possibility of energy being transferred to the electron so that the emitted photons are of lower energy relative to the incident.[7] Scattering in this case is therefore inelastic and described as Compton scattering. The Compton scattering length, λ_c, is calculated as:

$$\lambda_c = \frac{h}{mc} = 2.43 \times 10^{-2}\text{Å}. \qquad [2.3]$$

The energy loss due to Compton scattering can be determined from the following equation.[8]

$$\frac{hv_i}{hv_f} = \frac{k_i}{k_f} = \frac{\lambda_f}{\lambda_i} = 1 + \lambda_c k_i(1 - cos\psi)\,, \qquad [2.4]$$

where ψ is the scattering angle and subscripts i and f refer to the incident and scattered photons, respectively.

From Equation 2.4, energy loss from Compton scattering increases with increasing incident X-ray energy and decreasing scattering angle. At X-ray energies of around 100

keV, Compton scattering is almost constant and shows less dependence on the scattering angle.[9]

2.1.2 Refraction and Reflection

Refraction and reflection are resultant scattering effects of X-rays interacting with the multitude of atoms that make up a material. An X-ray wavefront experiences a change in shape on passing through a sample due to variation in thickness and X-ray refractive index.[10]

For X-rays the refractive index, n, is less than unity and is given by,

$$n = 1 - \delta + i\beta\,, \qquad [2.5]$$

where δ is the refractive index decrement and β is the absorption index.[7] δ is related to the scattering properties of the medium by

$$\delta(x,y,z) = \frac{r_0\lambda^2}{2\pi}\sum_k N_k(x,y,z)\,(Z_k + f_k'), \qquad [2.6]$$

where $N_k(x,y,z)$, Z_k, and f_k' are the atomic density, atomic number and the real part for the anomalous dispersion correction of element k, respectively.[11] r_0 is the earlier described classical electron radius.

The phase change, Φ, for a ray path through an object relative to vacuum is given by,

$$\Phi(x,y) = \frac{2\pi}{\lambda}\int \delta(x,y,z)\,dz\,, \qquad [2.7]$$

where the optic axis is parallel to z.[11] Thus Φ is the projection of δ across the object. The change in phase provides a contrast basis in X-ray imaging and would be further discussed in the interferometry section.

2.1.3 Absorption

A beam of X-rays encountering a body experiences an attenuation which can be calculated from,

$$\frac{I}{I_0} = e^{-\mu z}\,, \qquad [2.8]$$

where $I_0$and I are the incident and transmitted beams, respectively. z is the sample thickness and μ is referred to as the linear attenuation coefficient. It is worth noting that rather than μ, the mass absorption coefficient, μ_m, calculated as μ/ρ_m, is usually provided in literature. The attenuation coefficient, μ, also has a relationship with the imaginary part of the complex refractive index (Equation 2.5);[11]

$$\beta = \frac{\lambda}{4\pi}\mu\,. \qquad [2.9]$$

When a photon of X-ray is absorbed by an atom, if the energy is characteristic of an atomic shell, an electron acquires enough energy to transition into an unbound state. The absorption cross-section per atom, σ_a, is related to μ by the following equation,[8]

$$\mu = \sigma_a \rho_a = \left(\frac{\rho_m \mathrm{N}_A}{A}\right)\sigma_a. \qquad [2.10]$$

Where ρ_a and $\rho_m$are the atomic number and mass density, respectively. N_A is Avogadro's number and A is the atomic mass number. The absorption cross-section is inversely proportional to the third power of the photon energy, $\mathcal{E}$, but exhibits a sharp increase at characteristic energies.[7] It however varies approximately as the fourth power of the atomic number, Z, of an element.[7] Thus μ is element dependent.

The absorbed radiation can be calculated from Beer's Law as,

$$A = -\log\frac{I}{I_0} = -\log T\,, \qquad [2.11]$$

where T is the transmittance. Absorption contrast is the basic contrast mechanism applied in X-ray imaging applications.

2.2 X-ray Sources

This section describes the major sources of X-rays: X-ray tubes and synchrotrons. X-ray tubes have the widest application in medical imaging applications. Synchrotrons sources are generally for research activities.

2.2.1 X-ray Tubes

An X-ray tube consists of a cathode assembly, an anode assembly and the tube housing. The cathode and anode are encased by glass in a vacuum environment with external electrical connections (Figure 2.2).[12] The cathode is a tungsten filament inserted in a metal chamber or slot and produces electrons by thermionic emission. The shape of the slot determine the shape and size of the electron beam.[13,14] The electrical current applied to the filament and the size of the filament determines the amount of electrons emitted. The anode is a high-atomic number metal and is where radiation is produced. A high voltage applied between the anode and the cathode causes the emitted electrons to travel towards the anode at very high speeds. Electron bombardment of the anode is accompanied by the production of X-ray radiation. Since it is a portion or all the kinetic energy that is converted to X-rays, we can write

$$h\nu_0 = h\frac{c}{\lambda_0} = Ve\,, \qquad [2.12]$$

where Ve is the product of the accelerating voltage and charge of an electron. ν_0 is therefore the maximum frequency that can be produced at voltage V, and λ_0 is the lower limit of wavelengths that can be produced.[15] Thus, the applied voltage determines the maximum energy of emitted X-rays.

The choice of the target anode material depends on the desired X-ray energy range and its ability to withstand the local heating accompanying bombardment. Tungsten, rhodium and molybdenum are common examples of targets used. The thicker the target, the higher the probability of electrons losing their energy before radiating thus, increasing the occurrence of bremsstrahlung radiation.[16]

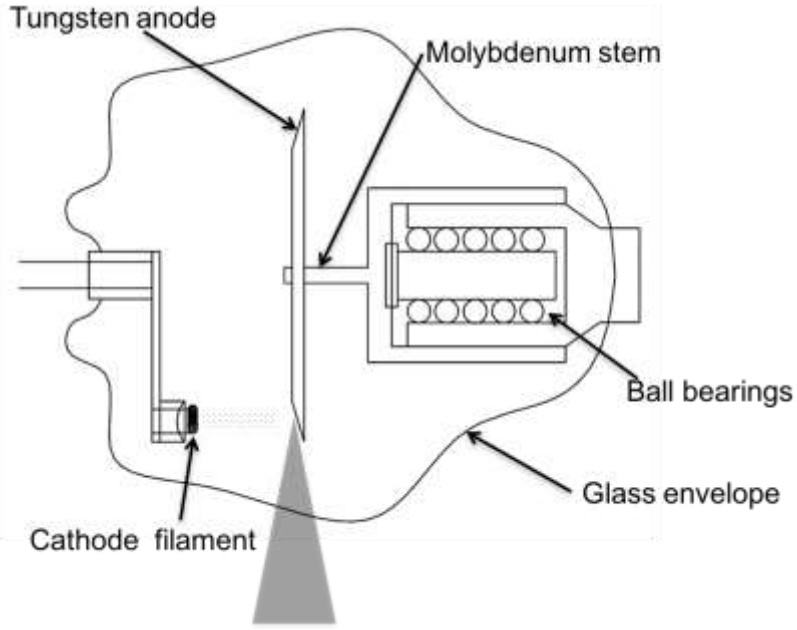

Figure 2.2. Schematics of a rotating anode X-ray tube. The housing is not shown. Adapted from reference 12.[12]

Fluorescent radiation is possible if the electron kinetic energy is no less than the energy of an inner atomic shell. For a given electron beam energy, lower Z materials display higher ratios of florescence to bremsstrahlung radiation.[16] Tube operation takes place within a vacuum confined by a glass envelope. The tube housing contains the glass envelope, electrical components as well as a cooling system.[12] It also contains lead shielding to ensure X-rays exit the instrument only through the exit port or window.[14]

Variations in the X-ray tube design have focused on increasing beam power and minimizing the effective focal spot. A rotating anode design, Fig 2.2, enabled increased

high-power operation. The effective focal spot depends on the actual focal spot size and the tube angle.[12] The smaller the effective focal spot size the better the image resolution. Transmission type X-ray tubes, where the target is a layer of thin metal just over the X-ray window, are also in use.[17-19]

A rotating envelope system has been reported to reduce cooling time thus enabling X-ray tube operation for a longer period of time.[20] It has been suggested that the use of microstructured targets in microfocus X-ray tubes eliminate the need for beam-focusing optics thus, achieving smaller sized tubes.[18]

2.2.2 Synchrotrons

Synchrotron radiation is produced when electrons moving at relativistic speeds are forced into circular trajectories using bending magnets. After its identification in 1947 at a General Electric electron synchrotron facility, experiments into the usefulness of this "radiation loss" commenced.[8,21] Current synchrotron facilities are exclusively designed for radiation production with brilliance over 10^{12} times that of the X-ray tube. The components of a synchrotron include an electron gun, a linear accelerator (LINAC), a booster ring, the storage ring, magnets (bending magnets and insertion devices), a radiofrequency (RF) cavity and beamlines.[8,22] Figure 2.3 is a simplified schematic of a synchrotron and its basic components.

The electrons are produced by thermionic emission and accelerated in the LINAC to kinetic energies in the MeV range. These electrons are then moved into the booster ring where they are further accelerated but now to GeV energy values after which they are injected into the storage ring. The storage ring consists of arcs where bending magnets are placed and straight sections for insertion devices.[8] The high-energy

electrons now moving at relativistic speeds, experience a Lorentz force at the bending magnets that force them to move in a circular trajectory emitting radiation in the process.

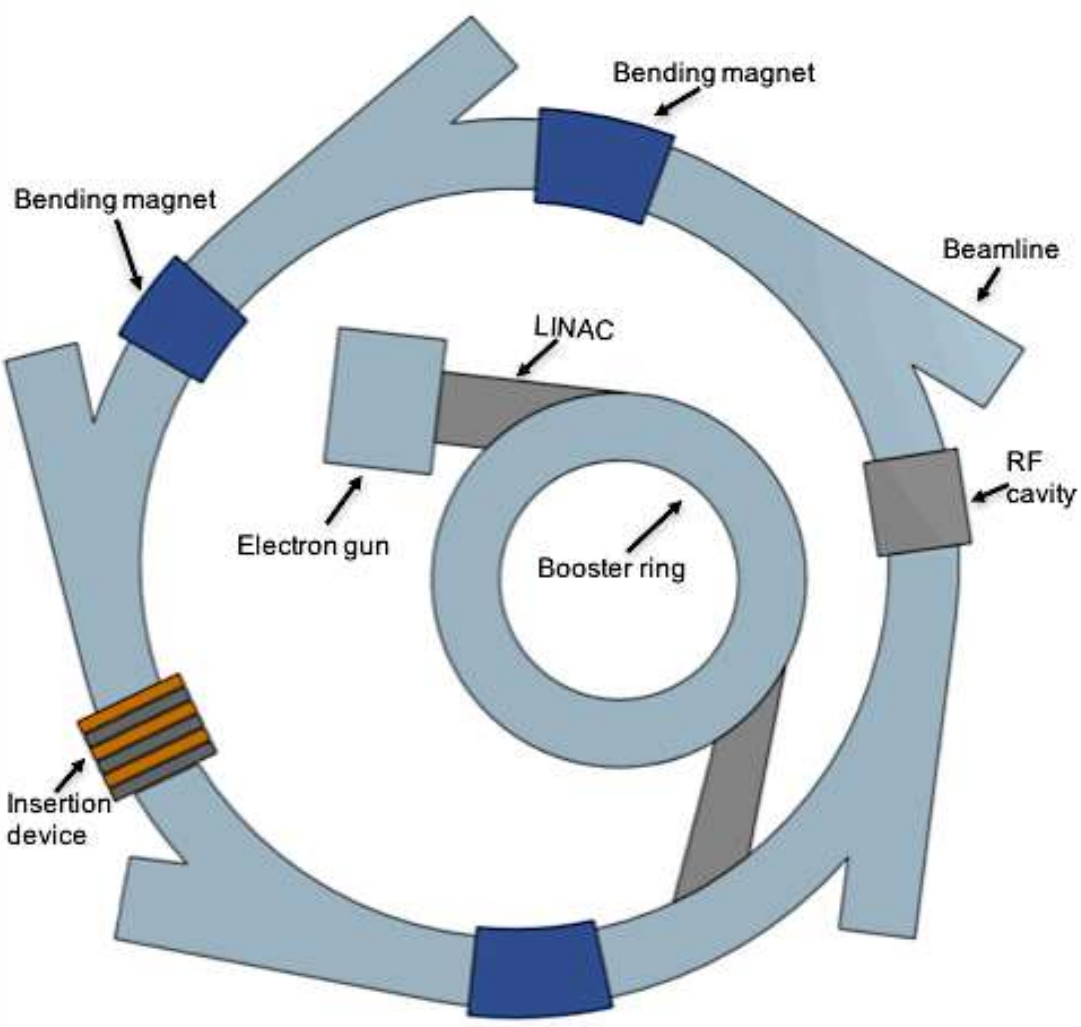

Figure 2.3. A schematic of a synchrotron and its basic components.

The insertion devices—wigglers and undulators—are used to improve the beam size. At the RF cavity, a RF voltage is applied to replenish the energy lost by the electrons as radiation. The beamlines are set up along the path of radiation with optics relevant to the desired energies.

A few important properties describe a synchrotron facility. The storage ring energy measured in GeV is the kinetic energy of the electrons and is usually expressed in a dimensionless parameter, γ, the Lorentz factor.

$$\gamma = \frac{E}{mc^2}, \qquad [2.13]$$

mc^2 is the rest mass energy of the electron (511 keV) and E is the energy of the electrons in the storage ring.[8] For electrons and positrons, $\gamma = 1957E$ with E in GeV. Current facilities have storage ring energies in the 1-8 GeV range.[8] For LSU CAMD it is 1.3 GeV (Table 1.1). The vertical divergence (natural opening angle) of the radiated beam is approximately equal to γ^{-1} in mrad.[23] This means with higher storage beam energy comes a vertically narrower beam. For a 2 GeV storage ring the divergence is about 0.25 mrad (about 0.014°) thus, synchrotron radiation is highly collimated.

Another property is the brilliance and is defined as photons per second, per unit source size and divergence in a given bandwidth.[23]

$$Brilliance = \frac{photons/second}{(mm^2)(mrad^2)(0.1\%\ bandwidth)} \qquad [2.14]$$

The implication of Equation 2.14 is that for increased brilliance a smaller source size and smaller divergences are needed. Due to the direction of electron travel through bending magnets, the radiation spreads out in the horizontal plane leading to a larger divergence restricted only by the collection beam-slit width and its distance from the electron orbit.[23] Insertion devices have helped to reduce this divergence hence, improved brilliance and will be addressed later.

Table 1.1 LSU CAMD Storage Ring Parameters

Ring Parameters	Value
Beam Energy (GeV)	1.3
Beam Current (mA)	200
Bending radius (meters)	2.928
Critical wavelength (Å)	7.45
Critical Energy (keV)	1.66
Beam half-life (hours)	9.5
Harmonic number	92
Radiative power (watts/mrad/mA)	0.014
Injection energy (MeV)	200
Natural emittance (m-rad)	~$2x10^{-7}$
Electron-beam width (mm)	~0.6
Electron-beam height (mm)	~0.15

Source: https://www.lsu.edu/camd/about/index.php (accessed October 25, 2018).

Synchrotron radiation covers a broad spectrum of electromagnetic radiation, from X-rays to infrared radiation. The critical energy, E_c, of the synchrotron radiation is an energy value that divides the beam spectrum into two equal parts—one side higher energy values, the other lower energy values.[8] It is calculated as;

$$E_c = \frac{3\hbar c\gamma^3}{2R}\,. \qquad [2.15]$$

R here is the radius of curvature of the electrons orbit while $\hbar$ is the reduced Plank's constant in angular considerations. By equating the Lorentz force to the centripetal force and replacing m with γm, R is calculated as;

$$R = \frac{\gamma mc}{eB} = \frac{E}{ceB} \qquad [2.16]$$

where B is the magnetic field strength, c is the speed of light and e is the charge of an electron.

In a storage ring the product of the source's transverse size and angular divergence in the horizontal or vertical plane is the emittance and is constant around the ring.[23] As mentioned earlier, due to the electron beam bend motion, there is an increase in the divergence in the horizontal axis.

Three kinds of magnets may feature in a synchrotron ring. Bending magnets are always present as they are primarily used to keep the electrons moving in the storage ring loop. With permanent magnets, the maximum magnetic field strength achievable is on the order of 1 Tesla.[24] The use of superconducting magnets makes higher value magnetic field strengths of over 5 Tesla achievable, thus access to higher X-ray energies than with simple magnets.[8] In practical units, the total power generated by a bending magnet is;[8]

$$P_T\ [kW] = 1.266E^2[GeV]B^2[T]L[m]I[A] \qquad [2.17]$$

where L is the magnet length, *I* is the current.

The introduction of insertion devices greatly impacted the performance of synchrotron facilities[25]. These devices are composed of magnets—a series of magnets—with alternating pole arrangement that force the electrons to make oscillatory motions in a horizontal plane. With each turn radiation is emitted hence, an overall increase in intensity compared to bending magnets, resulting in increased brilliance. Insertion devices are of two types—wigglers and undulators—differing in the extent to which electrons are deviated from a straight path. A dimensionless parameter, K, is used to

express the difference between wigglers and undulators. It is the ratio of the angle of electron deviation to the natural opening angle;[23]

$$K = \alpha\gamma. \qquad [2.18]$$

K can also be expressed in terms of spatial period, λ, and magnetic field as[23]

$$K = \frac{e\lambda B}{2\pi mc} = 0.934\,\lambda\,[cm]B[T]. \qquad [2.19]$$

For wigglers, K >> 1 but with undulators K ~ 1.[24]

To achieve many complete oscillations in a short distance, wigglers utilize magnetic fields higher than in bending magnets to bring about the needed smaller R value.[23] This is accompanied by the deviation of electrons from the straight path by angles much larger than γ^{-1}. Each pair of alternating magnets yield twice the radiation that will have been obtained with one magnet. For a series of N pairs of alternating magnets, in a wiggler, the resulting radiation is increased by a factor of 2N.[8] Total emitted power for a wiggler is;[8]

$$P_T\,[kW] = 0.633E^2[GeV]B^2[T]L[m]I[A] \qquad [2.20]$$

where B is the maximum magnetic field. The average B value is used here due to zero-value B-fields between magnet pairs.

In undulators, electrons are deviated from the straight path by an angle close to or smaller than γ^{-1}.[23] This subtle oscillation is achieved by reducing the spatial period.[8] The radiation emission accompanying each bend interfere with each other and those with wavelengths that are whole number fractions of the magnet spatial period add up constructively. The consequence of this is a beam with brightness increased by a factor ~ N^2.[23] Undulators can be used in-vacuum or out of vacuum, the latter providing better flexibility for ring operation as the gap between magnets can reach smaller values.[26,27] An

undulator where the electrons' sinusoidal motion is brought about by microwaves have been reported.[28] Research is still ongoing to further improve the performance of insertion devices in terms of brilliance and beam energy by reducing the oscillation period and magnet inter-pole distance.[27]

The LSU CAMD synchrotron makes use of a wiggler. The storage beam parameters for this facility are shown in Table 1.1.

2.3 Area Detectors for X-ray Imaging

X-ray detectors convert impinging photons to useful data from which information about X-ray interactions can be extracted. The choice of detector depends mainly on the X-rays energies of interest and experiment timescale. For imaging applications important parameters include: spatial resolution, detector efficiency, sensitivity and dynamic range, contrast and noise.[29] This section looks at the common type of detectors currently used in X-ray imaging applications.

2.3.1 Storage Phosphor Screens

These are common in medical imaging and have replaced screen films. They are image plates having a detective layer of photostimulable crystals of a family of phosphors BaFX:Eu^{2+}, where X can be bromine, chlorine, or iodine.[30,31] The phosphor crystals are usually cast into plates into resin material in an unstructured way.[31] When the plates are exposed to X-rays, the electrons in the crystals are excited from the valence bands to the conduction bands where they remain in stable states creating a latent image based on the of spatial distribution of these electrons.[31] Depending on the properties of the phosphor used, the image can be stored for hours though the stored energy decreases with time.[30]

The readout process involves scanning the plate with a high-energy laser beam of a specific wave length (flying-spot scanner), which stimulates the emission of light of different wavelength from that of the scanner.[30] This light is collected by photodiodes and converted digitally into an image.[30] Residual latent image is erased after the readout process using a high-intensity white light source that flushes the traps without reintroducing electrons from the ground energy level.[31] Storage phosphor screens have the advantage of size and don't require special expertise for replacement of defective screens. They are however of inferior quality compared to digital detectors.[30]

2.3.2 Multiwire and Microstrip Proportional Chambers

These are similar to gas proportional counters but have a patterned anode. For the multiwire type it is a grid of wires while for the microstrip type it is a microfabricated pattern of wire material on a substrate.[32,33] They are position-sensitive photon-counting detectors. Multiwire proportional counters are limited by the small number of pixels they have and large pixel size.

2.3.3 Scintillation Detectors

Scintillation detectors consist of a scintillator (phosphor) material followed by an optional optical relay element and a photodetector.[34] The differences between phosphors and scintillators arise from how the phosphor material is applied –phosphors in photon integrating mode (as in storage phosphors) and scintillators is photon counting mode.[34] Scintillators range from organic to inorganic materials in liquid, solid or even gaseous states. It was the glow of a phosphor – barium platino-cyanide – that drew Roentgen's attention to X-rays.[34] $CaWO_4$ powder and ZnS-based powders constitute the longest-in-use so-called phosphor material employed for the detection of X-rays.[34] Other examples

are Tl-doped NaI and CsI single crystals, Tb-doped oxysulfides (R_2O_2S,R = Y, La, Gd) and rare earth ion doped oxyhalides LnOX (Ln = Y, La, Gd; X = Cl, Br).[34] Of all scintillators (phosphors), silver doped ZnS is the most efficient.[35] Metal-organic frameworks based on Hf and Zr have been reported as possible scintillators for X-rays.[36] The more scintillator material used, the more X-rays are absorbed. However, there is a reduction in spatial resolution due to multiple scattering.[37] A method to increase the spatial resolution, without decreasing the height of the scintillator, consists of using an individual scintillator for each pixel, separated by layers of a reflector material.[37]

2.3.4 Charge-coupled Device (CCD) Detectors

The CCD was invented in 1969 at Bell Labs by Boyle and Smith and its application to image sensors was immediately apparent and first reported by Tompsett, Amelio and Smith in 1970.[38] In its simplest form, the basic structure of a CCD image sensor is formed from an array of electrodes running orthogonally to a series of isolated charge transfer channels (Figure 2.4).[39,40] Typically, each pixel consists an n-type silicon layer formed on a p-type silicon substrate.[40] The n-type layer is then covered with a thin layer of silicon dioxide followed by a metal electrode (or gate).[40] When a reverse bias is applied (a positive voltage to the electrode) a depletion region is formed at the p-n junction.[40] On exposure to X-rays, electron-hole pairs form in this region and the electrons migrate upwards into the n-type silicon layer and are trapped in the potential well.[40] The build-up of negative charge is thus directly proportional to the level of incident light.[40]

Following an exposure, the imaging area electrodes are pulsed or “clocked” to transfer the integrated image charge pattern down the array one line at a time to the readout register that runs orthogonally to the imaging area transfer channels or

columns.[39] The register reads out each pixel sequentially through a charge detection amplifier till the complete line has been read. After this, the next image line is transferred to the readout register and the sequence is repeated until all image lines have been read.[39] The CCD architecture described above is commonly referred to as a full-frame CCD array (Figure 2.5).[39] Other architectures are frame-transfer CCD and the interline-transfer CCD arrays.

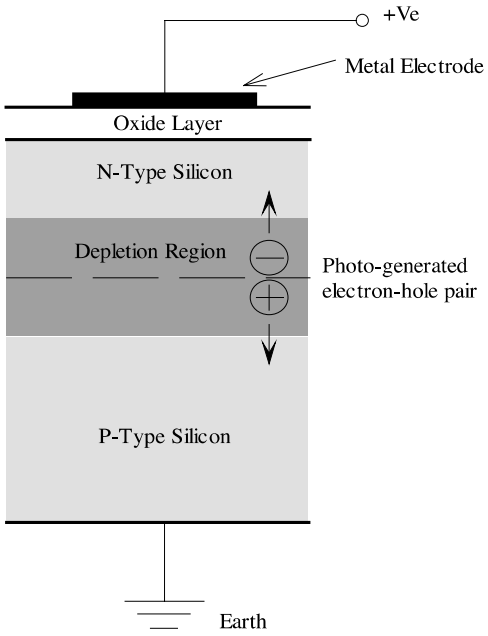

Figure 2.4. Schematic of a CCD Detector pixel.[40]

Though CCDs are directly responsive to x rays, as well as to light they are rarely used as direct conversion X-ray detectors.[41] The semiconductor of choice, namely silicon, has relatively low stopping power and thick detectors are hard to make.[41] Rather they are coupled with a scintillator. Thus, a CCD detector generally comprises a scintillator, an optional coupling element, an image intensifier as well as a CCD. Lens coupling is more

flexible and easy to use while fiber-coupling is more efficient and preferred for high speed imaging requirements.[42]

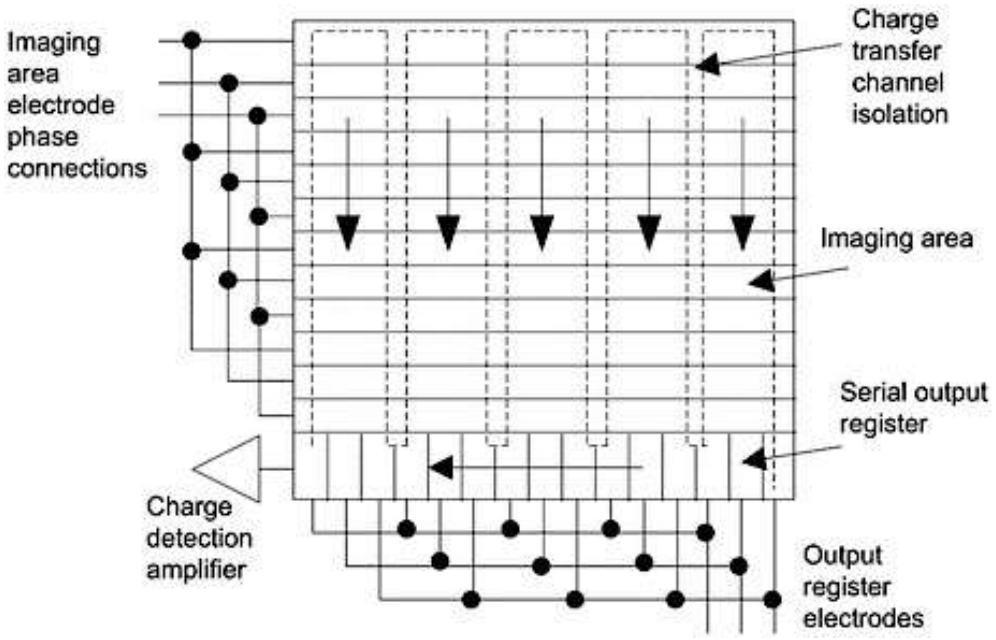

Figure 2.5. Schematic of a full-frame CCD array.[39]

CCDs are available in either front- or back-side illuminated versions.[41] The charge transfer efficiency in CCDs is over 99.999%.[40] Rows of pixels on the opposite side of the array will experience more transfers that those closer to the readout register, introduces slight differences in image quality. This effect contributes to the upper size limits of CCD arrays.[40] To reduce dark current, CCDs are usually cooled to below -30ºC.[33] One limitation of CCDs is their small active area which is limited to a few squared centimeters.[29] This limits their use in medical imaging. For large samples, image stitching or stacking of a few detectors might be necessary. CCD fabrication requires specialized silicon foundries which makes them expensive.[41]

2.3.4 Current-mode Semiconductor (CMOS) Detectors

CMOS image sensors exploit the same silicon chip technology used in

microprocessor systems.[39] Thus making it possible to integrate a large array of pixels, each with its own photodiode and readout transistors, alongside ancillary electronics.[39] Each CMOS pixel employs a photodiode, a capacitor and up to three transistors (Figure 2.6).[40] The pixel is describe as active if it contains an amplifier or passive if it does not contain an amplifier. Passive pixel devices have charge amplifiers at the bottom of each column of pixels.[40] Active pixel arrays are currently more widely used.[40] With the

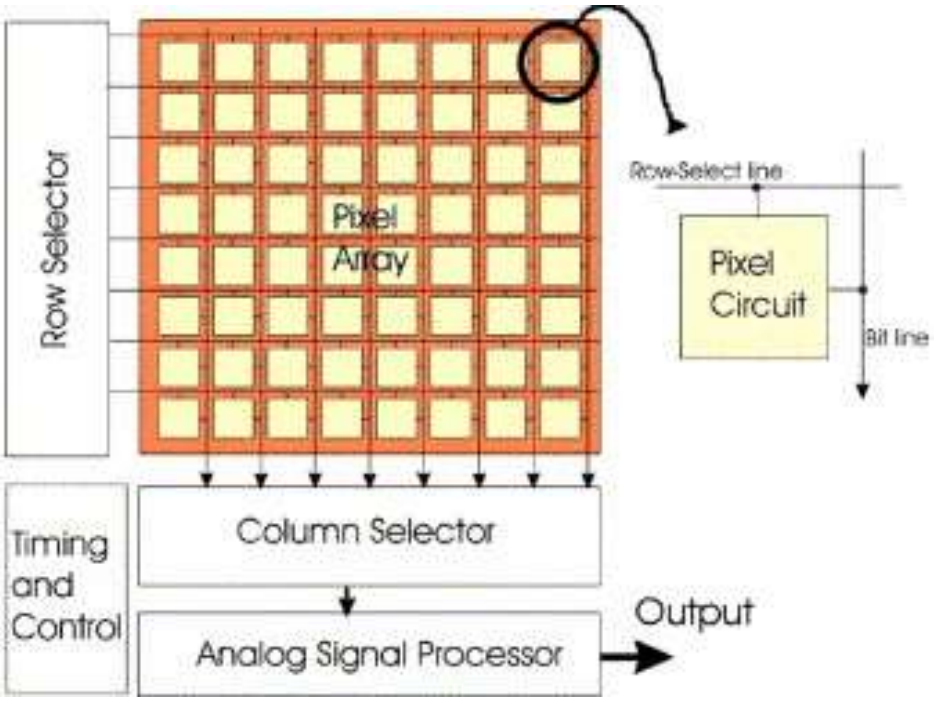

Figure 2.6. Schematic of a CMOS detector.[43]

integrated circuitry, pixels can be directly accessed and readout thus avoiding multiple charge transfers over long distances as in CCDs.[39,44]

Before exposure begins, the capacitor will be charged to some known voltage.[40] When the integration period begins, the charge on the capacitor is allowed to slowly drain away through the photodiode, the rate of drain being directly proportional to the level of incident light.[40] At the end of the integration period, the charge remaining in the capacitor

is read out and digitised.[40] As opposed to being discharged, the capacitor may be charged during the integration period.[40]

CMOS detectors are of lower power consumption and less expensive compared to CCDs.[39,43] As with CCDs, CMOS detectors need to be cooled to reduce dark current. The temperature to which a CMOS can be cooled is limited due to its size as uneven temperatures distribution and chip deformation may result.[45] Thus, they are generally of lower sensitivity compared to CCDs. Also, the linear dynamic range of today's best CMOS sensors is about 5000, considerably less than for a CCD.[39]

2.3.5 Thin-film Transistor Based Detectors

These devices are based off the realization that it was more cost-effective to fabricate large area arrays of electronic components using amorphous silicon than crystalline.[46] TFT arrays are typically deposited onto a glass substrate in multiple layers, with readout electronics at the lowest level, and charge collector arrays at higher levels (Figure 2.7).[31] Depending on the type of detector being manufactured, X-ray photoconductors or light sensing elements are deposited at the top layer of this ''electronic sandwich".[31]

When an X-ray photoconductor e.g. amorphous selenium is used, X-rays photons are directly converted to charges in the selenium layers.[31] Operation involves applying an electric field across the selenium layer which causes the generated charges to be drawn to the charge collecting electrodes where they are stored till readout.[31] When amorphous silicon is used, an additional layer of a scintillator is employed because in form of a thin film amorphous silicon offers insufficient absorption for direct X-ray detection.[46] The

amorphous silicon is in the form of a photodiode array to detect the light produced by the scintillator. The charge collected at each storage capacitor is amplified and quantified to

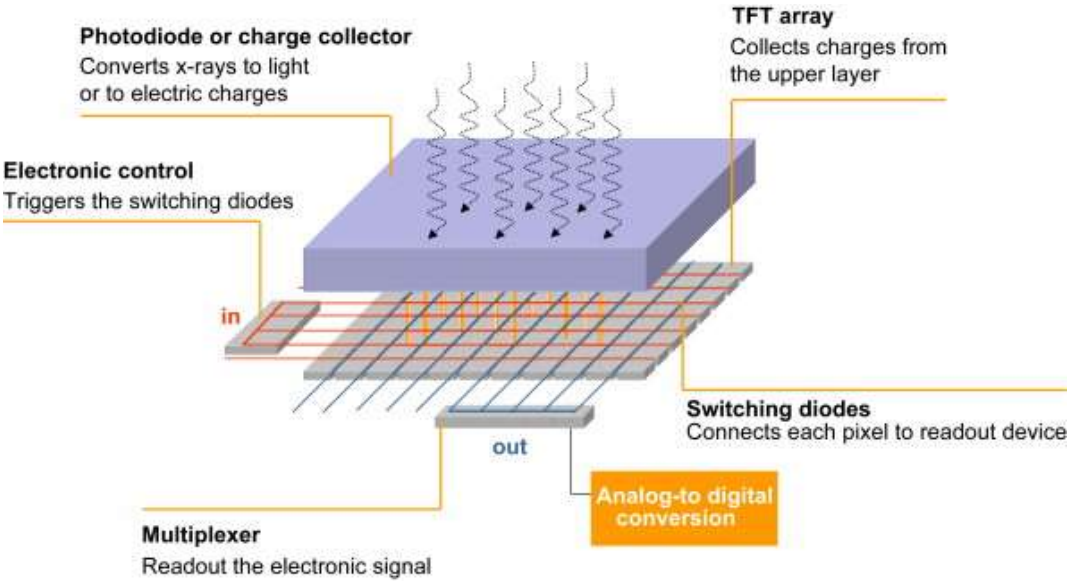

Figure 2.7. Schematic of a thin-film transistor pixel.[31]

a digital code value for the corresponding pixel.[31] During the readout, the charge of the capacitors of every row is conducted by the transistors to the amplifiers.[31]

2.3.6 Hybrid-Pixel Photon-counting Devices

A prime example is the Pilatus detectors. These combine silicon sensors with CMOS-processing chips by a 2D micro bump-bonding interconnection technology.[47] Unlike CCD detectors, the PILATUS detector does not add any noise to the data.[47] They register single-photon events by creating counting energy bins via pulse height analysis and thresholds.[48] By setting a low enough energy threshold, which remains above the pixel's noise level, electronic noise can be completely cut off.[48] This in turn can provide an imaging system, which requires no dark-count correction.[48] HPC detectors provide noise suppression, high and linear dynamic range, high count-rates and fast response,

as well as a virtually perfect point spread function due to the direct conversion of X-rays to charge within the sensor.[48]

2.4 Data Processing

The data recorded by area detectors can vary in data type and file format. For some applications, simple visualization of the images suffice. In other applications, further processing or analysis is required. There are a variety of software packages for these, the choice of which depends on availability, the file format and the complexity of processing required. Examples of image processing software available at no cost include ParaView, VisIt and ImageJ.[49-51] They have graphical user interfaces (GUI) for easy image manipulation and programming interface to tailor one's processing algorithm. Thermo Scientific's Amira-Avizo software is a commercial software with GUI and programming interface.[52] Mathematica is another commercial software package and is applicable to a wide range of computation extending to image processing, visualization, data science etc.[53] It requires the knowledge of a given programming language to carry out any operation.

In this work, Mathematica played a major role in image processing from quick analysis of image quality to preparing sinusoids for image volume reconstruction. The ASTRA toolbox was used for some image volume reconstruction based on sinusoids prepared in Mathematica.[54-56] An open-source Python-based package, TomoPy enabled one-stop data processing for tomography data sets.[57] The ASTRA toolbox and TomoPy are both open-source software.

2.4.1 Tomography Reconstruction

The X-ray photons detected by each pixel of the detector is the resultant of the interaction of the beam with all materials in its path as it propagates to the detector. This two-dimensional image (in the case of an area detector) is called a projection. Determining the distribution of a measured parameter, say the attenuation in the three-dimensional space, involves a reconstruction. To carry out a reconstruction, the sample is rotated around an axis perpendicular to the direction of beam propagation and projection acquired for the different views around the sample.[8] It is important that the sample of interest is fully within view in all the projections. The parameter of interest is calculated for each projection. These parameter projections are then manipulated to "fill in the gaps" of values in the spatial expanse.

Different reconstruction methods are available but can be broadly classified into two groups: analytical reconstruction methods e.g. filtered back projection (FBP) algorithms and iterative reconstruction (IR) methods.[58] The basics of FBP algorithms involve applying a filter to the projections first, the aim of which is to sharpen edges and dampen non-uniformities associated with the acquisition process.[59,60] After this, the filtered projections are back projected by equally distributing the measured pixel values equally across the ray path.[59]

Iterative reconstruction begins with the FBP steps but followed by a forward projection of the calculated volume and comparison with the original measured projection. Depending on the difference between the two, a correction is determined and applied to the calculated data.[61] Back projection and forward projection are repeated over and over again till a fixed number of iterations is reached or some predefined quality criterion is

reached.[61] Compared to FBP these IR algorithms enables the simultaneous reduction of image noise and the improvement of overall image quality.[59]

In this work, two reconstruction algorithms were employed, an improved FBP algorithm called Gridrec and an iterative reconstruction algorithm called simultaneous iterative reconstruction technique (SIRT).[62,63] The algorithms were executed using the ASTRA GPU package and the Tomopy package, both open-source software. When Tomopy was used, it was with integration of the ASTRA package.[64]

2.5 References

1. Röntgen, W. C., On a New Kind of Rays. *Science* **1896,** *3* (59), 227-231.

2. Assmus, A., Early history of X rays. *Beam Line* **1995,** *25* (2), 10-24.

3. Fukuda, D.; Nara, Y.; Kobayashi, Y.; Maruyama, M.; Koketsu, M.; Hayashi, D.; Ogawa, H.; Kaneko, K., Investigation of self-sealing in high-strength and ultra-low-permeability concrete in water using micro-focus X-ray CT. *Cement and Concrete Research* **2012,** *42* (11), 1494-1500.

4. Longuetaud, F.; Mothe, F.; Kerautret, B.; Krähenbühl, A.; Hory, L.; Leban, J. M.; Debled-Rennesson, I., Automatic knot detection and measurements from X-ray CT images of wood: A review and validation of an improved algorithm on softwood samples. *Computers and Electronics in Agriculture* **2012,** *85*, 77-89.

5. Miracle, A. C.; Mukherji, S. K., Conebeam CT of the Head and Neck, Part 2: Clinical Applications. *American Journal of Neuroradiology* **2009,** *30* (7), 1285-1292.

6. Drake, S. A. What are the Energy Range Definitions for the Various Types of Electromagnetic Radiation? https://heasarc.gsfc.nasa.gov/docs/heasarc/headates/spectrum.html (accessed September 20).

7. Als-Nielsen, J.; McMorrow, D., *Elements of modern X-ray physics*. John Wiley & Sons: 2001.

8. Willmott, P., *An introduction to synchrotron radiation: techniques and applications*. John Wiley & Sons: 2011.

9. Itou, M.; Orikasa, Y.; Gogyo, Y.; Suzuki, K.; Sakurai, H.; Uchimoto, Y.; Sakurai, Y., Compton scattering imaging of a working battery using synchrotron high-energy X-rays. *Journal of synchrotron radiation* **2015,** *22* (1), 161-164.

10. Wilkins, S. W.; Gureyev, T. E.; Gao, D.; Pogany, A.; Stevenson, A. W., Phase-contrast imaging using polychromatic hard X-rays. *Nature* **1996,** *384* (6607), 335-338.

11. Momose, A., Recent Advances in X-ray Phase Imaging. *Japanese Journal of Applied Physics* **2005,** *44* (9A), 6355-6367.

12. Zink, F. E., X-ray tubes. *RadioGraphics* **1997,** *17* (5), 1259-1268.

13. Frame, P. Coolidge X-ray Tubes. https://www.orau.org/ptp/collection/xraytubescoolidge/coolidgeinformation.htm (accessed October 25, 2018).

14. Seibert, J. A., X-ray imaging physics for nuclear medicine technologists. Part 1: Basic principles of x-ray production. *Journal of nuclear medicine technology* **2004,** *32* (3), 139-147.

15. Skoog, D. A.; Holler, F. J.; Crouch, S. R., Principles of instrumental analysis. Thomson Brooks/Cole: 2007.

16. Távora, L. M. N.; Morton, E. J.; Gilboy, W. B., Design considerations for transmission x-ray tubes operated at diagnostic energies. *Journal of Physics D: Applied Physics* **2000,** *33* (19), 2497-2507.

17. Dietz, K. X-ray tube having a ray transmission rotary anode. US3683223A, August 8, 1972.

18. Ihsan, A.; Heo, S. H.; Cho, S. O., A microfocus X-ray tube based on a microstructured X-ray target. *Nuclear Instruments and Methods in Physics Research Section B: Beam Interactions with Materials and Atoms* **2009,** *267* (21), 3566-3573.

19. Ihsan, A.; Heo, S. H.; Cho, S. O., Optimization of X-ray target parameters for a high-brightness microfocus X-ray tube. *Nuclear Instruments and Methods in Physics Research Section B: Beam Interactions with Materials and Atoms* **2007,** *264* (2), 371-377.

20. Schardt, P.; Deuringer, J.; Freudenberger, J.; Hell, E.; Knüpfer, W.; Mattern, D.; Schild, M., New x-ray tube performance in computed tomography by introducing the rotating envelope tube technology. *Medical Physics* **2004,** *31* (9), 2699-2706.

21. Robinson, A. L., History of Synchrotron Radiation. In *X-ray Data Booklet*, 2009.

22. Balerna, A.; Mobilio, S., Introduction to synchrotron radiation. In *Synchrotron radiation*, Springer: 2015; pp 3-28.

23. Mobilio, S.; Meneghini, C.; Boscherini, F., *Synchrotron radiation. Basics, methods and applications*. Springer-Verlag Berlin An: 2016.

24. Vinokurov, N. A.; Levichev, E. B., Undulators and wigglers for the production of radiation and other applications. *Physics-Uspekhi* **2015,** *58* (9), 850.

25. Kunz, C., Synchrotron radiation: third generation sources. *Journal of Physics: Condensed Matter* **2001,** *13* (34), 7499-7510.

26. Kitamura, H., Recent trends of insertion-device technology for X-ray sources. *Journal of Synchrotron Radiation* **2000,** *7* (3), 121-130.

27. Hwang, C. S.; Jan, J. C.; Chang, C. S.; Chen, S. D.; Chang, C. H.; Uen, T. M., Development trends for insertion devices of future synchrotron light sources. *Physical Review Special Topics - Accelerators and Beams* **2011,** *14* (4), No. 044801.

28. Tantawi, S.; Shumail, M.; Neilson, J.; Bowden, G.; Chang, C.; Hemsing, E.; Dunning, M., Experimental demonstration of a tunable microwave undulator. *Physical review letters* **2014,** *112* (16), No. 164802.

29. Pacella, D., Energy-resolved X-ray detectors: the future of diagnostic imaging. *Reports in Medical Imaging* **2015,** *8*, 1-13.

30. Körner, M.; Weber, C. H.; Wirth, S.; Pfeifer, K.-J.; Reiser, M. F.; Treitl, M., Advances in Digital Radiography: Physical Principles and System Overview. *RadioGraphics* **2007,** *27* (3), 675-686.

31. Lança, L.; Silva, A., Digital radiography detectors – A technical overview: Part 1. *Radiography* **2009,** *15* (1), 58-62.

32. Gruner, S.; Eikenberry, E.; Tate, M., Comparison of X-ray detectors. In *International Tables for Crystallography*, International Union of Crystallography: 2012; Vol. F, pp 177-182.

33. Thompson, A. C., X-ray Detectors. In *X-ray Data Booklet*, Second ed.; Lawrence Berkeley National Laboratory: 2001.

34. Martin, N., Scintillation detectors for x-rays. *Measurement Science and Technology* **2006,** *17* (4), R37-R54.

35. Nikl, M.; Yoshikawa, A., Recent R&D Trends in Inorganic Single-Crystal Scintillator Materials for Radiation Detection. *Advanced Optical Materials* **2015,** *3* (4), 463-481.

36. Wang, C.; Volotskova, O.; Lu, K.; Ahmad, M.; Sun, C.; Xing, L.; Lin, W., Synergistic Assembly of Heavy Metal Clusters and Luminescent Organic Bridging Ligands in Metal–Organic Frameworks for Highly Efficient X-ray Scintillation. *Journal of the American Chemical Society* **2014,** *136* (17), 6171-6174.

37. Rocha, J. G.; Lanceros-Mendez, S., Review on x-ray detectors based on scintillators and CMOS technology. *Recent Patents on Electrical & Electronic Engineering (Formerly Recent Patents on Electrical Engineering)* **2011,** *4* (1), 16-41.

38. Fossum, E. R.; Hondongwa, D. B., A review of the pinned photodiode for CCD and CMOS image sensors. *IEEE J. Electron Devices Soc* **2014,** *2* (3), 33-43.

39. Waltham, N., CCD and CMOS sensors. In *Observing Photons in Space: A Guide to Experimental Space Astronomy*, Huber, M. C. E.; Pauluhn, A.; Culhane, J. L.; Timothy, J. G.; Wilhelm, K.; Zehnder, A., Eds. Springer New York: New York, NY, 2013; pp 423-442.

40. Taylor, S. A. *CCD and CMOS imaging array technologies: technology review*; Xerox Research Centre Europe Cambridge, UK: 1998.

41. Gruner, S. M.; Tate, M. W.; Eikenberry, E. F., Charge-coupled device area x-ray detectors. *Review of Scientific Instruments* **2002,** *73* (8), 2815-2842.

42. Uesugi, K.; Hoshino, M.; Yagi, N., Comparison of lens-and fiber-coupled CCD detectors for X-ray computed tomography. *Journal of synchrotron radiation* **2011,** *18* (2), 217-223.

43. Bigas, M.; Cabruja, E.; Forest, J.; Salvi, J., Review of CMOS image sensors. *Microelectronics Journal* **2006,** *37* (5), 433-451.

44. Magnan, P., Detection of visible photons in CCD and CMOS: A comparative view. *Nuclear Instruments and Methods in Physics Research Section A: Accelerators, Spectrometers, Detectors and Associated Equipment* **2003,** *504* (1), 199-212.

45. Skarzynski, T., Collecting data in the home laboratory: evolution of X-ray sources, detectors and working practices. *Acta Crystallographica Section D: Biological Crystallography* **2013,** *69* (7), 1283-1288.

46. Cowen, A.; Kengyelics, S.; Davies, A., Solid-state, flat-panel, digital radiography detectors and their physical imaging characteristics. *Clinical radiology* **2008,** *63* (5), 487-498.

47. Henrich, B.; Bergamaschi, A.; Broennimann, C.; Dinapoli, R.; Eikenberry, E.; Johnson, I.; Kobas, M.; Kraft, P.; Mozzanica, A.; Schmitt, B., PILATUS: A single photon counting pixel detector for X-ray applications. *Nuclear Instruments and Methods in Physics Research Section A: Accelerators, Spectrometers, Detectors and Associated Equipment* **2009,** *607* (1), 247-249.

48. Gkoumas, S.; Wang, Z.; Abis, M.; Arboleda, C.; Tudosie, G.; Donath, T.; Brönnimann, C.; Schulze-Briese, C.; Stampanoni, M., Grating-based interferometry and hybrid photon counting detectors: Towards a new era in X-ray medical imaging. *Nuclear Instruments and Methods in Physics Research Section A: Accelerators, Spectrometers, Detectors and Associated Equipment* **2016,** *809*, 23-30.

49. Paraview Home Page. https://www.paraview.org/ (accessed Oct 31, 2018).

50. VisIt home page. https://visit.llnl.gov/ (accessed Oct 31, 2018).

51. ImageJ Home Page. https://imagej.nih.gov/ij/ (accessed Oct 31, 2018).

52. Amira-Avizo Software. https://www.fei.com/software/amira-avizo/ (accessed Oct 31, 2018).

53. Wolfram Mathematica Home Page. http://www.wolfram.com/mathematica/ (accessed Oct 31, 2018).

54. Palenstijn, W. J.; Batenburg, K. J.; Sijbers, J. In *The ASTRA tomography toolbox*, 13th International Conference on Computational and Mathematical Methods in Science and Engineering, CMMSE, 2013; pp 1139-1145.

55. van Aarle, W.; Palenstijn, W. J.; Cant, J.; Janssens, E.; Bleichrodt, F.; Dabravolski, A.; De Beenhouwer, J.; Batenburg, K. J.; Sijbers, J., Fast and flexible X-ray tomography using the ASTRA toolbox. *Optics express* **2016,** *24* (22), 25129-25147.

56. van Aarle, W.; Palenstijn, W. J.; De Beenhouwer, J.; Altantzis, T.; Bals, S.; Batenburg, K. J.; Sijbers, J., The ASTRA Toolbox: A platform for advanced algorithm development in electron tomography. *Ultramicroscopy* **2015,** *157*, 35-47.

57. Gürsoy, D.; De Carlo, F.; Xiao, X.; Jacobsen, C., TomoPy: a framework for the analysis of synchrotron tomographic data. *Journal of synchrotron radiation* **2014,** *21* (5), 1188-1193.

58. Hsieh, J.; Nett, B.; Yu, Z.; Sauer, K.; Thibault, J.-B.; Bouman, C. A., Recent advances in CT image reconstruction. *Current Radiology Reports* **2013,** *1* (1), 39-51.

59. Stiller, W., Basics of Iterative Reconstruction Methods in Computed Tomography: A Vendor-independent Overview. *European Journal of Radiology* **2018**.

60. Jacobson, M. W., Technology and Principles of Cone Beam Computed Tomography. *Cone Beam Computed Tomography: Oral and Maxillofacial Diagnosis and Applications* **2013**, 1-24.

61. Beister, M.; Kolditz, D.; Kalender, W. A., Iterative reconstruction methods in X-ray CT. *Physica Medica* **2012,** *28* (2), 94-108.

62. Marone, F.; Stampanoni, M., Regridding reconstruction algorithm for real-time tomographic imaging. *Journal of synchrotron radiation* **2012,** *19* (6), 1029-1037.

63. Gilbert, P., Iterative methods for the three-dimensional reconstruction of an object from projections. *Journal of theoretical biology* **1972,** *36* (1), 105-117.

64. Pelt, D. M.; Gürsoy, D.; Palenstijn, W. J.; Sijbers, J.; De Carlo, F.; Batenburg, K. J., Integration of TomoPy and the ASTRA toolbox for advanced processing and reconstruction of tomographic synchrotron data. *Journal of synchrotron radiation* **2016,** *23* (3), 842-849.

CHAPTER 3
X-RAY GRATING INTERFEROMETRY

In conventional X-ray imaging, contrast is obtained through the differences in the absorption cross-section of the constituents of the object with excellent results when highly absorbing structures are embedded in a matrix of relatively weakly absorbing material.[1] For important classes of samples such as biological tissues, polymers, and fiber composites, however, the use of conventional X-ray radiography is limited because these objects show only weak absorption.[2]

In addition to the decrease in intensity accompanying the absorption of radiation by an object, the wavefront experiences a change in phase due to refraction. This phase change or shift can be a source of contrast in imaging. The variation of the phase-shift cross-section, p, with atomic number, Z, can be up to a factor of 10^3 times greater than the absorption cross-section, σ_a, for low-Z elements.[3] Also, unlike σ_a, p falls off much slowly at higher energies. This high sensitivity benefits low-Z element sample compositions as well as composites of low-Z and high-Z elements. Since phase-contrast is still relatively more sensitive at higher energies, with operation at such energies there is the possibility of reduced X-ray dose in clinical applications.[4] Detecting the effect of an object on the phase of the wavefront, involves converting the wavefront into amplitude with contrast in the image plane.[5] There are various techniques used to do this all of which involve the introduction of a temporal phase modulation.[6]

A third contrast mechanism, the dark-field signal, is based on the reduction in the visibility of an interference pattern due to small-angle X-ray scattering from unresolvable microstructures i.e. those on a size scale much smaller than the spatial resolution of the imaging system.[7]

Grating interferometry with X-rays or neutrons simultaneously yields images with all three contrast mechanisms.

3.1 Talbot-Lau Stepped-Grating Interferometry

For a parallel beam source, a stepped-grating interferometer consists of two gratings labelled G1 and G2. The G1 grating is a phase grating which introduces a phase shift into the beam and splits the beam essentially into the +1st and -1st diffraction orders.[8] These diffracted beams form a periodic interference pattern in a plane perpendicular to the beam propagation axis.[9] The G2 grating is an absorption grating with the same periodicity and orientation as the interference pattern and is placed right in front of the detector. It acts as a transmission mask for the detector and converts local fringe position into a detectable signal intensity variation, magnifying the fringes so they can be conveniently and effectively recorded using X-ray detectors with large pixel sizes.[2,10] The detected signal profile thus contains quantitative information about the phase gradient of the object.[2]

The position of the G2 grating with respect to the G1 grating is determined by the Talbot effect – a self-imaging phenomenon of a periodic object under coherent illumination.[9] For a phase grating and a parallel beam, this distance is given by:[11]

$$d_m = \left(\frac{p_1}{\eta}\right)^2 \frac{m}{2\lambda}, \qquad m = 1, 3, 5, \ldots \qquad [3.1]$$

where p_1 is the grating period and λ is the wavelength of the applied radiation. The value for η depends on the phase shift introduced by the phase grating. It is 1 for a π/2 phase shift and 2 for a π phase shift.

When the source is a conical beam, as in X-ray tube sources, a third grating, G0, is included in the instrument setup and placed close to the source.[1] G0 is typically an

absorption grating and its grating apertures reduce an incoherent beam into several individually coherent but mutually incoherent sources.[1] Such a setup is described as a Talbot-Lau interferometer.[12] The Talbot distance for a cone beam source rescales to:[8]

$$d_{m*} = \frac{l}{l - d_m} d_m \,. \qquad [3.2]$$

For a parallel beam set-up, the interference pattern has a lateral period, $p_2 = p_1\ /2$, where p_1 is the period of the G1 grating.[8] The G2 grating period should match p_2. For a cone beam set-up, the grating magnification is taken into account so; [2]

$$p_2 = \frac{l + d}{l} \frac{p_1}{2} \,. \qquad [3.3]$$

Here d is the inter-grating distance and l is the distance from the source to G1.

The experimental set-up for a stepped-grating experiment is shown in Figure 3.1. Its operation involves moving the G2 gratings by a fraction of the grating period in a direction transverse to the grating structure and beam propagation direction. For each pixel, a sinusoidal intensity variation is recorded and the parameters: offset (a_{1_p}), amplitude (a_p), and phase ($\emptyset_{\boldsymbol{p}}$) need to be calculated. Intensity variations are recorded for both sample and sample-free (reference) setups. The reference values are used to normalize the sample values so as to exclude non-sample related effects.

A sample plot of intensity versus grating step distance —an interferogram— is shown in Figure 3.2 and can be described by the sinusoid equation:

$$\hat{c}_{gp} = \ a_{0_p} \ + a_{1_p} \ \sin\left(\frac{2\pi}{p_2} x_g \ + \ \emptyset_p\right) \qquad [3.4]$$

$$= [1]\ a_{0_p} \ + \left[sin\left(\frac{2\pi}{p_2} x_g\right)\right]\ a_{1_p} \cos \emptyset_p + \ \left[cos\left(\frac{2\pi}{p_2} x_g\right)\right]\ a_{1_p} \sin \emptyset_p \qquad [3.5]$$

where p and g represent a given pixel and a given grating position, respectively; p_2 is the period of the stepped grating and x_g is the distance of stepping.

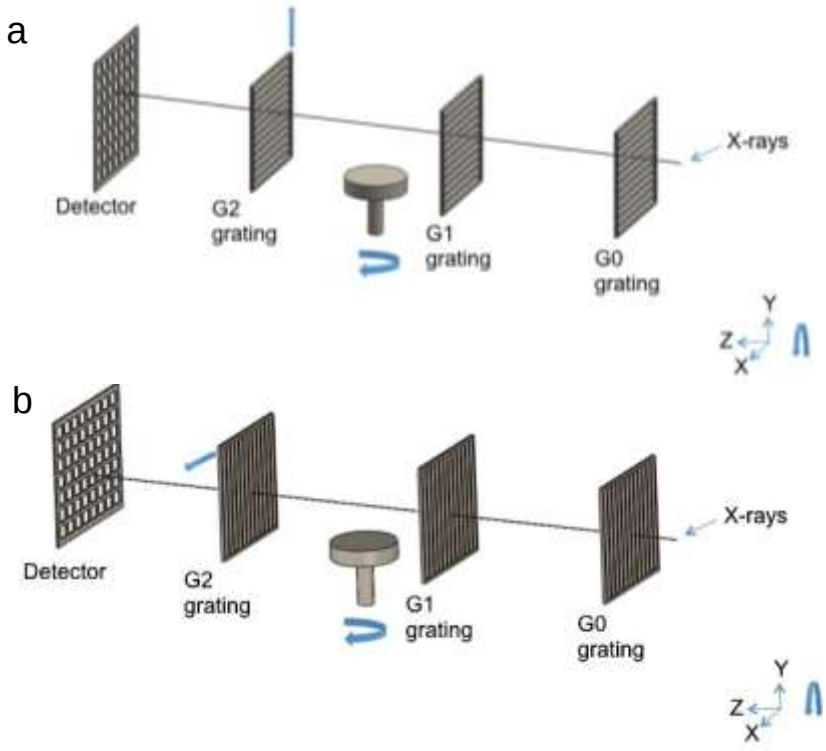

Figure 3.1. Stepped-grating interferometer set-up. a) Gratings oriented with grating features in the X-Z plane, referred to as the horizontal orientation. b) Gratings oriented with grating features in the Y-Z plane, referred to as the vertical orientation. Sample rotation is clockwise.

The sinusoid parameters a_{0_p}, a_{1_p}, and $\emptyset_{\boldsymbol{p}}$ for each pixel are calculated using a vectorized least-squares algorithm that can quickly process large datasets and work with non-uniformly spaced data.[13] In this algorithm, fitting of interferograms is approached as a simple matrix problem where the coefficients a_{0_p}, $a_{1_p}\cos\emptyset_p$ and $a_{1_p}\sin\emptyset_p$ of the expanded form of the sinusoid equation (Equation 3.5) in each pixel, are determined from a matrix expression,[13]

$$a = G \cdot c\,. \qquad [3.6]$$

In equation 3.6, a is a 3 x N matrix of the earlier mentioned coefficients for the N pixels of the detector and c is the M x N matrix of the M grating step positions and N pixels of the detector. $G = (B^T \cdot B)^{-1} \cdot B^T$, where B is the M x 3 matrix of the M grating step positions and the three fitting functions in square brackets.

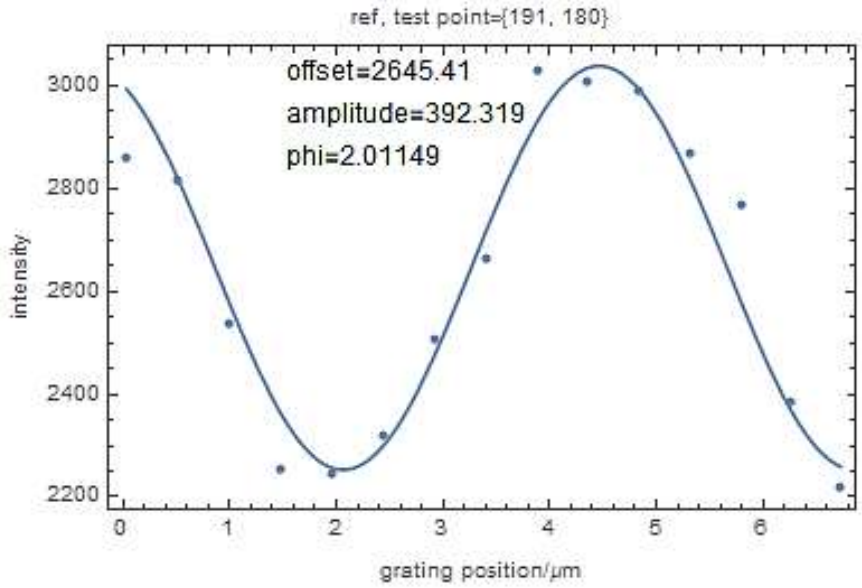

Figure 3.2. Sample interferogram from a pixel showing calculated offset (a_{0_p}), amplitude (a_{1_p}) and phi ($\emptyset_p$) of the sine curve.

The absorption, differential phase contrast and dark-field values are calculated as follows:

$$absorption = -Log\left(\frac{{a_{0_p}}^s}{{a_{0_p}}^r}\right) \quad [3.7]$$

$$differential\ phase\ contrast = {\phi_p}^s - {\phi_p}^r \quad [3.8]$$

$$dark - field = \frac{{a_{1_p}}^s / {a_{0_p}}^r}{{a_{0_p}}^s / {a_{1_p}}^r} \ . \quad [3.9]$$

where the superscripts s and r refer to sample and reference parameters.

X-ray grating interferometry has been applied to materials like cement where the dark-field signal was used to observe changes in the microstructure of cement during setting and hardening.[14] Phase contrast images of a concrete sample gave better contrast between aggregates and hardened cement paste than absorption images.[15] Phase contrast imaging has also been applied to wood samples.[16,17] Malecki *et al.* related the dark-field signal obtained with grating-based X-ray interferometry to fiber density and fiber orientation in a wood sample.[17]

In this work, grating-based interferometry will be applied to additively manufactured parts to study structural features within the parts. The dark-field signals will highlight sub-pixel voids while the phase-contrast signals should provide better contrast between different materials.

3.2 Contrast Generation in Stepped-Grating Interferometry

3.2.1 Absorption Contrast

The absorption contrast generation is straightforward as the average intensity in a pixel corresponds to the transmitted signal. With the sample and reference values the absorption is calculated as follows,

$$Absorption = -\ln T = -ln\frac{I}{I_0} = \mu z\,, \qquad [3.10]$$

where $I_0$and I are the incident and transmitted beams, respectively. z is the sample thickness and μ is referred to as the linear attenuation coefficient.

The absorption signal is the projection of the attenuation coefficient across the sample,

$$-\ln T\,(x,y) = \int \mu(x,y,z)dz\,. \qquad [3.11]$$

3.2.2 Phase Contrast

The interference pattern experiences a shift due to the refractive effect of an object. To determine this shift, the pattern is scanned by translating a grating in a direction transverse to the grating structure and beam propagation direction as described in Section 3.1. The lateral shift, s, is related to the angular deviation of a beam, $\Delta\alpha$, by $s = \Delta\alpha \times d$ and translates into a phase shift of $\varphi = 2\pi \times s/p_2$.[8]

The relation between the angular deviation of a beam $\Delta\alpha$ and the differential phase shift $((\partial\Phi\,(\mathrm{x},\mathrm{y}))/\partial x)$ is given by the equation

$$\Delta\alpha = \frac{\lambda}{2\pi}\frac{\partial\Phi\,(\mathrm{x},\mathrm{y})}{\partial x}, \qquad [3.12]$$

where *x* and *y* are the Cartesian coordinates perpendicular to the optical axis, $\Phi\,(\mathrm{x},\mathrm{y})$ represents the phase shift of the wavefront, and λ is the wavelength of the radiation.[1] By substituting for $\Delta\alpha$ in Equation 3.12 above, the differential phase shift is calculated from the equation:

$$\varphi = \frac{\lambda d}{p_2}\frac{\partial\Phi\,(\mathrm{x},\mathrm{y})}{\partial x}\,. \qquad [3.13]$$

Tomographic reconstruction of $\Phi\,(\mathrm{x},\mathrm{y})$ from projection images different angles around the sample yield the volumetric distribution of the X-ray refractive index decrement, δ, of the sample,

$$\Phi(x,y) = \frac{2\pi}{\lambda}\int \delta(x,y,z)dz\,, \qquad [3.14]$$

where the optic axis is parallel to z.[3]

3.2.3 Dark-Field Contrast

A third contrast mechanism, the dark-field contrast, based on small-angle X-ray scattering from sub-pixel sized microstructures has been identified and can provide structural information that is inaccessible from the absorption and differential-phase images.[7] In grating-based interferometry, it is detected as a relative decrease in the visibility of the fringe pattern. The visibility is calculated as:[18]

$$V_p = \frac{I_{max} - I_{min}}{I_{max} + I_{min}} = \frac{a_{1_p}}{a_{0_p}}, \qquad [3.15]$$

where I_{max} and $I_{max}$are the maximum and minimum intensities, respectively, for the recorded sinogram in pixel p. a_{1_p} is the amplitude of the sinusoid and a_{0_p} is the midline value which is the average intensity for a given pixel. The relative decrease in visibility due to the sample or the dark-field signal is obtained by dividing the sample visibility by the reference visibility i.e.

$$DF = \frac{{V_p}^s(m,n)}{{V_p}^r(m,n)} = \frac{{a_{1_p}}^s / {a_{0_p}}^r}{{a_{0_p}}^s / {a_{1_p}}^r}. \qquad [3.16]$$

When the sample is homogeneous, small-angle X-ray scattering contribution is negligible so the visibility remains unchanged (V=1).[18] Specimens with structural anisotropy on micrometer length scales produce strong small-angle X-ray scattering thus cause a significant decrease in the visibility.[19] Grating-based interferometers are only sensitive to scattering in the direction of scanning i.e. perpendicular to the grating structure.[20]

It has been demonstrated that the dark-field signal of the interferometer exponentially decays with sample thickness similar to the attenuation of X-rays in a sample (Beer-Lambert law), and that this decay is mathematically related to the width of

the scattering distribution σ.[21] Thus a material-dependent parameter, the diffusion coefficient ϵ was described and related to the dark-field signal by the expression,[21]

$$DF = exp\left(-2\pi^2 \frac{d^2}{{p_2}^2}\, \epsilon(t)\right), \qquad [3.17]$$

where d is the distance between the G1 and G2 gratings, p_2 is the period of the G2 grating and t is the sample thickness. ϵ is expressed in terms of σ^2 and t as $\epsilon \equiv \sigma^2/t$.[22] This dependence of the dark-field signal on sample thickness enables quantitative dark-field imaging computed tomography to be performed.

Based on the scanning technique, the dark-field signal has been shown to have a direct relationship with the autocorrelation function of the sample.[20] The expression is given by,[20]

$$DF(\xi_{corr}) = exp[\Sigma t\,(G\,(\xi_{corr}) - 1)], \qquad [3.18]$$

where G is the autocorrelation function of the sample and is a function of the correlation length, ξ_{corr}, probed by the interferometer. Σ is the scattering cross section and t is the sample thickness. ξ_{corr} is calculated as $\lambda l_s/p_2$, where λ is the wavelength of operation, l_s is the sample to G2 grating distance and p_2 is the period of the G2 grating.[23] However, for a cone beam and sample positioned between G0 and G1, ξ_{corr} becomes

$$\xi_{corr} = \frac{\lambda {l_s}'}{p_2} \qquad [3.19]$$

where ${l_s}' = (l + d - l_s)d/l$.[23] l is the G0 to G1 distance and d is the G1 to G2 distance. Since ξ_{corr} can be easily be tuned, the correlation function $G(\xi_{corr})$ can be determined by moving the sample either between *G*0 and *G*1 or between *G*1 and G2.[20]

Correlation functions for a number of shapes have been determined.[24] For spheres, it is approximated by the Gaussian function

$$G_{sphere}(\xi_{corr}) \approx exp\left[-\frac{9}{8}\left(\frac{\xi_{corr}}{R}\right)^2\right], \quad [3.20]$$

where R is approximately the radius of the sphere.[20]

Using the correlation function for spheres, the above relationship between the dark-field signal and G (Equation 3.20) have been shown to be in good agreement with theoretical expectation.[20]

3.3 Single-shot Grating Interferometry

This grating-based interferometry technique described as a spatial harmonic method does not involve a phase-stepping process.[25] A single transmission grating which may be linear or two-dimensional (comprising a grid of orthogonal grating structures) is used.[26,27] The projection image of the object is modulated by the periodic grid pattern.[27] Reference images i.e. without the sample are also acquired. Wavefront modifications arising from sample interaction can be quantified through spatial harmonic analysis of the recorded image.

First, the image is converted into its spatial frequency spectrum by 2D Fourier transformation.[27] With a 2D grating the resulting spectrum is a lattice of distinct peaks at (2πM/P, 2πN/P), where M and N are integers and P is the period of the grating projection image.[26] Each peak of interest is isolated by applying a mask then the area surrounding a peak is inverse Fourier transformed to yield the corresponding image.[25] Inverse Fourier transformation of the (1,0) and (0,1) peaks yield complex images of magnitude and phase.[26] Absorption and scattering are determined from the magnitude image while the differential phase contrast is extracted from the phase image. The central peak labelled

(0,0) is attributed to only attenuation effects, while the intensity of the (1,0) and (0,1) peaks result from both attenuation and scattering effects.[25,26] To obtain scatter-only harmonic images, the (1,0) and (0,1) images are normalizing by the (0,0) image.[26,27] The intensity of a pure diffraction image is then given by the logarithm of this ratio, which is proportional to the depth of X-ray penetration through the material.[25] The fundamental limitation of the spatial harmonic method is that in order to resolve the grating lines on the camera, the size of the camera pixel needs to be equal to or less than one-third of the projected grating period.[28]

3.4 References

1. Pfeiffer, F.; Weitkamp, T.; Bunk, O.; David, C., Phase retrieval and differential phase-contrast imaging with low-brilliance X-ray sources. *Nature Physics* **2006,** *2*, 258-261.

2. Weitkamp, T.; Diaz, A.; David, C.; Pfeiffer, F.; Stampanoni, M.; Cloetens, P.; Ziegler, E., X-ray phase imaging with a grating interferometer. *Optics express* **2005,** *13* (16), 6296-6304.

3. Momose, A., Recent Advances in X-ray Phase Imaging. *Japanese Journal of Applied Physics* **2005,** *44* (9A), 6355-6367.

4. Davis, T. J.; Gao, D.; Gureyev, T. E.; Stevenson, A. W.; Wilkins, S. W., Phase-contrast imaging of weakly absorbing materials using hard X-rays. *Nature* **1995,** *373* (6515), 595-598.

5. David, C.; Nöhammer, B.; Solak, H. H.; Ziegler, E., Differential x-ray phase contrast imaging using a shearing interferometer. *Applied physics letters* **2002,** *81* (17), 3287-3289.

6. Creath, K., Phase-measurement interferometry techniques. *Progress in optics* **1988,** *26* (26), 349-393.

7. Yashiro, W.; Terui, Y.; Kawabata, K.; Momose, A., On the origin of visibility contrast in x-ray Talbot interferometry. *Optics Express* **2010,** *18* (16), 16890-16901.

8. Engelhardt, M.; Kottler, C.; Bunk, O.; David, C.; Schroer, C.; Baumann, J.; Schuster, M.; Pfeiffer, F., The fractional Talbot effect in differential x-ray phase-contrast imaging for extended and polychromatic x-ray sources. *Journal of microscopy* **2008,** *232* (1), 145-157.

9. Momose, A.; Kawamoto, S.; Koyama, I.; Hamaishi, Y.; Takai, K.; Suzuki, Y., Demonstration of X-ray Talbot interferometry. *Japanese journal of applied physics* **2003,** *42* (7B), L866-L868.

10. Pfeiffer, F.; Bunk, O.; Schulze-Briese, C.; Diaz, A.; Weitkamp, T.; David, C.; Van Der Veen, J.; Vartanyants, I.; Robinson, I., Shearing interferometer for quantifying the coherence of hard X-ray beams. *Physical review letters* **2005,** *94* (16), No. 164801.

11. Donath, T.; Chabior, M.; Pfeiffer, F.; Bunk, O.; Reznikova, E.; Mohr, J.; Hempel, E.; Popescu, S.; Hoheisel, M.; Schuster, M., Inverse geometry for grating-based x-ray phase-contrast imaging. *Journal of Applied Physics* **2009,** *106* (5), No. 054703.

12. Momose, A.; Kuwabara, H.; Yashiro, W., X-ray phase imaging using Lau effect. *Applied physics express* **2011,** *4* (6), No. 066603.

13. Marathe, S.; Assoufid, L.; Xiao, X.; Ham, K.; Johnson, W. W.; Butler, L. G., Improved algorithm for processing grating-based phase contrast interferometry image sets. *Review of Scientific Instruments* **2014,** *85* (1), No. 013704.

14. Prade, F.; Chabior, M.; Malm, F.; Grosse, C. U.; Pfeiffer, F., Observing the setting and hardening of cementitious materials by X-ray dark-field radiography. *Cement and Concrete Research* **2015,** *74*, 19-25.

15. Sarapata, A.; Ruiz-Yaniz, M.; Zanette, I.; Rack, A.; Pfeiffer, F.; Herzen, J., Multi-contrast 3D X-ray imaging of porous and composite materials. *Applied Physics Letters* **2015,** *106* (15), 154102.

16. Trtik, P.; Dual, J.; Keunecke, D.; Mannes, D.; Niemz, P.; Stähli, P.; Kaestner, A.; Groso, A.; Stampanoni, M., 3D imaging of microstructure of spruce wood. *Journal of Structural Biology* **2007,** *159* (1), 46-55.

17. Malecki, A.; Eggl, E.; Schaff, F.; Potdevin, G.; Baum, T.; Garcia, E. G.; Bauer, J. S.; Pfeiffer, F., Correlation of X-Ray Dark-Field Radiography to Mechanical Sample Properties. *Microscopy and Microanalysis* **2014,** *20* (05), 1528-1533.

18. Pfeiffer, F.; Bech, M.; Bunk, O.; Kraft, P.; Eikenberry, E. F.; Brönnimann, C.; Grünzweig, C.; David, C., Hard-X-ray dark-field imaging using a grating interferometer. *Nature materials* **2008,** *7* (2), 134-137.

19. Pfeiffer, F.; Bech, M.; Bunk, O.; Donath, T.; Henrich, B.; Kraft, P.; David, C., X-ray dark-field and phase-contrast imaging using a grating interferometer. *Journal of Applied Physics* **2009,** *105* (10), No. 102006.

20. Prade, F.; Yaroshenko, A.; Herzen, J.; Pfeiffer, F., Short-range order in mesoscale systems probed by X-ray grating interferometry. *EPL (Europhysics Letters)* **2016,** *112* (6), No. 68002.

21. Bech, M.; Bunk, O.; Donath, T.; Feidenhans'l, R.; David, C.; Pfeiffer, F., Quantitative x-ray dark-field computed tomography. *Physics in Medicine & Biology* **2010,** *55* (18), 5529-5539.

22. Grünzweig, C.; Kopecek, J.; Betz, B.; Kaestner, A.; Jefimovs, K.; Kohlbrecher, J.; Gasser, U.; Bunk, O.; David, C.; Lehmann, E.; Donath, T.; Pfeiffer, F., Quantification of the neutron dark-field imaging signal in grating interferometry. *Physical Review B* **2013,** *88* (12), No. 125104.

23. Strobl, M., General solution for quantitative dark-field contrast imaging with grating interferometers. *Scientific Reports* **2014,** *4*, No. 07243.

24. Andersson, R.; van Heijkamp, L. F.; de Schepper, I. M.; Bouwman, W. G., Analysis of spin-echo small-angle neutron scattering measurements. *Journal of Applied Crystallography* **2008,** *41* (5), 868-885.

25. Stein, A. F.; Ilavsky, J.; Kopace, R.; Bennett, E. E.; Wen, H., Selective imaging of nano-particle contrast agents by a single-shot x-ray diffraction technique. *Optics express* **2010,** *18* (12), 13271-13278.

26. Wen, H. H.; Bennett, E. E.; Kopace, R.; Stein, A. F.; Pai, V., Single-shot x-ray differential phase-contrast and diffraction imaging using two-dimensional transmission gratings. *Optics letters* **2010,** *35* (12), 1932-1934.

27. Wen, H.; Bennett, E. E.; Hegedus, M. M.; Carroll, S. C., Spatial harmonic imaging of x-ray scattering—initial results. *IEEE transactions on medical imaging* **2008,** *27* (8), 997-1002.

28. Bennett, E. E.; Kopace, R.; Stein, A. F.; Wen, H., A grating-based single-shot x-ray phase contrast and diffraction method for in vivo imaging. *Medical physics* **2010,** *37* (11), 6047-6054.

CHAPTER 4
INTERFEROMETRIC DETECTION OF VOIDS AND GAPS IN FUSED DEPOSITION MODELED POLYMERIC OBJECTS

4.1 Introduction

X-ray stepped-grating interferometry, initially applied in phase contrast detection, has been reported to detect a third contrast mechanism –the darkfield. This signal is based on small angle scattering of the waves by structures of size scales smaller than the grating period.[1] This signal shows up as a loss in visibility i.e. a decrease in detected intensities after taking into account the absorption and refraction effects on the wavefront.[2]

X-ray grating interferometry is promising in medical imaging and a number of experiments have been carried out on biological samples.[2-6] Some studies have also been done on samples made of concrete, cement and fiber-reinforced polymers.[7-9] To further explore the possible applications of this technique, our group pioneered the extension of grating interferometry studies to additively manufactured samples.

Additive manufacturing is a fabrication process that involves layer-by-layer addition of material(s) till the bulk object is formed. The CAD file of the object's model is loaded into the software of the instrument that will build the object (the printer) where the model is pre-sliced. The printer then deposits energy or material according to the pattern of the slices, starting with the slice at one end till the whole object is formed. Many techniques are used to bring about the fusion of material. Examples of such techniques

The work reported in this chapter has been published as a journal article by *Kio et al.* titled "Non-destructive evaluation of additively manufactured polymer objects using X-ray interferometry", and is available online at https://doi.org/10.1016/j.addma.2018.04.014.

are selective laser sintering, selective laser melting, stereolithography, fused deposition modeling etc. Generally, it has been reported that additively manufactured parts have a mechanical weakness in the plane normal to the print bed.[10,11] This can be attributed to imperfect bonding of material in the parts as higher levels of porosity are seen with additively manufactured parts compared to conventional wrought, cast or molded parts.[12-14] These porosities may be due to thermal stresses during material solidification or the parameter settings of the printer. Porosities or imperfections in bonding have been detected directly by computed tomography.[14-16] Scanning electron microscopy (SEM) and optical microscopy have also been used for surface studies of printed or fractured samples.[15] Scattering of X-rays by porosities, cracks and gaps may contribute to the dark-field signal making them detectable by X-ray grating interferometry.

Based on interferometer visibility, V_p, the dark-field signal is calculated as an instrument dependent parameter using the following equation:[5]

$$DF = \frac{{V_p}^s(m,n)}{{V_p}^r(m,n)} = \frac{{a_{1_p}}^s / {a_{0_p}}^r}{{a_{0_p}}^s / {a_{1_p}}^r} \,. \qquad [4.1]$$

Here a_{1_p} is the amplitude of the inteferogram and a_{0_p} is the midline value which is the average intensity for a given pixel. Subscripts s and r refer to measurements acquired with and without the sample, respectively.

The dark-field signal can also be expressed in an instrument independent form by the equation:

$$DF = exp\left(-2\pi^2 \frac{d^2}{{p_2}^2}\, \epsilon(t)\right) \,, \qquad [4.2]$$

where the dark-field values are related to an instrument independent parameter, ϵ, the

linear diffusion coefficient. In Equation 4.2, d is the distance between the G1 and G2 gratings, p_2 is the period of the G2 grating and t is the sample thickness.

The correlation length of the interferometer, ξ_{corr}, which is the minimum size scale of scattering structures for which the instrument is sensitive contributes to the scattering signal. It is calculated from the following equation,[17,18]

$$\xi_{corr} = \frac{\lambda \cdot SDD_{eff}}{p_2} \ . \qquad [4.3]$$

Here λ is the wavelength of operation, p_2 is the period of the G2 grating. SDD_{eff} is generally the sample-to-detector distance but for a cone beam source and for sample position between G0 and G1, $SDD_{eff} = (l + d - l_s)d/l$ where l is the G0 to G1 distance and d is the G1 to G2 distance.

Our research group has applied grating interferometry to parts fabricated by additive manufacturing. While metallic and polymeric materials have been studied, this work focuses on polymeric parts fabricated by fused deposition modeling.[19-22] In fused deposition modeling, a semi-molten filament of material is extruded from a nozzle which moves according to the slice pattern. This technique majorly uses thermoplastic feedstock like acrylonitrile butadiene styrene copolymers (ABS), polylactide (PLA), polycarbonate (PC), and polyamides (PA).[23,24]

In this work, X-ray grating interferometry was applied to the non-destructive study of objects fabricated through the fused deposition modeling technique. The stepped-grating mode was applied for tomographic imaging while the single-shot mode was used for two-dimensional imaging. This work has been published as a journal article and forms the bulk of this chapter.[22]

The samples were two prints of the Stanford Bunny—one printed using ABS material and the other using PLA—and an object having three flat sides and a curved side, printed using PLA and embedded with silver tracks.[25] The dark-field images detected structures in the object that were not detected by the absorption image. By changing the grating orientation (grating structure plane parallel or normal to print layers), and comparing the dark-field images obtained, the presence of anisotropic voids in the plane parallel to the print layer was detected. Curvature analysis of the ABS bunny perimeter in reconstructed slices was also carried out.[26] This involved isolating the print perimeter and extracting the dark-field values within this region. The results revealed a slight correlation between the dark-field signal and curvature, meaning that highly curved regions were a bit more susceptible to the occurrence of voids or improper layer adhesion.

4.2 Materials and Methods

4.2.1 Samples

A CAD file of the Stanford Bunny in polygon (PLY) format was edited in Meshlab and used to print models of the bunny.[25] The model in stereolithography (STL) file format is shown in Figure 4.1a. One bunny sample was printed in ABS on a Stratasys Dimension Elite Printer using a filament of 1.7 mm diameter. The sample height was about 50 mm. The printer was set to use 0.254 mm thick layers with Sparse High Density fill and SMART support styles thus, the sample had internal support structures. Another bunny sample was printed to a height of about 50 mm on a Makerbot Replicator printer using PLA filament of diameter 1.75 mm. Printing was done with the high resolution setting and internal support. For both the ABS and PLA bunnies printing was done upwards from feet to ears.

A third sample referred to as a “quadratic object” was designed to have a curved side for which the differential phase was equal to a constant ($\partial\Phi/\partial x = a$), with the aim of testing the sensitivity of differential phase measurements. As seen in the STL image in Figure 4.1b**,** it comprises 3 flat sides and a curved side. The quadratic was printed on a Voxel8 printer using 1.75 mm diameter PLA filaments and silver-based ink which was used to embed silver tracks in the sample. Based on the printer settings the quadratic was set to be printed as a fully solid object composed of 0.19 mm thick layers. The printed dimensions were a height of 10 mm and with reference to Figure 4.1b had a maximum thickness of 7.3 mm along the y-axis with the width (x-axis) varying from 15.8 mm at the bottom to 8.5 mm at the top.

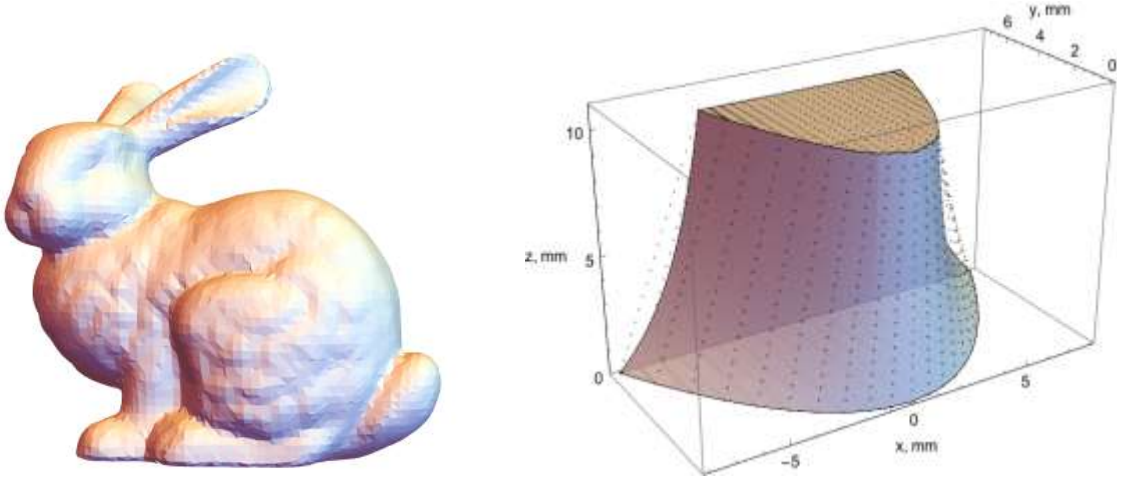

a b

Figure 4.1. STL images of printed samples. (a) Stanford Bunny and (b) Quadratic object.

4.2.2 Stepped-grating Interferometry with Tomography at LSU

A Talbot-Lau stepped-grating X-ray interferometer was used to acquire two-dimensional projections at a design energy of 26 keV for tomographic volume reconstruction. The X-ray source was a microfocus tungsten Hamamatsu X-ray tube,

L9181-02, operated without filtering at 45 kV, 300 μA with a 40 μm source size. The G0 and G2 analyzer gratings each had 150 μm high Au linear structures with a 4.8 μm period, on Si wafers. The G1 phase grating had 3.9 μm high Au linear structures on a Si wafer for a π phase shift at 26 keV, and had a 4.8 μm period. The three gratings were supplied by Microworks (Karlsruhe, Germany). The interferometer set-up for two different grating orientation is shown in Figure 4.2. The detector was a Pilatus 100K sensitive photon counter with square 172 μm pixels in a grid of 487 columns and 195 rows. Exposure time was typically 50 seconds. Other components of the instruments are rotation stages to align the gratings and translation stages for optimizing the grating-to-grating distances.

The G0−G1=G1−G2 distance was 362 mm, the third Talbot distance for a design energy of 26 keV, giving a two-fold magnification in the grating system.[27] The X-ray source-to-detector distance was 1053 mm and the source-to-sample distance was 761 mm (sample was between G1 and G2), yielding a sample magnification of 1.38 and an effective pixel size of approximately 125 μm. The G2 grating was translated in 12 steps, moving by 0.48 μm or 0.5 μm per step, in a direction transverse to the grating structures and the direction of beam propagation. Images were acquired at each step. Sample and reference images (without the sample) were acquired. The sinusoidal intensity variation in each pixel as the grating was stepped position was recorded and used to calculate absorption, differential phase and dark-field values and corresponding images.[28] The correlation length of the interferometer, ξ_{corr}, was determined to be 2.72 μm.

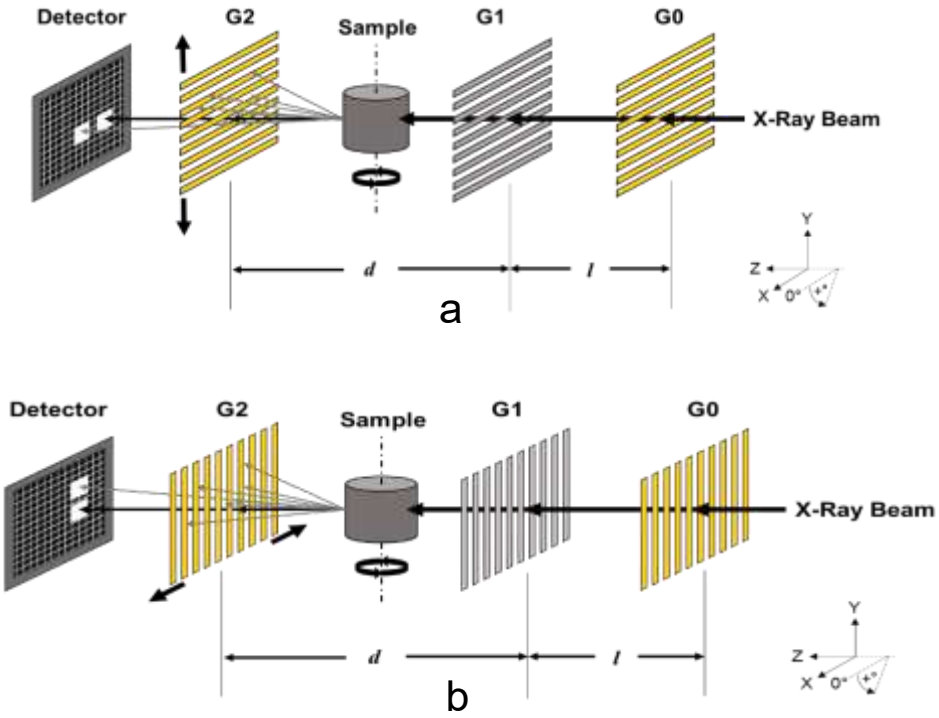

Figure 4.2. A Talbot-Lau stepped grating interferometer with two different grating configurations. (a) Gratings oriented for sensitivity to scattering along the laboratory Y-axis and (b) Gratings oriented for sensitivity to scattering along the laboratory X-axis.

The gratings were oriented for sensitivity to scattering transverse to the grating structures. Thus, for sensitivity to scattering in the vertical direction the gratings were oriented horizontally, while for sensitivity to scattering in the horizontal direction they were oriented vertically, Figures 4.2 and 4.2b, respectively. Two sets of tomography projections were acquired with the PLA bunny mounted feet-down with horizontal and vertical grating orientation, respectively. Tomography projections were acquired with the ABS bunny mounted feet-down as well as nose-down. Horizontal and vertical grating orientations, $\pm$ 45° grating orientations, two different values for the G2 stepping increment, 0.48 µm and 0.50 µm were explored with the ABS bunny. Tomography projections were acquired with the sample rotated by 180˚ in 2˚ increments. Absorption volumes were reconstructed

using the Gridrec algorithm while the dark-field volume reconstruction involved the use of the SIRT algorithm, both in the ASTRA GPU package.[29-31]

4.2.3 Single-Shot Interferometry at the Advanced Photon Source (APS)

Single-shot interferometry was performed at the 1-BM-B beamline at APS using a portable X-ray interferometer.[32] Only one grating, a checkerboard phase grating with a period of 4.8 μm, designed for a π phase shift at 18 keV was used. No source grating was needed as the synchrotron source was vertically coherent and no analyzer grating was needed due to the detector being of high resolution. The detector was an Andor NEO sCMOS camera coupled to a 100 μm thick Lu_2O_3:Eu scintillator by a 10 x Nikor lens. The camera had a 2560 x 2160 array of pixels, each of size 6.5 μm x 6.5 μm. The effective pixel size was determined to be 0.66 μm by imaging a Siemens star and other resolution elements fabricated at APS. Exposure time was 5 seconds.

The distance from the checkerboard phase grating to the scintillator was set to 84 mm and also 251 mm corresponding to the 1st and 3rd Talbot distances for an 18 keV design energy. The correlation length for this system was determined to be 1.705 μm and 5.094 μm for the 1st and 3rd Talbot distances, respectively. Single-shot interferometry was used to study the quadratic sample. However, due to the narrow beam size hence small field of view (1.25 mm x 1.19 mm), only a small portion specifically the upper left corner of the quadratic sample was imaged, Figure 4.1.

4.2.4 SEM Imaging

SEM imaging was carried out using a FEI Quanta™ 3D FIB-SEM instrument (FEI, Hillsboro, OR) at LSU. The sample was a portion of the ABS bunny ear prepared by freeze fracture, coated with platinum and imaged at an accelerating voltage of 2 kV.

4.2.5 Data Processing

Two-dimensional absorption and dark-field images were compared using line probes. Processing of reconstructed absorption and dark-field volumes involved the application of a mask to exclude stair-step surface roughness and the internal support structures. The first step was the generation of a mask from the absorption volume to focus on the sample perimeter. This involved binarization of the volume, dilation by three pixels then erosion by four pixels to minimize surface roughness that could contribute to the dark-field signal. To exclude the internal support structure a duplicate mask eroded by an additional six pixels was subtracted from the original mask. The resulting hollow mask was then applied to the absorption and dark-field volumes. The reconstructed volumes were rendered in Avizo 9.

The darkfield images of the ABS bunny acquired with the gratings in the horizontal orientation seemed to show more intense signal intensities at the more curved regions of the sample. This informed a curvature analysis to explore the correlation between curvature and the dark-field signal. The curvature analysis involved determining the coordinates of the perimeter pixels in a reconstructed slice, calculating the curvature for each pixel and comparing with the dark-field signal at each pixel. The curvature was calculated based on the following definition of curvature in a space plane,[26]

$$\gamma = \frac{|x'y'' - x''y'|}{((x')^2 + (y')^2)^{3/2}} \qquad [4.4]$$

where the space plane is described by a function $f(x(t), y(t))$ with x and y being the coordinates and t an independent variable. The pseudocode for the curvature analysis is provided in Appendix B. In summary, a reconstructed absorption slice is identified, binarized, magnified then smoothed. The $\{x, y\}$ coordinates are detected, demagnified

then ordered based on their position in the perimeter of the slice. Ordering involved a nearest point detection method which was rather slow. The curvature for corresponding $\{x, y\}$ coordinates is then calculated. Dark-field and absorption values used are the mean non-zero values within a radius of two pixels of the $\{x, y\}$ coordinates. Thus, the curvature, dark-field and absorption values for $\{x, y\}$ coordinates of the sample perimeter for the correlation investigation were obtained. Curvature analysis was however limited to the top portion of the reconstructed bunny slices namely the head and neck as perimeter slices from the lower portion were incomplete due to parts of the bunny e.g. the rump being outside the field-of-view.

4.3 Results

4.3.1 The ABS Stanford Bunny

The reconstructed volumes for the ABS bunny mounted feet-down i.e. such that the print layers are normal to the axis of sample rotation, Y, (Figure 4.1b) are shown in Figure 4.3 with opacities of 20%. The reconstructed absorption volume of the ABS bunny is shown in Figure 4.3a and was acquired with an instrument set-up where the gratings were oriented horizontally. The volume for a vertical grating orientation is not shown as the absorption signal is independent of grating orientation. As can be seen, the recorded absorption intensities are nearly uniform. Reconstructed dark-field volumes, are shown for two grating orientations—horizontal and vertical—in Figures 4.3b and 4.3c, respectively. Unlike the absorption signal, the dark-field signal detected by the interferometer is dependent on the grating orientation with the interferometer more sensitive to scattering in a direction transverse to grating structures. The horizontal grating orientation makes the interferometer more sensitive to scattering in the vertical

direction while the vertical grating orientation makes the interferometer more sensitive to scattering in the horizontal direction. Comparison of both dark-field images show higher intensities occur more in Figure 4.3b than in Figure 4.3c, indicative of the sample being more efficient in scattering X-rays in the vertical direction than in the horizontal direction. This further indicates that more scattering sites in the sample have a long axis aligned in the horizontal direction than in the vertical direction.

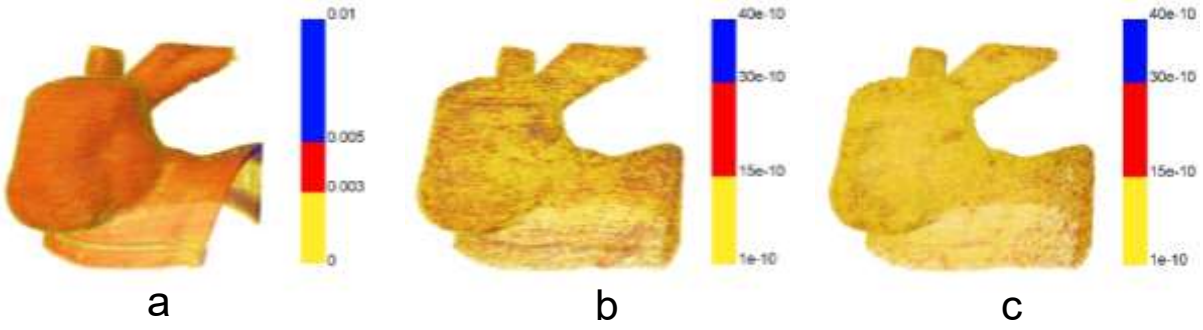

Figure 4.3. Volume rendering of reconstructed absorption and dark-field volumes with 20% opacity. (a) Absorption volume obtained with gratings oriented horizontally. Intensities are nearly constant. (b) Dark-field volume obtained with gratings oriented horizontally. (c) Dark-field volume obtained with gratings oriented horizontally. The dark-field signal is expressed as linear diffusion coefficient, ϵ, in m^{-1}. By comparison of images (b) and (c), the higher intensities obtained in (b) indicate that the sample is more effective in scattering X-rays in the vertical direction than in the horizontal direction**.**

Two-dimensional absorption and dark-field projections of higher magnification, 76 μm, were compared using a line probes, Figure 4.4. The absorption image, Figure 4.4a, detects the filament layers composing the sample. The effect of changing grating orientation is glaring in the dark-field images (Figures 4.4 b and 4.4c) and the more intense X-ray scattering obtained with the horizontal grating orientation suggests scattering centers aligned parallel to the filament layers. Line probes across the three projections (Figures 4.4a, 4.4 b and 4.4c) reveal that the absorption and dark-field intensities alternate in an opposing manner such that absorption maxima occur at dark-

field minima and vice versa (Figures 4.4d). Since absorption maxima should coincide with higher concentrations of material, the trend observed in the line probes indicate that while the absorption peaks correspond to the center of filament layers, the dark-field signal peaks arise from in-between filaments layers.

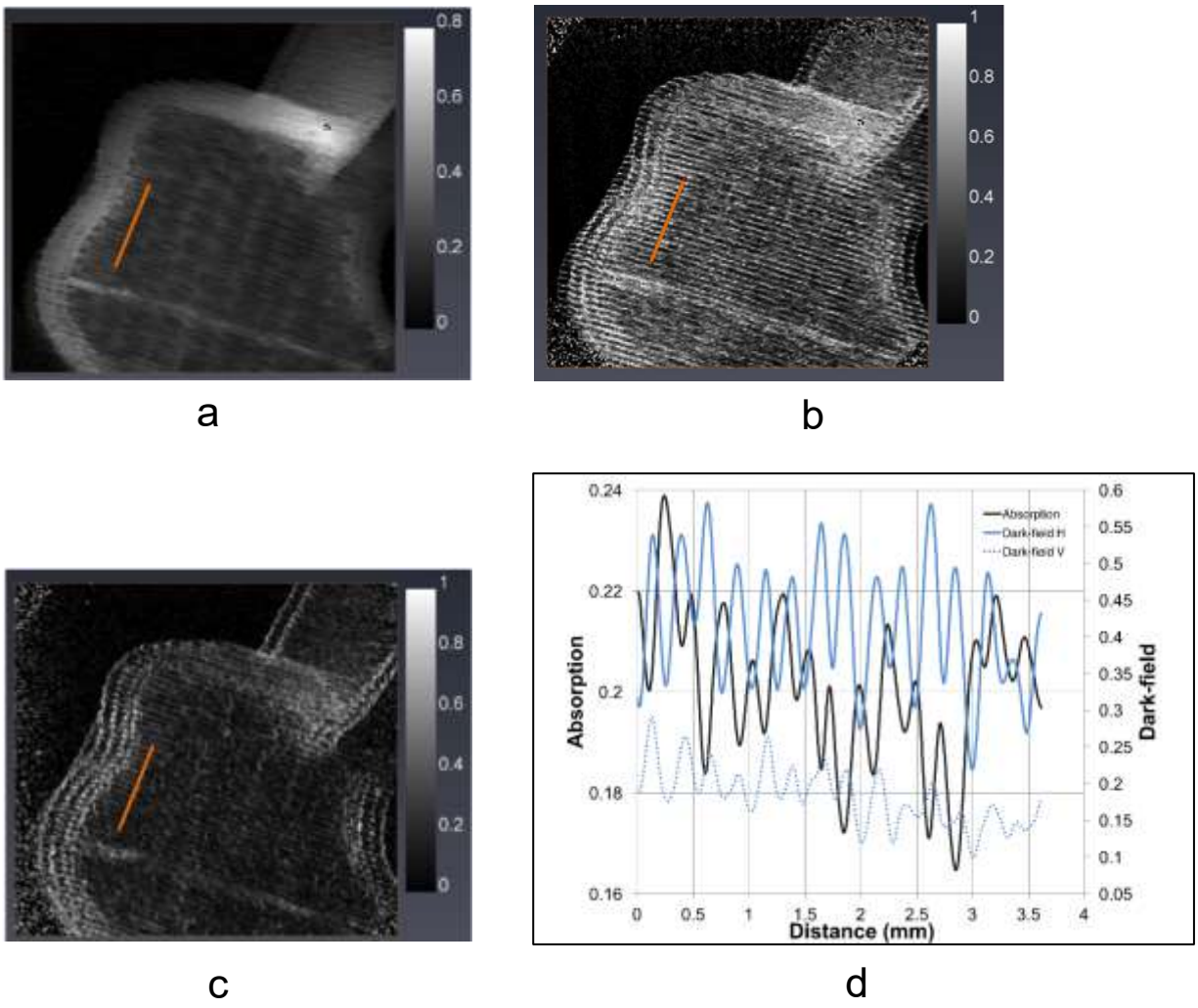

Figure 4.4. Absorption and dark-field projections of the ABS bunny with line probe plot. (a) Absorption and (b) dark-field projections with horizontal gratings. c) Dark-field projection with vertical gratings. (d) Line probe plot for projections (a), (b) and (c). Absorption and dark-field signals alternate in opposing fashion indicating that scattering (dark-field) arises from between filaments layers. Note that the width of the peaks is about 0.25 mm corresponding to the layer thickness setting of the printer.

A portion of the ear of another Stanford Bunny, also printed from ABS, was subjected to SEM imaging. The SEM images reveal gaps or cracks between filament layers with longitudinal axes of the right orientation to contribute to scattering in the vertical direction, Figure 4.5.

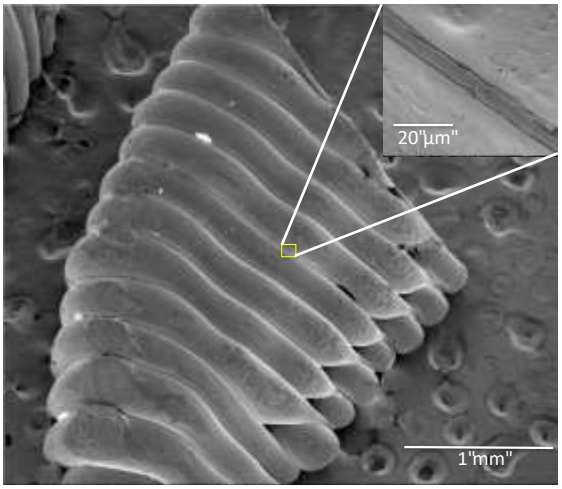

Figure 4.5. SEM image of a portion of an ABS bunny ear. Inset is a magnified image and reveals gaps between and parallel to the print layers.

4.3.2 The PLA Stanford Bunny

Reconstructed absorption and dark-field image modalities of the PLA bunny are shown in Figure 4.6 with 20% opacity. The dark-field images for the horizontal and vertical grating orientations are yet again clearly different with higher signal intensities characterizing the image for the horizontal grating orientation. Unlike with the ABS bunny however, the scatterers detected for the horizontal grating orientation seem to be homogenously distributed about the sample. It should be noted that the ABS and PLA samples also differ in terms of the printer used to print them; a Stratasys Dimension Elite printer for the ABS sample and a Makerbot printer for the PLA sample.

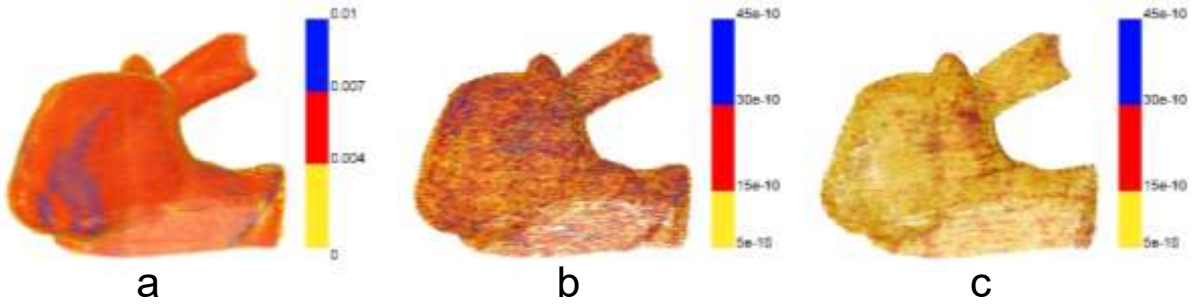

Figure 4.6. Reconstructed absorption and dark-field volumes for Stanford Bunny printed in PLA. (a) Absorption and (b) dark-field volumes with horizontal gratings. (c) Dark-field volume with vertical gratings. Opacity set to 20%.

4.3.3 The Quadratic Sample

Projections of the absorption and dark-field image modalities obtained using the single-shot interferometry technique are shown in Figure 4.7. In this technique no reorientation of gratings is needed as a checkerboard grating is used and scattering in a given direction is extracted by spatial harmonic analysis of the recorded raw projection. Two Talbot distances 84 mm and 251 mm corresponding to the 1st and 3rd Talbot distances for an 18 keV design energy, were probed. The correlation lengths were determined to be 1.705 μm and 5.094 μm for the 1st and 3rd Talbot distances, respectively. As mentioned earlier, the absorption image modality is independent of X-ray scattering direction and this can be seen in the near similar absorption images for the two Talbot distances probed (Figure 4.7a and 4.7d). Comparison of the dark-field images when scattering in the vertical and horizontal directions are probed reveal that scattering is more effective in the vertical direction indicating filament-to-filament print defects with orientation similar to that observed in both Stanford Bunny tomography volumes. As Expected, the scattering intensities increase from the 1st to the 3rd Talbot distance due to increase detection of scatterers.

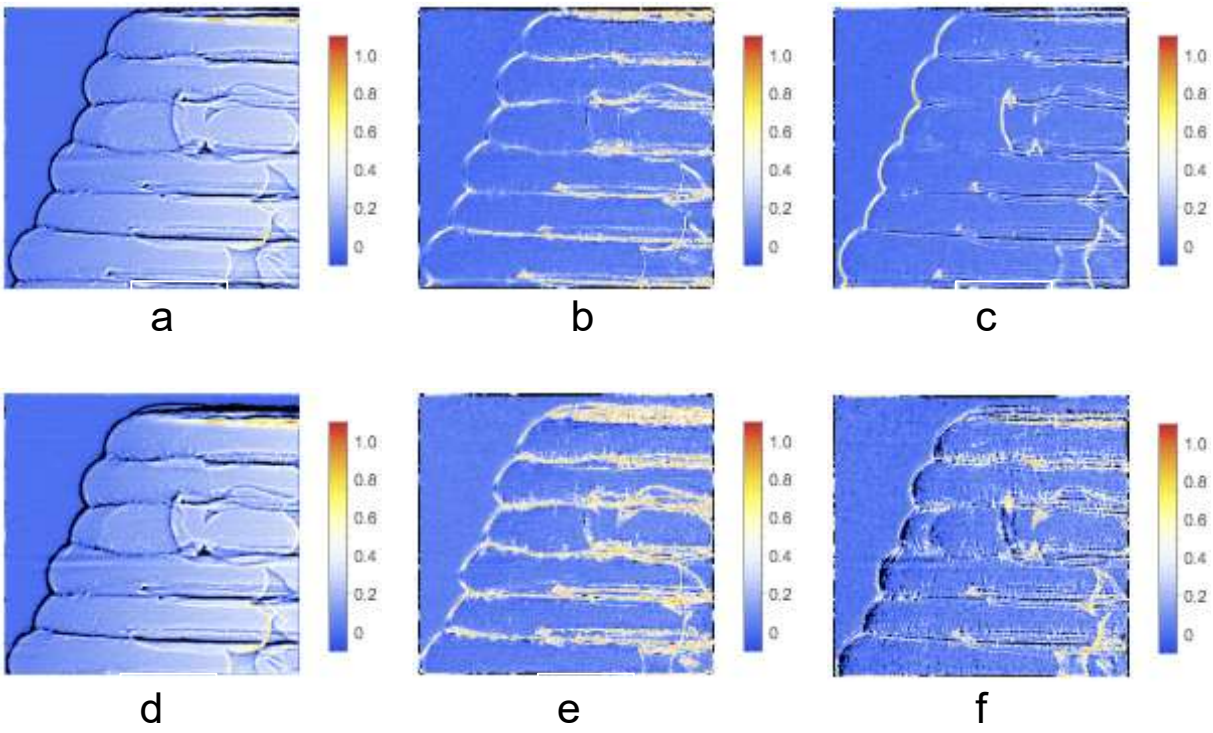

Figure 4.7. Absorption and dark-field projections of the PLA quadratic object obtained using single-shot interferometry. (a) Absorption projection, (b) dark-field projection of the vertical harmonic, and (c) dark-field projection of the horizontal harmonic acquired at the 1st Talbot distance. (d) Absorption projection, (e) dark-field projection of the vertical harmonic, and (f) dark-field projection of the horizontal harmonic acquired at the 3rd Talbot distance. Increased detection of scatterers observed as the Talbot distance is increased. Apart from the slight beam divergence effect, the absorption images are similar.

4.3.4 Curvature Analysis

As described in Section 4.2.5, a curvature analysis was carried out on the reconstructed slices of the ABS bunny. Following the application of the mask, the resulting absorption and dark-field slices are shown, with two traces, in Figures 4.8a and 4.8b. The pink trace is the interpolation function for the perimeter derived from the absorption image. The blue trace indicates the (row, column) coordinate centers used for intensity selection of absorption and dark field values within a radius of two pixels. Fig. 4.8c shows the reconstruction of the shape of the slice from the curvature values for corresponding $\{x, y\}$

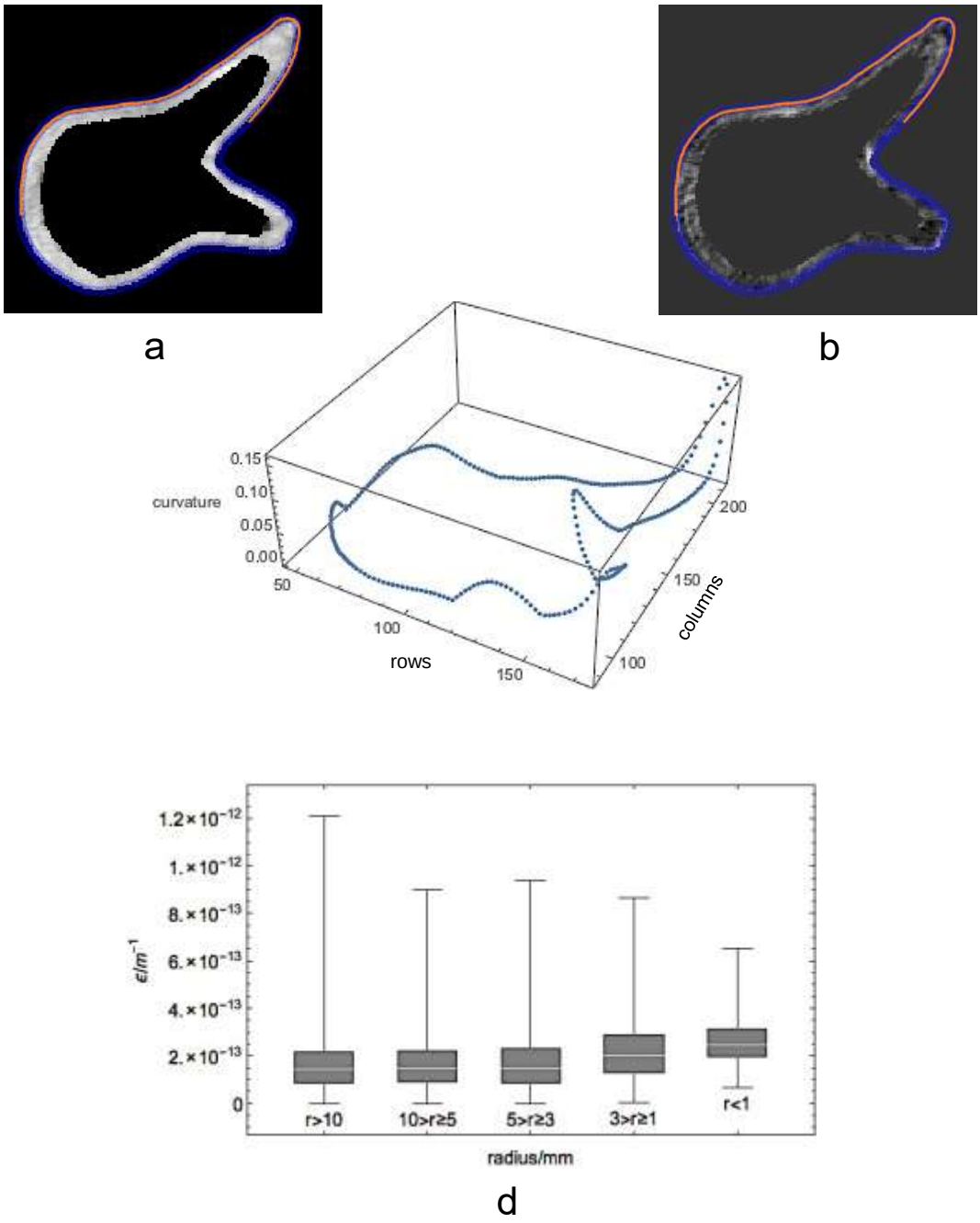

Figure 4.8. Curvature analysis. (a) Absorption slice (b) Dark-field slice for horizontal grating orientation. The blue trace is the sample perimeter derived form the mask while the pink trace show the coordinates of pixels selected for absorption and linear diffusion coefficients. (c) Reconstructed perimeter from calculated curvature and corresponding $\{x, y\}$ coordinates. (d) Plot of variation of dark-field with radii (inverse of curvature). Curvature values were put in groups. The plot shows a slight correlation between curvature and dark-field value as slightly higher mean dark-field values occur for radii of 3 mm or less.

coordinates which is in agreement with the original slice as inspected in ImageJ. The results of the curvature analysis on sixty-six slices are presented in Figure 4.8d where the dark-field values are in units of linear diffusion coefficients and curvature values have been converted to radii. The inverse relationship between curvature with radius means lower radii have higher curvature values. Inspection of the data plot in Figure 4.8d reveals a slightly higher mean of dark-field values for radii of 3 mm or less.

4.4 Conclusions

Anisotropy in the tensile strength of additively manufactured parts has been reported and usually attributed to improper adhesion of print material. This has been revealed with conventional tomography and microscopic imaging of fractures samples. However, x-ray grating interferometry —the dark-field signal in particular— has the advantage of revealing porosities on a size scale smaller than the detector pixels can and also provide some information on their orientation. A comparison of the images obtained with horizontal gratings with that obtained with vertical gratings shows that scattering is dominated by structures with elongated dimensions in the plane of the print layers. Thus, the orientation sensitivity of the dark-field signal provides some direction in determining the mechanism or source of porosity formation in additive manufacturing systems. The ABS dark-field image with grating in the horizontal position suggested a concentration anisotropic scatterers in specific regions like the bunny forehead and ears. This prompted a curvature analysis of the sample perimeter and showed a slight correlation between the darkfield signal and perimeter curvature.

4.5 References

1. Yashiro, W.; Terui, Y.; Kawabata, K.; Momose, A., On the origin of visibility contrast in x-ray Talbot interferometry. *Optics Express* **2010,** *18* (16), 16890-16901.

2. Pfeiffer, F.; Bech, M.; Bunk, O.; Donath, T.; Henrich, B.; Kraft, P.; David, C., X-ray dark-field and phase-contrast imaging using a grating interferometer. *Journal of Applied Physics* **2009,** *105* (10), No. 102006.

3. Yaroshenko, A.; Hellbach, K.; Yildirim, A. Ö.; Conlon, T. M.; Fernandez, I. E.; Bech, M.; Velroyen, A.; Meinel, F. G.; Auweter, S.; Reiser, M.; Eickelberg, O.; Pfeiffer, F., Improved In vivo Assessment of Pulmonary Fibrosis in Mice using X-Ray Dark-Field Radiography. *Scientific Reports* **2015,** *5*, No. 17492.

4. Lim, H.; Park, Y.; Cho, H.; Je, U.; Hong, D.; Park, C.; Woo, T.; Lee, M.; Kim, J.; Chung, N.; Kim, J.; Kim, J., Experimental setup and the system performance for single-grid-based phase-contrast x-ray imaging (PCXI) with a microfocus x-ray tube. *Optics Communications* **2015,** *348*, 85-89.

5. Pfeiffer, F.; Bech, M.; Bunk, O.; Kraft, P.; Eikenberry, E. F.; Brönnimann, C.; Grünzweig, C.; David, C., Hard-X-ray dark-field imaging using a grating interferometer. *Nature materials* **2008,** *7* (2), 134-137.

6. Eggl, E.; Schleede, S.; Bech, M.; Achterhold, K.; Loewen, R.; Ruth, R. D.; Pfeiffer, F., X-ray phase-contrast tomography with a compact laser-driven synchrotron source. *Proceedings of the National Academy of Sciences* **2015,** *112* (18), 5567-5572.

7. Sarapata, A.; Ruiz-Yaniz, M.; Zanette, I.; Rack, A.; Pfeiffer, F.; Herzen, J., Multi-contrast 3D X-ray imaging of porous and composite materials. *Applied Physics Letters* **2015,** *106* (15), No. 154102.

8. Prade, F.; Chabior, M.; Malm, F.; Grosse, C. U.; Pfeiffer, F., Observing the setting and hardening of cementitious materials by X-ray dark-field radiography. *Cement and Concrete Research* **2015,** *74*, 19-25.

9. Hannesschläger, C.; Revol, V.; Plank, B.; Salaberger, D.; Kastner, J., Fibre structure characterisation of injection moulded short fibre-reinforced polymers by X-ray scatter dark field tomography. *Case Studies in Nondestructive Testing and Evaluation* **2015,** *3*, 34-41.

10. Frazier, W. E., Metal Additive Manufacturing: A Review. *Journal of Materials Engineering and Performance* **2014,** *23* (6), 1917-1928.

11. Seppala, J. E.; Migler, K. D., Infrared thermography of welding zones produced by polymer extrusion additive manufacturing. *Additive manufacturing* **2016,** *12*, 71-76.

12. Ziemian, C.; Sharma, M.; Ziemian, S., Anisotropic mechanical properties of ABS parts fabricated by fused deposition modelling. In *Mechanical engineering*, InTechOpen: 2012.

13. Sallica-Leva, E.; Jardini, A. L.; Fogagnolo, J. B., Microstructure and mechanical behavior of porous Ti–6Al–4V parts obtained by selective laser melting. *Journal of the Mechanical Behavior of Biomedical Materials* **2013,** *26*, 98-108.

14. Waller, J. M.; Parker, B. H.; Hodges, K. L.; Burke, E. R.; Walker, J. L. *Nondestructive evaluation of additive manufacturing state-of-the-discipline report*; Nov 2014.

15. Maskery, I.; Aboulkhair, N. T.; Corfield, M. R.; Tuck, C.; Clare, A. T.; Leach, R. K.; Wildman, R. D.; Ashcroft, I. A.; Hague, R. J. M., Quantification and characterisation of porosity in selectively laser melted Al–Si10–Mg using X-ray computed tomography. *Materials Characterization* **2016,** *111*, 193-204.

16. Seifi, M.; Salem, A.; Beuth, J.; Harrysson, O.; Lewandowski, J. J., Overview of Materials Qualification Needs for Metal Additive Manufacturing. *JOM* **2016,** *68* (3), 747-764.

17. Strobl, M., General solution for quantitative dark-field contrast imaging with grating interferometers. *Scientific Reports* **2014,** *4*, No. 07243.

18. Betz, B.; Harti, R. P.; Strobl, M.; Hovind, J.; Kaestner, A.; Lehmann, E.; Van Swygenhoven, H.; Grünzweig, C., Quantification of the sensitivity range in neutron dark-field imaging. *Review of Scientific Instruments* **2015,** *86* (12), No. 123704.

19. Brooks, A. J.; Yao, H.; Yuan, J.; Kio, O.; Lowery, C. G.; Markötter, H.; Kardjilov, N.; Guo, S.; Butler, L. G., Early detection of fracture failure in SLM AM tension testing with Talbot-Lau neutron interferometry. *Additive Manufacturing* **2018,** *22*, 658-664.

20. Brooks, A. J.; Hussey, D. S.; Yao, H.; Haghshenas, A.; Yuan, J.; LaManna, J. M.; Jacobson, D. L.; Lowery, C. G.; Kardjilov, N.; Guo, S.; Khonsari, M. M.; Butler, L. G., Neutron interferometry detection of early crack formation caused by bending fatigue in additively manufactured SS316 dogbones. *Materials & Design* **2018,** *140*, 420-430.

21. Brooks, A. J.; Ge, J.; Kirka, M. M.; Dehoff, R. R.; Bilheux, H. Z.; Kardjilov, N.; Manke, I.; Butler, L. G., Porosity detection in electron beam-melted Ti-6Al-4V using high-resolution neutron imaging and grating-based interferometry. *Progress in Additive Manufacturing* **2017,** *2* (3), 125-132.

22. Kio, O. J.; Yuan, J.; Brooks, A. J.; Knapp, G. L.; Ham, K.; Ge, J.; Van Loo, D.; Butler, L. G., Non-destructive evaluation of additively manufactured polymer objects using X-ray interferometry. *Additive Manufacturing* **2018,** *24*, 364-372.

23. Ligon, S. C.; Liska, R.; Stampfl, J. r.; Gurr, M.; Mülhaupt, R., Polymers for 3D printing and customized additive manufacturing. *Chemical reviews* **2017,** *117* (15), 10212-10290.

24. Domingo-Espin, M.; Puigoriol-Forcada, J. M.; Garcia-Granada, A.-A.; Lluma, J.; Borros, S.; Reyes, G., Mechanical property characterization and simulation of fused deposition modeling Polycarbonate parts. *Materials & Design* **2015,** *83*, 670-677.

25. The Stanford 3D Scanning Repository. Stanford University Computer Graphics Laboratory: 1994.

26. Rovenski, V., *Modeling of Curves and Surfaces with MATLAB*. Springer: 2010.

27. Herzen, J., A grating interferometer for materials science imaging at a second-generation synchrotron radiation source [PhD Thesis]. *Hamburg University* **2010**.

28. Marathe, S.; Assoufid, L.; Xiao, X.; Ham, K.; Johnson, W. W.; Butler, L. G., Improved algorithm for processing grating-based phase contrast interferometry image sets. *Review of Scientific Instruments* **2014,** *85* (1), No. 013704.

29. Palenstijn, W. J.; Batenburg, K. J.; Sijbers, J. In *The ASTRA tomography toolbox*, 13th International Conference on Computational and Mathematical Methods in Science and Engineering, CMMSE, 2013; pp 1139-1145.

30. Marone, F.; Stampanoni, M., Regridding reconstruction algorithm for real-time tomographic imaging. *Journal of synchrotron radiation* **2012,** *19* (6), 1029-1037.

31. Gilbert, P., Iterative methods for the three-dimensional reconstruction of an object from projections. *Journal of theoretical biology* **1972,** *36* (1), 105-117.

32. Assoufid, L.; Shi, X.; Marathe, S.; Benda, E.; Wojcik, M. J.; Lang, K.; Xu, R.; Liu, W.; Macrander, A. T.; Tischler, J. Z., Development and implementation of a portable grating interferometer system as a standard tool for testing optics at the Advanced Photon Source beamline 1-BM. *Review of Scientific Instruments* **2016,** *87* (5), No. 052004.

CHAPTER 5
X-RAY INTERFEROMETRIC STUDIES ON THE EFFECT OF FLAME RETARDANT INCORPORATION INTO POLYMERIC OBJECTS BY FUSED DEPOSITION MODELING

5.1 Introduction

A wide variety of common plastics are flammable and their flammability needs to be addressed where fire safety is a concern.[1] Examples of such plastics include acrylonitrile butadiene styrene (ABS), low density polyethylene (LDPE), polycarbonate, polystyrene, high impact polystyrene (HIPS), polyvinyl chloride, polyurethanes etc.[1] These plastics are usually desirable due to one or more favorable material characteristics. For example, ABS has properties of insulation, easy processing, shiny surface, thermal stability, good mechanical strength, resistance to oil, resistance to weather and high impact strength.[2]

Flame retardants can make ignition more difficult and/or decrease the rate of flame propagation when an otherwise flammable material is exposed to a source of heat.[3] Introduction of flame retardants into flammable plastics is mostly done by melt blending as it is less expensive and does not degrade the physical properties for which the plastic had been chosen in the first place.[4,5] Fire retardancy is generally imparted to ABS this way.[6] The common flame retardants for ABS are halogen-containing compounds such as decabromodiphenyl oxide (DBDPO), tetrabromobisphenol A (TBBPA) and 1,2-bis (2,4,6-tribromophenoxy) ethane (BTBPOE).[2] In a study on the heat release of ABS in the presence of different concentrations of a brominated flame retardant (1,2-bis pentabromophenyl ethane), antimony oxide and zinc borate; peak heat release values decreased by 60-73 %.[1]

Another way to make polymeric objects less flammable is through the production or accumulation of a thermally stable surface layer, able to act as a barrier to mass (oxygen, smoke) and/or heat transfer.[5,7] Such a layer is built during the early stage of combustion as a consequence of the decomposition of the polymer surface layer in the presence of a fire retardant.[7] The flame retardant can be introduced to the surface by intumescent coatings, layer by layer assembly etc. Intumescent materials swell up and expand over the surface of the material when exposed to heat above a given temperature.[5] In the application of intumescent coatings, adhesion and retention of fire retardancy over time are concerns.[7] In layer-by-layer assembly, flame retardant species are adsorbed on a substrate by taking advantage of a specific interaction (e.g. electrostatic interactions) between the two.[7]

Exposure to heat, moisture, UV or gamma irradiation and abrasion can lead to the deterioration of the flame retardancy of polymers through leaching out of additives, chemical degradation of the flame-retardant system, and chemical or physical modification of the polymer structure.[8]

Evaluating the flammability of a material can be done in a variety of ways and depends on the intended application of the material. A number of nationally or internationally standardized flammability tests are known. Common examples are the UL-94 flame test, the limiting oxygen index and the glow-wire ignition test.[9-14] Another test, the cone calorimeter test is useful for extensive information of the burning behavior like heat release, ignitability, mass loss, and smoke release by burning materials.[1] X-ray K-edge tomography was used to study high impact polystyrene (HIPS) samples containing a brominated flame-retardant to determine the concentrations of antimony and bromine

on burning.[15] In the study of the flame retardancy performance of a brominated flame retardant, X-ray single-shot interferometry enabled real-time imaging of heated samples.[16] Three-dimensional tomography imaging has been used to study homogeneity of flame retardant-polymer blends.[17,18]

In this work, the flame retardant was restricted to specific portions of an otherwise flammable polymeric sample through fused deposition modeling; an additive manufacturing technique. Effects of heat propagation on the sample microstructure were then studied by X-ray grating interferometry. Near-real time two-dimensional images of heated samples were acquired with synchrotron X-rays. A laboratory system was used for tomographic imaging of samples post-heating. By varying the sample to detector distance, different correlation lengths were probed.

5.1.1 Phase-Step Error Due to Irreproducible Nanometer Stage Motion

Phase shifting interferometry is generally regarded as the most accurate phase measurement technique.[19] Due to the very small distances involved accuracy is very important. Inaccuracies in predetermined shifts can result from a faulty or poorly calibrated translation motor and vibration of instruments' component parts. Since the measured signal is supposed to represent the effect of the introduced phase shift, shift inaccuracies can lead to reduced image contrast and noisy datasets or images. Data acquired at LSU CAMD for this dissertation showed fringe-like noise after processing. This is by no means exclusive to the CAMD interferometer as some data acquired at the advanced photon source (APS), Chicago and more recently at Helmoltz Zentrum Berlin (HZB) exhibited a lot of residual fringes.

To achieve the very small translations involved in stepped-grating interferometry, the interferometer at LSU CAMD was equipped with a Physik Instrument P-542.2CL XY stage with a resolution of 0.7 nm in closed loop mode. The stage itself cost about $13,000 but with the chassis and amplifier the cost came to about $35,000. For a grating with a period of 4.8 μm, 12 steps each of 0.48 μm was typically used to cover slightly more than one period of the sinusoidal signal. It was estimated that motion errors of 1% or 48 nm, would be acceptable.

According to the data sheet for the P-542.2CL XY stage, the travel range was 200 μm with a linearity error of 0.03%.[a] Thus, over the travel range of 5 μm, the linearity error should not exceed 1.5 nm. The repeatability error was less than 5 nm. With these specifications the instrument was expected to exceed our needs. However, after successful image acquisition for less than two years the dark-field images obtained from the CAMD interferometer began to suffer from fringes.

Stepped grating interferometry images acquired at APS also suffered from fringes. Interestingly, the APS system utilized a similar Physik Instrument P-542.2CL XY stage. Investigation of the fringe structures in both cases strongly indicated errors in the P-542.2CL XY stage performance. When the sinusoidal interferogram was fitted with variability allowed in the motor position, the best fits indicated stage errors on the order of 100 to 200 um. The CAMD stage was returned to Physik Instrument for re-calibration and has been returned to CAMD. Unfortunately, reduced synchrotron performance has not allowed a test of the re-calibrated stage.

[a] https://www.physikinstrumente.com/en/products/nanopositioning-piezo-flexure-stages/xy-piezo-flexure-stages/p-5412-p-5422-xy-piezo-stage-201530

5.1.2 Phase-step Error Correction

Many attempts at the removal or reduction of fringe-like artifacts have been reported in published works showing that fringe artifacts have been around for a long time. Correction for errors in shift are largely composed of using spatial-carrier interferograms and iterative calculations of the phase of the wavefront.[19] For an iterative calculation it is important that the starting value is close to the true value. An example of the iterative methods is the least squares approach. A self-tuning phase-shifting algorithm was developed and reported to require very few iterations.[20] Combinations of the least squares approach with other algorithms have also been reported.[21,22] For the removal or reduction of residual fringes in processed data having a correlation to the fringe pattern in the raw data, an algorithm based on the determined correlations has been reported.[23] An algorithm based on determining a projection angle theta, for a set of interferograms acquired over a 2π phase-shift, at which a Radon transform is applied has also been reported.[24] The aim was to obtain a single sinusoidal waveform of the fringe patterns (interferograms) characterized by a similar amplitude and frequency.[24]

Phase-stepping correction based on Fourier-transform methods have been suggested; here no *a priori* information or initial guess values of the phase steps are required.[25,26] Fourier-based methods require a spatial carrier frequency.[26]

To avoid instrumental instabilities and other challenges associated with mechanical phase-stepping, Harmon et al. reported an electromagnetic phase-stepping technique where phase-stepping was achieved by moving the X-ray beam with the aid of a solenoid coil.[27] This mechanical-motion-free technique was found to be of similar sensitivity as the mechanical phase-stepping technique.[28]

The near-real time two-dimensional images acquired using the CAMD synchrotron interferometer were tainted by fringe artifacts. Least-squares fitting of raw interferograms to determine the actual phase-shifts was attempted. The first step was to determine if there was a pattern in the fringe spatial distribution across interferograms. In the absence of any pattern the vectorized least squares algorithm, used for fitting interferograms in each pixel, was modified to accommodate small deviations in the grating steps. This algorithm is somewhat similar to that described by de Marco *et al*.[23] The outcome was unsuccessful. Another approach involved simulating fringe noise in an image by varying factors such as phase wrap, grating tilt and grating step errors; followed by an attempt to remove the fringes with an iterative vectorized least square algorithm. Simulated fringes with phase wrap, grating step errors and zero tilt error were successfully corrected. This algorithm was then applied to experimental data and resulted in only a slight reduction in the fringes. Attempts were also made to "work around" the fringes in a bid to extract measurements from the filament-filament interface in the dark-field data but without success. Though efforts to remove or reduce the fringe artifacts in the CAMD data were unsuccessful thus making the images not ideal for quantitative analysis, some qualitative information can be extracted from these uncorrected two-dimensional images.

5.2 Materials and Methods

5.2.1 Samples

ABS and ABS-flame-retardant (ABSFR) filaments were purchased from Filabot. The ABSFR filament contained a brominated epoxy-oligomer flame retardant. Using a *Flashforge Creator Pro* dual filament printer, blocks of design dimensions 20 mm x 10 mm x 3mm were printed. Printed dimensions turned out to be 20.2 ±0.3 mm x 9.4 ±0.3

mm x 2.9 ±0.3 mm. The blocks were of different composition –ABS/ABSFR layers in ratio 3:1, ABS/ABSFR layers in ratio 1:1 and pure ABSFR. The printer nozzle temperatures were 235˚C and 230˚C for the ABS and ABSFR filaments, respectively. The build plate temperature was 60˚C and the layer thickness was set to 0.27 mm. Other parameters are; infill 100%, feed rate 80mm/s and travel federate 150 mm/s.

5.2.2 Two-Dimensional Imaging with A Talbot-Lau Stepped-Grating Interferometer

A Talbot-Lau stepped-grating interferometer set-up at LSU CAMD was used to acquire two-dimensional near-real time images of heated samples. Using a Si(111) double crystal Laue monochromator, 38.8 keV synchrotron X-rays were supplied to the system. The G0 and G2 analyzer gratings each had >200 μm high Au linear structures with a 4.8 μm period, on 200 μm thick Si wafers. The G1 phase grating had 6.7 μm high Au linear structures on a 200 μm Si wafer for a π phase shift at 35 keV, and had a 4.8 μm period.

The G0—G1=G1—G2 distance was 524 mm, the third Talbot distance for the effective energy of about 38 keV, and the sample was placed between G1 and G2, 335 mm downstream of G1. The gratings were oriented horizontally. The detector system was a Pco.edge 5.5 camera coupled to a 250 μm thick LuAg(Ce). The camera had a 2560 x 2160 array of pixels, each 6.5 μm x 6.5 μm in size and was operated in the 4 by 4 binning mode. With optical magnification the effective pixel size was determined to be approximately 15 μm. The heating system was a modified glow wire set-up where the narrow protrusion of a heater applied a force of 1 N in an orientation normal to the print layers. Heating was for 2 s after which the G2 grating was translated in 15 steps, moving by 0.48 μm per step, in a direction transverse to the grating structures and beam

propagation axis. Images were acquired at each step with each exposure lasting 2 s. Heating was repeated for a total of thirty times with a set of stepped-grating images acquired in-between heating. Reference images (without the sample) and dark images (with X-rays off), were also acquired. Two heating temperatures, 265˚C and 275˚C, were probed.

5.2.3 Tomography Imaging with A Talbot-Lau Stepped-Grating Interferometer

This involved the use of a laboratory-based W. M. Keck stepped-grating interferometer setup at LSU. The X-ray source was a microfocus tungsten Hamamatsu X-ray tube, L9181-02, operated with a source size of 40 μm at 45 kV and 290 μA. Operation was without any filtering and each exposure time was 8 s. All three gratings had a period of 4.8 μm and comprised periodic linear gold structures on silicon wafers. The G1 phase grating had 3.9 μm thick linear structures, for a π phase shift at 26 keV. The G0 and G2 absorption gratings had 150 μm thick linear structures.

The detector was a nitrogen-cooled Pilatus 100k photon counter with 172 μm sized pixels, in a 487 x 195 array. The G0—G2 distances was 725 mm and G2 was mounted in-between G1 and G2 for a grating magnification of 2. Thus, the third Talbot distance was used. The samples were the heated ABS/ABSFR samples from section 5.2.2 above. The samples were placed between G1 and G2 and imaged at four positions—80 mm, 90 mm, 100 mm and 110 mm—upstream from G2. For the set of distances, autocorrelation lengths probed were 0.78 μm, 0.88 μm, 0.98 μm and 1.08 μm. The effective pixel size was ~ 150 μm. The source to detector distance was 860 mm and the G2 to detector distance was 20mm. The sample was rotated by 190˚ in 1˚ increments and the G2 grating

translated by 12 steps that covered over one fringe period. Images without the samples were acquired as reference images.

5.2.4 Two-dimensional Correlation Length Scanning Experiment with A Talbot-Lau Stepped-Grating Interferometer.

To probe different correlation lengths, a Talbot-Lau Stepped-Grating Interferometer setup at LSU CAMD was used. A Si (111) double crystal Laue monochromator was used to select X-rays of 38 keV and the detector was a Pco.edge 5.5 camera coupled to a 250 μm thick LuAg(Ce) scintillator. The camera had a 2560 x 2160 array of pixels, each of size 6.5 μm x 6.5 μm and was operated in the 4 by 4 binning mode. The effective pixel size was determined to be ~16.6 μm with optical magnification. The G0 and G2 analyzer gratings each comprised 200 μm high Au linear structures with a 4.8 μm period, on graphite wafers. The G1 phase grating had 6.7 μm high Au linear structures on a 200 μm Si wafer for a π phase shift at 35 keV, and had a 4.8 μm period.

The G0—G1=G1—G2 distance was 540 mm for an effective energy of 38.8 keV. The sample was positioned between G1 and G2 and the sample-to-detector distance was scanned, from 31 mm to 281 mm in steps of 10 mm by moving the sample. Thus, correlation lengths of 0.21 μm to 1.87 μm were probed. Operation involved heating the sample with a modified glow wire set-up where the narrow heating element applied a force of 1N to the sample in a direction normal to the print layers. Heating was for 2 s after which phase-stepping images were acquired at each G1 grating position. Imaging was performed over 4 cycles of heating. Reference images were acquired at the beginning of the experiment and after each heating. For each sample design, two heating temperatures of 265˚C and 275˚C were used.

5.2.5 Data Processing

The data obtained in Sections 5.2.2 and 5.2.4 were processed in Mathematica and visualized with Avizo. Mathematica processing involved reading in the reference and samples files and calculating the absorption, differential phase and dark-field values for each pixel. Sample codes used are provided in Appendix C.1. Images acquired in the tomography experiment (Section 5.2.3) were processed in the Tomopy software package where image reconstruction was executed using the SIRT and Gridrec algorithms. Sample codes for processing in Tomopy are provided in Appendix C.2 and C.3. By definition, the calculated visibility/dark-field signal should be <1 when small angle scattering occurs; since air is ideally a non-scatterer, the signal in air should be ~1. Due to the requirements that the sample exterior be set to 0 for volume reconstruction, the dark-field signal for the reconstruction volumes was set to 1-DF. Therefore, higher values in the dark-field region correspond to increased scattering. Avizo was used for image visualization of two-dimensional and tomographic images. To exclude surface scattering contribution to the dark-field volumes, a mask was created from the absorption volume and applied to the dark-field volume. Mask creation involved binarization, dilation by one pixel and erosion by two pixels.

5.3 Results

5.3.1 Two-dimensional Imaging at One Position with Repetitive Heating

The intention of repeatedly heating a sample (30 cycles) with immediate imaging after each heating session was to track the effect of heat on the sample. Due to a faulty grating translation stage, the grating position was not reproducible thus a mismatch in the grating position for reference and sample data. This resulted in fringe artifacts in the

processed dark-field, absorption and differential phase images. However, by focusing on the higher intensity ABS flame retardant composite (ABSFR) layers, some useful information was obtained from the absorption images. Figure 5.1 shows the images

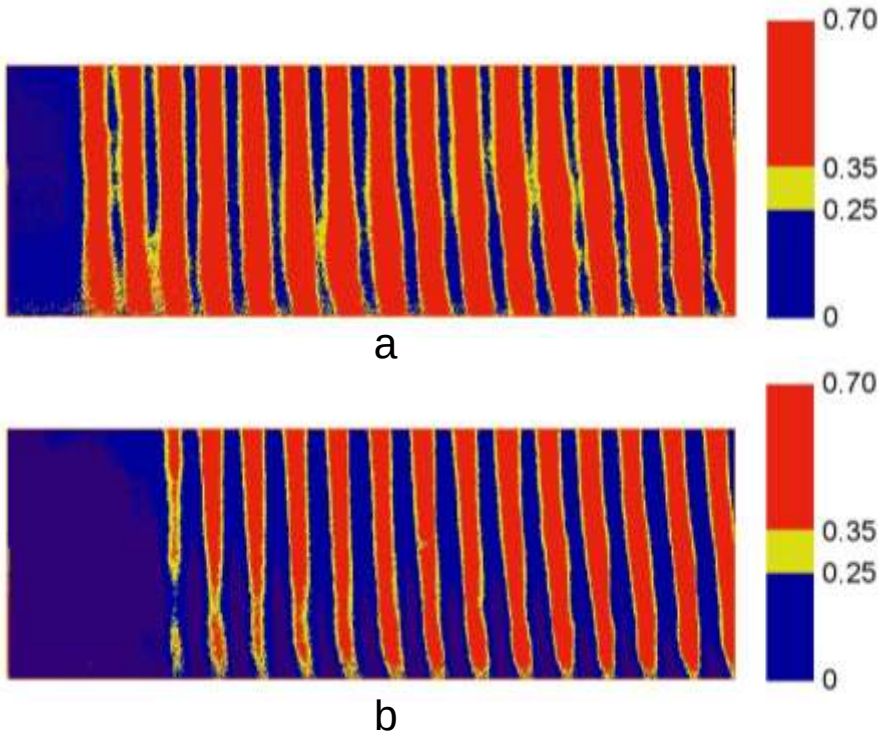

Figure 5.1. Absorption images of a 1:1 ABS/ABSFR sample heated at 265°C. (a) Image of a pristine sample. Sixteen ABSFR layers detected. (b) Image of the sample in (a) after the thirtieth heat application. Two full length ABSFR layers were lost. Point of heat application was at the left side. The seeming change in the size of higher intensity layers is due to fringe artifacts.

acquired for a 1:1 ABS/ABSFR sample heated at 265°C. Before the onset of heating (Figure 5.1a), sixteen ABSFR layers were detected but after the 30th heating cycle two layers were no longer detected (Figure 5.1b). The layers had mostly melted off due to direct contact with the heater. The width of the layers should be disregarded as it is due to fringe artifacts. Regardless of the width it is clear that a few layers have been lost.

Images acquired for a 3:1 ABS/ABSFR sample heated at 275°C are shown in Figure 5.2. The wider distance between ABSFR layers (three ABS layers in-between ABSFR layers versus one in-between for a 1:1 ABS/ABSFR sample), led to only one ABSFR layer coming into direct contact with the heater. After thirty heating cycles the layer is mostly undetected (Figure 5.2).

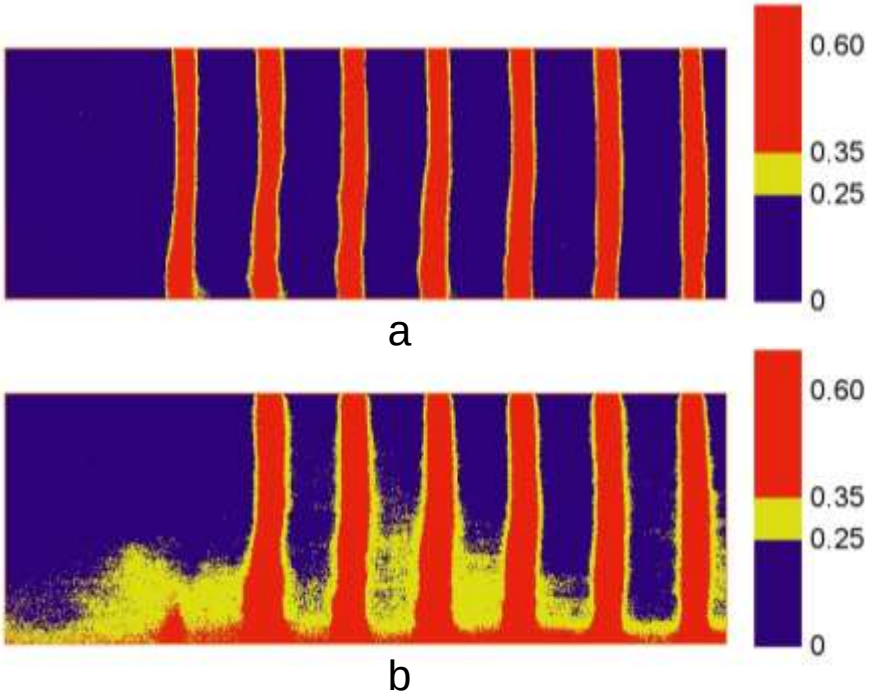

Figure 5.2. Absorption images of a 3:1 ABS/ABSFR sample heated at 275°C. (a) Image of a pristine sample. Seven ABSFR layers detected. (b) Image of the sample in (a) after the thirtieth heat application. The first ABSFR layer almost completely lost. Heat was applied from the left.

5.3.2 Tomography of Samples after Thirty Cycles of Heating

The reconstructed volumes were processed and displayed using Avizo software. Fully opaque mid-sectional views of the volumes are shown in all the images presented. The absorption images for samples with ABS/ABSFR ratios 1:1 and 3:1 are shown in Figure 5.3. The intensity distribution is as expected for the 3:1 and the 1:1 composition, with the lower intensity region arising from pure ABS layers and higher intensity regions

arising from the brominated flame retardant and ABS composite layers. A comparison of the absorption images of similar samples but at different heating temperatures seem to

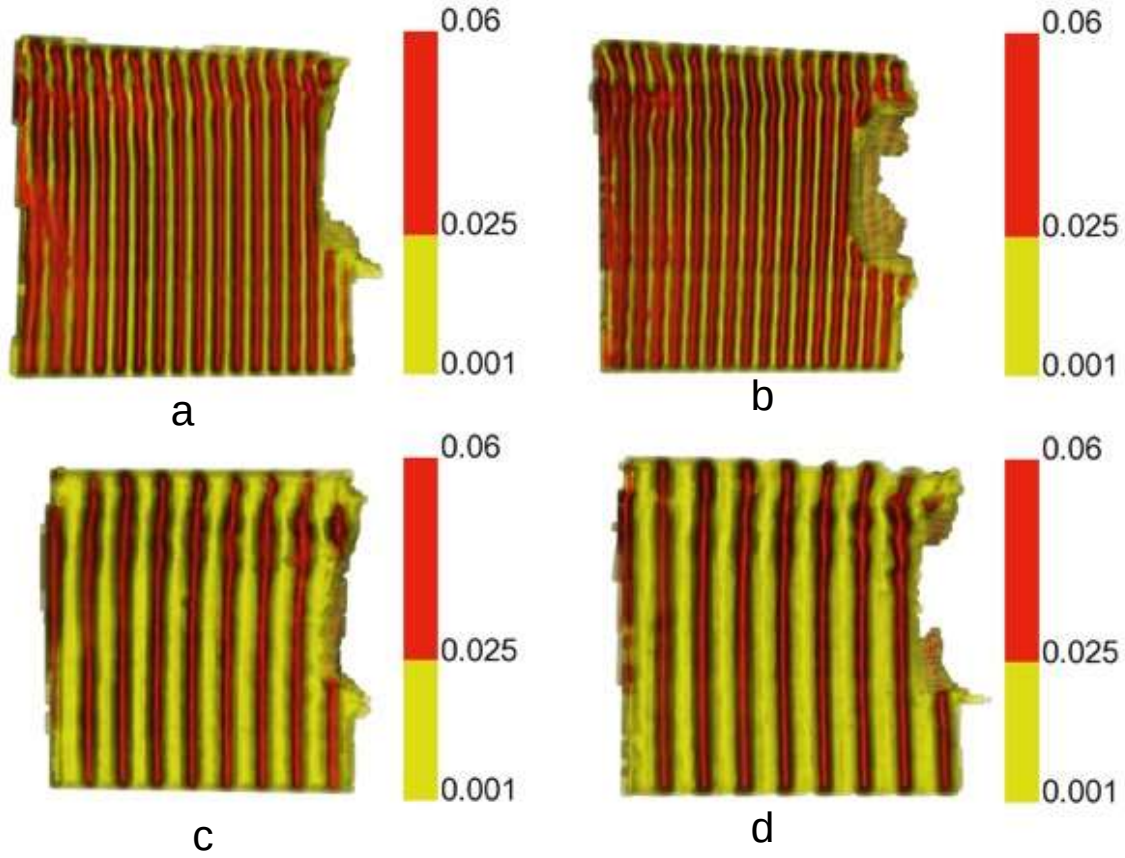

Figure 5.3. Sectional views of absorption volumes for 1:1 and 3:1 ABS/ABSFR samples. (a) Image for a 1:1 ABS/FR sample heated at 265°C and (b) heated at heated at 275°C. (c) Image for a 3:1 ABS/FR sample heated at 265°C and (b) heated at heated at 275°C. All four images are for a SDD of 80 mm. Heat application was at the right side.

reveal no visible differences. Correlation lengths are irrelevant in absorption imaging as the transmitted signal remains the same regardless of the sample-to-detector distance (SDD).

The dark-field volumes are a bit more interesting. It should be noted that scattering signal can arise from voids or lumps/particles in the sample. Surface scattering effects have been largely excluded by applying a mask as described in Section 5.2.5. The

samples showed a variation in the measured dark-field signal as the correlation length (SDD) was changed.

Figure 5.4 shows volume renderings of a sectional view of the dark-field volumes for a sample composing 1:1 layers of ABS and ABSFR heated at 265°C. At SDD 80 mm, corresponding to a correlation length of 0.78 μm (Figure 5.4a), scatterers having vertical dimensions ≤ 0.78 μm are detected. The figure shows lower intensities concentrated in

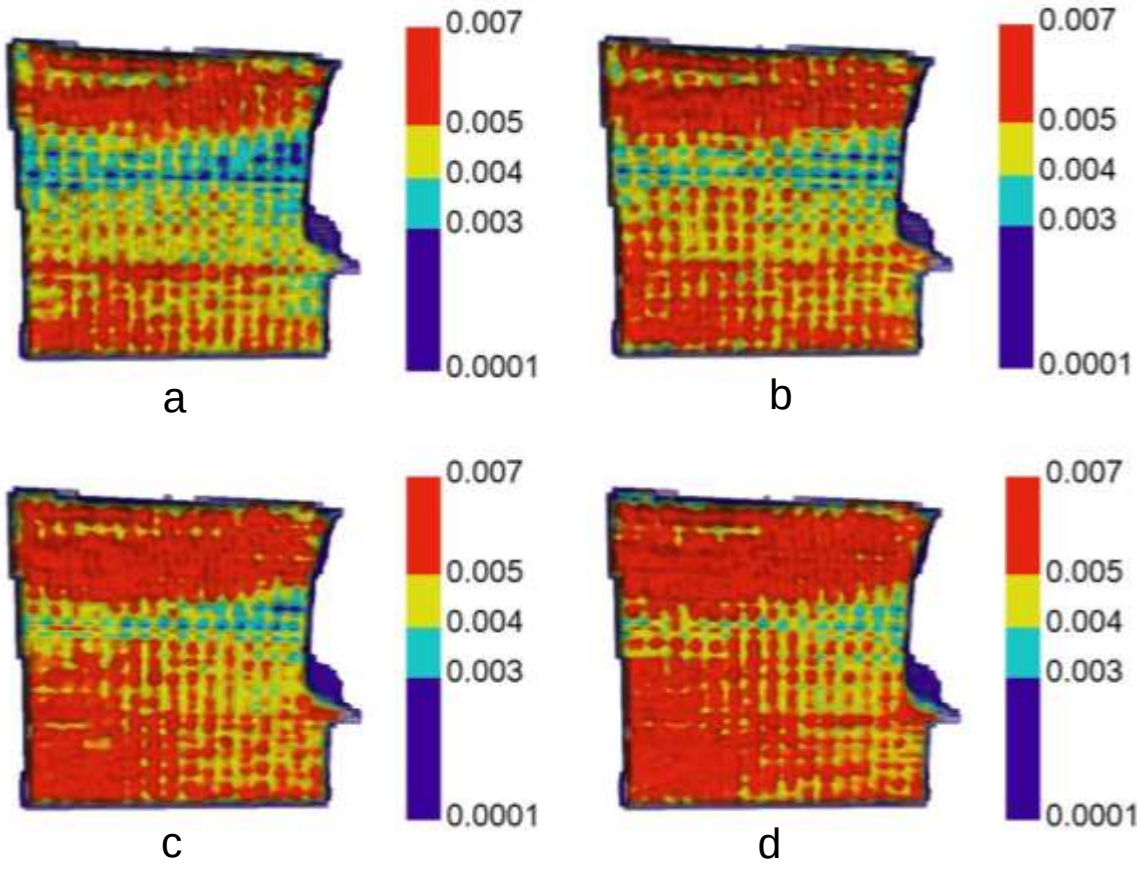

Figure 5.4. Sectional views of dark-field volumes for a 1:1 ABS/ABSFR sample heated at 265°C. (a) Image for correlation length 0.78 μm, (b) correlation length 0.88 μm, (c) correlation length 0.98 μm and (d) correlation length 1.08 μm. For (a) through (d), Sample to detector distances are 80 mm, 90 mm, 100 mm and 110 mm. Heat application was at the right side.

the region adjacent to the point where heating was applied. The lower intensities observed could be attributed to a lower concentration of scattering particles or voids in this region. As the SDD is varied from 80 mm to 110 mm, higher intensities gradually show up in this region (Figure 5.4 a-d). At SDD 110 mm, the instrument picks up additional scattering from scatters with vertical dimensions in the range of > 0.78 μm and ≥ 1.08 μm compared to SDD 80 mm. A possible explanation for the observed changes as the correlation length was varied is that due to the applied heat, particles in the region adjacent to the point where heating was applied underwent a change that led to them shrinking in size. Gases produced during the process in addition to original air pockets may have then contributed to larger-sized pores which were detected at higher correlation length settings.

For a 1:1 ABS/ABSFR sample heated at 275°C (Figure 5.5) similar effects were observed as for the 1:1 ABS/ABSFR sample heated at 265°C (Figure 5.4). Lower intensity dark-field signals concentrated in the region adjacent to the where heat was applied. As correlation length was increased from 0.78 μm to 0.88 μm, 0.98 μm and 1.08 μm, dark-field intensities gradually increased towards the heated region.

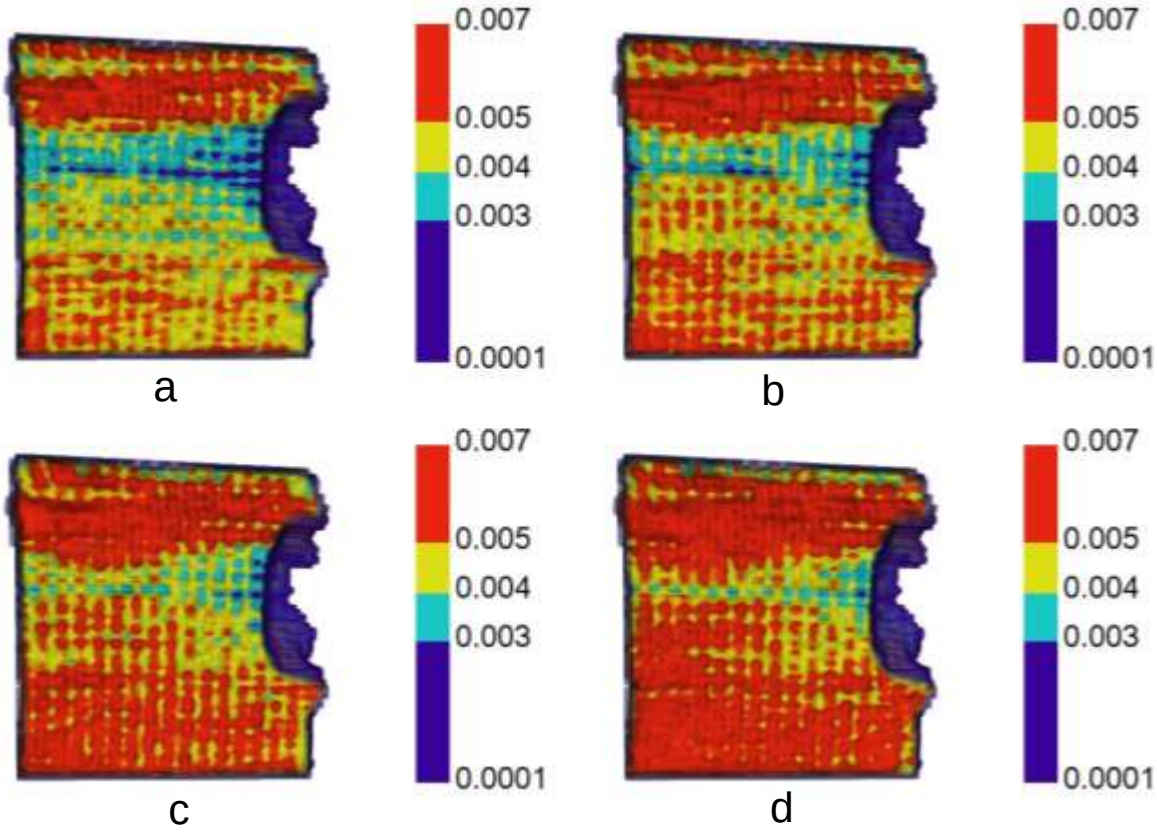

Figure 5.5. Sectional views of dark-field volumes for a 1:1 ABS/ABSFR sample heated at 275°C. (a) Image for correlation length 0.78 μm, (b) correlation length 0.88 μm, (c) correlation length 0.98 μm and (d) correlation length 1.08 μm. For (a) through (d), Sample to detector distances were 80 mm, 90 mm, 100 mm and 110 mm. Heat application was at the right side.

The reconstructed volumes for a 3:1 ABS/ABSFR sample heated at 265°C are shown in Figure 5.6. for different correlation lengths. This sample design seemed to throw more light on the effects of heat on the sample. First, based on the layer distribution, it is clear that ABSFR layers contribute more to scattering intensity than the ABS layers. It is then reasonable to say that the higher intensities detected in the ABSFR layers are due to the flame retardant molecules as this is the major difference between the ABS layers and the ABSFR layers. There may also be some contribution from the ABS-ABSFR interface. Looking at the region adjacent to the point where heat was applied, it is evident

that the high intensities characterizing the ABSFR layers above and below this region are relatively absent. This yet again points to the possibility of flame-retardant particles going into the gaseous state thus causing a lower concentration of scatterers in this region at a correlation length of 0.78 μm. The seeming uniformity of scattering intensity in the ABS layers indicate better adhesion of material within these layers.

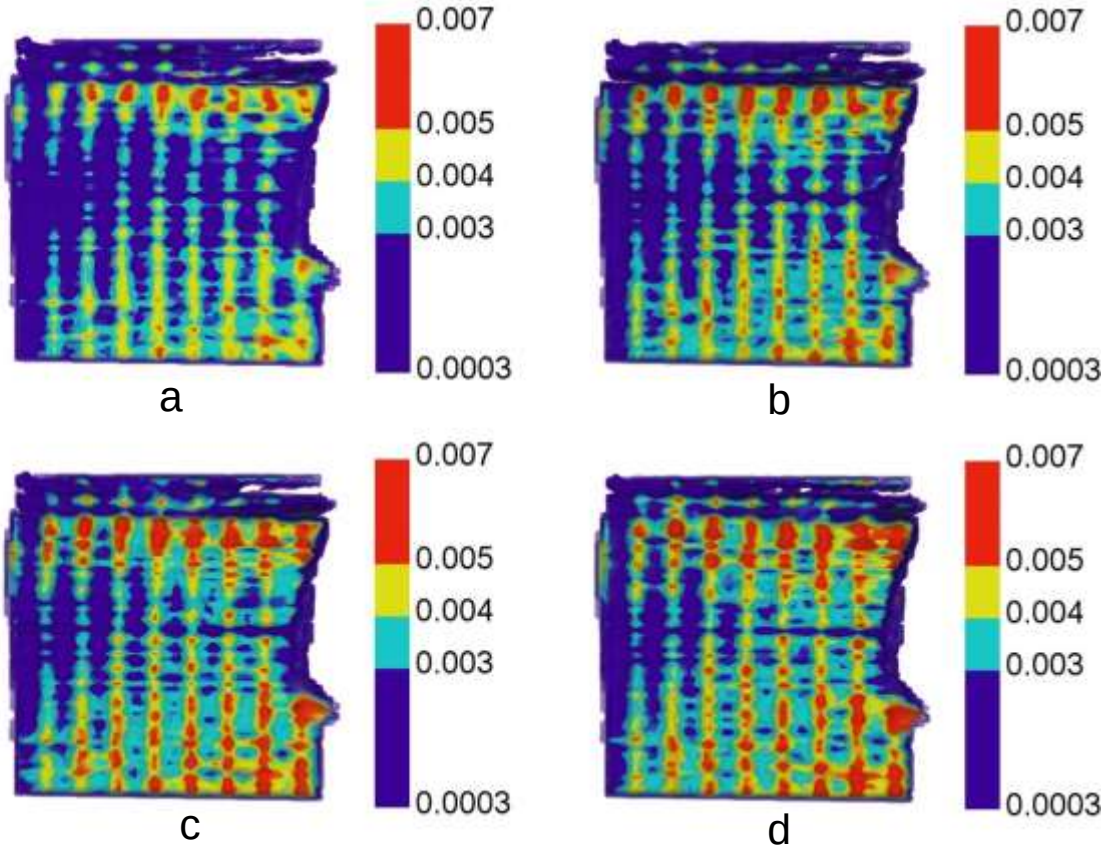

Figure 5.6. Sectional views of dark-field volumes for an ABS/ABSFR 3:1 sample heated at 265°C. (a) Image for correlation length 0.78 μm, (b) correlation length 0.88 μm, (c) correlation length 0.98 μm and (d) correlation length 1.08 μm. For (a) through (d), Sample to detector distances were 80 mm, 90 mm, 100 mm and 110 mm. Heat application was at the right side.

Figure 5.7 shows volume renderings of the ABS/ABSFR 3:1 sample heated at 275°C. Observations in this sample are similar to what was observed in the ABS/ABSFR 3:1 sample heated at 265°C (Figure 5.6) though there seems to be less scattering in this

than seen with the 265°C sample. For both ABS/ABSFR 3:1 samples, there seems to be an absence of strongly scattering flame retardant molecules at the opposite end from where heat was applied. It is possible that the particles in this region are of larger vertical dimensions and not detected at any of the correlation lengths used.

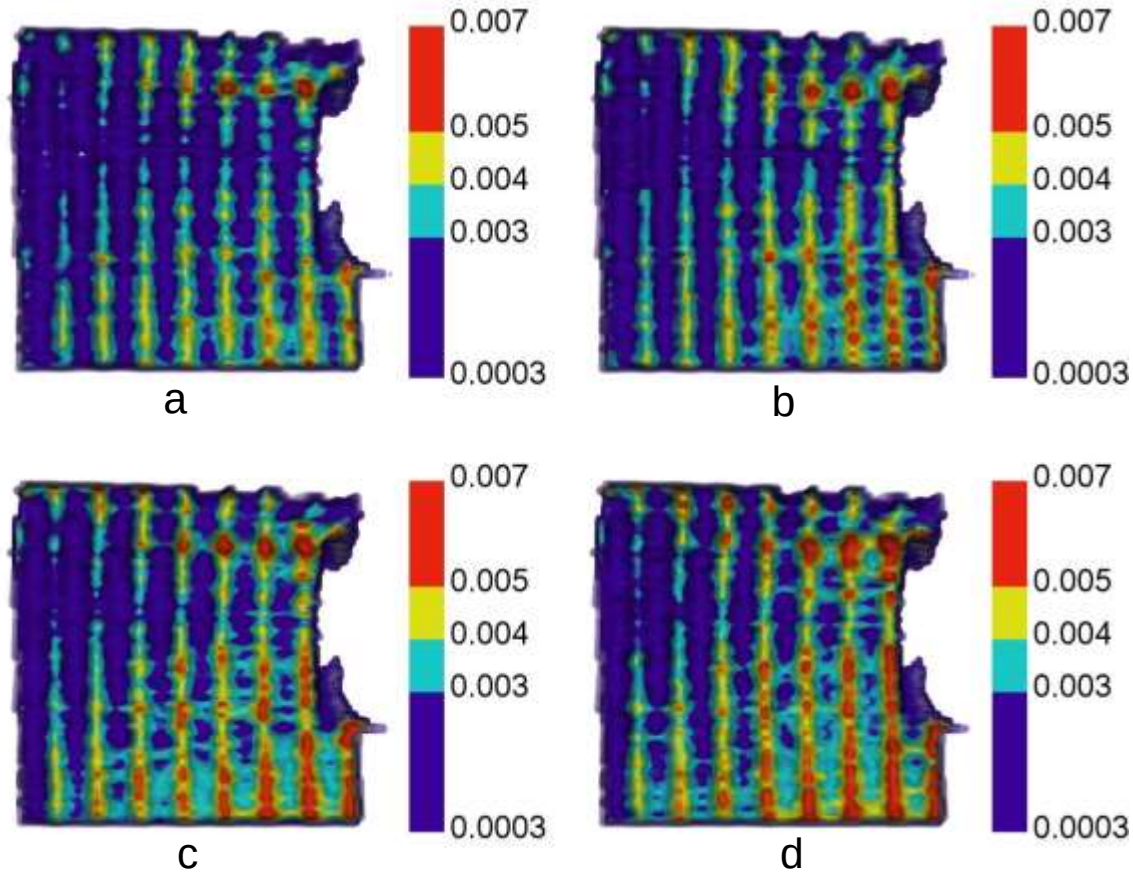

Figure 5.7. Sectional views of dark-field volumes for an ABS/ABSFR 3:1 sample heated at 275°C. (a) Image for correlation length 0.78 μm, (b) correlation length 0.88 μm, (c) correlation length 0.98 μm and (d) correlation length 1.08 μm. For (a) through (d), Sample to detector distances are 80 mm, 90 mm, 100 mm and 110 mm. Heat application was at the right side.

5.3.3 Two-dimensional Correlation Length Scanning Experiment.

The correlation length experiments were plagued by inaccurate grating step motions, leading to fringe artifacts in the processed images. The sample layer-based composition made it even more difficult to distinguish the fringe artifact from the sample

in the image. Figure 5.8 shows the fringing extent in images acquired at two consecutive SDDs, 17.1 mm and 18.1 mm, for a 3:1 ABSFR sample heated at 275°C. Since the fringe artifacts are not in a fixed position, it was difficult to isolate any region for signal analysis without a fringe correction or reduction processing step.

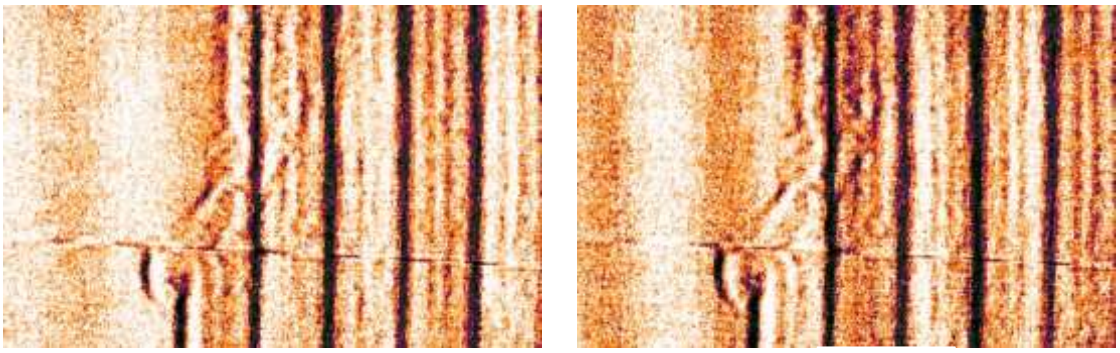

a b

Figure 5.8. Dark-field projections of a 3:1 ABS/ABSFR sample at two consecutive SDD positions. The sample was heated at 275°C. (a) SDD 17.1 mm for correlation length of 1.14 μm and (b) SDD 18.1 mm for a correlation length of 1.21 μm. The residual fringes introduce errors in the measured signal.

Regardless of the fringes, the images do reveal some changes in the signal detected across the different correlation lengths used. As an example, dark-field images for the same 3:1 ABSFR sample referred to above at SDD 7.1 mm (0.47 μm) and 28.1 mm (correlation length 1.87 μm) are shown in Figure 5.9. Here it is clear that at the correlation length of 1.87 μm, the system picks up scattering from the interface of ABS-ABS layers (Figure 5.9b).

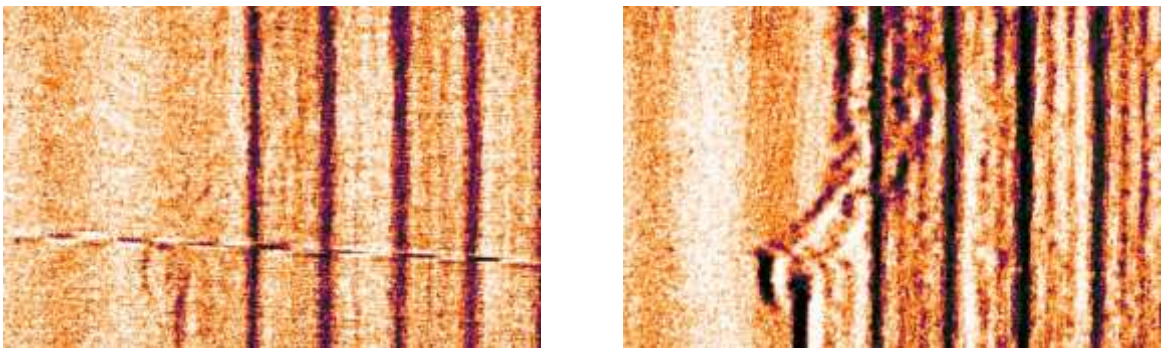

a b

Figure 5.9. Dark-field projections of a 3:1 ABS/ABSFR sample at two SDD positions. The sample was heated at 275°C. (a) SDD 7.1 mm for correlation length of 0.47 μm and (b) SDD 28.1 mm for a correlation length of 1.87 μm. An increased detection of structure in (b) compared to (a) is due to the correlation length of the instrument and independent of the residual fringes though it cannot be accurately measured in this noisy state.

5.4 Conclusions

X-ray grating interferometry was used to study fused-deposition modeled objects made of pure ABS and ABS-flame retardant composite (ABSFR) filaments with ABS to ABSFR ratios of 3:1 and 1:1, as well as 100% ABSFR. This was done to explore the feasibility of introducing flame retardants to specific portions of an otherwise flammable object and how such an object “holds up” when exposed to heat. Of most importance was the dark-field or scattering signal which has the potential to detect gaps or pores that could result from structural breakdown of layers or decomposition of constituent molecules.

Near-real time two-dimensional images of samples subjected to repeated heating at one correlation length and multiple correlation lengths were marred by fringe artifacts which inhibited the use of quantitative data from the images. The absorption images acquired at one sample-to-detector distance for repeatedly heated samples however

showed the gradual loss of ABSFR layer(s) due to melting as a result of direct contact with the heater.

X-ray grating interferometry tomography was applied to multiply-heated samples (30 cycles) at four sample-to-detector distances: 80 mm, 90 mm, 100 mm and 110 mm for correlation lengths 0.78 μm, 0.88 μm, 0.98 μm and 1.08 μm. The images acquired at a correlation length of 0.78 μm for 1:1 samples heated at 265°C and 275°C, showed that lower dark-field intensities concentrated in the region adjacent to where the heat was applied. Based on the absorption images –both 2D and tomographic– it can be concluded that this region of lower concentration did not result from direct contact between the layers and the heater since only very few layers actually came in contact with the heater, whereas the full region of sample adjacent to the point of heating show these lower scattering intensities. As the correlation length increased from 0.78 μm till 1.08 μm, higher intensities were gradually detected in this region indicating contribution to scattering from initially undetected particles i.e. particles of size-scales in the range 0.78 μm to 1.08 μm. Similar effects were observed in the dark-field images of the 3:1 samples. The 3:1 sample images also gave a clearer picture of the scattering contributions in the sample. Based on the distribution of component layers, it was easier to associate scattering intensity to a given layer type and it was clear that the ABS layers contributed less to scattering than the ABSFR layers. Since the difference in these layer types is the flame retardant, it can be concluded that the flame retardant is a major scatterer. Furthermore, the increase in intensities are most likely due to larger pores formed as a result of gaseous products formed from the thermal decomposition of the flame retardant molecules.

For the heating temperatures 265˚C and 275˚C probed, no visible difference in heat propagation effects were detected.

5.5 References

1. Hirschler, M. M., Flame retardants and heat release: review of data on individual polymers. *Fire and Materials* **2015,** *39* (3), 232-258.

2. Hu, X.; Guo, Y.; Chen, L.; Wang, X.; Li, L.; Wang, Y., A novel polymeric intumescent flame retardant: Synthesis, thermal degradation mechanism and application in ABS copolymer. *Polymer Degradation and Stability* **2012,** *97* (9), 1772-1778.

3. Camino, G.; Costa, L., Performance and mechanisms of fire retardants in polymers—A review. *Polymer Degradation and Stability* **1988,** *20* (3), 271-294.

4. Sang, B.; Li, Z.-w.; Li, X.-h.; Yu, L.-g.; Zhang, Z.-j., Graphene-based flame retardants: a review. *Journal of materials science* **2016,** *51* (18), 8271-8295.

5. Bourbigot, S.; Fontaine, G., Flame retardancy of polylactide: an overview. *Polymer Chemistry* **2010,** *1* (9), 1413-1422.

6. di Cortemiglia, M. L.; Camino, G.; Costa, L.; Roma, P.; Rossi, A., Mechanism of action and pyrolysis of brominated fire retardants in acrylonitrile-butadiene-styrene polymers. *Journal of Analytical and Applied Pyrolysis* **1987,** *11*, 511-526.

7. Malucelli, G.; Carosio, F.; Alongi, J.; Fina, A.; Frache, A.; Camino, G., Materials engineering for surface-confined flame retardancy. *Materials Science and Engineering: R: Reports* **2014,** *84*, 1-20.

8. Vahabi, H.; Sonnier, R.; Ferry, L., Effects of ageing on the fire behaviour of flame-retarded polymers: a review. *Polymer International* **2015,** *64* (3), 313-328.

9. Dupretz, R.; Fontaine, G.; Duquesne, S.; Bourbigot, S., Instrumentation of UL-94 test: understanding of mechanisms involved in fire retardancy of polymers. *Polymers for Advanced Technologies* **2015,** *26* (7), 865-873.

10. ASTM, Standard Test Method for Measuring the Comparative Burning Characteristics of Solid Plastics in a Vertical Position. ASTM International: West Conshohocken, PA 2010; Vol. D3801 − 10.

11. Claus, V.; Anett, M.; Dieter, L.; Frank, T., Characterization of the Burning Behaviour of Plastics by a New Method. *Open Journal of Polymer Chemistry* **2012,** *2*, 86-90.

12. Weil, E. D.; Patel, N. G.; Said, M.; Hirschler, M. M.; Shakir, S., Oxygen index: correlations to other fire tests. *Fire and materials* **1992,** *16* (4), 159-167.

13. Acquasanta, F.; Berti, C.; Colonna, M.; Fiorini, M.; Karanam, S., Glow wire ignition temperature (GWIT) and comparative tracking index (CTI) of glass fibre filled engineering polymers, blends and flame retarded formulations. *Polymer Degradation and Stability* **2011,** *96* (12), 2098-2103.

14. Guillaume, E.; Yardin, C.; Aumaitre, S.; Rumbau, V., Uncertainty determination of glow-wire test for ignition of materials. *Journal of Fire Sciences* **2011,** *29* (6), 509-518.

15. Olatinwo, M. B.; Ham, K.; McCarney, J.; Marathe, S.; Ge, J.; Knapp, G.; Butler, L. G., Analysis of flame retardancy in polymer blends by synchrotron X-ray K-edge tomography and interferometric phase contrast movies. *The Journal of Physical Chemistry B* **2016,** *120* (9), 2612-2624.

16. Olatinwo, M. B.; Ham, K.; McCarney, J.; Marathe, S.; Ge, J.; Knapp, G.; Butler, L. G., Recent applications of X-ray grating interferometry imaging to evaluate flame retardancy performance of brominated flame retardant. *Polymer Degradation and Stability* **2017,** *138*, 1-11.

17. Barnett, H. A.; Ham, K.; Butler, L. G., Synchrotron X-ray tomography for 3D chemical diffusion measurement of a flame retardant in polystyrene. *Nuclear Instruments and Methods in Physics Research Section A: Accelerators, Spectrometers, Detectors and Associated Equipment* **2007,** *582* (1), 202-204.

18. Barnett, H. A.; Ham, K.; Scorsone, J. T.; Butler, L. G., Synchrotron X-ray Tomography for 3D Chemical Distribution Measurement of a Flame Retardant and Synergist in a Fiberglass-Reinforced Polymer Blend. *The Journal of Physical Chemistry B* **2010,** *114* (1), 2-9.

19. Liu, Q.; Wang, Y.; He, J.; Ji, F., Modified three-step iterative algorithm for phase-shifting interferometry in the presence of vibration. *Appl. Opt.* **2015,** *54* (18), 5833-5841.

20. Estrada, J. C.; Servin, M.; Quiroga, J. A., A self-tuning phase-shifting algorithm for interferometry. *Optics Express* **2010,** *18* (3), 2632-2638.

21. Xu, J.; Jin, W.; Chai, L.; Xu, Q., Phase extraction from randomly phase-shifted interferograms by combining principal component analysis and least squares method. *Optics Express* **2011,** *19* (21), 20483-20492.

22. Zhang, Y.; Tian, X.; Liang, R., Random two-step phase shifting interferometry based on Lissajous ellipse fitting and least squares technologies. *Optics Express* **2018,** *26* (12), 15059-15071.

23. De Marco, F.; Marschner, M.; Birnbacher, L.; Noël, P.; Herzen, J.; Pfeiffer, F., Analysis and correction of bias induced by phase stepping jitter in grating-based X-ray phase-contrast imaging. *Optics express* **2018,** *26* (10), 12707-12722.

24. Ramirez-delreal, T. A.; Mora-Gonzalez, M.; Casillas-Rodriguez, F. J.; Muñoz-Maciel, J.; Paz, M. A., Steps length error detector algorithm in phase-shifting interferometry using Radon transform as a profile measurement. *Optics express* **2017,** *25* (6), 7150-7160.

25. Goldberg, K. A.; Bokor, J., Fourier-transform method of phase-shift determination. *Appl. Opt.* **2001,** *40* (17), 2886-2894.

26. Wen, H.; Miao, H.; Bennett, E. E.; Adamo, N. M.; Chen, L., Flexible Retrospective Phase Stepping in X-Ray Scatter Correction and Phase Contrast Imaging Using Structured Illumination. *PLOS ONE* **2013,** *8* (10), No. e78276.

27. Miao, H.; Chen, L.; Bennett, E. E.; Adamo, N. M.; Gomella, A. A.; DeLuca, A. M.; Patel, A.; Morgan, N. Y.; Wen, H., Motionless phase stepping in X-ray phase contrast imaging with a compact source. *Proceedings of the National Academy of Sciences* **2013,** *110* (48), No. 19268.

28. Harmon, K. J.; Miao, H.; Gomella, A. A.; Bennett, E. E.; Foster, B. A.; Bhandarkar, P.; Wen, H., Motionless electromagnetic phase stepping versus mechanical phase stepping in x-ray phase-contrast imaging with a compact source. *Physics in Medicine & Biology* **2015,** *60* (8), No. 3031.

CHAPTER 6
CORRELATION LENGTH STUDIES OF FUSED DEPOSITION MODELED SAMPLES WITH X-RAY GRATING INTERFEROMETRY AND SMALL ANGLE X-RAY SCATTERING

6.1 Introduction

The dark-field signal in grating interferometry shows up as a decrease in visibility due to small angle scattering, offering another source of image contrast to complement attenuation and phase contrasts.[1] The dark-field signal has also been shown to decay exponentially with sample thickness making tomographic dark-field imaging possible.[2-4] The structure sizes measured correspond to a propagation distance hence, the interferometer can be tuned to be sensitive to particular sizes/correlation lengths, ξ_{corr} , of scattering structures.[5-7] Thus, the system reveals scattering structure of sizes ≤ ξ_{corr} , with the probed dimension in the axis normal to the grating structure.[6]

A qualitative relationship between the dark-field signal and the size and shape of the scattering structure exist through the autocorrelation function, an expression given by[6]

$$DF(\xi_{corr}) = exp[\Sigma t\ (G\ (\xi_{corr}) - 1)]\,. \qquad [6.1]$$

Here G is the autocorrelation function of the sample, Σ is the scattering cross section and t is the sample thickness.[4,8] For many simple shapes, the autocorrelation function has been determined analytically.[9] This relationship depicted in Equation 6.1 has been tested on known systems, mostly solution of spherical samples, in both neutron and X-ray grating interferometry.[1,6,7,10] Results have also been compared with those obtained with conventional small angle scattering (SAS) technique.[1] Harti *et al*. carried out correlation length imaging of ordered and unordered phases resulting from gravity induced sedimentation of polystyrene microspheres.[8] With appropriate scaling to remove

macroscopic scattering effects, structure factor effects were isolated. As reported in chapter 5 of this document, we have carried out correlation experiments on fused deposition modeled (FDM) samples of acrylonitrile butadiene styrene (ABS) and a brominated flame retardant to see heat propagation effects on printed layers.

Conventional small-angle X-ray scattering (SAXS) involves the measurement of the q vector at scattering angle 2θ. As mentioned in section 2.1.1 of chapter 2, q has a magnitude of $4\pi/\lambda \sin\theta$. Taking into account Bragg's law, the scattering vector q is related to a dimension *d* in the system by $q=2\pi/d$.[11] Also, the SAXS signal generally lies within an angular range of about $2\theta = \lambda/d$.[12] For incident radiation of constant wavelength, for all scattering phenomena, the larger the irradiated object, the smaller the scattering angle.[13] SAXS enables the study of systems where long-range order is absent and can be applied to solution and solid samples.

The SAXS experiment involves illuminating the sample with a monochromatic X-ray beam and collecting the scattered radiation behind the sample as close as possible to the transmitted beam. Hence, the beam needs to be small or vary narrow.[13] So, by changing the detector position i.e. the scattering angle, detected size scales can be tuned. For a typical pin-hole setup, SAXS detects structural size-scale of 1 to 100 nm though a ultra-small angle scattering (USAXS) set up which utilizes a narrow beam, size-scales can be extended to 1000 nm.[14] With these size scales, the spatial variation in the electron density detected by the instrument due to the X-ray interaction with the sample are on size-scales larger than the atomic scale i.e. SAXS is not sensitive to electronic density fluctuation on an atomic scale[13,15] Contrast can therefore arise from particles, voids or matrices in otherwise homogeneous material.[15]

The measured intensities are plotted against q values (Å^{-1} unit) for the scattering angles. The plot is then interpreted by using scattering functions that relate intensity distribution to structural information like shape and size distribution.[12]

The spatial and quantitative information of scattering structures available through the dark-field signal gives it the potential to be widely utilized as a small angle scattering measurement technique. The scattering vector measured in SAXS can be related to the dark-field measurements through the scattering angle, $\Delta\alpha$ (or 2θ as mentioned above), as follows:[16]

$$\Delta\alpha = \frac{s}{l_s} \quad and \quad \Delta\alpha = \frac{q\lambda}{2\pi} \tag{6.2}$$

$$\varphi = 2\pi \times \frac{s}{p_2} \tag{6.3}$$

$$\varphi = \frac{l_s\,\lambda}{p_2} \times q \; = \; \xi_{corr} \times q \tag{6.4}$$

Where s is the lateral shift of the scattered ray, l_s is the sample to detector distance, λ is the X-ray wavelength, φ is the phase shift and angle and p_2 is the grating period for a grating interferometer set-up.

The aim of this work is to validate the spatial and quantitative information obtained by X-ray grating interferometry imaging of a non-model system like a fused deposition modeled object by comparing interferometry measurements with measurements obtained using the conventional small angle X-ray scattering (SAXS) technique. To do this, the choice of polylactic acid polymer (PLA) as feedstock material was made due to its simplicity as a one-monomer based polymer. Some ABS/flame retardant-based samples were also imaged.

PLA filaments—pristine and heated—were characterized by solid-state ^{13}C NMR to determine the presence of crystalline domains that could contribute to scattering data as well as their purity.[17] The presence of crystalline and amorphous domains should show up in the spectrum as narrow peaks (from the crystalline domain) superimposed on broad peaks (from the amorphous domain); spin-lattice relaxation time measurement should differentiate between the two domains types.[17] Scanning electron microscopy (SEM) imaging of printed samples was also carried out to give an idea of the size scales of voids or porosities present in printed PLA samples. Small-angle and ultra-small angle X-ray scattering data (SAXS and USAXS) were acquired at beamline 9-ID-B,C of the APS USAXS facility. In the following, the techniques and results obtained so far are presented. It should be noted that X-ray grating interferometry experiments are yet to be done.

6.2 Materials and Methods

6.2.1 Sample preparation

PLA samples were printed using a Makerbot PLA filament of 1.75mm diameter on a Flash Forge Creator Pro dual extrusion printer. Sample dimension was designed to be 20 mm x 1mm x 10mm (LxBxH). However, printed samples had dimensions of 20 ±0.5 mm, 1 ±0.1 mm and 10 ±1 mm (LxBxH). The printer settings included 0.27 mm layer thickness, 100% density and 65°C print bed temperature. Print speed and travel speed was set to 120 mm/s. Printing was done with varying nozzle temperatures, from 170°C to 215°C in steps of 5°C for a total of ten samples. The aim was to have samples ranging in quality; from high quality (215°C) to poor quality (170°C). The poor adhesion of layers was visible by eye in the poorest quality samples.

The ABS/flame retardant-based blocks were printed on a Flash Forge Creator Pro dual extrusion printer using Filabot ABS and ABSFR filaments. Sample composition included 3:1 and 1:1 ABS/ABSFR layers and pure ABSFR. Nozzle temperature was 230°C and 225°C for the ABS and ABSFR filaments respectively. Layer thickness was 0.27 mm, print bed temperature was 60°C (80°C for pure ABSFR), travel speed was 40 mm/s and print speed 60 mm/s. Sample dimension was designed to be 20 mm x 1mm x 10mm (LxBxH) but printed dimensions were 20 ±0.5 mm, 1 ±0.1 mm and 10 ±1 mm (LxBxH).

6.2.2 Solid-State ^{13}C NMR

The degree of crystallinity and purity of pristine PLA filaments and filaments printed at 170°C and 215°C were determined by solid-state ^{13}C NMR. The measurements were carried out on a Bruker AV-400 (9.39T, 400 MHz) NMR spectrometer using a triple resonance 4 mm MAS probe. MAS rate was 10 kHz and 12 kHz for the pristine and heated samples, respectively. The acquisition temperature was 300K (26.85°C). ^{13}C spectra was acquired using the cross-polarization technique, with a contact time of 6 ms, a delay of 6 s between consecutive scans and acquisition time of 48 ms. Alpha-glycine was used for the chemical shift reference.

The spin-lattice relaxation times $T_1(^1H)$ were determined by saturation recovery with ^{13}C CP MAS. The parameters are as described above.

6.2.3 SEM imaging

SEM imaging was carried out using a FEI Quanta™ 3D FIB-SEM instrument (FEI, Hillsboro, OR) at LSU. The samples were coated with platinum and imaged at an accelerating voltage of 5 kV and a current of 1.5 pA.

6.2.4 Small-Angle X-ray Scattering at APS

Scattering measurements were acquired at beamline 9-ID-B,C of the APS USAXS facility. The USAXS instrument was equipped with SAXS (and WAXS) integration capability where optics changeover between USAXS and SAXS systems occur in less than 30 seconds.[18] The X-ray energy was 21 keV. While the USAXS system had a slit source, and offers a q range of about 0.0001 to 0.3 $Å^{-1}$, the SAXS system had a pinhole source and with typical q range about 0.05 to 1.7 $Å^{-1}$.[18] The USAXS experiment was carried out with a beam size of 800 µm by 50 µm and acquisition time of 20 seconds per sample. Acquisition time for the SAXS experiment was 90 seconds per sample. Data reduction of acquired data was done using the Igor Pro 8 software: the USAXS package was used for the USAXS data and the Irena package was used for the SAXS data.[19-23] The USAXS data was desmeared to remove slit smearing effects so that the USAXS and SAXS data could be merged and plotted on one graph.

Scattering measurements were acquired for four PLA samples (nozzle temperatures 175°C, 185°C, 195°C and 215°C), one pure ABSFR sample, and one each of ABS/ABSFR sample ratio 1:1 and 3:1. Samples were mounted such that the print layers where orthogonal to the incident beam and vertical plane. Scattering measurements where acquired for a minimum of five positions on each sample. Scattering from pristine ABS, ABSFR and PLA filaments were also measured.

6.3 Results

6.3.1 Solid-State ^{13}C NMR

With ^{13}C NMR the presence of both crystalline and amorphous domains in the PLA sample is indicated by narrow peaks superimposed on broad peaks. Spin-lattice

relaxation studies of the superimposed peaks should reveal more than one T_1 relaxation time. In the NMR spectrum for the pristine PLA sample, the characteristic CO, CH_2 and CH_3 peaks (169.89 ppm, 69.5 ppm and 16.8 ppm, respectively) seem to be singular peaks, Figure 6.1. This is confirmed by the $T_1(^1H)$ measurements which give only one T_1 value for each peak: 806.8 ms for the CO peak, 801.8 ms for the CH_2 peak and 806.8 ms for the CH_3 peak, Figures 6.2, 6.3 and 6.4. With the T_1 measurements it can be concluded that there is no detectable crystallinity in the pristine PLA sample.

To determine if the heating of the filaments during printing modifies the molecular arrangement of PLA polymers, solid-state ^{13}C NMR measurements were carried out on filaments heated to 170°C and 215°C. The ^{13}C peaks and associated $T_1(^1H)$ values show that the heating associated with the printing process introduces no detectable crystallinity into the PLA samples. The ^{13}C NMR spectra for the 170°C and 215°C samples indicate singular peaks for CO, CH_2 and CH_3 (Figures 6.5 and 6.6 respectively). The $T_1(^1H)$ values associated with the peaks remain single-valued for each sample. For the 170°C sample, T_1 is 774.2 ms for the CO peak, 830.3 ms for the CH_2 peak and 800.6 ms for the CH_3 peak (Figures 6.7, 6.8 and 6.9). For the 215°C sample, T_1 is 731.7 ms for the CO peak, 723.5 ms for the CH_2 peak and 751.2 ms for the CH_3 peak (Figures 6.10, 6.11 and 6.12).

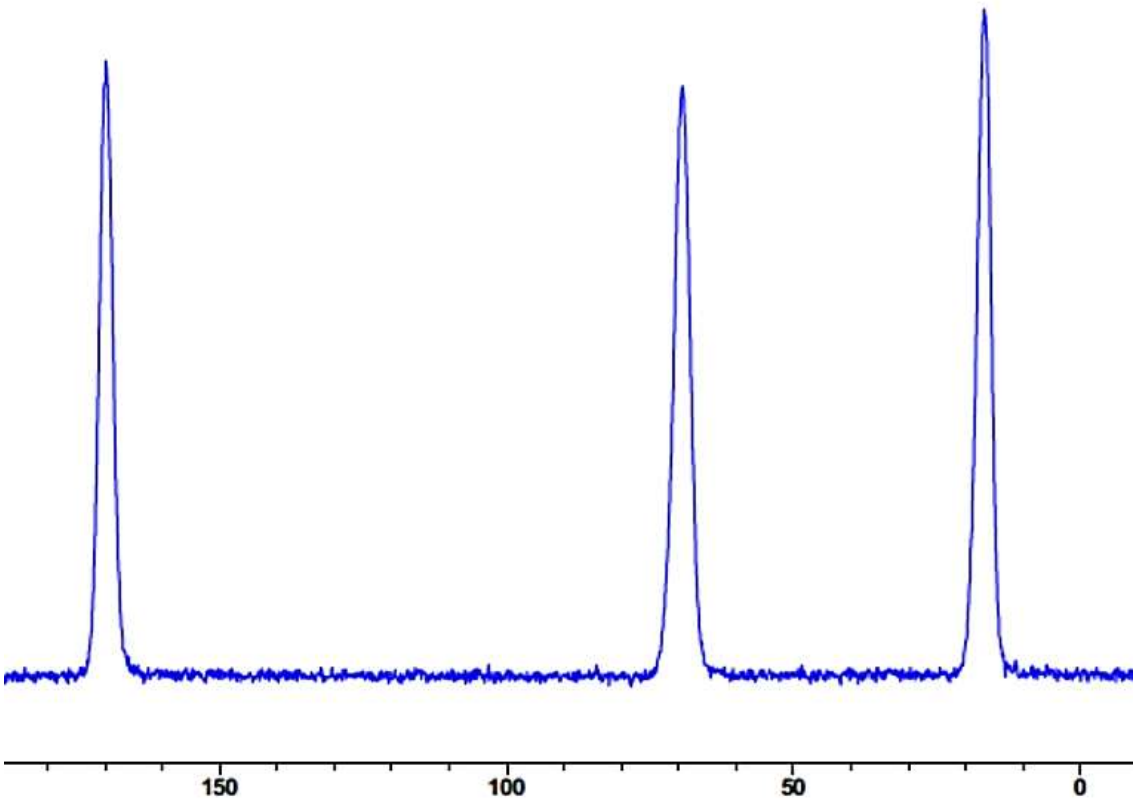

Figure 6.1. ^{13}C NMR spectrum for pristine PLA. Peaks for CH_3, CH_2 and CO are at 16.8 ppm, 69.5 ppm and 169.89 ppm, respectively.

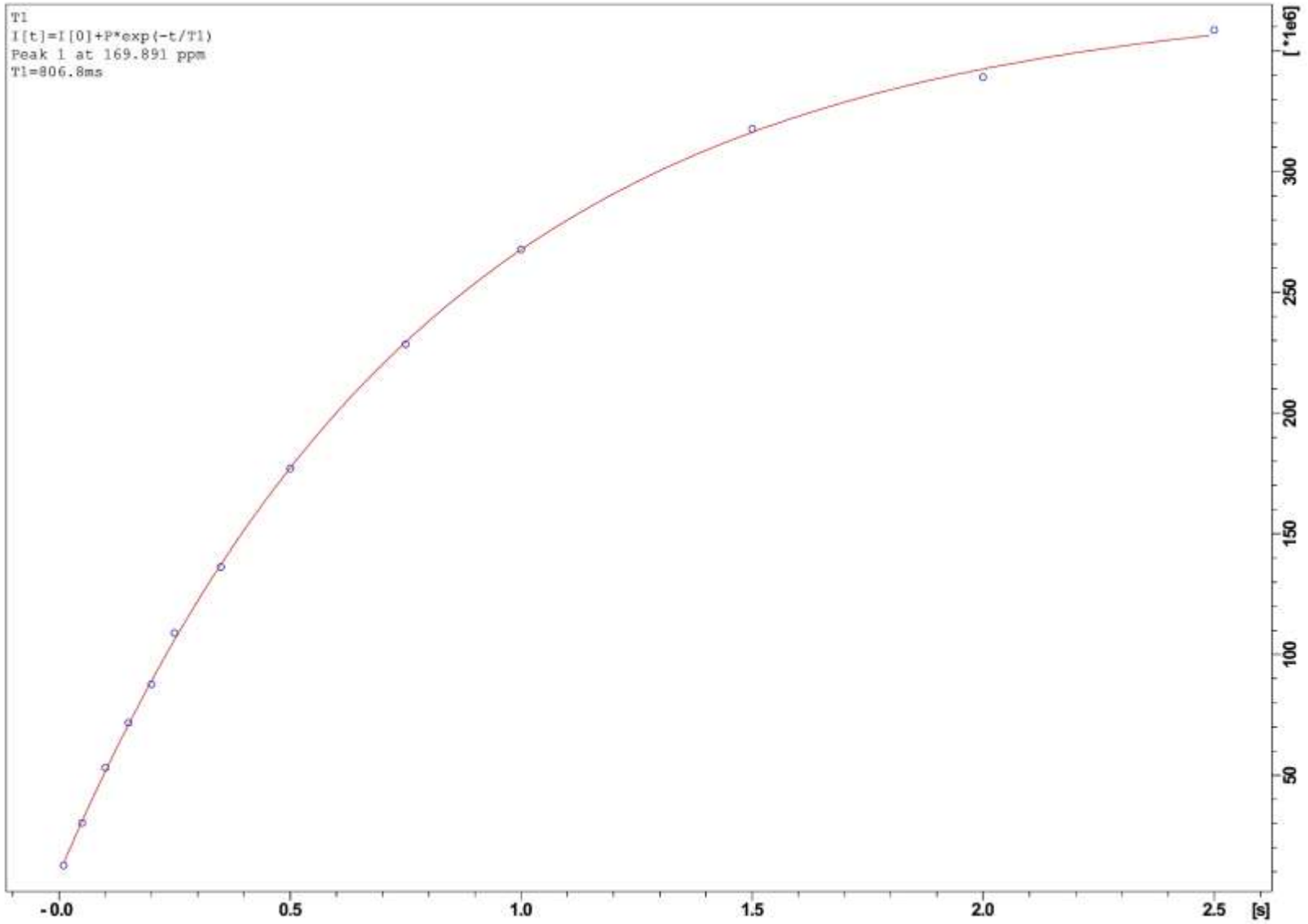

Figure 6.2. $T_1(^1H)$ measurement for peak 169.89 ppm (CO) of the pristine PLA sample.

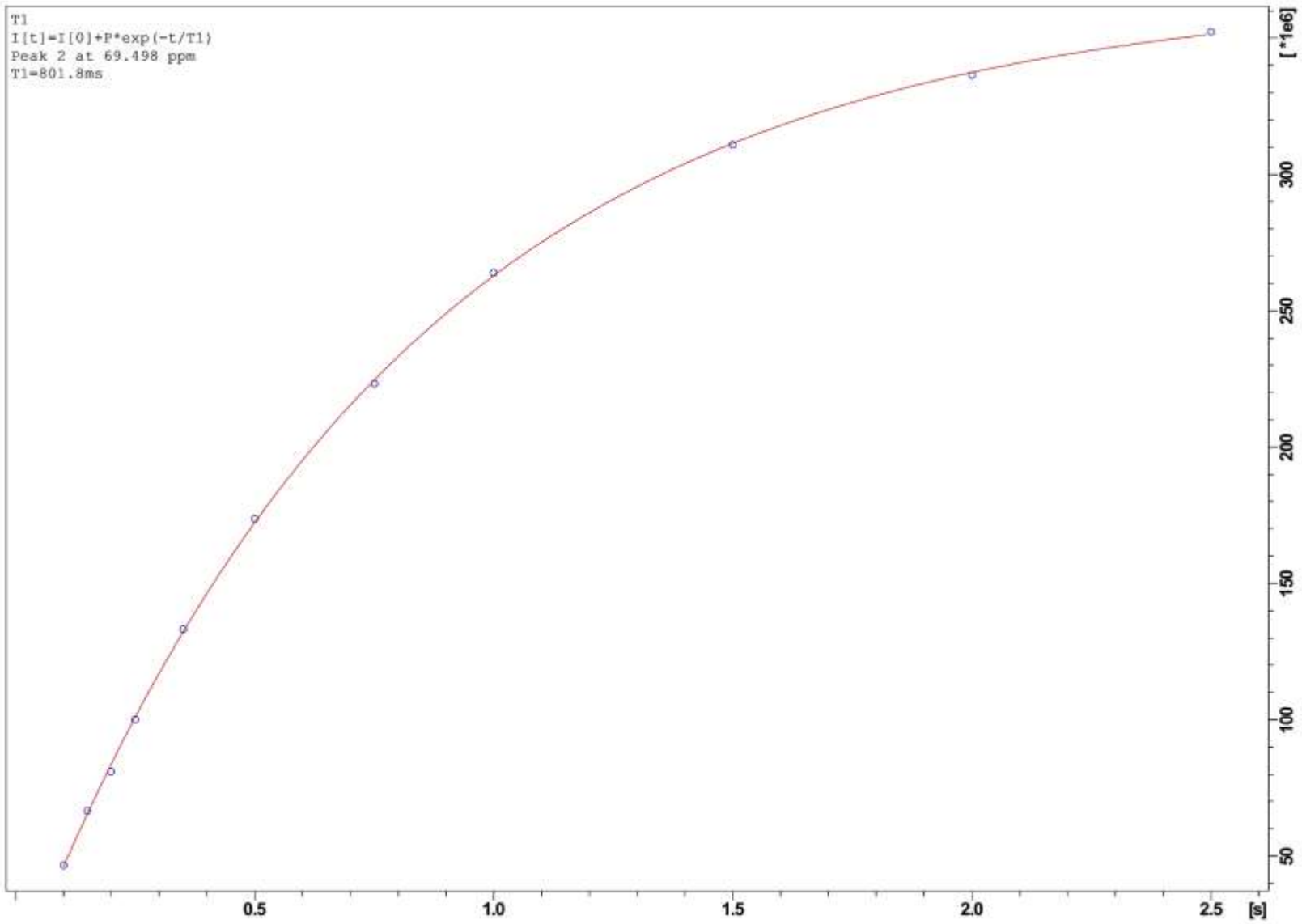

Figure 6.3. $T_1(^1H)$ measurement for peak 69.5 ppm (CH_2) of the pristine PLA sample.

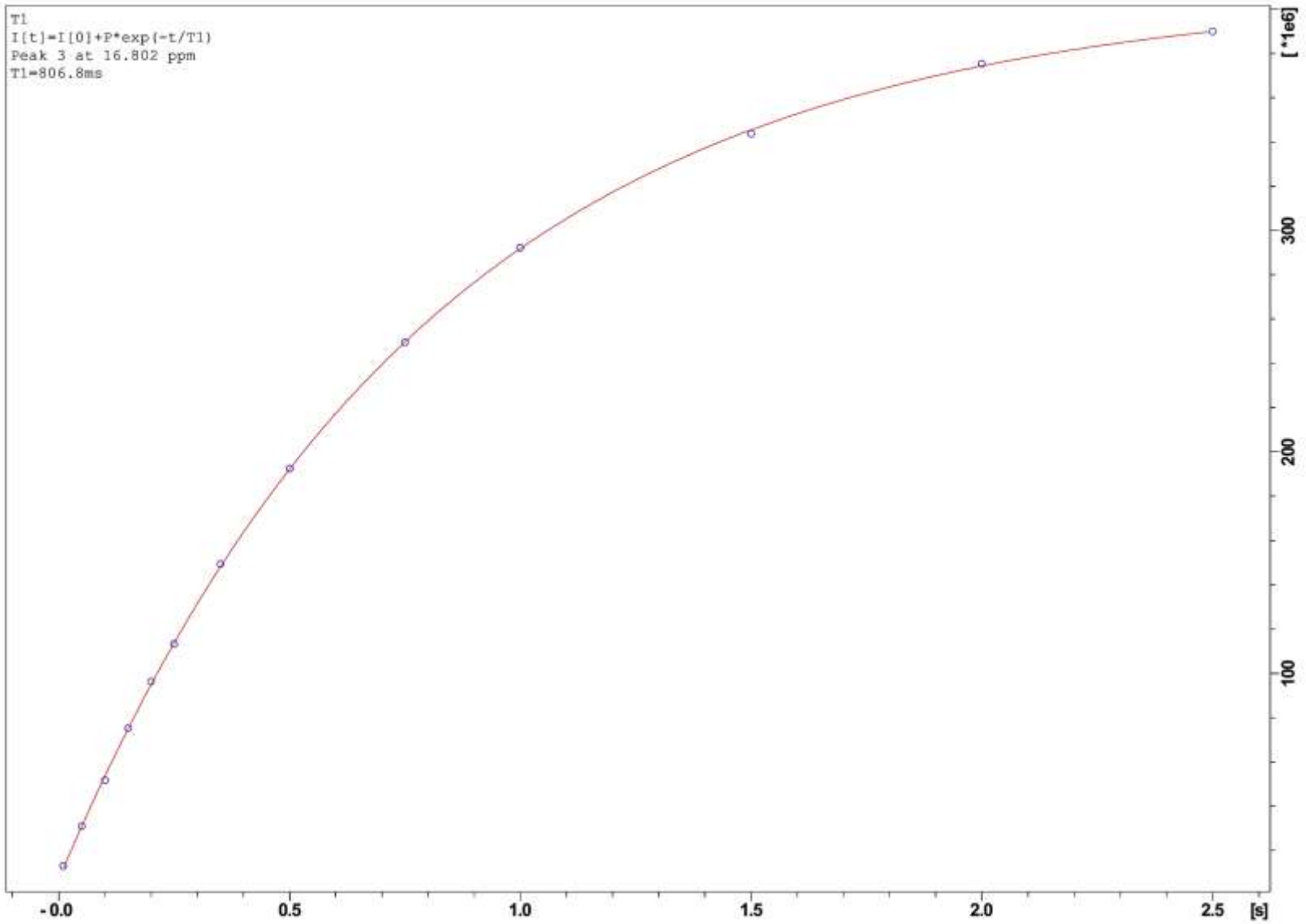

Figure 6.4. $T_1(^1H)$ measurement for peak 16.8 ppm (CH_3) of the pristine PLA sample.

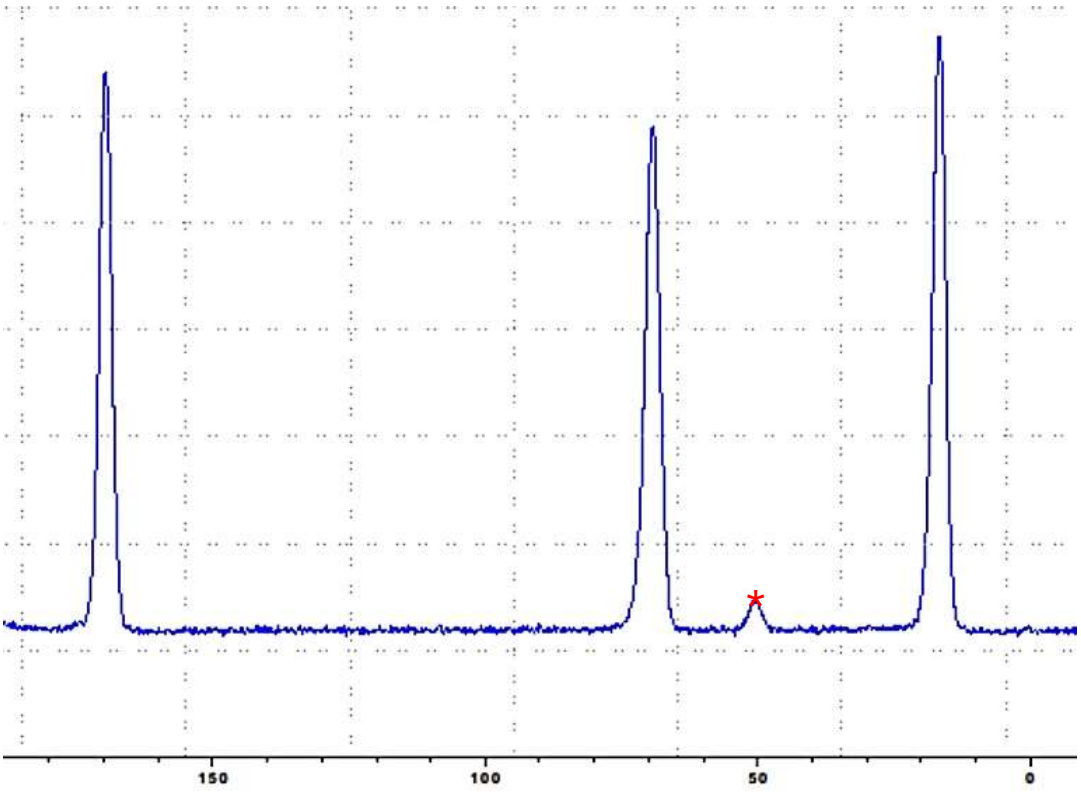

Figure 6.5. ^{13}C NMR spectrum for PLA heated to 170°C. Peaks for CH_3, CH_2 and CO are at 16.8 ppm, 69.5 ppm and 169.89 ppm, respectively. The peak at 50 ppm is a spinning sideband of the CO peak.

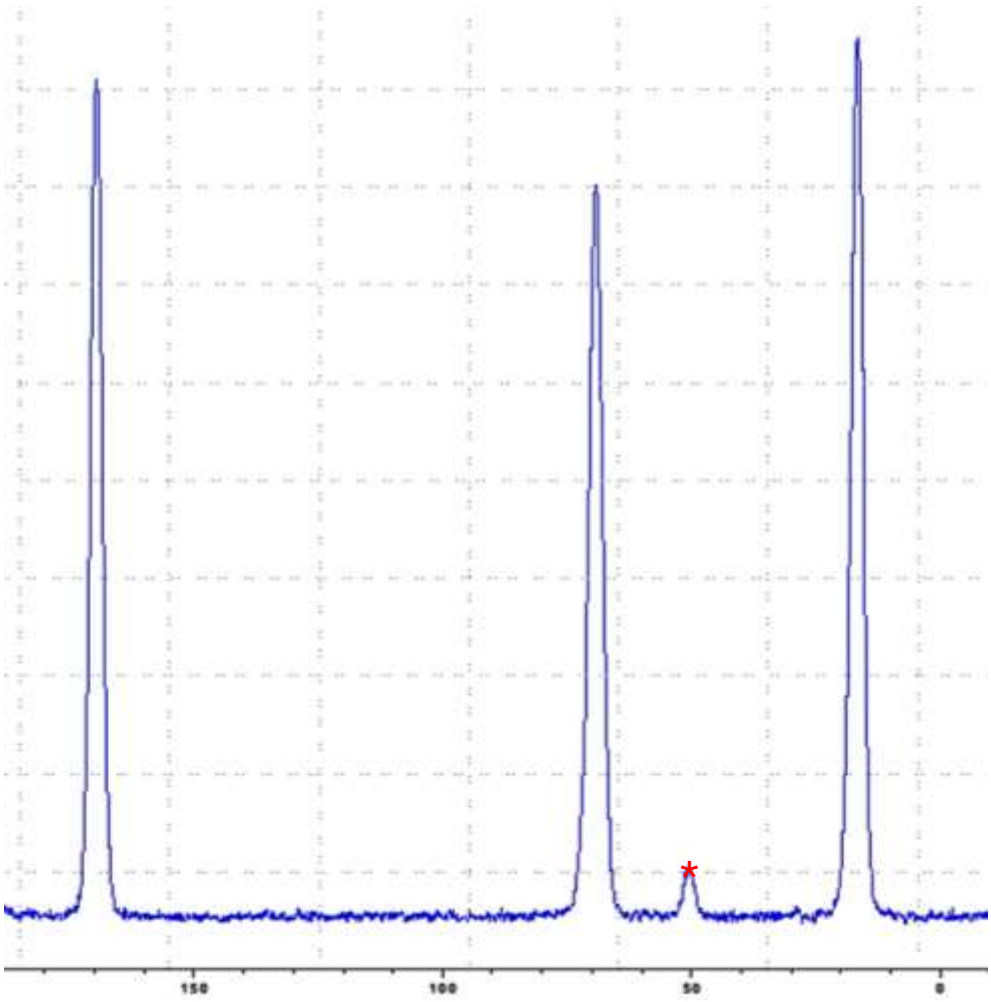

Figure 6.6. ^{13}C NMR spectrum for PLA heated to 215°C. Peaks for CH_3, CH_2 and CO are at 16.8 ppm, 69.5 ppm and 169.89 ppm, respectively. The peak at 50 ppm is a spinning sideband of the CO peak.

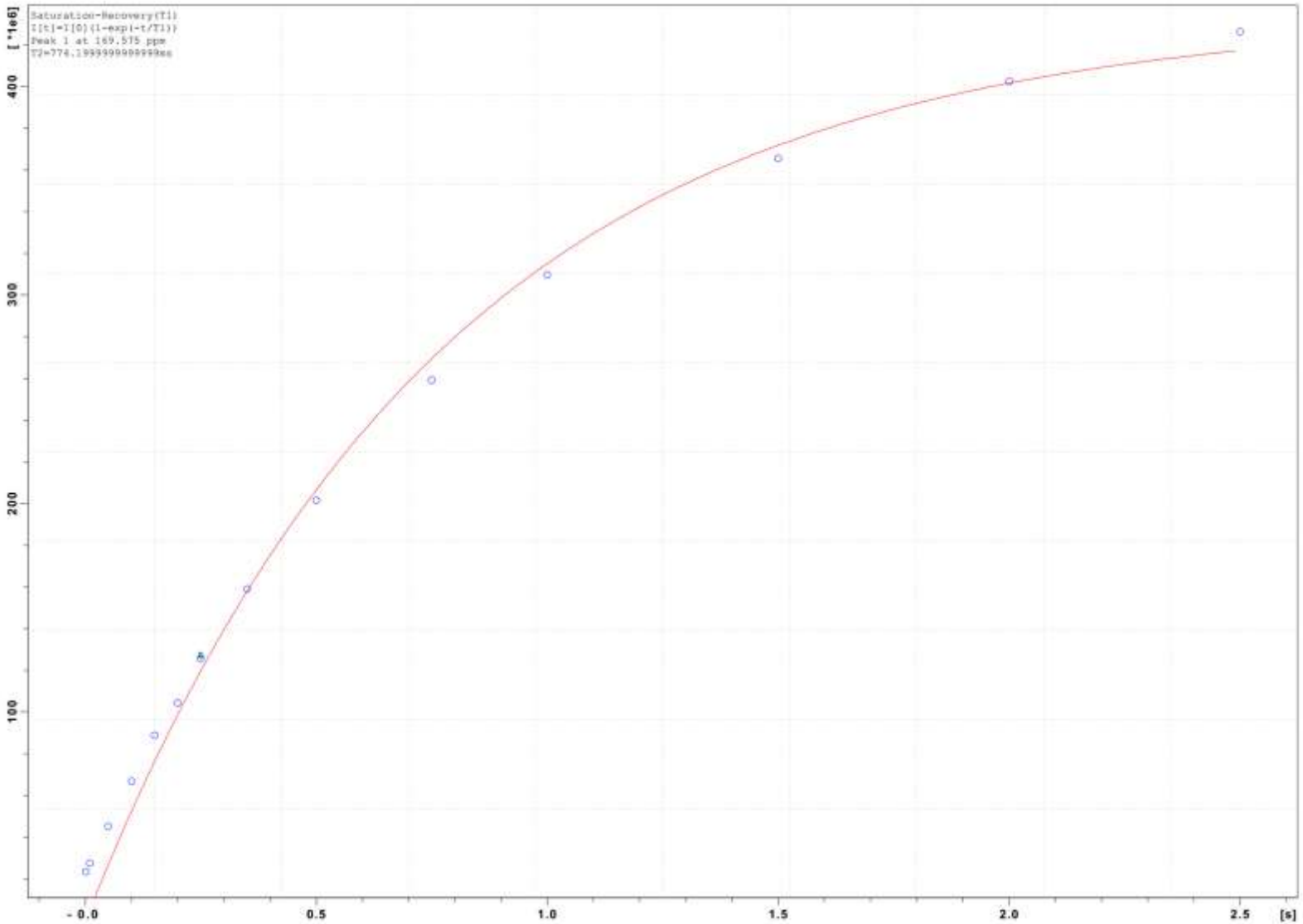

Figure 6.7. $T_1(^1H)$ measurement for peak 169.6 ppm (CO) of the 170°C PLA sample.

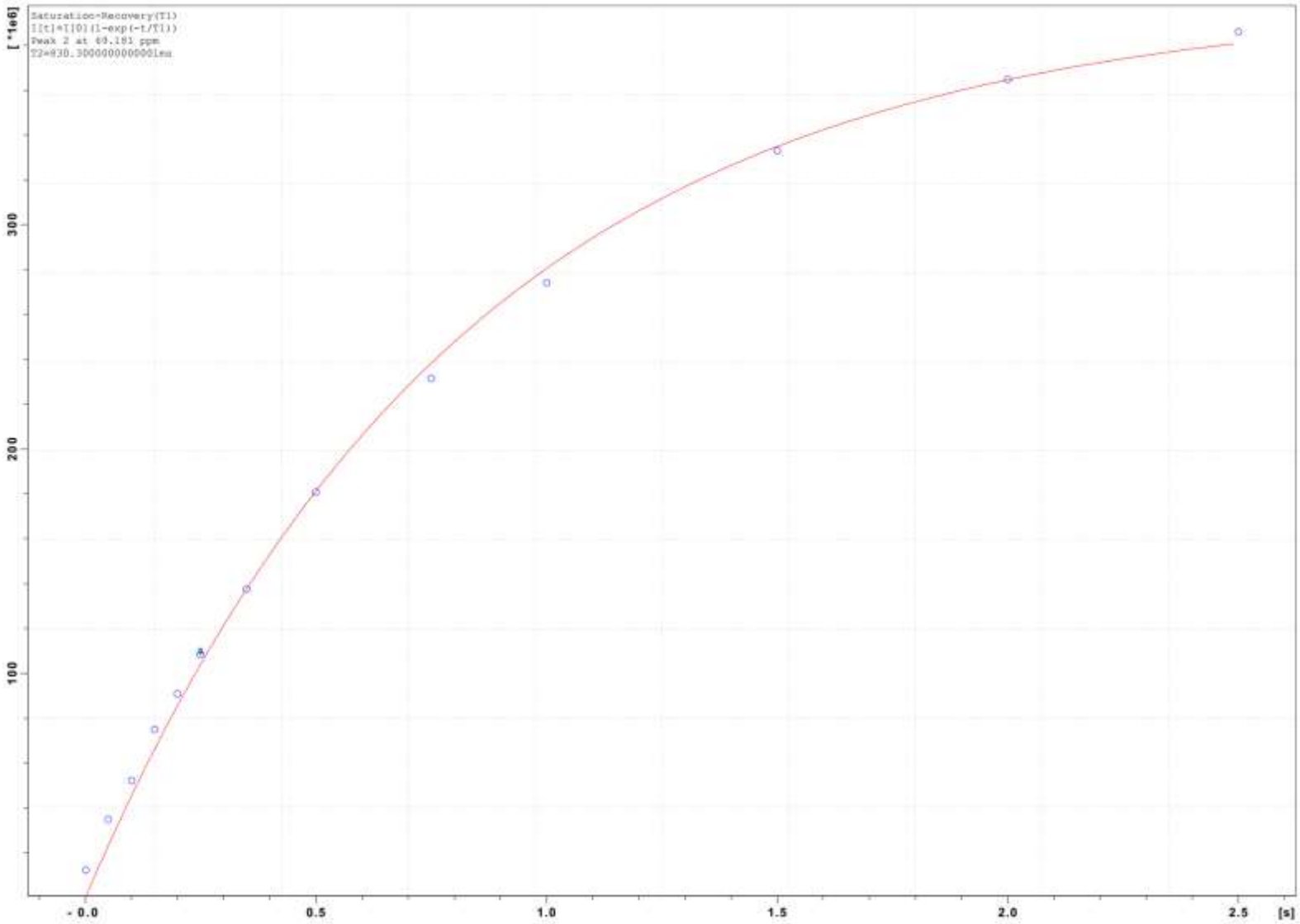

Figure 6.8. $T_1(^1H)$ measurement for peak 69.2 ppm (CH_2) of the 170°C PLA sample.

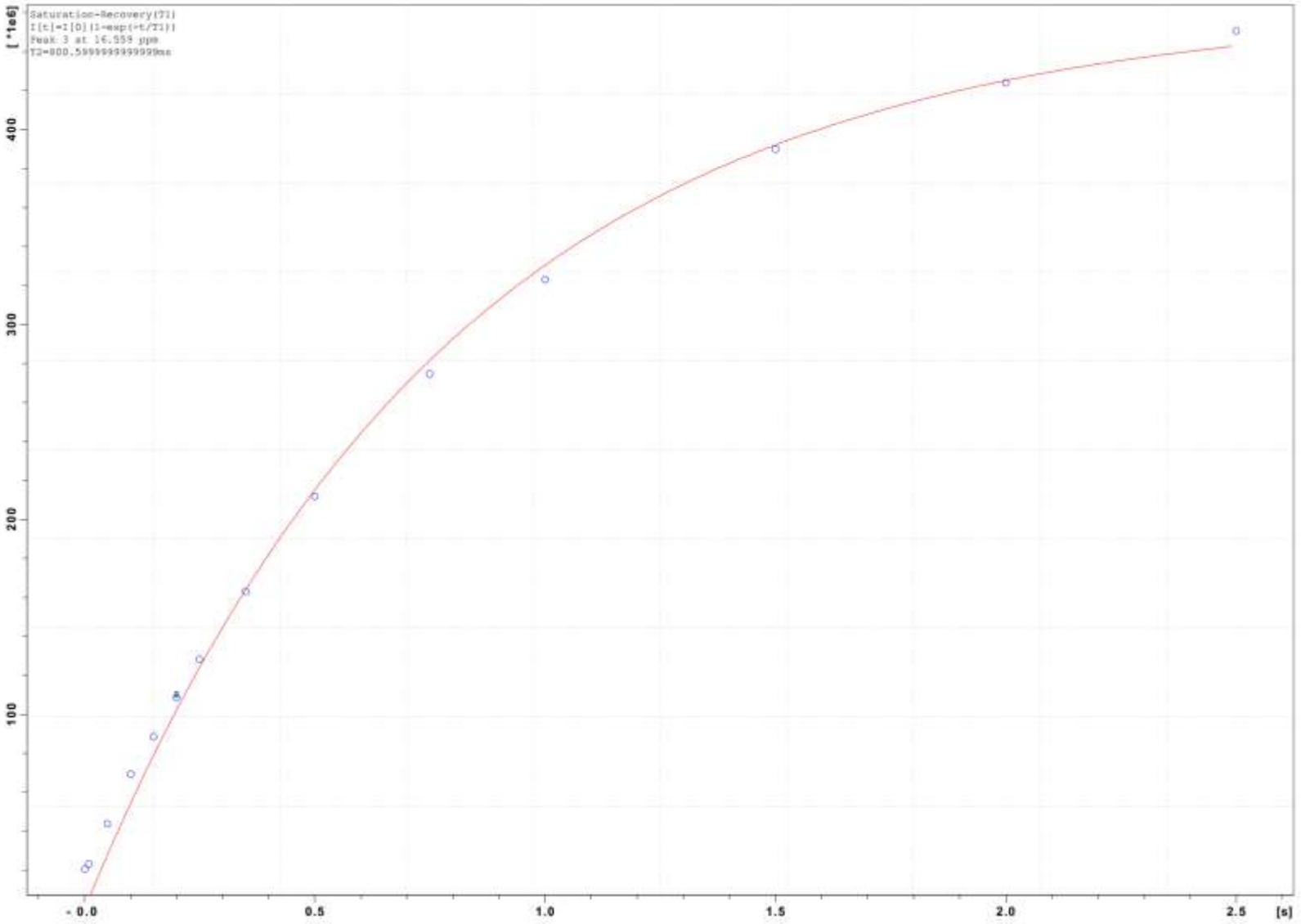

Figure 6.9. $T_1(^1H)$ measurement for peak 16.6 ppm (CH_3) of the 170°C PLA sample.

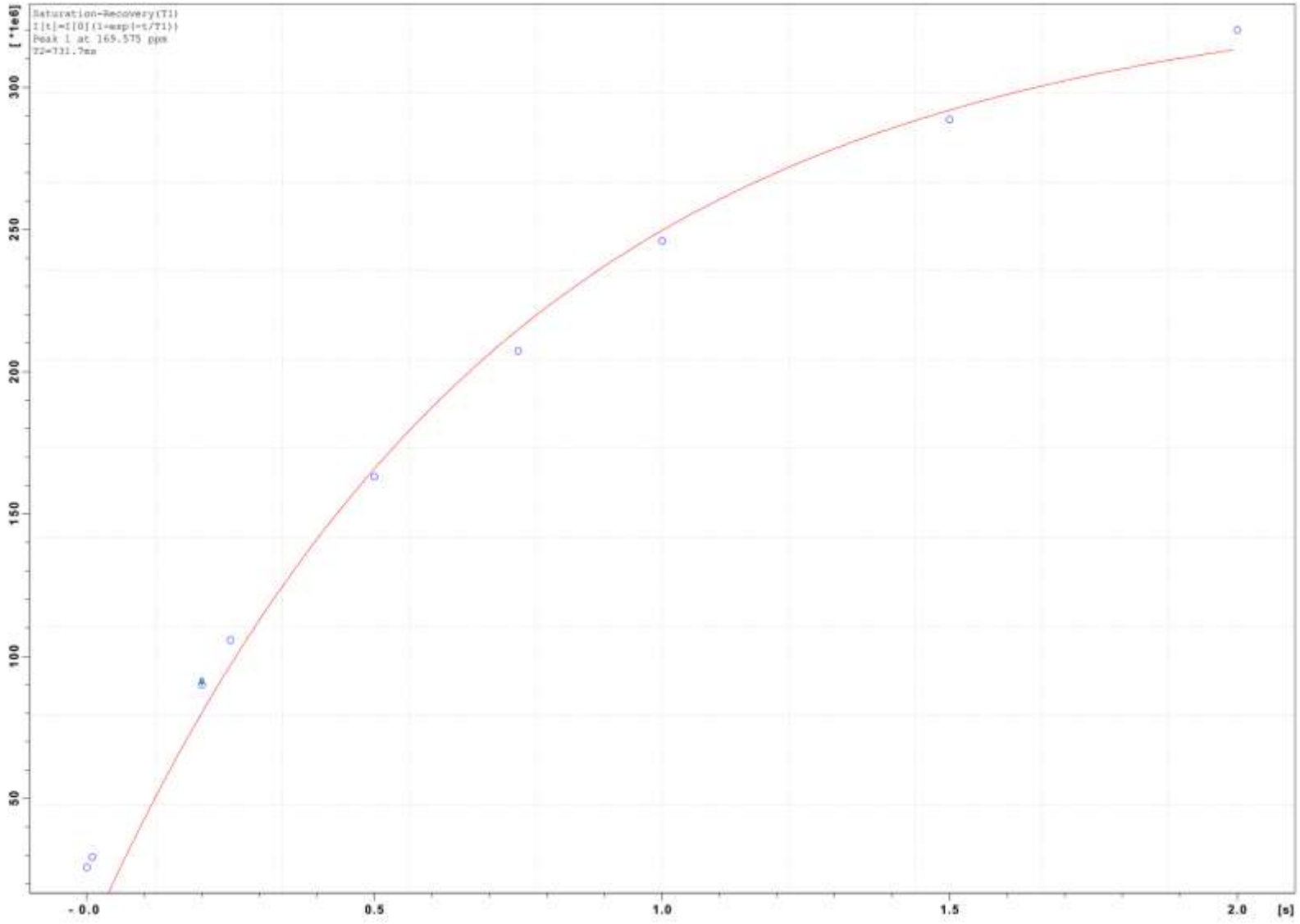

Figure 6.10. $T_1(^1H)$ measurement for peak 169.6 ppm (CO) of the 215°C PLA sample.

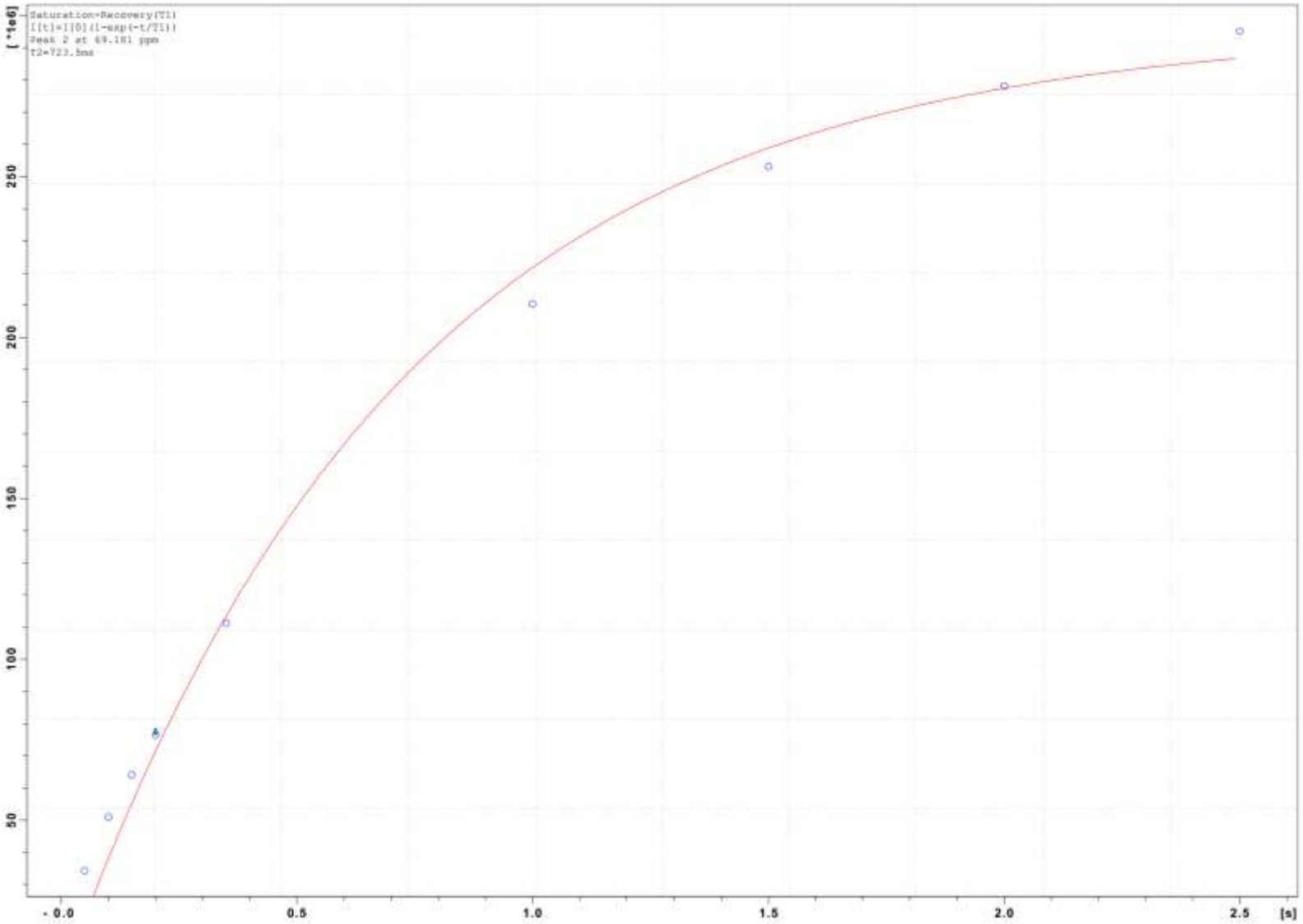

Figure 6.11. $T_1(^1H)$ measurement for peak 69.2 ppm (CH_2) of the 215°C PLA sample.

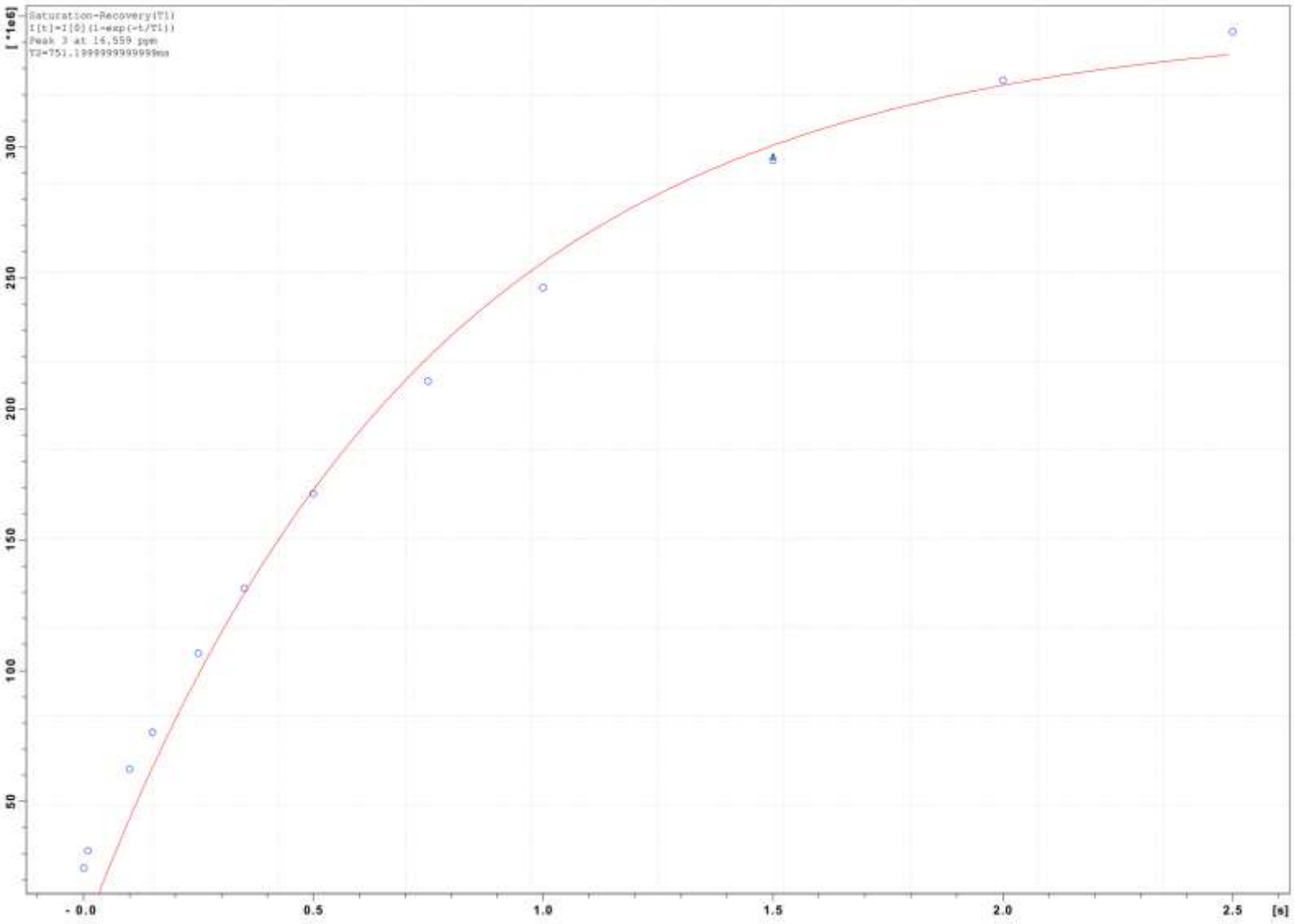

Figure 6.12. $T_1(^1H)$ measurement for peak 16.6 ppm (CH_3) of the 215°C PLA sample.

6.3.2 SEM Imaging

The variation in nozzle temperature from 170°C to 215°C resulted in PLA samples ranging from poor quality (170°C) to high quality (215°C). SEM imaging was done to have an idea of some of the size scales of scatterers/voids present in samples based on the voids that open up to the surface. The samples were PLA blocks printed at 175°C, 185°C, 195°C, 205°C and 215°C. On inspection of the images, Figure 6.13 and Figure 6.14, as

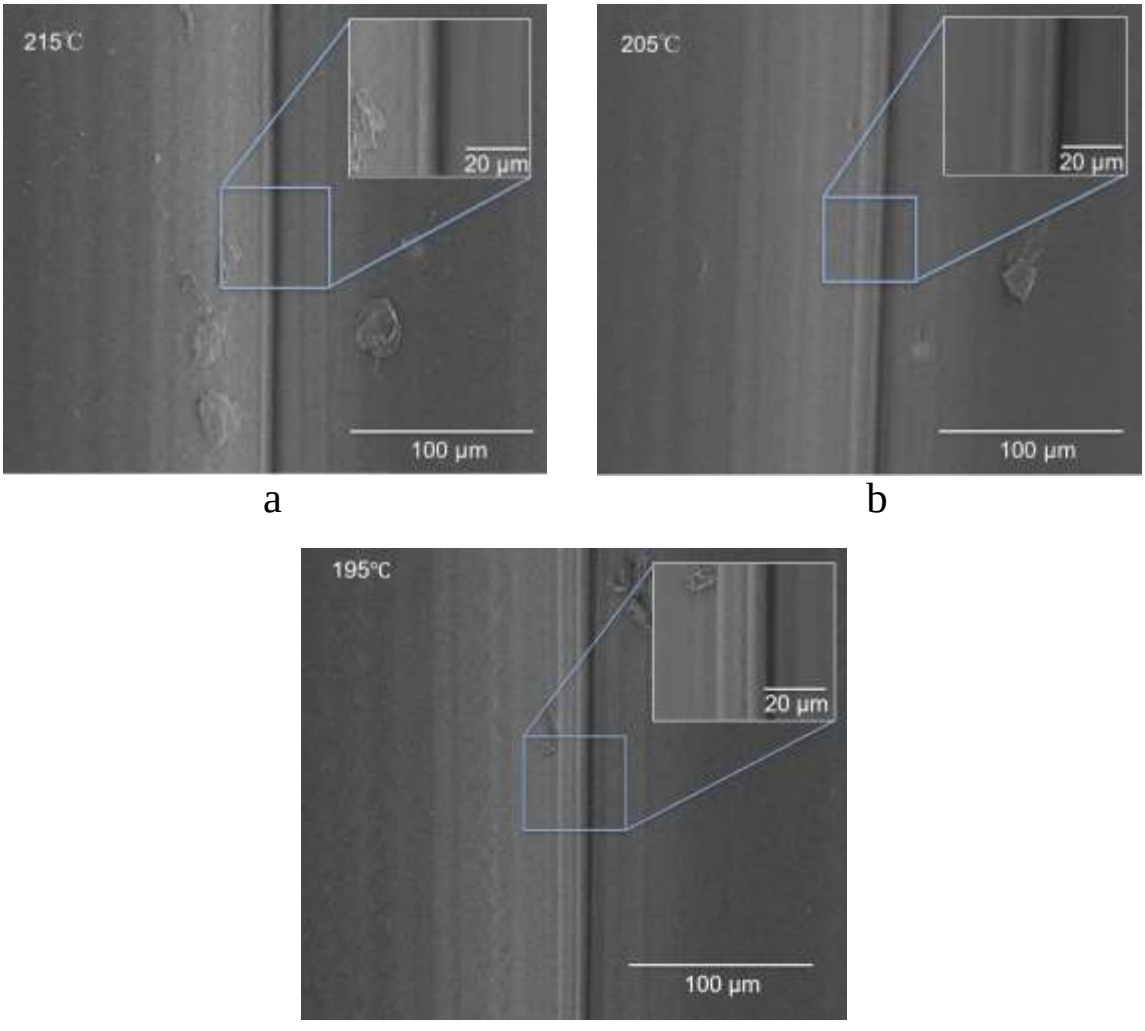

Figure 6.13. SEM images of PLA blocks printed with nozzle temperatures (a) 215°C, (b) 205°C, and (c) 195°C. The 215°C sample is ranked highest quality. As one goes to lower print temperatures imperfection and features begin to show up at the layer-layer interface as well as along the layers. Print direction is leftward.

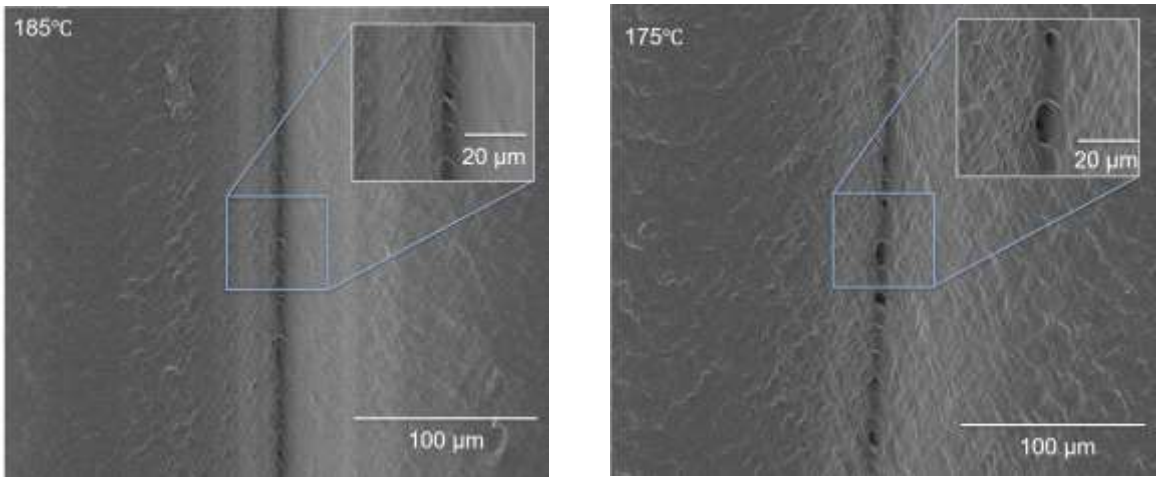

a b

Figure 6.14. SEM images of PLA blocks printed with nozzle temperatures (a) 185°C and (b) 175°C. By 185°C, voids become evident at the interface. Print direction is leftward.

the nozzle temperature is decreased features or imperfections begin to show up at the layer-layer interface becoming more obvious in the 195°C sample. Voids become visible at the interface in the 175°C and 185°C samples. Regions adjacent to the interface also show increased features or imperfections as one goes to lower temperatures.

6.3.3 Small-Angle X-ray Scattering at APS

SAXS and USAXS measurements were acquired for portions of the PLA and ABS/ABSFR blocks. The region of measurement was such that layer-interface-layer regions were sampled. The USAXS/SAXS graph for regions within filaments/layers of the PLA samples is shown in Figure 6.15. For the interface region, the graph is presented in Figure 6.16. By comparing both graphs one can see that from about $q \geq 0.001$ $Å^{-1}$ the scattering curves are similar with one correlation peak at about 1 $Å^{-1}$ in that q range. This portion of the curves is most likely related to the packing of the PLA polymer chains. This means that on size scales of about 0.628 µm or less ($d=2\pi/q$), the interface and layer regions comprise similar scattering features. The additional peak that shows up in the

interface plot (from $q \leq 2 \times 10^{-4}$ Å^{-1}) may then be attributed to features exclusive to the interface e.g. voids. The exact source of these peaks is yet to be determined. A plot of the difference between the interface region curves and layer region curves is shown in Figure 6.17.

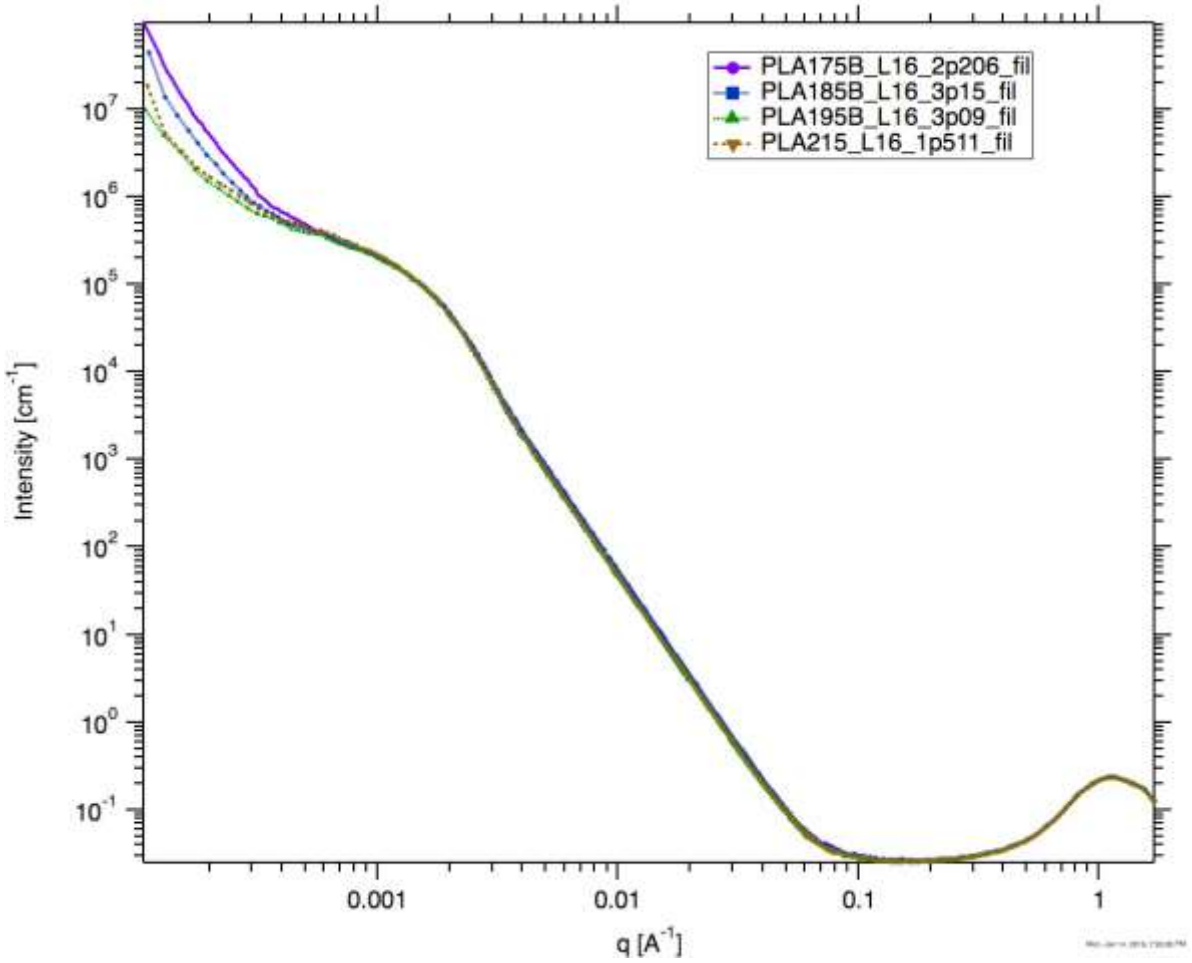

Figure 6.15. SAXS measurements within a layer each of the 175°C, 185°C, 195°C and 215°C samples. The scattering curves show uniformity for values of about $q \geq 0.001$ Å^{-1}.

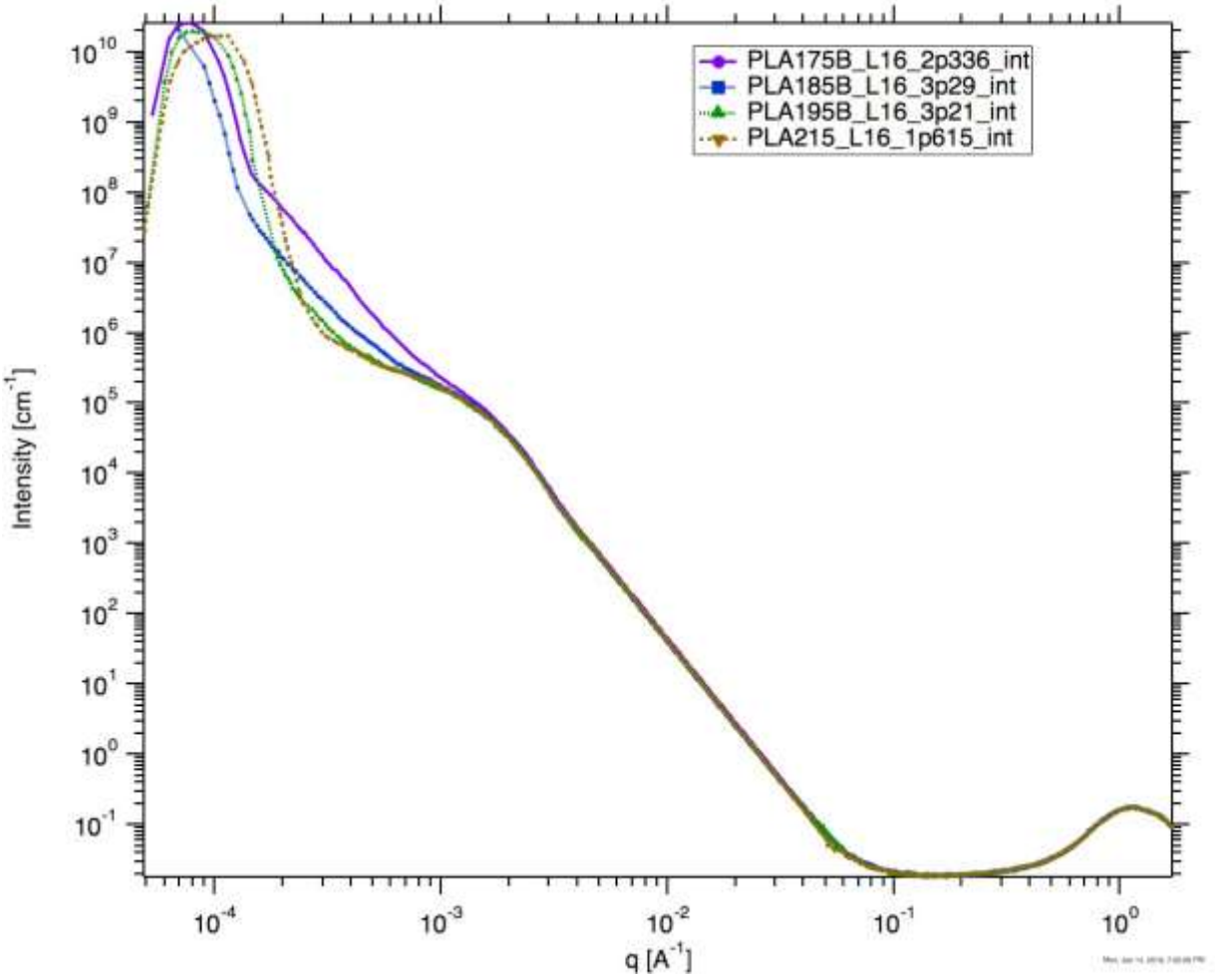

Figure 6.16. SAXS measurements at layer-layer interfaces for 175°C, 185°C, 195°C and 215°C samples. The curves show uniformity for values of about q ≥ 0.001 Å^{-1}. The leftmost peak is indicative of features exclusive to the interface region.

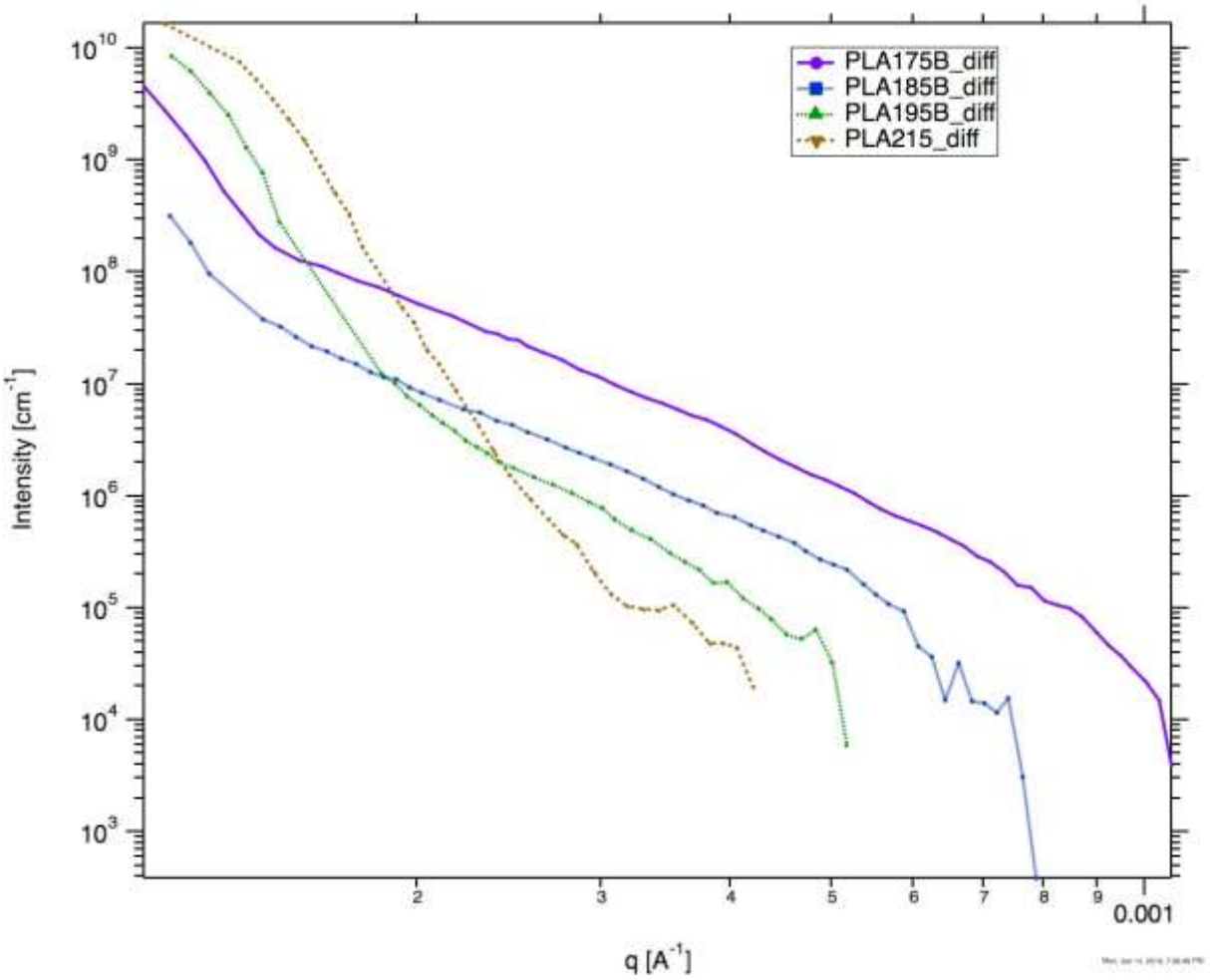

Figure 6.17. Plot of the difference between the scattering measurements for the interface region and layer region for the PLA 175°C, 185°C, 195°C and 215°C samples.

For the ABS/ABSFR block samples, the SAXS measurements across the filaments/layers of 1:1 and 3:1 samples differentiate between the ABS and ABSFR layers, Figures 6.18. The ABS filaments' curves share a similar pattern while the ABSFR filaments share a different pattern. This is likely due to the structure factor associated with the ABS polymer being evened out by the presence of flame retardant molecules.

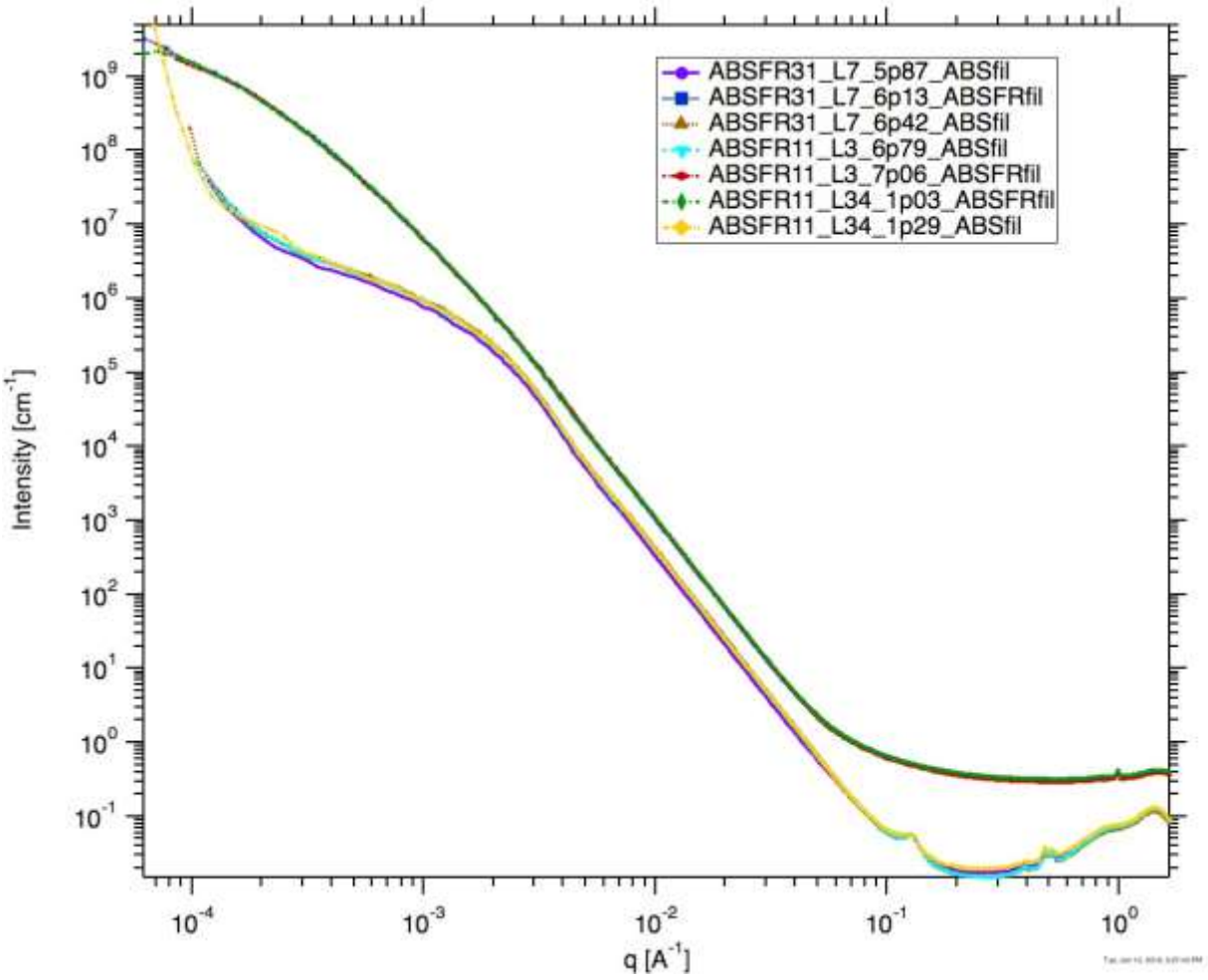

Figure 6.18. SAXS measurements for ABS/ABSFR blocks. The graph is divided into two distinct trace patterns where the features in the trace for ABS layers are absent in the ABSFR trace. The label ABSFR31 refer to the 3:1 blocks and ABSFR11 refers to the 1:1 blocks.

Scattering curves for the interface regions in the ABS/ABSFR block samples are shown in Figure 6.19 for the 1:1 samples and Figure 6.20 for a 3:1 sample. As a point of note, the measurements were acquired with the sample oriented in the direction it was printed i.e. bottom-up. The curve label ABS/ABSFR refers to an interface where the ABS layer is above and the ABSFR layer is below while the curve label ABSFR/ABS refers to an interface where the ABSFR layer is above and the ABS layer is below. It is interesting

to note that for the 1:1 samples, the curves seem to differentiate, in pattern and intensity, in a way that that coincides with the difference in print order. This is also evident in the 3:1 sample.

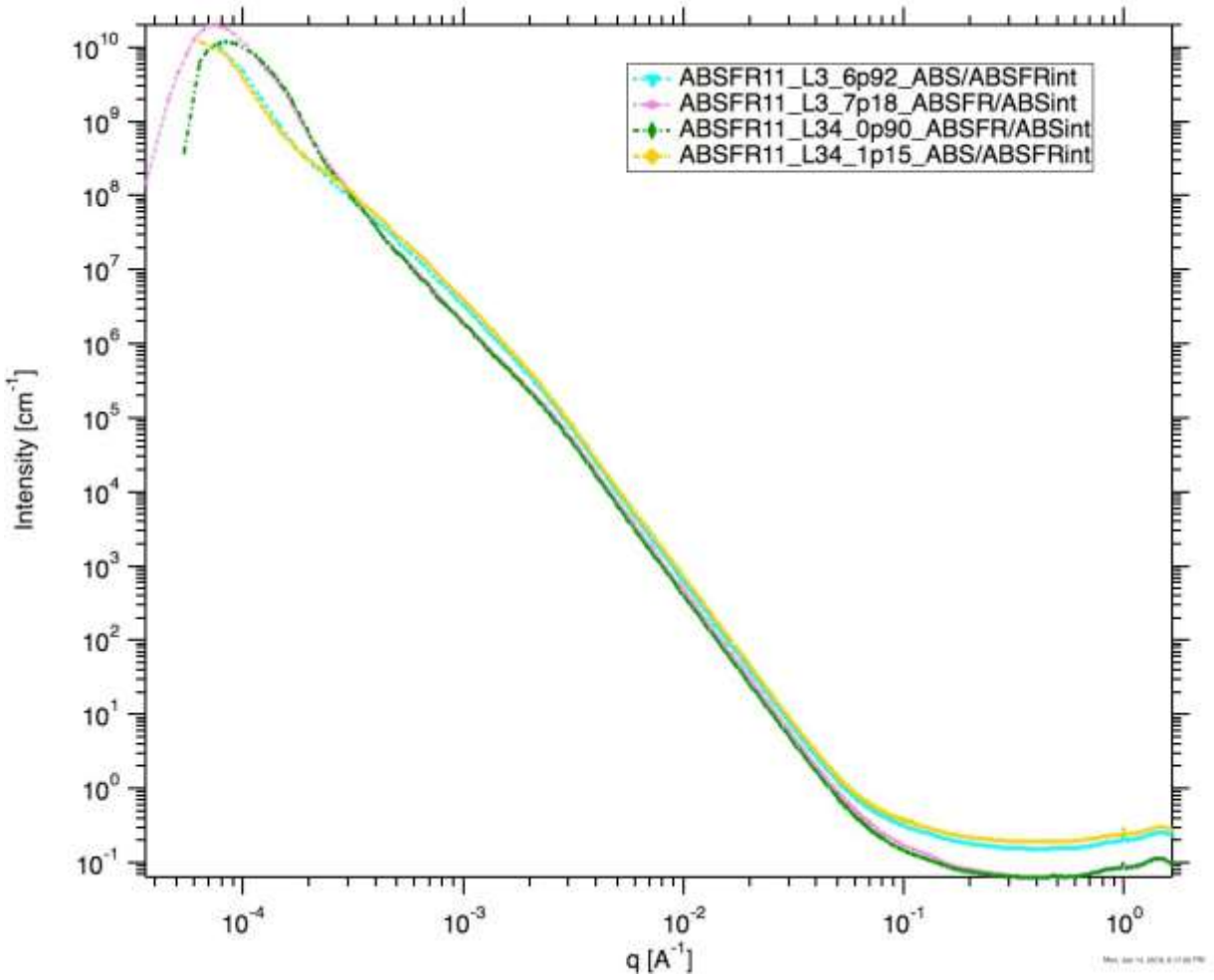

Figure 6.19. SAXS curves for interface regions in ABS/ABSFR blocks of 1:1 composition. The trace patterns seem to differentiate based on print layer order.

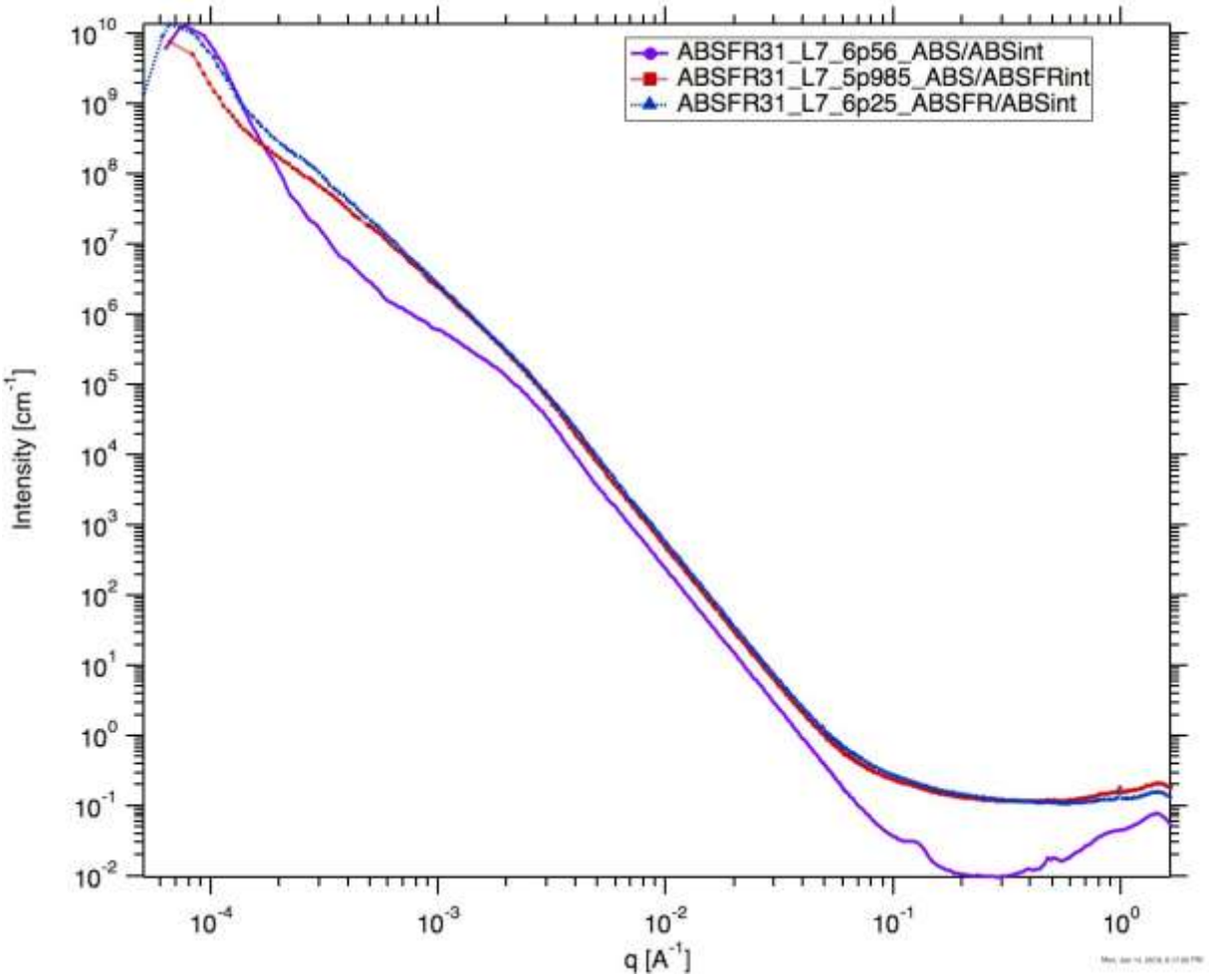

Figure 6.20. SAXS curves for interface regions in an ABS/ABSFR block of 3:1 composition. Slight differentiation in the scattering pattern based on print layer order ABS/ABSFR vs ABSFR/ABS. The purple trace is clearly different being for ABS/ABS print order.

6.4 Conclusions

X-ray grating interferometry has the potential to be as widely used as the conventional small-angle scattering technique. Though some quantitative information can be obtained from dark-field images the extraction of quantitative data on structure and distribution is still in the developmental stages. Few examples exist on retrieving

quantitative data using dark-field interferometry and have mostly been on known ordered systems. This work contributes to the area of studying unknown systems.

For the characterization of the PLA filaments solid-state NMR measurements were taken. $T_1(^1H)$ measurements, determined by saturation recovery with ^{13}C CP MAS, did not detect crystallization in pristine or heated filaments. SEM imaging of PLA samples was also carried out and showed how printed samples could vary due to nozzle temperature differences. Voids in the interface were detected. Features based on print direction were also seen in the SEM images.

Small- and ultra-small angle X-ray scattering (SAXS and USAXS) was used to study fused deposition modeled samples of PLA and of ABS/ABSFR blends. For the PLA samples, the USAXS/SAXS curves detected interface-related features in the USAXS region and for $q \leq 2 \times 10^{-4}$ $Å^{-1}$. Measurements on the ABS/ABSFR samples showed a differentiation between ABS and ABSFR layers where the features associated with ABS polymers seem to be phased-out, probably due to the flame retardant molecules. Interestingly, the print orientation and order seemed to influence the curves as seen in the differentiation for ABS on ABSFR vs ABSFR on ABS interfaces for the 1:1 and 3:1 samples.

Having studied these samples with the conventional SAXS technique, X-ray grating interferometric studies will follow for a full comparison of both techniques. Experiments at the LSU CAMD facility are in the works.

6.5 References

1. Yashiro, W.; Terui, Y.; Kawabata, K.; Momose, A., On the origin of visibility contrast in x-ray Talbot interferometry. *Optics Express* **2010,** *18* (16), 16890-16901.

2. Bech, M.; Bunk, O.; Donath, T.; Feidenhans'l, R.; David, C.; Pfeiffer, F., Quantitative x-ray dark-field computed tomography. *Physics in Medicine & Biology* **2010,** *55* (18), 5529-5539.

3. Pfeiffer, F.; Bech, M.; Bunk, O.; Kraft, P.; Eikenberry, E. F.; Brönnimann, C.; Grünzweig, C.; David, C., Hard-X-ray dark-field imaging using a grating interferometer. *Nature materials* **2008,** *7* (2), 134-137.

4. Grünzweig, C.; Kopecek, J.; Betz, B.; Kaestner, A.; Jefimovs, K.; Kohlbrecher, J.; Gasser, U.; Bunk, O.; David, C.; Lehmann, E.; Donath, T.; Pfeiffer, F., Quantification of the neutron dark-field imaging signal in grating interferometry. *Physical Review B* **2013,** *88* (12), No. 125104.

5. Betz, B.; Harti, R. P.; Strobl, M.; Hovind, J.; Kaestner, A.; Lehmann, E.; Van Swygenhoven, H.; Grünzweig, C., Quantification of the sensitivity range in neutron dark-field imaging. *Review of Scientific Instruments* **2015,** *86* (12), No. 123704.

6. Prade, F.; Yaroshenko, A.; Herzen, J.; Pfeiffer, F., Short-range order in mesoscale systems probed by X-ray grating interferometry. *EPL (Europhysics Letters)* **2016,** *112* (6), No. 68002.

7. Hussey, D. S.; Miao, H.; Yuan, G.; Pushin, D.; Sarenac, D.; Huber, M. G.; Jacobson, D. L.; LaManna, J. M.; Wen, H., Demonstration of a white beam far-field neutron interferometer for spatially resolved small angle neutron scattering. *arXiv preprint arXiv:1606.03054* **2016**.

8. Harti, R. P.; Strobl, M.; Betz, B.; Jefimovs, K.; Kagias, M.; Grünzweig, C., Sub-pixel correlation length neutron imaging: Spatially resolved scattering information of microstructures on a macroscopic scale. *Scientific Reports* **2017,** *7*, No. 44588.

9. Andersson, R.; van Heijkamp, L. F.; de Schepper, I. M.; Bouwman, W. G., Analysis of spin-echo small-angle neutron scattering measurements. *Journal of Applied Crystallography* **2008,** *41* (5), 868-885.

10. Strobl, M.; Betz, B.; Harti, R.; Hilger, A.; Kardjilov, N.; Manke, I.; Gruenzweig, C., Wavelength-dispersive dark-field contrast: micrometre structure resolution in neutron imaging with gratings. *Journal of Applied Crystallography* **2016,** *49* (2), 569-573.

11. De Jeu, W. H., *Basic X-ray scattering for soft matter*. Oxford University Press: 2016.

12. Willmott, P., *An introduction to synchrotron radiation: techniques and applications*. John Wiley & Sons: 2011.

13. Polizzi, S.; Spinozzi, F., Small Angle X-Ray Scattering (SAXS) with Synchrotron Radiation Sources. In *Synchrotron Radiation*, Springer: 2015; pp 337-359.

14. Zhang, F.; Ilavsky, J., Ultra-Small-Angle X-ray Scattering of Polymers. *Polymer Reviews* **2010,** *50* (1), 59-90.

15. Mobilio, S.; Meneghini, C.; Boscherini, F., *Synchrotron radiation. Basics, methods and applications*. Springer-Verlag Berlin An: 2016.

16. Strobl, M., General solution for quantitative dark-field contrast imaging with grating interferometers. *Scientific Reports* **2014,** *4*, No. 07243.

17. Olčák, D.; Hronský, V.; Kovaľaková, M.; Vrábel, P.; Chodák, I.; Alexy, P., High-Resolution Solid-State NMR Characterization of Morphology in Annealed Polylactic Acid. *International Journal of Polymer Analysis and Characterization* **2015,** *20* (5), 396-405.

18. Ilavsky, J.; Zhang, F.; Andrews, R. N.; Kuzmenko, I.; Jemian, P. R.; Levine, L. E.; Allen, A. J., Development of combined microstructure and structure characterization facility for in situ and operando studies at the Advanced Photon Source. *Journal of Applied Crystallography* **2018,** *51* (3), 867-882.

19. Wavemetrics Igor Pro 8 (2018). https://www.wavemetrics.com.

20. Ilavsky, J.; Jemian, P. R., Irena: tool suite for modeling and analysis of small-angle scattering. *Journal of Applied Crystallography* **2009,** *42* (2), 347-353.

21. Zhang, F.; Ilavsky, J.; Long, G. G.; Quintana, J. P.; Allen, A. J.; Jemian, P. R., Glassy carbon as an absolute intensity calibration standard for small-angle scattering. *Metallurgical and Materials Transactions A* **2010,** *41* (5), 1151-1158.

22. Nelson, A., Co-refinement of multiple-contrast neutron/X-ray reflectivity data using MOTOFIT. *Journal of Applied Crystallography* **2006,** *39* (2), 273-276.

23. Beaucage, G., Approximations leading to a unified exponential/power-law approach to small-angle scattering. *Journal of Applied Crystallography* **1995,** *28* (6), 717-728.

CHAPTER 7
CONCLUSIONS AND RECOMMENDATIONS

7.1 Conclusions

X-ray grating interferometry has been applied in this dissertation to study parts fabricated by the fused deposition modelling technique of additive manufacturing. Three signals are retrieved using this interferometric technique –the absorption signal, the differential phase contrast signal and the dark-field signal. Our interest in the failures, faults and porosities in the layers composing an additively manufactured part caused us to focus on the dark-field signal. The dark-field signal is a small-angle scattering signal showing up as an attenuation in X-ray intensity after the absorption and phase change effects have been accounted for. It represents the scattering of microstructures of size scales much smaller than those of the pixels of the detector system. The dark-field signal is orientation sensitive and based on the interferometer setup, can be made to be sensitive to specific size scales. The ability to tune the dark-field signal to be sensitive to specific size scales makes it possible to fully probe a sample to determine the size range and shapes of structures composing it.

X-ray grating interferometry imaging was carried out on two fused deposition modelled Stanford bunnies, one made from ABS using a Stratasys Dimension Elite Printer and the other from PLA using a Makerbot Replicator printer; and an object having three flat sides and a curved side, printed using PLA and embedded with silver lines. Two grating orientations—grating structures oriented vertically and horizontally—were probed. For the ABS bunny, the dark-field images showed higher scattering intensities when the gratings were oriented horizontally than when the gratings were oriented vertically. This indicated that microstructure in this ABS sample scattered more efficiently in the vertical

direction and were probably composed more of structures elongated along the horizontal axis (an anisotropic shape). A comparison of line probe plots performed on two-dimensional dark-field and absorption images, covering many layers, showed that the dark-field layers arose between filaments. The horizontally elongated scatterers were therefore attributed to porosities or gaps arising from imperfections in layer fusion. When SEM imaging of a portion of the ABS bunny ear was carried out, anisotropic gaps and pores that could contribute to vertical scattering were observed between layers. The higher intensity regions seemed to concentrate around higher curvature regions e.g. the bunny ear and forehead, and prompted a curvature analysis. The curvature analysis was carried out on the bunny ears and head, and involved extracting the dark-field intensities in the perimeter regions and comparing with the perimeter curvature. However, only a very slight correlation was observed.

For the PLA bunny, the dark-field image obtained with the gratings in the horizontal orientation yet again showed higher intensities than that obtained with the vertical grating orientation. However, the higher intensities obtained with horizontal grating orientation were more widespread across the sample than for the ABS sample.

Darkfield images of the third sample i.e. the object having three flat sides and a curved side, printed using PLA and embedded with silver lines, emphasize the interlayer scattering when the gratings are oriented horizontally.

To investigate the effect on performance and feasibility of incorporating flame-retardant into an otherwise flammable object through additive manufacturing, X-ray grating interferometry was used to study sample blocks comprising pure different ratios of ABS polymer and ABS/flame retardant layers. Two heating temperatures, 265°C and

275°C, were probed. While the absorption images give no clear indication of the heat propagation effects the dark-field images are very informative.

For samples with a 1:1 ratio of ABS polymer and ABS/flame retardant layers, the dark-field images at a correlation length of 0.78 μm showed lower scattering intensities and seemed to concentrate in the region adjacent to the point where heat was applied. As the instrument correlation length was increased from 0.78 μm to 0.88 μm, 0.98 μm and 1.08 μm, the lower intensity region gradually shrunk, meaning the instrument began to picked up scattering from initially undetected scatterers i.e. with vertical dimensions in the range of ≥ 0.78 μm and ≥ 1.08 μm. For the samples with a 3:1 ratio of ABS polymer and ABS/flame retardant layers thus, wider distances between the ABS/flame retardant layers; the dark-field images show that higher scattering intensities occurred mainly in the ABS/flame retardant layer. The lower intensities in the ABS layers indicate better homogeneity in the ABS filaments. The ABSFR layers show decreased intensities in the region adjacent to the point of heating at the correlation 0.78 μm with the intensities increasing as the correlation length is changed to 1.08 μm, similar to the 1:1-layer samples. The increasing intensities were attributed to the detection of larger pores formed as a result of gaseous products of the thermal decomposition of the flame retardant molecules.

Dark-field images from x-ray grating interferometry have the potential to be as widely applied as the conventional small-angle scattering technique (SAXS). This however, requires more research into extracting quantitative information about scattering centers. SAXS studies were carried out on fused deposition modelled samples printed from PLA and from ABS/ABSFR. Traces for the PLA samples showed additional structure

in interface regions than in layer regions. Characterization of pristine PLA filaments by ^{13}C CPMAS solid-state NMR measurements detected no crystalline domains in the polymer. Similar characterization of heated filament also detected no crystalline domains.

Scattering measurements for the ABS/ABSFR samples gave similar curves for the ABS layers and similar curves for the ABSFR layers. For the 1:1 ABS/ABSFR samples, the curves seemed to differentiate between the print order i.e. where ABS was printed on ABSFR versus where ABSFR was printed on ABS. This distinction was also seen in the 3:1 sample.

7.2 Recommendations

In this dissertation, X-ray Talbot-Lau and single-shot interferometry was used to study polymeric objects made through fused deposition modelling with meaningful results. Further studies on the incorporation of flame retardants through additive manufacturing should involve using a known flame retardant. To fully explore the feasibility of constraining flame retardant molecules to subsurface layers, additional experiments are necessary. Samples of subsurface-layer-confined flame–retardants and samples made from blended polymer/flame-retardant i.e. by conventional manufacturing methods need to be compared. The concentration of flame retardant in both classes of samples should be the same and the flame inhibiting performance compared through the UL-94 technique. X-ray interferometry images of samples, acquired before and after burning, should inform on the extent of flame retardant participation during burning for both sample classes. This can be followed by tuning the number of flame-retardant layers till the number of layers needed for efficient flame-retardancy is determined.

Fused deposition modelling in not widely used in manufacturing therefore other AM techniques that make use of polymer feedstock e.g. selective laser sintering, need to be studied. It will be important to see how grating orientation in X-ray grating interferometry contributes to identifying the source of voids in such processes where elongated or stretched material is not used.

For X-ray grating interferometry to gain wide acceptance as the conventional small angle scattering technique, more work needs to be done in quantitatively studying inhomogeneous or unknown micro-structure.

In the case of low-absorbing polymer-based objects like ABS and PLA reported in this dissertation, another technique, far-field interferometry, may potentially yield better images. In far-field interferometry only phase gratings are used and the periods are on the order of a few hundred nanometers thus, making for higher fluxes reaching the detector and a higher sensitivity to changes in the wavefront. A higher sensitivity would translate to the detection of even smaller structure sizes by the dark-field imaging.

The removal of fringe-like artifacts in images is still very challenging though a variety of algorithms have been published. It is therefore necessary that a review of this algorithms is attempted to isolate the handful that are most robust in application.

APPENDIX A
COPYRIGHT INFORMATION

A.1. Copyright Information for Paper Reprinted in Chapter 4

Rightslink® by Copyright Clearance Center 10/17/18, 12:06 PM

Copyright Clearance Center RightsLink®

Home | Create Account | Help

ELSEVIER

Title: Non-Destructive Evaluation of Additively Manufactured Polymer Objects using X-ray Interferometry

Author: Omoefe J. Kio,Jumao Yuan,Adam J. Brooks,Gerald L. Knapp,Kyungmin Ham,Jinghua Ge,Denis van Loo,Leslie G. Butler

Publication: Additive Manufacturing

Publisher: Elsevier

Date: Available online 22 April 2018

© 2018 Elsevier B.V. All rights reserved.

LOGIN

If you're a copyright.com user, you can login to RightsLink using your copyright.com credentials.

Already a RightsLink user or want to learn more?

Please note that, as the author of this Elsevier article, you retain the right to include it in a thesis or dissertation, provided it is not published commercially. Permission is not required, but please ensure that you reference the journal as the original source. For more information on this and on your other retained rights, please visit: https://www.elsevier.com/about/our-business/policies/copyright#Author-rights

BACK CLOSE WINDOW

Copyright © 2018 Copyright Clearance Center, Inc. All Rights Reserved. Privacy statement. Terms and Conditions.
Comments? We would like to hear from you. E-mail us at customercare@copyright.com

https://s100.copyright.com/AppDispatchServlet Page 1 of 1

A.2. Copyright Permission for Figure 1.2

Regarding Incident 2331763 Permission to reuse

support@services.acs.org

Tue 10/30/2018 8:59 PM

To: Omoefe J Kio <okio1@lsu.edu>;

ACS Chemistry for Life®

Dear Dr. Omoefe Kio,

Thank you for contacting ACS Publications Support.

Your permission request is granted and there is no fee for this reuse. In your planned reuse, you must cite the ACS article as the source, add this direct link <https://pubs.acs.org/doi/abs/10.1021/acs.chemrev.7b00074>, and include a notice to readers that further permissions related to the material excerpted should be directed to the ACS.

Should you need further assistance, please let us know.

Sincerely,

Noemi D. Cabalza
ACS Customer Services & Information
Website: https://help.acs.org/

Incident Information:

Incident #: 2331763
Date Created: 2018-10-31T06:47:03
Priority: 3
Customer: Omoefe Kio
Title: Permission to reuse
Description: Hello All,

I have originally requested permission to use a figure from one of your publications in my thesis (Incident 2311976) but omitted some information. Kindly consider this a fresh request and treat accordingly.

The title is "Polymers for 3D Printing and Customized Additive Manufacturing"

Here is the link to the article: https://pubs.acs.org/doi/abs/10.1021/acs.chemrev.7b00074

DOI: 10.1021/acs.chemrev.7b00074.

The figure of interest is Figure 48 and will be used in my thesis.

Please note the following;

- My thesis will be submitted to LSU Digital Commons, an open- access institutional repository.

- The university reserves a nonexclusive, paid-up, royalty-free right to distribute copies of theses and dissertations, both internally and to third parties, whether by electronic means, microfilm, or otherwise.

Thank you.

Best regards,
Omoefe Kio

Graduate Assistant
Butler Research Group
Department of Chemistry
Louisiana State University

{CMI: MCID364812}

A.3. Copyright Permission for Figure 1.3

ELSEVIER LICENSE
TERMS AND CONDITIONS

Nov 08, 2018

This Agreement between Mrs. Omoefe Kio ("You") and Elsevier ("Elsevier") consists of your license details and the terms and conditions provided by Elsevier and Copyright Clearance Center.

License Number	4464360706828
License date	Nov 08, 2018
Licensed Content Publisher	Elsevier
Licensed Content Publication	Materials Science and Engineering: R: Reports
Licensed Content Title	Materials engineering for surface-confined flame retardancy
Licensed Content Author	Giulio Malucelli,Federico Carosio,Jenny Alongi,Alberto Fina,Alberto Frache,Giovanni Camino
Licensed Content Date	Oct 1, 2014
Licensed Content Volume	84
Licensed Content Issue	n/a
Licensed Content Pages	20
Start Page	1
End Page	20
Type of Use	reuse in a thesis/dissertation
Portion	figures/tables/illustrations
Number of figures/tables/illustrations	1
Format	both print and electronic
Are you the author of this Elsevier article?	No
Will you be translating?	No
Original figure numbers	figure 1
Title of your thesis/dissertation	Application of X-ray Grating Interferometry to Polymer/Flame Retardant Blends in Additive Manufacturing
Expected completion date	May 2019
Estimated size (number of pages)	200
Requestor Location	Mrs. Omoefe Kio 1221 Bob Pettit Blvd. Apt 215

BATON ROUGE, LA 70820
United States
Attn: Mrs. Omoefe Kio

Publisher Tax ID	98-0397604
Total	0.00 USD

Terms and Conditions

INTRODUCTION

1. The publisher for this copyrighted material is Elsevier. By clicking "accept" in connection with completing this licensing transaction, you agree that the following terms and conditions apply to this transaction (along with the Billing and Payment terms and conditions established by Copyright Clearance Center, Inc. ("CCC"), at the time that you opened your Rightslink account and that are available at any time at http://myaccount.copyright.com).

GENERAL TERMS

2. Elsevier hereby grants you permission to reproduce the aforementioned material subject to the terms and conditions indicated.
3. Acknowledgement: If any part of the material to be used (for example, figures) has appeared in our publication with credit or acknowledgement to another source, permission must also be sought from that source. If such permission is not obtained then that material may not be included in your publication/copies. Suitable acknowledgement to the source must be made, either as a footnote or in a reference list at the end of your publication, as follows:
"Reprinted from Publication title, Vol /edition number, Author(s), Title of article / title of chapter, Pages No., Copyright (Year), with permission from Elsevier [OR APPLICABLE SOCIETY COPYRIGHT OWNER]." Also Lancet special credit - "Reprinted from The Lancet, Vol. number, Author(s), Title of article, Pages No., Copyright (Year), with permission from Elsevier."
4. Reproduction of this material is confined to the purpose and/or media for which permission is hereby given.
5. Altering/Modifying Material: Not Permitted. However figures and illustrations may be altered/adapted minimally to serve your work. Any other abbreviations, additions, deletions and/or any other alterations shall be made only with prior written authorization of Elsevier Ltd. (Please contact Elsevier at permissions@elsevier.com). No modifications can be made to any Lancet figures/tables and they must be reproduced in full.
6. If the permission fee for the requested use of our material is waived in this instance, please be advised that your future requests for Elsevier materials may attract a fee.
7. Reservation of Rights: Publisher reserves all rights not specifically granted in the combination of (i) the license details provided by you and accepted in the course of this licensing transaction, (ii) these terms and conditions and (iii) CCC's Billing and Payment terms and conditions.
8. License Contingent Upon Payment: While you may exercise the rights licensed immediately upon issuance of the license at the end of the licensing process for the transaction, provided that you have disclosed complete and accurate details of your proposed use, no license is finally effective unless and until full payment is received from you (either by publisher or by CCC) as provided in CCC's Billing and Payment terms and conditions. If full payment is not received on a timely basis, then any license preliminarily granted shall be

deemed automatically revoked and shall be void as if never granted. Further, in the event that you breach any of these terms and conditions or any of CCC's Billing and Payment terms and conditions, the license is automatically revoked and shall be void as if never granted. Use of materials as described in a revoked license, as well as any use of the materials beyond the scope of an unrevoked license, may constitute copyright infringement and publisher reserves the right to take any and all action to protect its copyright in the materials.

9. Warranties: Publisher makes no representations or warranties with respect to the licensed material.

10. Indemnity: You hereby indemnify and agree to hold harmless publisher and CCC, and their respective officers, directors, employees and agents, from and against any and all claims arising out of your use of the licensed material other than as specifically authorized pursuant to this license.

11. No Transfer of License: This license is personal to you and may not be sublicensed, assigned, or transferred by you to any other person without publisher's written permission.

12. No Amendment Except in Writing: This license may not be amended except in a writing signed by both parties (or, in the case of publisher, by CCC on publisher's behalf).

13. Objection to Contrary Terms: Publisher hereby objects to any terms contained in any purchase order, acknowledgment, check endorsement or other writing prepared by you, which terms are inconsistent with these terms and conditions or CCC's Billing and Payment terms and conditions. These terms and conditions, together with CCC's Billing and Payment terms and conditions (which are incorporated herein), comprise the entire agreement between you and publisher (and CCC) concerning this licensing transaction. In the event of any conflict between your obligations established by these terms and conditions and those established by CCC's Billing and Payment terms and conditions, these terms and conditions shall control.

14. Revocation: Elsevier or Copyright Clearance Center may deny the permissions described in this License at their sole discretion, for any reason or no reason, with a full refund payable to you. Notice of such denial will be made using the contact information provided by you. Failure to receive such notice will not alter or invalidate the denial. In no event will Elsevier or Copyright Clearance Center be responsible or liable for any costs, expenses or damage incurred by you as a result of a denial of your permission request, other than a refund of the amount(s) paid by you to Elsevier and/or Copyright Clearance Center for denied permissions.

LIMITED LICENSE

The following terms and conditions apply only to specific license types:

15. **Translation**: This permission is granted for non-exclusive world **English** rights only unless your license was granted for translation rights. If you licensed translation rights you may only translate this content into the languages you requested. A professional translator must perform all translations and reproduce the content word for word preserving the integrity of the article.

16. **Posting licensed content on any Website**: The following terms and conditions apply as follows: Licensing material from an Elsevier journal: All content posted to the web site must maintain the copyright information line on the bottom of each image; A hyper-text must be included to the Homepage of the journal from which you are licensing at http://www.sciencedirect.com/science/journal/xxxxx or the Elsevier homepage for books at http://www.elsevier.com; Central Storage: This license does not include permission for a

scanned version of the material to be stored in a central repository such as that provided by Heron/XanEdu.
Licensing material from an Elsevier book: A hyper-text link must be included to the Elsevier homepage at http://www.elsevier.com . All content posted to the web site must maintain the copyright information line on the bottom of each image.

Posting licensed content on Electronic reserve: In addition to the above the following clauses are applicable: The web site must be password-protected and made available only to bona fide students registered on a relevant course. This permission is granted for 1 year only. You may obtain a new license for future website posting.
17. **For journal authors:** the following clauses are applicable in addition to the above:
Preprints:
A preprint is an author's own write-up of research results and analysis, it has not been peer-reviewed, nor has it had any other value added to it by a publisher (such as formatting, copyright, technical enhancement etc.).
Authors can share their preprints anywhere at any time. Preprints should not be added to or enhanced in any way in order to appear more like, or to substitute for, the final versions of articles however authors can update their preprints on arXiv or RePEc with their Accepted Author Manuscript (see below).
If accepted for publication, we encourage authors to link from the preprint to their formal publication via its DOI. Millions of researchers have access to the formal publications on ScienceDirect, and so links will help users to find, access, cite and use the best available version. Please note that Cell Press, The Lancet and some society-owned have different preprint policies. Information on these policies is available on the journal homepage.
Accepted Author Manuscripts: An accepted author manuscript is the manuscript of an article that has been accepted for publication and which typically includes author-incorporated changes suggested during submission, peer review and editor-author communications.
Authors can share their accepted author manuscript:

- immediately
  - via their non-commercial person homepage or blog
  - by updating a preprint in arXiv or RePEc with the accepted manuscript
  - via their research institute or institutional repository for internal institutional uses or as part of an invitation-only research collaboration work-group
  - directly by providing copies to their students or to research collaborators for their personal use
  - for private scholarly sharing as part of an invitation-only work group on commercial sites with which Elsevier has an agreement
- After the embargo period
  - via non-commercial hosting platforms such as their institutional repository
  - via commercial sites with which Elsevier has an agreement

In all cases accepted manuscripts should:

- link to the formal publication via its DOI
- bear a CC-BY-NC-ND license - this is easy to do

- if aggregated with other manuscripts, for example in a repository or other site, be shared in alignment with our hosting policy not be added to or enhanced in any way to appear more like, or to substitute for, the published journal article.

Published journal article (JPA): A published journal article (PJA) is the definitive final record of published research that appears or will appear in the journal and embodies all value-adding publishing activities including peer review co-ordination, copy-editing, formatting, (if relevant) pagination and online enrichment.
Policies for sharing publishing journal articles differ for subscription and gold open access articles:
Subscription Articles: If you are an author, please share a link to your article rather than the full-text. Millions of researchers have access to the formal publications on ScienceDirect, and so links will help your users to find, access, cite, and use the best available version.
Theses and dissertations which contain embedded PJAs as part of the formal submission can be posted publicly by the awarding institution with DOI links back to the formal publications on ScienceDirect.
If you are affiliated with a library that subscribes to ScienceDirect you have additional private sharing rights for others' research accessed under that agreement. This includes use for classroom teaching and internal training at the institution (including use in course packs and courseware programs), and inclusion of the article for grant funding purposes.
Gold Open Access Articles: May be shared according to the author-selected end-user license and should contain a CrossMark logo, the end user license, and a DOI link to the formal publication on ScienceDirect.
Please refer to Elsevier's posting policy for further information.
18. **For book authors** the following clauses are applicable in addition to the above:
Authors are permitted to place a brief summary of their work online only. You are not allowed to download and post the published electronic version of your chapter, nor may you scan the printed edition to create an electronic version. **Posting to a repository:** Authors are permitted to post a summary of their chapter only in their institution's repository.
19. **Thesis/Dissertation**: If your license is for use in a thesis/dissertation your thesis may be submitted to your institution in either print or electronic form. Should your thesis be published commercially, please reapply for permission. These requirements include permission for the Library and Archives of Canada to supply single copies, on demand, of the complete thesis and include permission for Proquest/UMI to supply single copies, on demand, of the complete thesis. Should your thesis be published commercially, please reapply for permission. Theses and dissertations which contain embedded PJAs as part of the formal submission can be posted publicly by the awarding institution with DOI links back to the formal publications on ScienceDirect.

Elsevier Open Access Terms and Conditions
You can publish open access with Elsevier in hundreds of open access journals or in nearly 2000 established subscription journals that support open access publishing. Permitted third party re-use of these open access articles is defined by the author's choice of Creative Commons user license. See our open access license policy for more information.
Terms & Conditions applicable to all Open Access articles published with Elsevier:
Any reuse of the article must not represent the author as endorsing the adaptation of the article nor should the article be modified in such a way as to damage the author's honour or

reputation. If any changes have been made, such changes must be clearly indicated.
The author(s) must be appropriately credited and we ask that you include the end user license and a DOI link to the formal publication on ScienceDirect.
If any part of the material to be used (for example, figures) has appeared in our publication with credit or acknowledgement to another source it is the responsibility of the user to ensure their reuse complies with the terms and conditions determined by the rights holder.
Additional Terms & Conditions applicable to each Creative Commons user license:
CC BY: The CC-BY license allows users to copy, to create extracts, abstracts and new works from the Article, to alter and revise the Article and to make commercial use of the Article (including reuse and/or resale of the Article by commercial entities), provided the user gives appropriate credit (with a link to the formal publication through the relevant DOI), provides a link to the license, indicates if changes were made and the licensor is not represented as endorsing the use made of the work. The full details of the license are available at http://creativecommons.org/licenses/by/4.0.
CC BY NC SA: The CC BY-NC-SA license allows users to copy, to create extracts, abstracts and new works from the Article, to alter and revise the Article, provided this is not done for commercial purposes, and that the user gives appropriate credit (with a link to the formal publication through the relevant DOI), provides a link to the license, indicates if changes were made and the licensor is not represented as endorsing the use made of the work. Further, any new works must be made available on the same conditions. The full details of the license are available at http://creativecommons.org/licenses/by-nc-sa/4.0.
CC BY NC ND: The CC BY-NC-ND license allows users to copy and distribute the Article, provided this is not done for commercial purposes and further does not permit distribution of the Article if it is changed or edited in any way, and provided the user gives appropriate credit (with a link to the formal publication through the relevant DOI), provides a link to the license, and that the licensor is not represented as endorsing the use made of the work. The full details of the license are available at http://creativecommons.org/licenses/by-nc-nd/4.0.
Any commercial reuse of Open Access articles published with a CC BY NC SA or CC BY NC ND license requires permission from Elsevier and will be subject to a fee.
Commercial reuse includes:

- Associating advertising with the full text of the Article
- Charging fees for document delivery or access
- Article aggregation
- Systematic distribution via e-mail lists or share buttons

Posting or linking by commercial companies for use by customers of those companies.

20. **Other Conditions**:

v1.9

Questions? customercare@copyright.com or +1-855-239-3415 (toll free in the US) or +1-978-646-2777.

A.4. Copyright Permission for Figures 1.7 and 1.8

ELSEVIER LICENSE TERMS AND CONDITIONS

Oct 26, 2018

This Agreement between Mrs. Omoefe Kio ("You") and Elsevier ("Elsevier") consists of your license details and the terms and conditions provided by Elsevier and Copyright Clearance Center.

License Number	4453880921996
License date	Oct 21, 2018
Licensed Content Publisher	Elsevier
Licensed Content Publication	Materials Science and Engineering: R: Reports
Licensed Content Title	New prospects in flame retardant polymer materials: From fundamentals to nanocomposites
Licensed Content Author	F. Laoutid,L. Bonnaud,M. Alexandre,J.-M. Lopez-Cuesta,Ph. Dubois
Licensed Content Date	Jan 29, 2009
Licensed Content Volume	63
Licensed Content Issue	3
Licensed Content Pages	26
Start Page	100
End Page	125
Type of Use	reuse in a thesis/dissertation
Portion	figures/tables/illustrations
Number of figures/tables/illustrations	5
Format	both print and electronic
Are you the author of this Elsevier article?	No
Will you be translating?	No
Original figure numbers	Figures 3, 4, 5, 7, 14
Title of your thesis/dissertation	Application of X-ray Grating Interferometry to Polymer/Flame Retardant Blends in Additive Manufacturing
Expected completion date	May 2019
Estimated size (number of pages)	200
Requestor Location	Mrs. Omoefe Kio 1221 Bob Pettit Blvd. Apt 215 BATON ROUGE, LA 70820 United States Attn: Mrs. Omoefe Kio
Publisher Tax ID	98-0397604
Total	**0.00 USD**
Terms and Conditions	

INTRODUCTION

1. The publisher for this copyrighted material is Elsevier. By clicking "accept" in connection with completing this licensing transaction, you agree that the following terms and conditions apply to this transaction (along with the Billing and Payment terms and conditions established by Copyright Clearance Center, Inc. ("CCC"), at the time that you opened your Rightslink account and that are available at any time at http://myaccount.copyright.com).

GENERAL TERMS

2. Elsevier hereby grants you permission to reproduce the aforementioned material subject to the terms and conditions indicated.
3. Acknowledgement: If any part of the material to be used (for example, figures) has appeared in our publication with credit or acknowledgement to another source, permission must also be sought from that source. If such permission is not obtained then that material may not be included in your publication/copies. Suitable acknowledgement to the source must be made, either as a footnote or in a reference list at the end of your publication, as follows:
"Reprinted from Publication title, Vol /edition number, Author(s), Title of article / title of chapter, Pages No., Copyright (Year), with permission from Elsevier [OR APPLICABLE SOCIETY COPYRIGHT OWNER]." Also Lancet special credit - "Reprinted from The Lancet, Vol. number, Author(s), Title of article, Pages No., Copyright (Year), with permission from Elsevier."
4. Reproduction of this material is confined to the purpose and/or media for which permission is hereby given.
5. Altering/Modifying Material: Not Permitted. However figures and illustrations may be altered/adapted minimally to serve your work. Any other abbreviations, additions, deletions and/or any other alterations shall be made only with prior written authorization of Elsevier Ltd. (Please contact Elsevier at permissions@elsevier.com). No modifications can be made to any Lancet figures/tables and they must be reproduced in full.
6. If the permission fee for the requested use of our material is waived in this instance, please be advised that your future requests for Elsevier materials may attract a fee.
7. Reservation of Rights: Publisher reserves all rights not specifically granted in the combination of (i) the license details provided by you and accepted in the course of this licensing transaction, (ii) these terms and conditions and (iii) CCC's Billing and Payment terms and conditions.
8. License Contingent Upon Payment: While you may exercise the rights licensed immediately upon issuance of the license at the end of the licensing process for the transaction, provided that you have disclosed complete and accurate details of your proposed use, no license is finally effective unless and until full payment is received from you (either by publisher or by CCC) as provided in CCC's Billing and Payment terms and conditions. If full payment is not received on a timely basis, then any license preliminarily granted shall be deemed automatically revoked and shall be void as if never granted. Further, in the event that you breach any of these terms and conditions or any of CCC's Billing and Payment terms and conditions, the license is automatically revoked and shall be void as if never granted. Use of materials as described in a revoked license, as well as any use of the materials beyond the scope of an unrevoked license, may constitute copyright infringement and publisher reserves the right to take any and all action to protect its copyright in the materials.
9. Warranties: Publisher makes no representations or warranties with respect to the licensed material.
10. Indemnity: You hereby indemnify and agree to hold harmless publisher and CCC, and their respective officers, directors, employees and agents, from and against any and all claims arising out of your use of the licensed material other than as specifically authorized pursuant to this license.
11. No Transfer of License: This license is personal to you and may not be sublicensed, assigned, or transferred by you to any other person without publisher's written permission.
12. No Amendment Except in Writing: This license may not be amended except in a writing signed by both parties (or, in the case of publisher, by CCC on publisher's behalf).
13. Objection to Contrary Terms: Publisher hereby objects to any terms contained in any purchase order, acknowledgment, check endorsement or other writing prepared by you, which terms are inconsistent with these terms and conditions or CCC's Billing and Payment terms and conditions. These terms and conditions, together with CCC's Billing and Payment terms and conditions (which are incorporated herein), comprise the entire agreement between you and publisher (and CCC) concerning this licensing transaction. In the event of any conflict between your obligations established by these terms and conditions and those established by CCC's Billing and Payment terms and conditions, these terms and conditions shall control.
14. Revocation: Elsevier or Copyright Clearance Center may deny the permissions described in this License at their sole discretion, for any reason or no reason, with a full refund payable to you. Notice of such denial will be made using the contact information provided by you. Failure to receive such notice will not alter or invalidate the denial. In no event will Elsevier or Copyright Clearance Center be responsible or liable for any costs, expenses or damage incurred by you as a result of a denial of your permission request, other than a refund of the amount(s) paid by you to Elsevier and/or Copyright Clearance Center for denied permissions.

LIMITED LICENSE

The following terms and conditions apply only to specific license types:
15. **Translation**: This permission is granted for non-exclusive world **English** rights only unless your license was granted for translation rights. If you licensed translation rights you may only translate this content into the languages you requested. A professional translator must perform all translations and reproduce the content word for word preserving the integrity of the article.
16. **Posting licensed content on any Website**: The following terms and conditions apply as follows: Licensing material from an Elsevier journal: All content posted to the web site must maintain the copyright information line on the bottom of each image; A hyper-text must be included to the Homepage of the journal from which you are licensing at http://www.sciencedirect.com/science/journal/xxxxx or the Elsevier homepage for books at http://www.elsevier.com; Central Storage: This license does not include permission for a scanned version of the material to be stored in a central repository such as that provided by Heron/XanEdu.
Licensing material from an Elsevier book: A hyper-text link must be included to the Elsevier homepage at http://www.elsevier.com . All content posted to the web site must maintain the copyright information line on the bottom of each image.

Posting licensed content on Electronic reserve: In addition to the above the following clauses are applicable: The web site must

be password-protected and made available only to bona fide students registered on a relevant course. This permission is granted for 1 year only. You may obtain a new license for future website posting.

17. **For journal authors:** the following clauses are applicable in addition to the above:

Preprints:

A preprint is an author's own write-up of research results and analysis, it has not been peer-reviewed, nor has it had any other value added to it by a publisher (such as formatting, copyright, technical enhancement etc.).

Authors can share their preprints anywhere at any time. Preprints should not be added to or enhanced in any way in order to appear more like, or to substitute for, the final versions of articles however authors can update their preprints on arXiv or RePEc with their Accepted Author Manuscript (see below).

If accepted for publication, we encourage authors to link from the preprint to their formal publication via its DOI. Millions of researchers have access to the formal publications on ScienceDirect, and so links will help users to find, access, cite and use the best available version. Please note that Cell Press, The Lancet and some society-owned have different preprint policies. Information on these policies is available on the journal homepage.

Accepted Author Manuscripts: An accepted author manuscript is the manuscript of an article that has been accepted for publication and which typically includes author-incorporated changes suggested during submission, peer review and editor-author communications.

Authors can share their accepted author manuscript:

- immediately
  - via their non-commercial person homepage or blog
  - by updating a preprint in arXiv or RePEc with the accepted manuscript
  - via their research institute or institutional repository for internal institutional uses or as part of an invitation-only research collaboration work-group
  - directly by providing copies to their students or to research collaborators for their personal use
  - for private scholarly sharing as part of an invitation-only work group on commercial sites with which Elsevier has an agreement
- After the embargo period
  - via non-commercial hosting platforms such as their institutional repository
  - via commercial sites with which Elsevier has an agreement

In all cases accepted manuscripts should:

- link to the formal publication via its DOI
- bear a CC-BY-NC-ND license - this is easy to do
- if aggregated with other manuscripts, for example in a repository or other site, be shared in alignment with our hosting policy not be added to or enhanced in any way to appear more like, or to substitute for, the published journal article.

Published journal article (JPA): A published journal article (PJA) is the definitive final record of published research that appears or will appear in the journal and embodies all value-adding publishing activities including peer review co-ordination, copy-editing, formatting, (if relevant) pagination and online enrichment.

Policies for sharing publishing journal articles differ for subscription and gold open access articles:

Subscription Articles: If you are an author, please share a link to your article rather than the full-text. Millions of researchers have access to the formal publications on ScienceDirect, and so links will help your users to find, access, cite, and use the best available version.

Theses and dissertations which contain embedded PJAs as part of the formal submission can be posted publicly by the awarding institution with DOI links back to the formal publications on ScienceDirect.

If you are affiliated with a library that subscribes to ScienceDirect you have additional private sharing rights for others' research accessed under that agreement. This includes use for classroom teaching and internal training at the institution (including use in course packs and courseware programs), and inclusion of the article for grant funding purposes.

Gold Open Access Articles: May be shared according to the author-selected end-user license and should contain a CrossMark logo, the end user license, and a DOI link to the formal publication on ScienceDirect.

Please refer to Elsevier's posting policy for further information.

18. **For book authors** the following clauses are applicable in addition to the above: Authors are permitted to place a brief summary of their work online only. You are not allowed to download and post the published electronic version of your chapter, nor may you scan the printed edition to create an electronic version. **Posting to a repository:** Authors are permitted to post a summary of their chapter only in their institution's repository.

19. **Thesis/Dissertation**: If your license is for use in a thesis/dissertation your thesis may be submitted to your institution in either print or electronic form. Should your thesis be published commercially, please reapply for permission. These requirements include permission for the Library and Archives of Canada to supply single copies, on demand, of the complete thesis and include permission for Proquest/UMI to supply single copies, on demand, of the complete thesis. Should your thesis be published commercially, please reapply for permission. Theses and dissertations which contain embedded PJAs as part of the formal submission can be posted publicly by the awarding institution with DOI links back to the formal publications on ScienceDirect.

Elsevier Open Access Terms and Conditions

You can publish open access with Elsevier in hundreds of open access journals or in nearly 2000 established subscription journals that support open access publishing. Permitted third party re-use of these open access articles is defined by the author's choice of Creative Commons user license. See our open access license policy for more information.

Terms & Conditions applicable to all Open Access articles published with Elsevier:

Any reuse of the article must not represent the author as endorsing the adaptation of the article nor should the article be modified in such a way as to damage the author's honour or reputation. If any changes have been made, such changes must be clearly indicated.

The author(s) must be appropriately credited and we ask that you include the end user license and a DOI link to the formal publication on ScienceDirect.

If any part of the material to be used (for example, figures) has appeared in our publication with credit or acknowledgement to another source it is the responsibility of the user to ensure their reuse complies with the terms and conditions determined by the rights holder.

Additional Terms & Conditions applicable to each Creative Commons user license:

CC BY: The CC-BY license allows users to copy, to create extracts, abstracts and new works from the Article, to alter and revise the Article and to make commercial use of the Article (including reuse and/or resale of the Article by commercial entities), provided the user gives appropriate credit (with a link to the formal publication through the relevant DOI), provides a link to the license, indicates if changes were made and the licensor is not represented as endorsing the use made of the work. The full details of the license are available at http://creativecommons.org/licenses/by/4.0.

CC BY NC SA: The CC BY-NC-SA license allows users to copy, to create extracts, abstracts and new works from the Article, to alter and revise the Article, provided this is not done for commercial purposes, and that the user gives appropriate credit (with a link to the formal publication through the relevant DOI), provides a link to the license, indicates if changes were made and the licensor is not represented as endorsing the use made of the work. Further, any new works must be made available on the same conditions. The full details of the license are available at http://creativecommons.org/licenses/by-nc-sa/4.0.

CC BY NC ND: The CC BY-NC-ND license allows users to copy and distribute the Article, provided this is not done for commercial purposes and further does not permit distribution of the Article if it is changed or edited in any way, and provided the user gives appropriate credit (with a link to the formal publication through the relevant DOI), provides a link to the license, and that the licensor is not represented as endorsing the use made of the work. The full details of the license are available at http://creativecommons.org/licenses/by-nc-nd/4.0. Any commercial reuse of Open Access articles published with a CC BY NC SA or CC BY NC ND license requires permission from Elsevier and will be subject to a fee.

Commercial reuse includes:

- Associating advertising with the full text of the Article
- Charging fees for document delivery or access
- Article aggregation
- Systematic distribution via e-mail lists or share buttons

Posting or linking by commercial companies for use by customers of those companies.

20. **Other Conditions**:

v1.9

Questions? customercare@copyright.com or +1-855-239-3415 (toll free in the US) or +1-978-646-2777.

APPENDIX B
PSEUDOCODE FOR CURVATURE ANALYSIS

```
function GenerateListRowColumnCurvature(AbsorptionSlice, MagnificationFactor, GaussianFilterRadius)
   {
   input AbsorptionSlice[r][c]
   [r, c] = size(AbsorptionSlice)
   s=zeros[r][c]
   s ⟵ apply function Binarize(AbsorptionSlice)
   s ⟵ apply function Magnify(s,MagnificationFactor)
   s ⟵ apply function GaussianFilter(s,GaussianFilterRadius)
   p=zeros[r'][c']
   p ⟵ apply function DetectPerimeter(s)
   p ⟵ apply function Magnify(p,1/MagnificationFactor)
   for index = 1 to length(p)
   p[index][] ⟵ apply function Order(p)
   end
   t = zeros[r"][c"]
   t ⟵ apply function Interpolate(p)
   for index=1 to length(p)
   γ[index] ⟵ apply function Curvature(t)
   end
   return(row,column, γ)
   }
   function MaskDarkField(AbsorptionSlice, DarkField)
   {
   input AbsorptionSlice[r][c]
   s[r][c] ⟵ apply function Binarize(AbsorptionSlice)
   s[r][c] ⟵ apply function Erode(Dilate(s,1),2)
   input DarkField[r][c]
   d[r][c] ⟵ apply function Mask(DarkField, s)
   return(d[r][c])
   }
   function Order(p)
   {
   p ⟵ append(p, p[1])
   orderedP ⟵ p[1]
   p ⟵ drop(p[1])
   orderedP ⟵ append(orderedP, p[1])
   p ⟵ drop(p[1])
   while (length(p) > 0)
   {
   lastPoint ⟵ last(orderedP)
   nextPoint ⟵ nearest(p, lastpoit)[1]
   if(norm(nextPoint - lastPoint) >= maxDistanceBetweenPerimeterPoints)
   break;
   orderedP ⟵ append(orderedP, nextPoint)
   indexUnordered ⟵ position(p != nextPoint)[1,1]
   p ⟵ drop(p, indexUnordered)
   }
   return orderedP[]
   }
   function Curvature(t)
   {
   for s=1 to length(orderedP)
   {
   listCurvature ⟵ table(Δx1 = interpolation[s]; Δx2 = interpolation[s]; Δy1 = interpolation[s]; Δy2 = in-
terpolation[s])
   chop(abs(Δx1Δy2 - Δx2Δy1) /(Δx1^2 + Δy1^2)^(3/2);
   }
   listCurvature ⟵ rotateRight(listCurvature, 10);
   gap ⟵ take(listCurvature, [8, 15]);
   gap ⟵ movingAverage(gap, 3);
   listCurvature[8:13] ⟵ gap;
   listCurvature ⟵ rotateLeft(listCurvature, 10);
   return listCurvature;
   }
```

APPENDIX C
PROCESSING CODES FOR INTERFEROMETRY

This Appendix presents sample processing codes for data processing in Tomopy. The first Section (C.1) presents an example of mathematica codes used to calculate the three image contrast types accessible from grating-based interferometry—absorption, differential phase and dark-field—for the projection images. The steps involve importing the data files obtained from the detector, ordering them and grouping sample files with their corresponding reference files. The images are then calculated.

Python codes for use in Tomopy for similar processing as described above are provided in Section C.2. Section C.3 presents typical Python codes used for tomographic reconstruction and based on the two-dimensional absorption, differential phase and dark-field images obtained from Section C.2. Here, the center of rotation for the sample, the axis where the region of interest remains in the field of view for all projections, is determined then sinograms are generated for the volume reconstruction. The Gridrec and SIRT algorithms are used for the reconstruction.

C.1. Sample Mathematica Codes for Stepped-grating Interferometry

One Reference Set and Many Raws at an angle
GRATING position read from header

Step 1: Define functions

Functions for reading file, finding number of groups of reference files and sample files

funcReadPCOFile[filename_] This will read data from a PCO integer-16 binary file.
funcFindReferenceB16files[pathTIFF_] Finds files based on ".white." and orders the list based on the image sequence number.
funcFindSampleB16files[pathTIFF_] Finds files based on ".raw." and orders the list based on the image sequence number.
funcFindReferenceGroups[] Based on sequence number, finds the grouping of the reference files.
funcFindSampleGroups[] Based on sequence number, finds the grouping of the sample files.

```
funcReadPCOFileHeader[filename_] := Module[{GRATING},
   HeaderStr = FindList[filename, ":", 1];
   text = StringSplit[HeaderStr,
      { "X Start:", "X End:", "X Binning:", "Y Start:", "Y End:", "Y Binning:",
       "Exposure(msec):", "Pixel2Micron:", "Angle:", "Grating:", "Time :"}][[1]];
   XSTART = ToExpression[text[[1]]];
   XEND = ToExpression[text[[2]]];
   XBIN = ToExpression[text[[3]]];
   YSTART = ToExpression[text[[4]]];
   YEND = ToExpression[text[[5]]];
   YBIN = ToExpression[text[[6]]];
   EXPOSURE = ToExpression[text[[7]]];
   PIXEL2MICRON = ToExpression[text[[8]]];
   ANGLE = ToExpression[text[[9]]];
   GRATING = ToExpression[text[[10]]];
   timeImage = DateList[text[[11]]];

   columns = XEND - XSTART + 1;
   rows = YEND - YSTART + 1;
   Grating = GRATING];
```

```
funcReadPCOFile[filename_] := Module[{rows, columns, stream, data},
   HeaderStr = FindList[filename, ":", 1];
   text = StringSplit[HeaderStr,
      {"X Start:", "X End:", "X Binning:", "Y Start:", "Y End:", "Y Binning:",
       "Exposure(msec):", "Pixel2Micron:", "Angle:", "Grating:", "Time :"}][[1]];
   XSTART = ToExpression[text[[1]]];
   XEND = ToExpression[text[[2]]];
   XBIN = ToExpression[text[[3]]];
   YSTART = ToExpression[text[[4]]];
   YEND = ToExpression[text[[5]]];
   YBIN = ToExpression[text[[6]]];
   EXPOSURE = ToExpression[text[[7]]];
   PIXEL2MICRON = ToExpression[text[[8]]];
   ANGLE = ToExpression[text[[9]]];
   GRATING = ToExpression[text[[10]]];
   timeImage = DateList[text[[11]]];

   columns = XEND - XSTART + 1;
   rows = YEND - YSTART + 1;

   stream = OpenRead[filename, BinaryFormat → True];
   Skip[stream, Byte, 220];
   data = BinaryReadList[stream, "UnsignedInteger16", ByteOrdering → -1];
   Close[stream];
   Partition[data, columns] - referenceDarkfield ];
```

```
funcReadPCOFileUncorrected[filename_] := Module[{rows, columns, stream, data},
   HeaderStr = FindList[filename, ":", 1];
   text = StringSplit[HeaderStr,
      {"X Start:", "X End:", "X Binning:", "Y Start:", "Y End:", "Y Binning:",
       "Exposure(msec):", "Pixel2Micron:", "Angle:", "Grating:", "Time :"}][[1]];
   XSTART = ToExpression[text[[1]]];
   XEND = ToExpression[text[[2]]];
   XBIN = ToExpression[text[[3]]];
   YSTART = ToExpression[text[[4]]];
   YEND = ToExpression[text[[5]]];
   YBIN = ToExpression[text[[6]]];
   EXPOSURE = ToExpression[text[[7]]];
   PIXEL2MICRON = ToExpression[text[[8]]];
   ANGLE = ToExpression[text[[9]]];
   GRATING = ToExpression[text[[10]]];
   timeImage = DateList[text[[11]]];

   columns = XEND - XSTART + 1;
   rows = YEND - YSTART + 1;

   stream = OpenRead[filename, BinaryFormat → True];
   Skip[stream, Byte, 220];
   data = BinaryReadList[stream, "UnsignedInteger16", ByteOrdering → -1];
   Close[stream];
   Partition[data, columns]];

funcFindReferenceB16files[pathTIFF_] := Module[{},
   filenamesReference = FileNames["*.white.*.b16", pathTIFF];
   numberOfReferenceFiles = Length[filenamesReference];
   listReferenceSequenceNumbers = Table[
     ToExpression[StringSplit[Last[FileNameSplit[filenamesReference[[i]]]], "."][[5]]],
     {i, numberOfReferenceFiles}];
   listReferenceIndexSequenceGratingNumbers = Table[{i, ToExpression[
       StringSplit[Last[FileNameSplit[filenamesReference[[i]]]], "."][[5]]],
      ToExpression[StringSplit[Last[FileNameSplit[filenamesReference[[i]]]], "."][[
        6]]]}, {i, numberOfReferenceFiles}];
   indexOrdering = Ordering[listReferenceSequenceNumbers];
   filenamesReference = filenamesReference[[indexOrdering]];
   listReferenceIndexSequenceGratingNumbers =
    listReferenceIndexSequenceGratingNumbers[[indexOrdering]];
   numberOfReferenceFiles = Length[filenamesReference];
   numberGratingSteps = Max[Table[listReferenceIndexSequenceGratingNumbers [[i]][[3]],
      {i, numberOfReferenceFiles}]]; ];
```

```
funcFindSampleB16files[pathTIFF_] := Module[{},
   filenamesSample = FileNames["*.raw.*.b16", pathTIFF];
   numberOfSampleFiles = Length[filenamesSample];
   listSampleSequenceNumbers = Table[
     ToExpression[StringSplit[Last[FileNameSplit[filenamesSample[[i]]]], "."][[5]]],
     {i, numberOfSampleFiles}];
   indexOrdering = Ordering[listSampleSequenceNumbers];
   filenamesSample = filenamesSample[[indexOrdering]];
   numberOfSampleFiles = Length[filenamesSample];
   testNameStr = Last[FileNameSplit[First[filenamesReference]]];
   testNameStr = StringSplit[testNameStr, ".white."] // First; ];

funcFindDarkB16files[pathTIFF_] := Module[{},
   filenamesDark = FileNames["*.Dark.*.b16", pathTIFF];
   numberOfDarkFiles = Length[filenamesDark];
   listDarkSequenceNumbers =
    Table[ToExpression[StringSplit[Last[FileNameSplit[filenamesDark[[i]]]], "."][[5]]],
     {i, numberOfDarkFiles}];
   indexOrdering = Ordering[listDarkSequenceNumbers];
   filenamesDark = filenamesDark[[indexOrdering]];
   numberOfDarkFiles = Length[filenamesDark];];
(*testNameStr = Last[FileNameSplit[First[filenamesReference]]];
  testNameStr = StringSplit[testNameStr,".white."]//First;  ];*)

funcFindReferenceGroups[] := Module[{},
   listReferenceAnglesAll = Table[angleBeforeDecimalPoint =
      StringSplit[Last[FileNameSplit[filenamesReference[[i]]]], "."][[3]];
     angleAfterDecimalPoint = StringSplit[
        Last[FileNameSplit[filenamesReference[[i]]]], "."][[4]];
     angle = ToExpression[angleBeforeDecimalPoint <> "." <> angleAfterDecimalPoint],
     {i, numberOfReferenceFiles}];
   listReferenceAngles = Union[listReferenceAnglesAll];
   listReferenceSequenceNumbers = Table[
     ToExpression[StringSplit[Last[FileNameSplit[filenamesReference[[i]]]], "."][[5]]],
     {i, numberOfReferenceFiles}];
   listReferenceSequenceNumbersGroups = Partition[
     listReferenceSequenceNumbers, numberGratingSteps];
   numberOfReferenceGroups = Dimensions[listReferenceSequenceNumbersGroups][[1]];
   listReferenceSequenceNumbersGroupsBounds =
    Table[{First[listReferenceSequenceNumbersGroups[[i]]],
      Last[listReferenceSequenceNumbersGroups[[i]]]},
     {i, Dimensions[listReferenceSequenceNumbersGroups][[1]]}]; ];
```

```
funcFindSampleGroups[] := Module[{},
   listSampleAnglesAll =
    Table[angleBeforeDecimalPoint =
      StringSplit[Last[FileNameSplit[filenamesSample[[i]]]], "."][[3]];
     angleAfterDecimalPoint = StringSplit[
        Last[FileNameSplit[filenamesSample[[i]]]], "."][[4]];
     angle = ToExpression[angleBeforeDecimalPoint <> "." <> angleAfterDecimalPoint],
     {i, numberOfSampleFiles}];
   listSampleAngles = Union[listSampleAnglesAll];
   listSampleSequenceNumbers = Table[
     ToExpression[StringSplit[Last[FileNameSplit[filenamesSample[[i]]]], "."][[5]]],
     {i, numberOfSampleFiles}];
   listSampleIndexSequenceAngleGratingNumbers =
    Table[{i, listSampleSequenceNumbers[[i]], listSampleAnglesAll[[i]],
      ToExpression[StringSplit[Last[FileNameSplit[filenamesSample[[i]]]], "."][[6]]]},
     {i, numberOfSampleFiles}];
   listSampleSequenceNumbersGroups = Split[listSampleSequenceNumbers, #2 - #1 == 1 &];
   listSampleSequenceNumbersGroups =
    Partition[listSampleSequenceNumbers, numberGratingSteps];
   numberOfSampleGroups = Dimensions[listSampleSequenceNumbersGroups][[1]];
   listSampleSequenceNumbersGroupsBounds =
    Table[{First[listSampleSequenceNumbersGroups[[i]]],
      Last[listSampleSequenceNumbersGroups[[i]]]},
     {i, Dimensions[listSampleSequenceNumbersGroups][[1]]}]; ];

funcReadDarkfield[listfilenamesDarkfield_] :=
  Module[{filename, allDarkfield, image, data},
   allDarkfield = ConstantArray[0, {rows, columns, Length[listfilenamesDarkfield]}];
   For[index = 1, index <= Length[listfilenamesDarkfield], index++,
    filename = listfilenamesDarkfield[[index]];
    data = funcReadPCOFileUncorrected[filename];
    allDarkfield[[All, All, index]] = data;
   ];
   referenceDarkfield = Total[allDarkfield, {3}] / Length[listfilenamesDarkfield] ];
```

Functions for interferometry

```
funcPrepareBvectorArbitrarySteps[gratingPeriodMicrons_, listGratingStepsMicrons_] :=
  Module[{b1, b2, b3, numberGratingSteps},
   (*xExpt =listGratingStepsMicrons;
   b1 = Table[xExpt[[i]]/gratingPeriod,{i,Length[xExpt]}];*)
   numberGratingSteps = Length[listGratingStepsMicrons];
   b1 = Table[1, {i, numberGratingSteps}];
   b2 = Table[Sin[2 π listGratingStepsMicrons[[i]] / gratingPeriodMicrons] // N,
     {i, numberGratingSteps}];
   b3 = Table[Cos[2 π listGratingStepsMicrons[[i]] / gratingPeriodMicrons] // N,
     {i, numberGratingSteps}];
   Chop[ Transpose[{b1, b2, b3} ]] ];

funcPrepareAllVectors[gratingPeriodMicrons_,
  listGratingStepsMicrons_, rows_, columns_] := Module[{},
  bVector = funcPrepareBvectorArbitrarySteps[
    gratingPeriodMicrons, listGratingStepsMicrons];
  aVector = cVector = ConstantArray[0, {3, rows * columns}];
  aMatrix = ConstantArray[0, {rows, columns, 3}];
  visibility = phi = ConstantArray[0, {rows, columns}];
  gMatrix = Inverse[Transpose[bVector] . bVector] . Transpose[bVector]; ]

funcReadListGratingStepsMicrons[
   listFilenamesOneInterferogram_, numberGratingSteps_] := Module[{filename},
   (*numberGratingSteps=Length[listGratingStepsMicrons];*)
   allData = ConstantArray[0, numberGratingSteps];
   For[index = 1, index <= numberGratingSteps, index++,
    filename = listFilenamesOneInterferogram[[index]];
    GRATING = funcReadPCOFileHeader[filename];
    allData[[index]] = GRATING;
   ];
   allData];

funcReadOneInterferogram[listFilenamesOneInterferogram_, rows_,
   columns_, listGratingStepsMicrons_] := Module[{filename, intensity},
   numberGratingSteps = Length[listGratingStepsMicrons];
   allData = ConstantArray[0, {rows, columns, numberGratingSteps}];
   For[index = 1, index <= numberGratingSteps, index++,
    filename = listFilenamesOneInterferogram[[index]];
    intensity = Take[funcReadPCOFile[filename], cropRows, cropColumns];
    allData[[All, All, index]] = intensity;
   ];
   allData];
```

```
funcCalculateTransmissionVisibilityPhi[data_] := Module[{transmission, visibility, phi},
   cVector = Transpose[Flatten[data, {1, 2}]];
   aVector = gMatrix.cVector;
   aMatrix = Partition[Transpose[aVector], columns];
   transmission = aMatrix[[All, All, 1]];
   visibility = Sqrt[aMatrix[[All, All, 2]]^2 + aMatrix[[All, All, 3]]^2 ];
   phi = ArcTan[aMatrix[[All, All, 2]], aMatrix[[All, All, 3]] ];
   {transmission, visibility, phi}];

funcCorrectForZeroValuePixels[dataOriginal_] :=
  Module[{coordinatesZeroIntensityPixels, dataCorrected, dataMedianFilter, r, c},
   coordinatesZeroIntensityPixels = Position[dataOriginal, p_?(# == 0 &)];
   If[Length[coordinatesZeroIntensityPixels] > 0,
    Module[{},
      dataCorrected = dataOriginal;
      dataMedianFilter = MedianFilter[dataOriginal, 1];
      For[index = 1, index ≤ Length[coordinatesZeroIntensityPixels], index++,
       {r, c} = coordinatesZeroIntensityPixels[[index]];
       dataCorrected[[r, c]] = dataMedianFilter[[r, c]];
      ];
     ];
   ];
   If[Length[coordinatesZeroIntensityPixels] > 0, dataCorrected, dataOriginal] ];

funcCorrectForOutOfRangeDarkField[dataOriginal_] :=
  Module[{coordinatesBadIntensityPixels, dataCorrected, r, c},
   coordinatesBadIntensityPixels = Position[dataOriginal, p_?(# <= 0 &)];
   dataCorrected = dataOriginal;
   For[index = 1, index ≤ Length[coordinatesBadIntensityPixels], index++,
    {r, c} = coordinatesBadIntensityPixels[[index]];
    dataCorrected[[r, c]] = 1;
   ];
   coordinatesBadIntensityPixels = Position[dataOriginal, p_?(# > 1 &)];
   For[index = 1, index ≤ Length[coordinatesBadIntensityPixels], index++,
    {r, c} = coordinatesBadIntensityPixels[[index]];
    dataCorrected[[r, c]] = 1;
   ];
   dataCorrected];
```

```
funcCorrectLargeDPCvalue[data_] := Module[{coordinatesLargeDPC, dataCorrected, r, c},
   dataCorrected = data;
   coordinatesLargeDPC = Position[data, p_?(# > π &)];
   If[Length[coordinatesLargeDPC] > 0,
    Module[{},
      For[index = 1, index ≤ Length[coordinatesLargeDPC], index++,
        {r, c} = coordinatesLargeDPC[[index]];
        dataCorrected[[r, c]] = data[[r, c]] - 2 π;
       ];
     ];
   ];
   coordinatesLargeDPC = Position[data, p_?(# < -π &)];
   If[Length[coordinatesLargeDPC] > 0,
    Module[{},
      For[index = 1, index ≤ Length[coordinatesLargeDPC], index++,
        {r, c} = coordinatesLargeDPC[[index]];
        dataCorrected[[r, c]] = data[[r, c]] + 2 π;
       ];
     ];
   ];
   dataCorrected];
```

Functions for finding correct files for a given rotation angle

```
funcGetSampleFilenamesForSpecificAngle[angle_] := Module[{},
   indexAngle = Flatten[Position[
      listSampleIndexSequenceAngleGratingNumbers[[All, 3]], p_? (# == angle &)]];
   indexFilename = listSampleIndexSequenceAngleGratingNumbers[[indexAngle, 1]];
   listSampleFilenamesAtThatAngle = filenamesSample[[indexFilename]] ];

funcGetSampleFilenamesForSpecificGroup[samplegroup_] := Module[{},
   (*indexGroup = Flatten[Position[
       listSampleSequenceNumbersGroupBounds[[All,1]], p_? (#==samplegroup &)]];*)
   indexGroup = listSampleSequenceNumbersGroups[[samplegroup]] -
     sequenceNumberSampleMinimum + 1 ;
   listSampleFilenamesAtThatGroup = filenamesSample[[indexGroup]] ];

funcGetSampleMininumSeqenceNumberForSpecificAngle[angle_] := Module[{},
   indexAngle = Flatten[Position[
      listSampleIndexSequenceAngleGratingNumbers[[All, 3]], p_? (# == angle &)]];
   sequenceNumber = listSampleIndexSequenceAngleGratingNumbers[[indexAngle, 2]];
   Min[sequenceNumber] ];
```

```
funcGetReferenceFilenamesforSpecficAngle[angle_] := Module[{},
   sequenceNumberSampleMinimum =
    funcGetSampleMininumSeqenceNumberForSpecificAngle[angle];
   listFilenamesAtSpecificAngle = funcGetSampleFilenamesForSpecificAngle[angle];
   groupNumberReference = Last[Position[listReferenceSequenceNumbersGroups,
       p_?(# ≤ sequenceNumberSampleMinimum &)]][[1]];
   indexReferenceSeqenceNumbers = listReferenceSequenceNumbersGroups[[
     groupNumberReference, All]];
   indexReferenceFilenames = Flatten[Table[
      Position[listReferenceIndexSequenceGratingNumbers[[All, 2]],
       indexReferenceSeqenceNumbers[[i]]], {i, Length[indexReferenceSeqenceNumbers]}]];
   filenamesReference[[indexReferenceFilenames]] ];
```

Plot functions for interferometry results

```
funcPlotTransmissionVisbilityPhiFit[testPoint_, plotLabel_,
  transmissionMatrix_, visbilityMatrix_, phiMatrix_, interferogram_] := Module[{},
  gReferenceTransmission = ArrayPlot[transmissionMatrix,
    PlotRange → {All, All, climTrans}, ColorFunction → "GrayTones",
    ClippingStyle → {Black, White}, Frame → False,
    PlotLabel → plotLabel <> " transmission, θ=" <>
      ToString[angle] <> ", test point=" <> ToString[testPointOne],
    Axes → True, AspectRatio → rows / columns, ImageSize → 300,
    PlotLegends → {Placed[BarLegend[{"GrayTones", climTrans}], Right]},
    Epilog → {PointSize → Large, Point[{testPoint}]}];
  gReferenceVisibility = ArrayPlot[visbilityMatrix,
    PlotRange → {All, All, climVis}, ColorFunction → "GrayTones",
    ClippingStyle → {Black, White}, Frame → False,
    PlotLabel → plotLabel <> " visibility",
    Axes → True, AspectRatio → rows / columns, ImageSize → 300,
    PlotLegends → {Placed[BarLegend[{"GrayTones", climVis}], Right]}];

  gReferencePhi =
   ArrayPlot[phiMatrix, PlotRange → {All, All, climPhi}, ColorFunction → "GrayTones",
    ClippingStyle → {Black, White}, Frame → False,
    PlotLabel → plotLabel <> " phi",
    Axes → True, AspectRatio → rows / columns, ImageSize → 300,
    PlotLegends → {Placed[BarLegend[{"GrayTones", climPhi}], Right]}];
  yExpt = interferogram[[testPointOne[[2]], testPointOne[[1]], All]];
  xExpt = listGratingStepsMicrons;
  transmission = transmissionMatrix[[testPoint[[2]], testPoint[[1]]]];
  visibility = visbilityMatrix[[testPoint[[2]], testPoint[[1]]]];
  phi = phiMatrix[[testPoint[[2]], testPoint[[1]]]];
  yCalc = Table[transmission +
     visibility Sin[2 π xExpt[[i]] / gratingPeriodMicrons + phi], {i, Length[xExpt]}];
   plotString = "transmission=" <> ToString[transmission] <> "\n" <>
```

```
    "visibility=" <> ToString[visibility] <> "\n" <>
    "phi=" <> ToString[phi];
  gFitReference = ListPlot[
    {Transpose[{xExpt, yExpt}], Transpose[{xExpt, yCalc}]}, Joined → {False, True},
    Frame → True, FrameLabel → {{"intensity", ""},
      {"grating position/μm", plotLabel <> ", test point=" <> ToString[testPoint]}},
    Epilog → Inset[Style[Text[plotString], 12], Scaled[{0.4, 0.85}]]], ImageSize → 300];
  gAllReference = Grid[
    {{gReferenceTransmission, gReferenceVisibility}, {gReferencePhi, gFitReference}}] ]

funcPlotAbsorptionDPCDarkFieldILDC[plotLabel_,
  absorptionMatrix_, dpcMatrix_, darkfieldMatrix_] := Module[{},
  gAbsorption = ArrayPlot[absorptionMatrix,
    PlotRange → {All, All, climAbs}, ColorFunction → "GrayTones",
    ClippingStyle → {Black, White}, Frame → False,
    PlotLabel → "absorption, θ=" <> ToString[angle],
    Axes → True, AspectRatio → rows / columns, ImageSize → 300,
    PlotLegends → {Placed[BarLegend[{"GrayTones", climAbs}], Right]}];
  gDPC =
   ArrayPlot[dpcMatrix, PlotRange → {All, All, climDPC}, ColorFunction → "GrayTones",
    ClippingStyle → {Black, White}, Frame → False,
    PlotLabel → "DPC, θ=" <> ToString[angle],
    Axes → True, AspectRatio → rows / columns, ImageSize → 300,
    PlotLegends → {Placed[BarLegend[{"GrayTones", climDPC}], Right]}];
  gDarkField = ArrayPlot[darkfieldMatrix,
    PlotRange → {All, All, climDarkField}, ColorFunction → "GrayTones",
    ClippingStyle → {Black, White}, Frame → False,
    PlotLabel → "dark-field, θ=" <> ToString[angle],
    Axes → True, AspectRatio → rows / columns, ImageSize → 300,
    PlotLegends → {Placed[BarLegend[{"GrayTones", climDarkField}], Right]}];

  x = Range[rows];
  listColumns = Range[50, columns - 50, 200];
  numberOfColumns = Length[listColumns];
  lineProbeVertical = Take[absorptionMatrix, All, {50, columns - 50, 200}];
  gAbsorptionLineProbe =
   ListPlot[Table[Transpose[{x, (i - 1) * Max[climAbs] + lineProbeVertical[[All, i]]}],
     {i, numberOfColumns}], Joined → True, Frame → True,
    FrameLabel → {{"absorption", ""}, {"row", plotLabel}},
    Epilog → Table[Style[Text[listColumns[[i]], {10, (i - 1) * Max[climAbs]}],
      12, Background → White], {i, numberOfColumns}], ImageSize → 300];
  lineProbeVertical = Take[dpcMatrix, All, {50, columns - 50, 200}];
  gDPCLineProbe =
   ListPlot[Table[Transpose[{x, (i - 1) * Max[climDPC] + lineProbeVertical[[All, i]]}],
     {i, numberOfColumns}], Joined → True, Frame → True,
    FrameLabel → {{"DPC", ""}, {"row", plotLabel}},
```

```
  Epilog → Table[Style[Text[listColumns[[i]], {10, (i - 1) * Max[climDPC]}],
     12, Background → White], {i, numberOfColumns}], ImageSize → 300];
linePrObeVertical = Take[darkfieldMatrix, All, {50, columns - 50, 200}];
gDarkFieldLineProbe = ListPlot[
  Table[Transpose[{x, (i - 1) * Max[climDarkField] + linePrObeVertical[[All, i]]}],
   {i, numberOfColumns}], PlotRange →
   {All, (1 + numberOfColumns) * Max[climDarkField]}, Joined → True, Frame → True,
  FrameLabel → {{"dark-field", ""}, {"row", plotLabel}},
  Epilog → Table[Style[Text[listColumns[[i]], {10, (i) * Max[climDarkField]}],
     12, Background → White], {i, numberOfColumns}], ImageSize → 300];
gAllAbsDPCDarkFieldILDC = Grid[{{gAbsorption, gDPC, gDarkField, gILDC},
   {gAbsorptionLineProbe, gDPCLineProbe, gDarkFieldLineProbe, gILDCLineProbe}}]   ]
```

Step 2: Paths, filenames, and grouping: Set interferometer steps and period

```
Clear[pathTIFF, pathHDF5]
pathTIFF = NotebookDirectory[] <> "data/"
pathDark = NotebookDirectory[] <> "data/"
pathHDF5 = NotebookDirectory[] <> "HDF5_g/";
pathFITS = NotebookDirectory[] <> "FITS_g/";
pathSlices = NotebookDirectory[] <> "slices_muhrec/";
pathFigures = NotebookDirectory[] <> "figures_g/";
pathVolumes = NotebookDirectory[] <> "volumes/";
pathSino = NotebookDirectory[] <> "sinograms/";

G2gratingPeriodMicrons = 4.8;
(*distanceSampletoG2=171000;*) (*microns,  mm*)

funcFindDarkB16files[pathDark];
FirstDark = filenamesDark[[1]]
{rows, columns} = Dimensions[funcReadPCOFileUncorrected[FirstDark]]
referenceDarkfield = funcReadDarkfield[filenamesDark];
Dimensions[referenceDarkfield]


funcFindReferenceB16files[pathTIFF];
funcFindSampleB16files[pathTIFF];
funcFindReferenceGroups[];
funcFindSampleGroups[];
```

```
cropRows = {1, rows};
cropColumns = {1, columns};
{rows, columns} =
  {(Max[cropRows] - Min[cropRows] + 1), (Max[cropColumns] - Min[cropColumns] + 1)};
gratingPeriodMicrons = 4.8
(* input for numberGratingSteps *)
numberGratingSteps
listGratingStepsMicrons = Table[(i - 1) * 0.48, {i, 1, numberGratingSteps}]
doseROI = {{10, 150}, {35, 190}}; (* same coordinates as Muhrec **)
```

```
TableForm[{{"sample name", testNameStr},
  {"grating period (in microns)", gratingPeriodMicrons},
  {"grating steps (in microns)", {listGratingStepsMicrons}},
  {"# of grating steps", numberGratingSteps},
  {"# of reference images", numberOfReferenceFiles},
  {"# of reference groups", numberOfReferenceGroups},
  {"bounds: reference groups", listReferenceSequenceNumbersGroupsBounds},
  {"# of sample images", numberOfSampleFiles},
  {"# of sample groups", numberOfSampleGroups},
  {"bounds: sample groups", listSampleSequenceNumbersGroupsBounds} }]
```

```
listSampleAngles
numberOfAngles = Length[listSampleAngles]
```

```
listSampleAngles[[1]]
```

```
numberOfSampleGroups
```

Step 3: For any angle, process reference and sample

initialize vectors used for the calculation

```
funcPrepareAllVectors[gratingPeriodMicrons, listGratingStepsMicrons, rows, columns]
{Dimensions[gMatrix], Dimensions[bVector], Dimensions[aVector],
 Dimensions[aMatrix], Dimensions[visibility], Dimensions[phi]}
```

set angle for calculation, find the correct filenames

```
listSampleAngles
```

```
listSampleGroup = Table[i, {i, 1, numberOfSampleGroups}]
```

```
angle = First[listSampleAngles]

(*angle =89.995*)
listFilenamesReferenceOneInterferogram =
 funcGetReferenceFilenamesforSpecficAngle[angle]
listFilenamesSampleOneInterferogram =
 funcGetSampleFilenamesForSpecificGroup[First[listSampleGroup]]
(*listFilenamesSampleOneInterferogram=funcGetSampleFilenamesForSpecificAngle[angle]*)
```

calculate transmission, visibility, and phi for reference and sample

```
numberGratingSteps

listGratingStepsMicrons = funcReadListGratingStepsMicrons[
  listFilenamesReferenceOneInterferogram, numberGratingSteps]
funcPrepareAllVectors[gratingPeriodMicrons, listGratingStepsMicrons, rows, columns]
{Dimensions[gMatrix], Dimensions[bVector], Dimensions[aVector],
 Dimensions[aMatrix], Dimensions[visibility], Dimensions[phi]}

interferogramReference = funcReadOneInterferogram[
   listFilenamesReferenceOneInterferogram, rows, columns, listGratingStepsMicrons];
Dimensions[interferogramReference]
{referenceTransmission, referenceVisibility, referencePhi} =
  funcCalculateTransmissionVisibilityPhi[interferogramReference];
{Dimensions[referenceTransmission], Min[referenceTransmission],
 Mean[Flatten[referenceTransmission]] // N, Max[referenceTransmission]}
{Dimensions[referenceVisibility], Min[referenceVisibility],
 Mean[Flatten[referenceVisibility]] // N, Max[referenceVisibility]}
{Dimensions[referencePhi], Min[referencePhi],
 Mean[Flatten[referencePhi]] // N, Max[referencePhi]}
timeImage

listGratingStepsMicrons =
 funcReadListGratingStepsMicrons[listFilenamesSampleOneInterferogram, numberGratingSteps]
funcPrepareAllVectors[gratingPeriodMicrons, listGratingStepsMicrons, rows, columns]
{Dimensions[gMatrix], Dimensions[bVector], Dimensions[aVector],
 Dimensions[aMatrix], Dimensions[visibility], Dimensions[phi]}
```

```
interferogramSample = funcReadOneInterferogram[
   listFilenamesSampleOneInterferogram, rows, columns, listGratingStepsMicrons];
Dimensions[interferogramSample]
{sampleTransmission, sampleVisibility, samplePhi} =
  funcCalculateTransmissionVisibilityPhi[interferogramSample];
{Dimensions[sampleTransmission], Min[sampleTransmission],
 Mean[Flatten[sampleTransmission]] // N, Max[sampleTransmission]}
{Dimensions[sampleVisibility], Min[sampleVisibility],
 Mean[Flatten[sampleVisibility]] // N, Max[sampleVisibility]}
{Dimensions[samplePhi], Min[samplePhi], Mean[Flatten[samplePhi]] // N, Max[samplePhi]}
timeImage
```

correct for bad pixels: referenceTransmission, sampleTransmission, referenceVisibility

plot transmission, visibility, and phi for reference and sample

```
testPointOne = {(Round[columns / 2] + 60), Round[rows / 2]};
(*climTrans = {Min[referenceTransmission],Max[referenceTransmission]};*)
climTrans = {Min[referenceTransmission], 8000};
(*climVis = {Min[referenceVisibility],Max[referenceVisibility]};*)
climVis = {Min[referenceVisibility], 1500};
climPhi = {Min[referencePhi], Max[referencePhi]};
gAllReference = funcPlotTransmissionVisbilityPhiFit[testPointOne, "ref",
  referenceTransmission, referenceVisibility, referencePhi, interferogramReference]
```

```
Dimensions[sampleTransmission]
```

```
gAllSample = funcPlotTransmissionVisbilityPhiFit[testPointOne, "sample",
  sampleTransmission, sampleVisibility, samplePhi, interferogramSample]
```

```
Export[pathFigures <> "trans_DPC_DF_fit_" <> ToString[angle] <> ".png", gAllSample, "PNG"]
```

calculate absorption, differential phase contrast, and dark-field

```
absorption = -Log[sampleTransmission / referenceTransmission] // N;
{Min[absorption], Mean[Flatten[absorption]], Max[absorption]}
```

```
differentialPhase = samplePhi - referencePhi;
{Min[differentialPhase], Mean[Flatten[differentialPhase]], Max[differentialPhase]}
differentialPhase = funcCorrectLargeDPCvalue[differentialPhase];
{Min[differentialPhase], Mean[Flatten[differentialPhase]], Max[differentialPhase]}
```

```
darkfield = (sampleVisibility / referenceVisibility) / (sampleTransmission / referenceTransmission);
{Min[darkfield], Mean[Flatten[darkfield]], Max[darkfield]}
```

plot absorption, differential phase contrast, and dark-field

```
plotLabel = "vertical sensitivity";
climAbs = {0, 1.2}; climDPC = 0.5 * {-π, π};
climDarkField = {0, 1}; climILDC = {0, 1`*^-11};

gAbsDpcDF =
 funcPlotAbsorptionDPCDarkFieldILDC[plotLabel, absorption, differentialPhase, darkfield]

Export[pathFigures <> "abs_DPC_DF_" <> ToString[angle] <> ".png", gAbsDpcDF, "PNG"]
```

plot doseROI

```
doseROI
columnROI = {doseROI[[1, 2]], doseROI[[2, 2]]}
rowROI = {doseROI[[1, 1]], doseROI[[2, 1]]}
ImageResize[ImageAdjust[Image[Take[absorption, columnROI, rowROI], "Real"]], 500]
meanBackgroundAbsorptionSelectedAngle =
 Mean[Flatten[Take[absorption, columnROI, rowROI]]]
meanBackgroundDPCSelectedAngle =
 Mean[Flatten[Take[differentialPhase, columnROI, rowROI]]]
meanBackgroundDarkFieldSelectedAngle = Mean[Flatten[Take[darkfield, columnROI, rowROI]]]
```

Step 4: For all angles, process reference and sample

initialize vectors used for the calculation

```
funcPrepareAllVectors[gratingPeriodMicrons, listGratingStepsMicrons, rows, columns]
{Dimensions[gMatrix], Dimensions[bVector], Dimensions[aVector],
 Dimensions[aMatrix], Dimensions[visibility], Dimensions[phi]}
```

for all angles, calculate transmission, visibility, and phi for reference and sample, store HDF5, FITS

```
listReferenceAngles

listSampleGroup

oldlistFilenamesReferenceOneInterferogram = {" "};
listTimeAngle = Table[Module[{},
```

```
(*angle =listReferenceAngles[[indexListAngle]];*)
samplegroup = listSampleGroup[[indexListGroup]];
listFilenamesReferenceOneInterferogram =
 funcGetReferenceFilenamesforSpecficAngle[angle];
Print[{1, "# of ref images =", Length[listFilenamesReferenceOneInterferogram]}];
If[First[oldlistFilenamesReferenceOneInterferogram] !=
  First[listFilenamesReferenceOneInterferogram],
 listGratingStepsMicrons = funcReadListGratingStepsMicrons[
   listFilenamesReferenceOneInterferogram, numberGratingSteps];
 funcPrepareAllVectors[gratingPeriodMicrons, listGratingStepsMicrons, rows, columns] =
  {Dimensions[gMatrix], Dimensions[bVector], Dimensions[aVector],
   Dimensions[aMatrix], Dimensions[visibility], Dimensions[phi]};
 interferogramReference = funcReadOneInterferogram[
   listFilenamesReferenceOneInterferogram,
   rows, columns, listGratingStepsMicrons]; ];
{referenceTransmission, referenceVisibility, referencePhi} =
 funcCalculateTransmissionVisibilityPhi[interferogramReference];

listFilenamesSampleOneInterferogram =
 funcGetSampleFilenamesForSpecificGroup[samplegroup];
Print[{indexListGroup, "# of sample images =",
  Length[listFilenamesSampleOneInterferogram]}];
listGratingStepsMicrons = funcReadListGratingStepsMicrons[
  listFilenamesSampleOneInterferogram, numberGratingSteps];
funcPrepareAllVectors[gratingPeriodMicrons, listGratingStepsMicrons, rows, columns] =
 {Dimensions[gMatrix], Dimensions[bVector], Dimensions[aVector],
  Dimensions[aMatrix], Dimensions[visibility], Dimensions[phi]};
interferogramSample = funcReadOneInterferogram[listFilenamesSampleOneInterferogram,
  rows, columns, listGratingStepsMicrons];
Print[{indexListGroup, samplegroup, timeImage}];
{sampleTransmission, sampleVisibility, samplePhi} =
 funcCalculateTransmissionVisibilityPhi[interferogramSample];

referenceTransmission = funcCorrectForZeroValuePixels[referenceTransmission];
sampleTransmission = funcCorrectForZeroValuePixels[sampleTransmission];
referenceVisibility = funcCorrectForZeroValuePixels[referenceVisibility];

absorption = -Log[ sampleTransmission / referenceTransmission ]  // N;
    meanBackgroundAbsorption = Mean[Flatten[Take[absorption, columnROI, rowROI]]];
    absorption = absorption - meanBackgroundAbsorption;
differentialPhase = samplePhi - referencePhi;
    differentialPhase = funcCorrectLargeDPCvalue[differentialPhase];
    meanBackgroundDPC = Mean[Flatten[Take[differentialPhase, columnROI, rowROI]]];
    differentialPhaseCorr = differentialPhase - meanBackgroundDPC;
```

```
    differentialPhaseCorr = funcCorrectLargeDPCvalue[differentialPhaseCorr];

    darkfield =
     sampleVisibility / referenceVisibility / sampleTransmission / referenceTransmission;

    darkfield = funcCorrectForOutOfRangeDarkField[darkfield];

    sampleVisibilityPer = 100 * sampleVisibility / sampleTransmission;


    filenameHDF5 = testNameStr <> "_" <> IntegerString[indexListGroup, 10, 5] <> "_" <>
      ToString[NumberForm[angle, {6, 4}, NumberPadding → {"0", "0"}]] <> ".h5";
    filenameFITSabs = testNameStr <> "_3B" <> "_abs_" <>
      IntegerString[indexListGroup, 10, 5] <> ".fits";
    filenameFITSdpc = testNameStr <> "_3B" <> "_dpc_" <>
      IntegerString[indexListGroup, 10, 5] <> ".fits";
    filenameFITSdpcCorr = testNameStr <> "_3B" <> "_dpcCorr_" <>
      IntegerString[indexListGroup, 10, 5] <> ".fits";
    filenameFITSdarkfield = testNameStr <> "_3B" <> "_darkfield_" <>
      IntegerString[indexListGroup, 10, 5] <> ".fits";
    Export[pathHDF5 <> filenameHDF5, {absorption, differentialPhase,
      differentialPhaseCorr, darkfield, sampleVisibilityPer},
     {"Datasets", {"absorption", "dpc", "dpcCorr", "darkfield", "sampleVisibilityPer"}}];
    Export[pathFITS <> filenameFITSabs, absorption];
    Export[pathFITS <> filenameFITSdpc, differentialPhase];
    Export[pathFITS <> filenameFITSdpcCorr, differentialPhaseCorr];
    Export[pathFITS <> filenameFITSdarkfield, darkfield];
    (*Export[pathFITS<>filenameFITSiLDC,iLDC];*)
    Export[pathFITS <> filenameFITSsampleVisibilityPer, sampleVisibilityPer];
    {timeImage, angle}],
   {indexListGroup, numberOfSampleGroups}];
DateListPlot[listTimeAngle,
 DateTicksFormat -> {"MonthShort", "/", "Day", ":", "Hour"}, Joined → False,
 Frame → True, FrameLabel → {{"rotation angle", ""}, {"date:24-hr time", testNameStr}}]
```

C.2. Sample Tomopy Codes for Stepped-grating Interferometry

Step 1: Initialization

In [ ]:
```
# -*- coding: utf-8 -*-
from __future__ import print_function
import os
from os import listdir
from os.path import isfile, join
import numpy
from PIL import Image
import matplotlib.pyplot as plt
import numpy as np
import string
from numpy.linalg import inv  #matrix calc
import math #log
import scipy
import scipy.ndimage
import scipy.signal #median filter for zero bad pixels
from astropy.io import fits #fits file read and writeTo
np.set_printoptions(suppress=True) #no scientific notations
import re #sort fits files
from IPython.display import clear_output #clear output
```

Descriptions: make sure you put "raw/" file in the correct path

In [ ]:
```
# user defined section
workdir = "/run/media/tomouser/MercurySSD/1to1FRBL-265C_p141_dataProcessing/" #change your path here
rawPath = "/run/media/tomouser/MercurySSD/1to1FRBL-265C_p141/"
yourRawFilename = rawPath
angleIncrement = 1
par = angleIncrement
try:
    os.stat(os.path.join(workdir, 'FITS')) #create export file: FITS
except:
    os.mkdir(os.path.join(workdir, 'FITS'))
```

Step 2: functions

Step 2.1: Reading files

In [ ]:
```
def readFile(path, string):   #search string "white" and "raw"
    allFiles = [f for f in listdir(path) if isfile(join(path,f))]
    for n in range(0, len(allFiles)):
        allFiles[n] = join(path,allFiles[n])
    allFiles.sort(key=lambda var:[int(x) if x.isdigit() else x for x in re.findall(r'[^0-9]|[0-9]+', var)])
    #use "regular expression" to sort filenames
    listfile = [];
    for seq in range (0, len(allFiles)):
        if string in allFiles[seq]:
            listfile.append(allFiles[seq])
    print ('There are '+ str(len(listfile))+ ' '+ string + ' files')
    return(listfile)
```

Step 2.2: grouping

In [ ]:
```
def grouping(listfiles):
    GroupList = [np.int(listfiles[0].split(".")[seqNum])]
    numfiles = len(listfiles)
    for i in range(numfiles-1):
        if (np.int(listfiles[i+1].split(".")[seqNum]) > np.int(listfiles[i].split(".")[seqNum]) + 1):
            GroupList.append(np.int(listfiles[i].split(".")[seqNum]))
            GroupList.append(np.int(listfiles[i+1].split(".")[seqNum]))
    GroupList.append(np.int(listfiles[len(listfiles)-1].split(".")[seqNum]))
    GroupList = np.transpose(GroupList)
    Group = np.reshape(GroupList, (len(GroupList)/2, 2))
    return(Group)
```

In [ ]:
```
def funcGetSampleFilenamesForSpecificAngle(angle):
    sampleFileForThisAngle = []
    for i in range(0, numSample):
        if (angle == np.float(".".join([sampleFiles[i].split(".")[angle1], sampleFiles[i].split(".")[angle2]]))):
          sampleFileForThisAngle.append(sampleFiles[i])
    return(sampleFileForThisAngle)
```

In [ ]:
```
def funcGetWhiteFilenamesForSpecificAngle(angle):
    seq1 = np.int(funcGetSampleFilenamesForSpecificAngle(angle)[0].split(".")[seqNum])
    pos = np.array(np.where(sampleGroup[:,1] >= seq1)).flatten()[0]
    for i in range(numWhite):
        if (refGroup[pos,:][0] == np.int(whiteFiles[i].split(".")[seqNum])):
            startNum = i
    listRefFilenamesAtThatAngle = []
    for i in range(12):
       listRefFilenamesAtThatAngle.append(whiteFiles[startNum + i])
    return(listRefFilenamesAtThatAngle)
```

Step 2.3: Function for interferometry

In [ ]:
```
def funcPrepareBvectorArbitrarySteps(gratingPeriodMicrons, listGratingStepsMicrons):
    numberGratingSteps = len(listGratingStepsMicrons)
    b1 = np.ones((numberGratingSteps))
    b2 = np.zeros((numberGratingSteps))
    b3 = np.zeros((numberGratingSteps))
    for i in range(numberGratingSteps):
        b2[i] = np.sin(2*np.pi*listGratingStepsMicrons[i] / gratingPeriodMicrons)
        b3[i] = np.cos(2*np.pi*listGratingStepsMicrons[i] / gratingPeriodMicrons)
    return(np.column_stack((b1,b2,b3)))
#funcPrepareBvectorArbitrarySteps(gratingPeriodMicrons, listGratingStepsMicrons)
```

In [ ]:
```
def funcPrepareAllVectors(gratingPeriodMicrons, listGratingStepsMicrons, rows, columns):
    bVector = funcPrepareBvectorArbitrarySteps(gratingPeriodMicrons, listGratingStepsMicrons)
    aVector = cVector = np.zeros((3, rows * columns))
    aMatrix = np.zeros((rows, columns, 3))
    amplitude = phi = np.zeros((rows, columns))
    gMatrix = np.dot(inv(np.dot(np.transpose(bVector), bVector)), np.transpose(bVector))
    return(gMatrix, bVector, aVector, aMatrix, amplitude, phi)
```

In [ ]:
```
def funcReadOneInterferogram(listFilenamesOneInterferogram, rows, columns, listGratingStepsMicrons):
    numberGratingSteps = len(listGratingStepsMicrons)
    allData = np.zeros((rows, columns, numberGratingSteps))
    for index in range(numberGratingSteps):
        filename = listFilenamesOneInterferogram[index]
        intensity = np.array(Image.open(filename))
        allData[:,:,index] = intensity
    return(allData)
```

In [ ]:
```
def funcCalculateOffsetAmplitudePhi(data):
    numberGratingSteps = len(listGratingStepsMicrons)
    cVector = np.transpose(np.reshape(data, (rows*columns, numberGratingSteps)))
    aVector = np.dot(gMatrix, cVector)
    aMatrix = np.reshape(np.transpose(aVector), (rows, columns, 3))
    offset = aMatrix[:,:,0]
    amplitude = np.sqrt(aMatrix[:,:,1]**2 + aMatrix[:,:,2]**2)
    phi = np.arctan2(aMatrix[:,:,2], aMatrix[:,:,1])
    #visibilityPercent = 100 * amplitude / offset
    return(offset, amplitude, phi)
```

In [ ]:
```
def funcCorrectForZeroValuePixels(dataOriginal):
    coordinatesZeroIntensityPixels = np.transpose(np.where(dataOriginal == 0))
    if (len(coordinatesZeroIntensityPixels > 0)):
        dataCorrected = dataOriginal
        dataMedianFilter = scipy.signal.medfilt(dataOriginal, 3) # medfilt Ordering = 1 doesn't work
    for index in range(len(coordinatesZeroIntensityPixels)):
        [r, c] = coordinatesZeroIntensityPixels[index]
        dataCorrected[r, c] = dataMedianFilter[r, c]
    return(dataCorrected)
```

In [ ]:
```
def funcCorrectLargeDPCValue(data):
    dataCorrected = data
    coordinatesLargeDPC = np.transpose(np.where(data > np.pi))
    if (len(coordinatesLargeDPC) > 0):
        for index in range(len(coordinatesLargeDPC)):
            [r, c] = coordinatesLargeDPC[index]
            dataCorrected[r,c] = data[r, c] - 2*np.pi
    coordinatesLargeDPC = np.transpose(np.where(differentialPhase < -np.pi))
    if (len(coordinatesLargeDPC) > 0):
        for index in range(len(coordinatesLargeDPC)):
            [r, c] = coordinatesLargeDPC[index]
            dataCorrected[r, c] = data[r, c] + 2*np.pi
    return(dataCorrected)
```

Step 3: Paths, filenames and grouping

In [ ]:
```
rawData = os.path.join(rawPath, yourRawFilename)
fitsFile = os.path.join(workdir, 'FITS/')
print ('Your working directory is "', workdir, '"')
print ()
```

In [ ]:
```
whiteFiles = readFile(rawData, '.white.')
sampleFiles = readFile(rawData, '.raw.')

print()
numWhite = len(whiteFiles)
numSample = len(sampleFiles)
print (np.transpose(whiteFiles[0:4]))
print()
print (np.transpose(sampleFiles[0:4]))
```

In [ ]:
```
#user defined
print (whiteFiles[50])
print ()
print (whiteFiles[50].split("."))
seqNum = 5; #user defined number
print ()
print ("Is " + whiteFiles[50].split(".")[seqNum] + " the correct sequence number for grouping?" )
print ("(If not, please change 'seqNum' value above. Thanks!)")
```

In [ ]:
```
#user defined for angle searching
print ('is this the angle for the filename?')
print ()
angle1 = 3
angle2 = 4
print(np.float(".".join([whiteFiles[40].split(".")[angle1], whiteFiles[40].split(".")[angle2]])))
print("\n(please change angle1 and angle2 values above if this number is incorrect. Thanks!)")
```

In [ ]:
```
#run grouping function for white and raw files
print('Reference files grouping:')
print (grouping(whiteFiles))
print()
print ("Sample files grouping:")
print (grouping(sampleFiles))
refGroup = grouping(whiteFiles)
sampleGroup = grouping(sampleFiles)
```

Step 4: Look at one angle here

In [ ]:
```
#user defined
angle = 145 #integer here 0-190 degree with 1 degree increment
print ('the one angle you want to look at is: ', angle, '\n')
print('If not, please change angle =', angle, 'above. Thanks!')
```

In [ ]:
```
listFilenamesSampleOneInterferogram = funcGetSampleFilenamesForSpecificAngle(angle)
print (np.transpose(listFilenamesSampleOneInterferogram))
print('\nNumber of angle', angle, 'sample files:', len(listFilenamesSampleOneInterferogram))
```

In [ ]:
```
listFilenamesReferenceOneInterferogram = funcGetWhiteFilenamesForSpecificAngle(angle)
print (np.transpose(listFilenamesReferenceOneInterferogram))
```

In [ ]:
```
[rows, columns] = np.array(Image.open(sampleFiles[0])).shape
#no cropping
print ('rows = ', rows)
print ('columns = ', columns)
gratingPeriodMicrons = 4.8 #pixel size = ? microns
listGratingStepsMicrons = np.zeros((12))
for i in range(0, 12):
    listGratingStepsMicrons[i] = i*0.48
print (listGratingStepsMicrons)
```

In [ ]:
```
print ('sample name:                    ', whiteFiles[0].split("/")[seqNum].split(".")[0])
print ('grating period (in microns):    ', gratingPeriodMicrons)
print ('grating steps (in microns):     ', listGratingStepsMicrons)
print ('# of grating steps:             ', len(listGratingStepsMicrons))
print ('# of reference images (white):  ', len(whiteFiles))
print ('# of reference groups:          ', len(refGroup))
print ('# of sample images (raw):       ', len(sampleFiles))
```

In [ ]:
```
listSampleAngles = np.zeros((np.int(190/par+1)))
for i in range(len(listSampleAngles)):
    listSampleAngles[i] = i*par
print ('There are', len(listSampleAngles), 'angles:', '\n\n', listSampleAngles)
numberOfAngles = len(listSampleAngles)
clear_output()
```

initialize vectors used for the calculation

In [ ]:
```
[gMatrix, bVector, aVector, aMatrix, amplitude, phi] = funcPrepareAllVectors(gratingPeriodMicrons,
                                                                             listGratingStepsMicrons, rows, columns)
print (gMatrix.shape)
print (bVector.shape)
print (aVector.shape)
print (aMatrix.shape)
print (amplitude.shape)
print (phi.shape)
```

In [ ]:
```
interferogramReference = funcReadOneInterferogram(listFilenamesReferenceOneInterferogram, rows, columns,
                                                  listGratingStepsMicrons)
print (interferogramReference.shape)
```

In [ ]:
```
np.seterr(divide='ignore', invalid='ignore') #code have some "divided by zero" or "Nan" appears
[referenceOffset, referenceAmplitude, referencePhi] = \
    funcCalculateOffsetAmplitudePhi(interferogramReference)
print ('reference Offset:')
print (referenceOffset.shape, np.min(referenceOffset),
      np.mean(referenceOffset.flatten()), np.max(referenceOffset))
print ('reference Amplitude')
print (referenceAmplitude.shape, np.min(referenceAmplitude),
      np.mean(referenceAmplitude.flatten()), np.max(referenceAmplitude))
print ('reference Phi')
print (referencePhi.shape, np.min(referencePhi),
      np.mean(referencePhi.flatten()), np.max(referencePhi))
```

In [ ]:
```
interferogramSample = funcReadOneInterferogram(listFilenamesSampleOneInterferogram, rows, columns,
                                               listGratingStepsMicrons)
print (interferogramSample.shape)
```

In [ ]:
```
[sampleOffset, sampleAmplitude, samplePhi] = funcCalculateOffsetAmplitudePhi(interferogramSample)
print ('sample Tranmission:')
print (sampleOffset.shape, np.min(sampleOffset),
      np.mean(sampleOffset.flatten()), np.max(sampleOffset))
print ('sample Amplitude')
print (sampleAmplitude.shape, np.min(sampleAmplitude),
      np.mean(sampleAmplitude.flatten()), np.max(sampleAmplitude))
print ('sample Phi')
print (samplePhi.shape, np.min(samplePhi),
      np.mean(samplePhi.flatten()), np.max(samplePhi))
```

In [ ]:
```
print (np.transpose(np.where(referenceOffset == 0)))
referenceOffset = funcCorrectForZeroValuePixels(referenceOffset)
print (np.transpose(np.where(referenceOffset == 0)))

print (np.transpose(np.where(sampleOffset == 0)))
sampleOffset = funcCorrectForZeroValuePixels(sampleOffset)
print (np.transpose(np.where(sampleOffset == 0)))

print (np.transpose(np.where(referenceAmplitude == 0)))
referenceAmplitude = funcCorrectForZeroValuePixels(referenceAmplitude)
print (np.transpose(np.where(referenceAmplitude == 0)))
```

plot trans, vis, and phi for ref and sample

In [ ]:
```
testPointOne = (np.round(columns/2), np.round(rows/2))
print (testPointOne)
climOffset = [np.min(referenceOffset), np.max(referenceOffset)]
climAmplitude = [np.min(referenceAmplitude), np.max(referenceAmplitude)]
climPhi = [np.min(referencePhi), np.max(referencePhi)]
```

In [ ]:
```
plt.imshow(referenceOffset, cmap='gray')
#plt.colorbar()
plt.show()
plt.imshow(referenceAmplitude, cmap='gray')
plt.show()
plt.imshow(referencePhi, cmap='gray')
plt.show()
clear_output()
```

In [ ]:
```
plt.imshow(sampleOffset, cmap='gray')
plt.show()
plt.imshow(sampleAmplitude, cmap='gray')
plt.show()
plt.imshow(samplePhi, cmap='gray')
plt.show()
clear_output()
```

calculate abs, dpc, and dark-field

In [ ]:
```
absorption = -np.log(sampleOffset / referenceOffset)
print (np.min(absorption), np.mean(absorption.flatten()), np.max(absorption))
```

In [ ]:
```
differentialPhase = samplePhi - referencePhi
print (np.min(differentialPhase), np.mean(differentialPhase.flatten()), np.max(differentialPhase))
```

In [ ]:
```
differentialPhase = funcCorrectLargeDPCValue(differentialPhase)
print (np.min(differentialPhase), np.mean(differentialPhase.flatten()), np.max(differentialPhase))
```

In [ ]:
```
darkfield = (sampleAmplitude / referenceAmplitude) / (sampleOffset / referenceOffset)
print (np.min(darkfield), np.mean(darkfield), np.max(darkfield))
```

In [ ]:
```
plt.imshow(absorption, cmap = 'gray')
plt.show()
plt.imshow(differentialPhase, cmap = 'gray', vmax = np.pi, vmin = -np.pi)
plt.show()
plt.imshow(darkfield, cmap = 'gray', vmax = 1, vmin = 0)
plt.show()
#clear_output()
```

Step 5: for all angles, process ref and sample

In [ ]:
```
[gMatrix, bVector, aVector, aMatrix, amplitude, phi] = funcPrepareAllVectors(gratingPeriodMicrons,
                                                                             listGratingStepsMicrons, rows, columns)
print (gMatrix.shape, bVector.shape, aVector.shape, aMatrix.shape, amplitude.shape, phi.shape)
```

In [ ]:
```
sampleNamePosi = 6
oldlistFilenamesReferenceOneInterferogram = " "
sampleName = whiteFiles[0].split("/")[sampleNamePosi].split(".")[0]
print('sample name:', sampleName)
numberOfAngles
```

In [ ]:
```
for indexListAngle in range(numberOfAngles):
    angle = listSampleAngles[indexListAngle]
    listFilenamesReferenceOneInterferogram = funcGetWhiteFilenamesForSpecificAngle(angle)

    print (indexListAngle, '# of ref images =', len(listFilenamesReferenceOneInterferogram))
    if (oldlistFilenamesReferenceOneInterferogram != listFilenamesReferenceOneInterferogram[0]):
        interferogramReference = funcReadOneInterferogram(listFilenamesReferenceOneInterferogram, rows,
                                                          columns, listGratingStepsMicrons)
    [referenceOffset, referenceAmplitude, referencePhi] = funcCalculateOffsetAmplitudePhi(interferogramReference)

    listFilenamesSampleOneInterferogram = funcGetSampleFilenamesForSpecificAngle(angle)
    print (indexListAngle, '# of sample images =', len(listFilenamesSampleOneInterferogram))
    interferogramSample = funcReadOneInterferogram(listFilenamesSampleOneInterferogram, rows,
                                                   columns, listGratingStepsMicrons)
    print (indexListAngle, angle)
    [sampleOffset, sampleAmplitude, samplePhi] = funcCalculateOffsetAmplitudePhi(interferogramSample)
    referenceOffset = funcCorrectForZeroValuePixels(referenceOffset)
    sampleOffset = funcCorrectForZeroValuePixels(sampleOffset)
    referenceAmplitude = funcCorrectForZeroValuePixels(referenceAmplitude)
    absorption = -np.log(sampleOffset / referenceOffset)
    differentialPhase = samplePhi - referencePhi
    #differentialPhase = funcCorrectLargeDPCValue(differentialPhase)
    darkfield = (sampleAmplitude / referenceAmplitude) / (sampleOffset / referenceOffset)
    #darkfield = 1 - darkfield
    #fits file writeTo http://docs.astropy.org/en/stable/io/fits/
    visibilityPercent = 100* sampleAmplitude/referenceAmplitude

    #write abs FITS files
    absFilename = os.path.join(fitsFile, sampleName + '_abs_' + np.str(angle/par+1) + '.fits')
    try: #remove file if exits
        os.remove(absFilename)
    except OSError:
        pass
    absFits = fits.HDUList([fits.PrimaryHDU(absorption)])
    absFits.writeto(absFilename)
    absFits.close()
```

```
#write dpc FITS files
dpcFilename = os.path.join(fitsFile, sampleName + '_dpc_' + np.str(angle/par+1) + '.fits')
try: #remove file if exits
    os.remove(dpcFilename)
except OSError:
    pass
dpcFits = fits.HDUList([fits.PrimaryHDU(differentialPhase)])
dpcFits.writeto(dpcFilename)
dpcFits.close()

#write darkfield FITS files
dfFilename = os.path.join(fitsFile, sampleName + '_darkfield_' + np.str(angle/par+1) + '.fits')
try: #remove file if exits
    os.remove(dfFilename)
except OSError:
    pass
dfFits = fits.HDUList([fits.PrimaryHDU(darkfield)])
dfFits.writeto(dfFilename)
dfFits.close()

#write visibilityPercent FITS files
visPerFilename = os.path.join(fitsFile, sampleName + '_visibilityPercent_' + np.str(angle/par+1) + '.fits')
try: #remove file if exits
    os.remove(visPerFilename)
except OSError:
    pass
visPerFits = fits.HDUList([fits.PrimaryHDU(visibilityPercent)])
visPerFits.writeto(visPerFilename)
visPerFits.close()
clear_output()
```

C.3. Sample Tomopy Codes for Volume Reconstruction

Reconstruction with Tomopy/Astra modules

Descriptions: "FITS" folder is needed

In [ ]:
```
path = '/mnt/wwn-0x588891410021e4f3-part1/1to1FRBL-265C_p141_dataProcessing/'
absFitsFileName = 'FITS/'
darkFitsFileName = 'FITS/'
dpcFitsFileName = 'FITS/'
angleIncrement = 1
par = angleIncrement
```

Step 1: Initialization

In [ ]:
```
# -*- coding: utf-8 -*-
from __future__ import print_function
import tomopy
import os
from os import listdir
from os.path import isfile, join
import numpy
from PIL import Image
import matplotlib.pyplot as plt
import numpy as np
import string
from numpy.linalg import inv  #matrix calc
import math #log
import scipy
import scipy.ndimage
import scipy.signal #median filter for zero bad pixels
from astropy.io import fits #fits file read and writeTo
import re #sort fits files
from IPython.display import clear_output #clear output
```

Step 2: Functions

Step 2.1: Read files

In [ ]:
```
def readFile(path, string):   #search string "white" and "raw"
    allFiles = [f for f in listdir(path) if isfile(join(path,f))]
    for n in range(0, len(allFiles)):
        allFiles[n] = join(path,allFiles[n])
    allFiles.sort(key=lambda var:[int(x) if x.isdigit() else x for x in re.findall(r'[^0-9]|[0-9]+', var)])
    #use "regular expression" to sort filenames
    listfile = [];
    for seq in range (0, len(allFiles)):
        if string in allFiles[seq]:
            listfile.append(allFiles[seq])
    print ('There are '+ str(len(listfile))+ ' '+ string + ' files')
    return(listfile)
```

Step 3: path, read files and filenames

set path and filenames

In [ ]:
```
workdir = path
absFITS = os.path.join(workdir, absFitsFileName)
darkFITS = os.path.join(workdir, darkFitsFileName)
dpcFITS = os.path.join(workdir, dpcFitsFileName)
print ('Your working directory is: ', workdir)
print (absFITS)
```

read abs fits files and create abs volume

In [ ]:
```
index = 80 #look at one fit file here
absFitsFiles = readFile(absFITS, 'abs')
numFiles = len(absFitsFiles)
print (absFitsFiles[index])
oneImage = fits.open(absFitsFiles[index])
oneImage.info()
#oneImage.close()
oneImageArray = oneImage[0].data
oneImageArray.shape
plt.imshow(oneImageArray[:, 1:487], 'gray')
plt.show()

print ('Image dimension is', oneImageArray.shape)
[X, Y] = oneImageArray.shape
print ('X is', X, 'and Y is', Y)
allAbs = np.zeros((numFiles, X, Y)) #create abs volume
print (allAbs.shape)

for index in range(numFiles):
    oneImage = fits.open(absFitsFiles[index])
    oneImageArray = oneImage[0].data
    allAbs[index, :, :] = oneImageArray
#plt.imshow(allAbs[index, :, :], 'gray')
#plt.show()
allAbs.dtype
```

read darkfield fits files and create (1-dark) volume

In [ ]:
```
darkFitsFiles = readFile(darkFITS, 'dark')
oneImage = fits.open(darkFitsFiles[index])
oneImage.info()
#oneImage.close()
oneImageArray = oneImage[0].data
oneImageArray.shape
plt.imshow(oneImageArray, 'gray', vmin = 0, vmax=1)
plt.show()
print ('Image dimension is', oneImageArray.shape)
[X, Y] = oneImageArray.shape
print ('X is', X, 'and Y is', Y)
allDark = np.zeros((numFiles, X, Y))
print (allDark.shape)
for index in range(numFiles):
    oneImage = fits.open(darkFitsFiles[index])
    oneImageArray = oneImage[0].data
    allDark[index, :, :] = 1 - oneImageArray
#plt.imshow(allDark[index, :, :], 'gray',vmin =0, vmax = 1)
#plt.show()
allDark.dtype
```

read dpc fits files

In [ ]:
```
dpcFitsFiles = readFile(dpcFITS, 'dpc')
oneImage = fits.open(dpcFitsFiles[index])
oneImage.info()
#oneImage.close()
oneImageArray = oneImage[0].data
oneImageArray.shape
plt.imshow(oneImageArray, 'gray', vmin = -np.pi, vmax=np.pi)
plt.show()
print ('Image dimension is', oneImageArray.shape)
[X, Y] = oneImageArray.shape
print ('X is', X, 'and Y is', Y)
allDPC = np.zeros((numFiles, X, Y))
print (allDPC.shape)
for index in range(numFiles):
    oneImage = fits.open(dpcFitsFiles[index])
    oneImageArray = oneImage[0].data
    allDPC[index, :, :] = oneImageArray
#plt.imshow(allDPC[index, :, :], 'gray',vmin =-np.pi, vmax = np.pi)
#plt.show()
allDPC.dtype
```

cropping images

In [ ]:
```
absProj = allAbs[:, 75:196, 1:487]
dpcProj = allDPC[:, 75:196, 1:487]
darkProj = allDark[:, 75:196, 1:487]
absProj.shape
```

In [ ]:
```
plt.imshow(absProj[:, 80, :], cmap='Greys_r')
plt.show()
plt.imshow(absProj[90, :, :], cmap='Greys_r')
plt.show()
#clear_output()
```

In [ ]:
```
plt.imshow(dpcProj[80, :, :], cmap='Greys_r', vmax = np.pi, vmin = -np.pi)
#plt.colorbar()
plt.show()
plt.imshow(dpcProj[:, 80, :], cmap='Greys_r', vmax = np.pi, vmin = -np.pi)
#plt.colorbar()
plt.show()
#clear_output()
```

In [ ]:
```
plt.imshow(darkProj[80, :, :], cmap='Greys_r', vmin = 0, vmax=1)
#plt.colorbar()
plt.show()
plt.imshow(darkProj[:, 80, :], cmap='Greys_r', vmin = 0, vmax=1)
#plt.colorbar()
plt.show()
print (np.max(darkProj))
print (np.min(darkProj))
#clear_output()
```

In [ ]:
```
proj = dpcProj
print (np.max(proj))
print (np.min(proj))
#theta = tomopy.angles(proj.shape[0])
startAngle = 0
endAngle = 190
print (startAngle, endAngle*np.pi/180, proj.shape[0])
theta = []
for i in range(proj.shape[0]):
    theta.append(i*par*np.pi/180)
print (np.transpose(theta))
#clear_output()
```

find rotation center

In [ ]:
```
rot_center = tomopy.find_center(proj, theta, init=236, ind=28, tol=0.5)
#proj = tomopy.minus_log(proj)
#remove outlier before recon
print (rot_center)
```

In [ ]:
```
#defined by yourself
rot_center = 263
```

Step 4: TomoPy Reconstruction

In [ ]:
```
recon = tomopy.recon(absProj, theta, center=rot_center, algorithm='gridrec')
recon = tomopy.circ_mask(recon, axis=0, ratio=0.99)
plt.imshow(recon[95, :,:], cmap='Greys_r')
plt.colorbar()
plt.show()
```

In [ ]:
```
#save the reconstructed volume
import h5py
with h5py.File(os.path.join(workdir, 'absRecon_Tomopy_Gridrec.h5'), 'w') as hf:
    hf.create_dataset('slice', data=recon)
```

In [ ]:
```
recon = tomopy.recon(darkProj, theta, center=rot_center, algorithm='gridrec')
recon = tomopy.circ_mask(recon, axis=0, ratio=0.99)
plt.imshow(recon[95, :,:], cmap='Greys_r')
plt.colorbar()
plt.show()
```

In [ ]:
```
#save the reconstructed volume
import h5py
with h5py.File(os.path.join(workdir, 'darkRecon_Tomopy_Gridrec.h5'), 'w') as hf:
    hf.create_dataset('slice', data=recon)
```

In [ ]:
```
recon = tomopy.recon(dpcProj, theta, center=rot_center, algorithm='gridrec')
recon = tomopy.circ_mask(recon, axis=0, ratio=0.99)
plt.imshow(recon[95, :,:], cmap='Greys_r')
plt.colorbar()
plt.show()
```

Step 5: ASTRA Reconstruction

Step 5.1 sirt for dpc

In [ ]:
```
#tomopy.astra?
extra_options ={'MinConstraint':-np.pi}
options = {'proj_type':'cuda', 'method':'SIRT_CUDA', 'num_iter':40,'extra_options':extra_options}
dpcRecon = tomopy.recon(dpcProj, theta, center=rot_center, algorithm=tomopy.astra, options=options)
dpcRecon = tomopy.circ_mask(dpcRecon, axis=0, ratio=0.99)
plt.imshow(dpcRecon[95, :,:], cmap='Greys_r', vmin = np.min(dpcRecon)/2, vmax = np.max(dpcRecon)/2)
plt.colorbar()
plt.show()
```

In [ ]:
```
import h5py
with h5py.File(os.path.join(workdir, 'dpcRecon_Astra_SIRT_CUDA_iter40.h5'), 'w') as hf:
    hf.create_dataset('slice', data=dpcRecon)
```

sirt for dark-field

In [ ]:
```
#tomopy.astra?
extra_options ={'MinConstraint':-1}
options = {'proj_type':'cuda', 'method':'SIRT_CUDA', 'num_iter':40,'extra_options':extra_options}
darkRecon = tomopy.recon(darkProj, theta, center=rot_center, algorithm=tomopy.astra, options=options)
darkRecon = tomopy.circ_mask(darkRecon, axis=0, ratio=0.85)
plt.imshow(darkRecon[95, :,:], cmap='Greys_r', vmin = np.min(darkRecon), vmax = np.max(darkRecon))
plt.colorbar()
plt.show()
```

In [ ]:
```
import h5py
with h5py.File(os.path.join(workdir, 'darkRecon_Astra_SIRT_CUDA_iter40.h5'), 'w') as hf:
    hf.create_dataset('slice', data=darkRecon)
```

sirt for absorption

In [ ]:
```
#tomopy.astra?
extra_options ={'MinConstraint':0}
options = {'proj_type':'cuda', 'method':'SIRT_CUDA', 'num_iter':40,'extra_options':extra_options}
absRecon = tomopy.recon(absProj, theta, center=rot_center, algorithm=tomopy.astra, options=options)
absRecon = tomopy.circ_mask(absRecon, axis=0, ratio=0.85)
```

In [ ]:
```
plt.imshow(absRecon[95, :,:], cmap='Greys_r', vmin = np.min(absRecon), vmax = np.max(absRecon))
plt.colorbar()
plt.show()
```

In [ ]:
```
import h5py
with h5py.File(os.path.join(workdir, 'absRecon_Astra_SIRT_CUDA_iter40.h5'), 'w') as hf:
    hf.create_dataset('slice', data=absRecon)
```

VITA

Omoefe Kio was born in Oyo state, Nigeria. She had her secondary school education at St. Lukes Grammar School, Lagos, Nigeria. Following her secondary school studies, she proceeded to the University of Lagos where she obtained her Bachelor of Science degree in Industrial Chemistry. Her undergraduate research involved the study of the corrosion inhibitive properties of naturally occurring products like *Gossypium hirsutum* L under the supervision of Dr. Olusegun K. Abiola.

She joined the graduate program of the Louisiana State University Chemistry department in January 2014 with Dr. Leslie Butler as her research advisor. Her research focuses on X-ray grating-based interferometry and its potential application in additive manufacturing. She has co-authored a number of conference papers and peer-reviewed publication during her graduate studies.